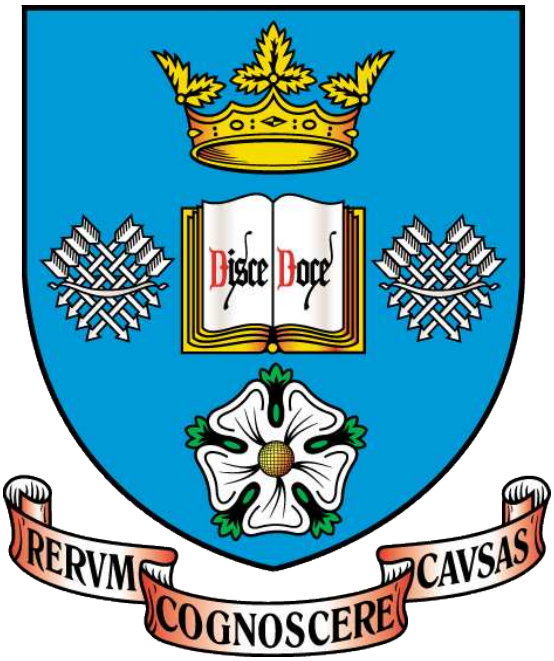

Evaluation of the Solute Transport Characteristics of Surcharged Manholes using a RANS Solution

A thesis submitted to the University of Sheffield in partial fulfilment of the requirements for the degree of Doctor of Philosophy

Paul Bennett M.Eng.

Supervised by Virginia Stovin and Ian Guymer

2012

This document was prepared using LaTeX

Declaration

I declare that the work in this thesis has been composed by myself and no portion of the work has been submitted in support of an application for another degree or qualification of this or any other university or other institute of learning. The work has been my own except where indicated and all quotations have been distinguished by quotations marks and the sources of information have been acknowledged.

Abstract

Urban drainage networks contain a large number of structures; the most common of which is a manhole. Previous studies investigating solute transport through manholes identified a threshold level of surcharge at which the hydraulic conditions in the manholes sharply altered. At high levels of surcharge, a dead zone formed above the main jet, potentially retaining solute for later discharge. This phenomenon could have significant impacts on the results obtained from 1D urban drainage network models which only consider pure advection. Previous research (including other CFD based studies) concentrated on steady flow conditions through these structures which are not thought to be representative of the dynamic flow conditions experienced in practice.

During large storm events, the capacity of combined sewer networks may be exceeded. This leads to the discharge of untreated sewage to receiving watercourses. Discharges such as these are governed by legislation and, therefore, an understanding of pollutant transfer through urban drainage networks is required.

Using existing laboratory and Computational Fluid Dynamics (CFD) data, this study produced a primary and secondary validated methodology for meshing and modelling manholes using CFD. This was then extended to free-surface multiphase modelling allowing for more realistic unsteady conditions to be considered. This included an in-depth comparison of suitable turbulence models and solute-modelling options. It was found that, whilst it was possible to model multiphase free-surface flow within such a structure, it was unnecessarily computationally expensive as temporal changes in the flow field are rapid when compared with a practical time-step for use with 1D models.

The validated modelling methodology was then used to recreate the original study that identified the hydraulic threshold. This included a selection of manholes with a range of inlet to manhole diameter ratios. However, this was extended further to include manholes with a ratio less than five (commonly found in UK sewer systems). It was shown that the hydraulic threshold broke down below this limit, removing the need for this to be modelled in 1D systems.

Keywords: Manhole, Mixing, RANS, Solute, Surcharge, Unsteady, k-ϵ Realizable.

Acknowledgements

My thanks must firstly go to Dr. Virginia Stovin for her help, support and guidance throughout this entire process. Without it, I'm sure the information contained within would have been of a lesser quality.

Professor Ian Guymer (Warwick) and Amy Jones (Warwick) offered endless advice and discussion which allowed the thesis to follow a logical progression due to frequent in-depth meetings for which I am very grateful. I only hope that any advice offered by myself was of equal quality and use.

I must also thank the residents of D106 (at times a mixed bunch) for their support. No matter how small or large the issue, someone was always able and willing to help.

Finally, thanks to my Fiancée Natalie, for the endless support and patience shown throughout my time completing this Thesis.

Table of Contents

List of Figures

List of Tables

Notation

$\%u_{diff}$	Percentage error in velocity at a given point
α_q	Cell volume fraction
δ	Discrete-time interval equivalent of the time delay $\tau/\Delta t$
ϵ	Turbulent dissipation rate
Γ	Volumetric mass transfer coefficient
$\hat{p}$	Piezometric pressure
μ	Dynamic viscosity
ν	Kinematic viscosity
$\bar{t}$	Travel time $(t_2 - t_1)$
ρ	Density
σ_ϵ	Empirical constant
σ_k	Empirical constant
τ	Time delay $(t'_2 - t'_1)$
$\vec{v}$	Velocity Vector
A_{ratio}	Cell aspect ratio
$c(x_1, t)$	Concentration at longitudinal position, x_i at time t

C_μ	Empirical constant
$C_{1\epsilon}$	Empirical constant
$C_{2\epsilon}$	Empirical constant
$E(\tau)$	RTD
M_e	Maximum Entropy
R_t^2	Goodness of fit
S_a	Cross-sectional averaged tracer concentration
S_{ij}	Mean strain rate
t_i'	First arrival time at location i
t_i	Time of passage of the centroid of a tracer cloud at site i
$t_{nominal}$	Nominal travel time
u_{CFD}	Velocity at a given point according to CFD data
u_{PIV}	Velocity at a given point according to PIV data
u_{VOF}	Velocity at a given point according to VOF data
y^+	Non-dimensional wall distance
${\sigma_t}^2(x_i)$	Temporal variance at x_i
${\sigma_v}^2(x_i)$	Volumetric variance at x_i
${\sigma_x}^2(x_i)$	Spatial variance at x_i
$\mathrm{D_M}$	Manhole diameter
$\mathrm{D_p}$	Pipe diameter
A	Cross-sectional area
c	Concentration
D	Dispersion coefficient

d	RTD estimate
K_x	Longitudinal dispersion coefficient
l	Length scale
M	Tracer Mass
MF	Mass fraction
P	Pressure
Q	flow-rate
Re	Reynolds number
S	Surcharge ratio
s	Surcharge
s'	Hydraulic threshold surcharge level
u	Mean fluid velocity
u*	Shear velocity
V	Volume
V_x	Cross-sectional averaged velocity
vol	Change in cumulative volume
x	Distance

Acronyms

ADE Advection-Diffusion Equation

ADZ Aggregated Dead-Zone

CFD Computational Fluid Dynamics

CHP Central Horizontal Plane

CICSAM Compressive Interface Capturing Scheme for Arbitrary Meshes

CIS Cells in Series

CRTD Cumulative Residence Time Distribution

CSO Combined Sewer Overflow

CSTR Continually Stirred Tank Reactor

CTCP Cumulative Temporal Concentration Profiles

CVP Central Vertical Plane

DNS Direct Numerical Simulation

DRW Discrete Random Walk

DWF Dry Weather Flow

EWT Enhanced Wall Treatment

FFF First Foul Flush

HRIC High Resolution Interface Capturing

LES Large Eddy Simulation

LIF Laser Induced Fluorescence

PIV Particle Image Velocimetry

PT Particle Tracking

RANS Reynolds Averaged Navier-Stokes

RNG Renormalisation k-ϵ Turbulence Model

RSM Reynolds Stress Model

RTD Residence Time Distrubtion

TCP Temporal Concentration Profiles

TSC Time Scale Constant

VOF Volume of Fluid

WWTW Waste Water Treatment Works

Chapter 1

Introduction

1.1 Background

In the UK the majority of sewer systems are combined (70% by total length, Butler and Davies (2004)). In dry weather, a combined system carries wastewater. During a rainfall event the flow within the sewers increases because of additional stormwater. Even during light rainfall events the flow within the system is predominantly stormwater. This stormwater can be between fifty and one hundred times the average wastewater flow during heavy storm events (Butler and Davies, 2004). As it is infeasible to provide the capacity to deal with such volume (as for the majority of the time only a small proportion would be utilised), the solution implemented was to add Combined Sewer Overflows (CSOs) which allow for the discharge of excess water to neighbouring water courses. It was initially thought that, due to the high amount of stormwater, any discharge would be sufficiently diluted as to avoid pollution issues. However, this is not always the case; high flows lead to increased flushing of sewers, and pollution is also incorporated during surface run-off, thus leading to unsatisfactory discharges from CSOs. This has become a common problem and the focus of modern regulations and legislation.

The current 6^{th} phase of the Water Framework Directive (2000) sets new goals for the conditions of EU water. *'The overall goal is a good and non-deteriorating status for all waters (surface, underground and coastal)'.* This is on top of any

nation-wide existing legislation (such as 'The Bathing Water Directive', 1976, and 'The Urban Waste Water Treatment Directive', 1991). For surface waters *'the objective is that of a good ecological and chemical quality status'* (Kallis and Butler, 2001).

As legislation requires increasingly stringent targets on water quality it is becoming necessary to better understand the behaviour and interaction of sewer networks and storm events (usually through 1D modelling). It is important to know both the quantity and quality of water discharged at sensitive downstream locations (such as CSOs).

Commercial computational analysis software, such as Infoworks (Wallingford Software Ltd.), Storm Water Management Model (SWMM) and MOUSETRAP (Danish Hydraulic Institute) used to predict sewer performance, are increasingly used by the water industry for hydraulic and water quality simulation. These models use fundamental hydraulic theory and water quality models to predict the transport of solute and sediment in an urban drainage network. However, whilst modelling flow and transport through a pipe is simple (Guymer *et al.*, 2005a) other structures (such as manholes, storage tanks and CSOs) are less so, requiring energy loss coefficients and mixing parameters (such as travel time and dispersion parameters) to make accurate predictions.

Guymer and O'Brien (1995) began investigating solute transport in manholes (section 2.6) in order to provide information that could be utilised by commercial sewerage system modelling software such as MOUSETRAP. The study aimed to quantify dispersion due to surcharged manholes. The effects of a number of different configurations were then considered in later work by Guymer and O'Brien (1996, 1998 and 2000), Saiyudthong (2003) and Guymer *et al.* (2005a). These studies investigated the effects of, diameter, step height, change in pipe direction and benching on the mixing processes within manholes.

Guymer *et al.* (2005a) studied the effects of manhole diameter on longitudinal dispersion in surcharged manholes. Four unbenched manholes were considered with D_M/D_p ratios (manhole diameter / pipe diameter) of 4.4, 5.5, 6.8 and 9.1 (these relate to manhole diameters of 385, 485, 600 and 800 mm with a fixed pipe diameter of 88 mm) under a wide range of surcharge conditions and flow rates.

Guymer *et al.* (2005a) identified a surcharge level at which the solute transport

characteristic of the manholes sharply altered; at low surcharge (termed 'pre-threshold') the travel times varied linearly with surcharge, at high surcharge (termed 'post-threshold') the travel times dropped to a low, constant level. This threshold was more pronounced for the manholes with high D_M/D_p ratios. The existence of two distinctly different flow regimes was confirmed by Lau (2008) using Particle Image Velocimetry (PIV) techniques. At high levels of surcharge, a dead zone formed above the main jet, (potentially) retaining solute for later discharge. It was thought that this phenomenon could have significant impacts on the results obtained from 1D urban drainage network models (used by industry) which only consider pure advection. These studies (Guymer *et al.*, 2005a, Lau, 2008) concentrated on steady flow conditions through these structures which are not thought to be representative of the dynamic flow conditions experienced in practice.

The optimised Advection-Diffusion Equation (ADE) and Aggregated Dead-Zone (ADZ) model coefficient results showed travel time, dispersion coefficients and dispersive fraction for models with the same discharge and surcharge conditions to increase with manhole diameter. This is in agreement with theory, as the manhole diameter increases, so too does the volume of water available for mixing.

The study determined sets of parameters for ADE and ADZ model coefficients, discharge and surcharge level for the four manholes investigated. It was suggested that, as per the original aim, these model parameters could be used in water quality models to improve temporal and spatial water quality predictions. However, it was also noted that the laboratory results were limited to the range of configurations and hydraulic conditions used.

Water Research Centre PLC (2006) suggests the configurations investigated by Guymer *et al.* (2005a) ($D_M/D_p > 4.4$) may not be representative of those found in UK sewer systems (typically with a $D_M/D_p < 4$). Therefore, the solute transport characteristics of 'small diameter' manholes ($D_M/D_p < 4.4$) is currently unknown.

Computational Fluid Dynamics (CFD) (as a tool) is increasingly being used in the water industry (Jarman *et al.*, 2007, Tabor, 2010) as it offers benefits over laboratory based studies/scale models. Once a validated modelling methodology has been produced it allows for changes in geometry, configurations, flowrate etc. to be evaluated with comparative ease. This makes it especially suitable where

it is necessary to model a high number of configurations. Stovin (1996), Grimm (2003) and Lau (2008) (which includes extensive validation) have shown CFD to be a robust method of modelling flow fields, as well as sediment and solute transport within urban drainage structures during the evaluation of such changes.

1.2 Aims

Previous manhole studies (Guymer and O'Brien (2000), Guymer *et al.* (2005a), Saiyudthong (2003) and Lau (2008)) concentrated on the solute transport characteristics of manholes in steady conditions, for manhole sizes uncommon to that found in UK sewer networks (Water Research Centre PLC, 2006) and were limited by the range of configurations investigated. Therefore, the current study aims to build on, and extend previous work by:

- Developing a highly-validated CFD modelling methodology to allow solute transport characteristics to be established for multiple manhole configurations
- Investigating the feasibility of extending work into 'more realistic' unsteady conditions including free-surface modelling (as suggested by Lau (2008))
- Extending work into smaller (more realistic) D_M/D_p sized manholes (more common to UK sewer networks and previously unstudied)

1.3 Structure of the Thesis

- Chapter 1 (the current chapter) introduces the background and context of the work, as well as its aims, and the structure in which it has been addressed.
- Chapter 2 contains a thorough literature review which details previous theoretical and experimental work relevant to the study.
- Chapter 3 presents a number of questions which have been tested through a logical progression of modelling scenarios undertaken before the main

programme of the study. This allowed the author to determine the feasible scope of the core study and offered insight into the physical limitations that would likely be encountered going forward to more complex scenarios.

- Chapter 4 contains the methodology and results for creating the validated modelling strategy used in chapter 6 (including mesh independence). It contains a detailed look into three possible turbulence modelling options and their resultant flow fields when compared to existing laboratory PIV data as well as existing CFD manhole models previously investigated by Lau (2008). This chapter also investigates FLUENTs solute transport modelling options and determines a validated method of using the discrete-phase particle tracking model. Multiphase models within FLUENT are tested, allowing for pseudo-steady free-surface scenarios to be modelled, these are compared with the 'fixed (rigid) lid' (section 2.5.10.2.3) simulations.

- Chapter 5 presents a CFD representation of a manhole laboratory set-up currently under investigation at The University of Warwick (Jones, 2012). Using the validated modelling procedure developed in chapter 4, laboratory results relating specifically to the identification of the threshold are replicated using CFD offering further validation. Methods for determining the threshold location from CFD and laboratory data are also evaluated.

- Chapter 6 uses the validated methodology presented in chapters 4 and 5 to create a CFD version of the original Guymer *et al.* (2005a) study. This was extended to include manholes with a ratio (D_M/D_p) more commonly found in UK sewer networks. A new flow regime was encountered and detailed within.

- Chapter 7 contains conclusions from the prior chapters and presents potential scope for further work relevant to the study and methodologies used throughout.

Throughout this thesis, flow is from left to right (unless otherwise indicated).

Chapter 2

Literature Review

2.1 Introduction

This chapter aims to provide a review of literature relevant to this research. Section 2.3 introduces fundamental hydraulic principles. This is then followed by a brief introduction to mixing in turbulent flows and solute transport modelling, including an overview of the ADE frozen cloud routing procedure. Computational Fluid Dynamics (CFD) is introduced as well as the relevant turbulence models, discretization schemes and options for modelling solute transport. Recommendations for best practice when using these models and relevant parameters are also detailed. After this, a brief overview of relevant previous work is presented.

2.2 Urban Drainage

In urban areas drainage systems are needed because of the interaction between human activity and the natural water cycle. These interactions have two main types:

- The abstraction of water from the cycle to provide a water supply for living.
- The covering of land with impermeable surfaces that divert rainwater away

from the natural system of drainage.

These two types of interactions give rise to two types of water that requires drainage:

- Wastewater - Originating from both home and industrial use. After use, if this is not drained correctly it could present pollution and health risks. Wastewater contains dissolved material, fine solids and larger solids.
- Stormwater - Rainwater (or water from any other type of precipitation) that has fallen on a built up area. If stormwater is not drained properly it can cause flooding, damage and potential further health risks. Stormwater can contain pollutants that originate from both air and run-off surfaces.

Most urban areas rely on a completely artificial system of sewers, pipes and structures that collect and dispose of this water. However, in isolated communities this is not always the case. In this instance wastewater is treated locally and stormwater is drained naturally. In the UK two types of sewerage systems are implemented (Butler and Davies, 2004), combined or separate.

2.2.1 Combined Sewer System

In the UK the majority of sewer systems are combined (70% by total length, Butler and Davies (2004)). In dry weather a combined system carries wastewater. During a rainfall event the flow within the sewers increases because of the additional stormwater. Even during light rainfall events the flow within the system will predominantly be stormwater. This stormwater can be between fifty and one hundred times the average wastewater flow during heavy storm events (Butler and Davies, 2004). It is obviously infeasible to provide the capacity to deal with such volumes, as for the majority of the time only a small proportion would be utilised. The solution implemented was to add Combined Sewer Overflows (CSOs) which allowed for the discharge of excess water to neighbouring water courses. It was initially thought that, due to the high amount of stormwater, any discharge would be sufficiently diluted as to avoid any pollution issues (Butler and Davies, 2004). However this is not always the case. High flows lead

to increased flushing of sewers, pollution is also incorporated during overland flows thus leading to unsatisfactory discharges from CSOs which have become a common problem.

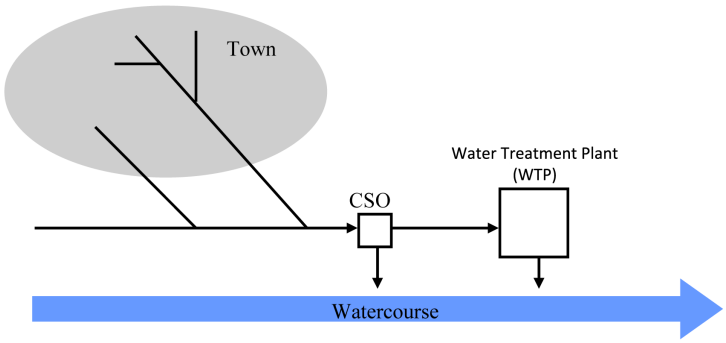

Figure 2.1: Schematic diagram of a combined system (after Butler and Davies 2004)

2.2.2 Separate Sewer System

Since 1945 most sewer systems constructed in the UK are separate (30% by total length) (Butler and Davies, 2004). In a separate system, wastewater and stormwater are carried in separate pipes (usually laid side by side). Wastewater flows vary throughout the day. However, the pipes have the required capacity to carry the maximum flow to treatment. The stormwater remains separate from this system and is discharged to a water course at a convenient location. This type of system removes the need for CSOs and hence the pollution issues associated with them. However, it does have some disadvantages. One obvious disadvantage is cost, although the increase in cost is not proportional to the number of pipes added and is mainly due to an increased excavation width required to lay both pipes. Perfect separation of the two flow types is effectively impossible. It is very hard to stop infiltration from rain water into the foul pipe and it is impossible to ensure that only polluted material is carried by this pipe as wrong connections are a high possibility as well as pollutant from the catchment run-off.

A comparison of both systems is shown in table 2.1.

Separate System	Combined system
Advantages	**Disadvantages**
No CSOs - potentially less pollution of watercourse	CSOs necessary to keep main sewers and treatment works feasible size
Smaller Waste Water Treatment Works (WWTW)	Larger treatment works inlets necessary, probably with provision for stormwater diversion and storage
Stormwater pumped only if necessary	Line is a compromise, and may necessitate long branch connections. Optimum depth for stormwater collection might not suit wastewater
Wastewater and storm sewers may follow own optimum line and depth	Slow Shallow flow in large sewers in dry weather flow may cause deposition and decomposition of solids
Wastewater sewer small, and greater velocities maintained at low flows	Wide variation in flow to pumps, flow strength and flow to wastewater treatment works
Less variation in flow and strength of wastewater	Grit removal (if necessary)
No road grit in wastewater sewers	If flooding and surcharge of manholes occurs, foul conditions will be caused
Any flooding will be storm water only	
Disadvantages	**Advantages**
Extra cost of two pipes	Lower pipe construction costs
Additional space occupied in narrow streets and built up areas	Economical in space
More house drains, with risk of wrong connections	House drainage simpler and cheaper
No flushing of deposited wastewater by stormwater	Deposited wastewater solids flushed out in times of storm
No treatment of stormwater	Some treatment of stormwater

Table 2.1: Comparison of combined and separate sewer systems (after Butler and Davies 2004

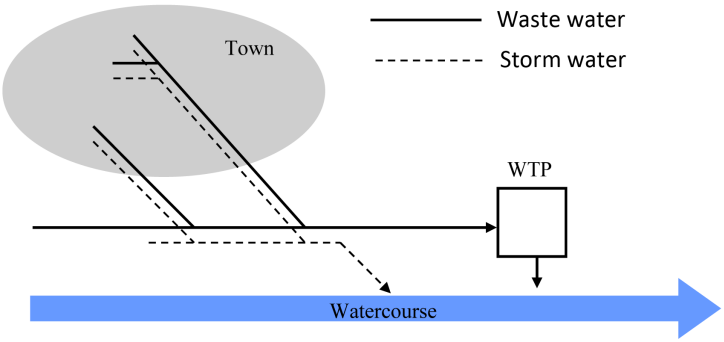

Figure 2.2: Schematic diagram of a separate system (after Butler and Davies 2004)

2.2.3 Urbanisation

When rainwater falls on a natural surface, some evaporates or is returned to the atmosphere via transpiration of plants, some infiltrates into the surface to become groundwater and the rest is surface run-off. The proportions of this depend on the surface properties and vary during a storm event (run-off increases with ground saturation). Development in urban areas involves paving and covering the ground with artificial surfaces, which has a significant impact on these processes. Surface run-off is increased as infiltration is more difficult. This run-off travels quicker over artificial surfaces and in sewers than over natural surfaces and watercourses. This leads to a flow that arrives and dies away faster and therefore a higher peak flow. This increases the danger of sudden flooding as well as having implications on water quality. Extra run-off is more likely to encounter pollution on artificial surfaces than the natural environment (Butler and Davies, 2004). Combined drainage systems allow in-sewer mixing which may cause sanitary sewage pollutants to be discharged to a natural watercourse via a CSO.

2.2.4 The First Foul Flush (FFF)

In early storm flows a significant feature is the First Foul Flush (FFF) (Butler and Davies, 2004). The FFF may contain high pollutant loads which are likely to have originated from:

- Catchment surface wash off and gully pots

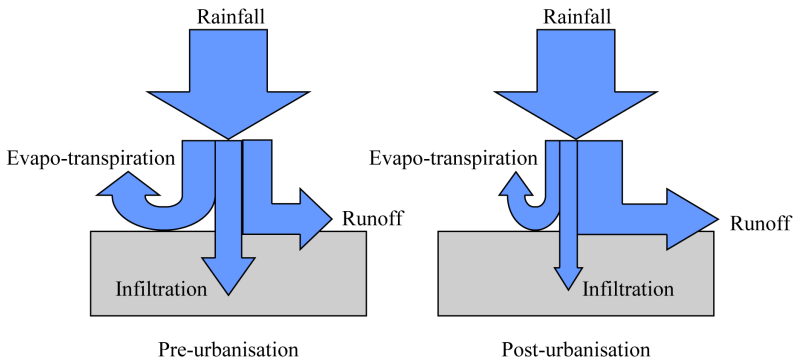

Figure 2.3: Effect of urbanisation on fate of rainfall (after Butler and Davies 2004)

- Wastewater flow
- Near-bed solids
- Pipe sediments

A FFF can be identified by a sharp increase in pollutant load near the start of a storm even. A plot of cumulative load against cumulative flowrate (figure 2.4) also allows for the identification of the FFF, a 45° line indicates a uniform distribution of pollutant throughout the storm.

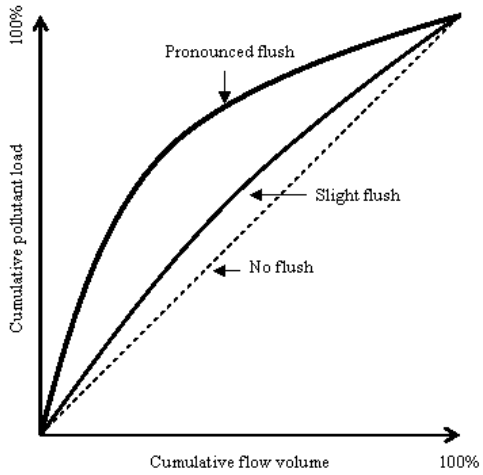

Figure 2.4: Representation of the FFF (after Butler and Davies 2004)

If pollutant concentration varies in time (e.g. according to the FFF), then dispersion processes in the sewer system may be critical in determining when, and

at what concentrations, they arrive at vulnerable downstream locations such as CSOs.

2.2.5 Manholes

Manholes are an integral part of any sewerage systems and are commonly constructed out of pre-cast concrete rings. Manholes are provided at (BS EN 752-3: 1997):

- changes in direction
- heads of runs
- changes in gradient
- changes in size
- major junctions with other sewers
- every 90 m

In larger pipes where man-access is possible (although undesirable) this spacing may be increased up to 200 m (Butler and Davies, 2004). The main purpose of a manhole is to allow human access to the sewer (this may be for inspection, cleaning or maintenance etc.). Sizing is dependent on the size of sewer and the orientation and number of inlets, guidelines for manhole sizing can be found in BS EN 479:1997. In combined systems, under storm conditions, manholes may surcharge to considerable depths. It is the hydraulic conditions and subsequent solute transport conditions that develop, that form the focus of this thesis.

2.3 Fundamental Hydraulic Principles

2.3.1 Laminar and Turbulent Flows

Reynolds conducted an experiment towards the latter end of the 19^{th} century where a filament of dye was injected into a flow of water. The discharge was

controlled, and observations were made using a glass tube through which the fluid flowed (figure 2.5). At low velocities the dye would flow smoothly. As the flow was increased, a point would be reached at which the dye would become wavy. Any further increase caused the dye to mix completely with the water.

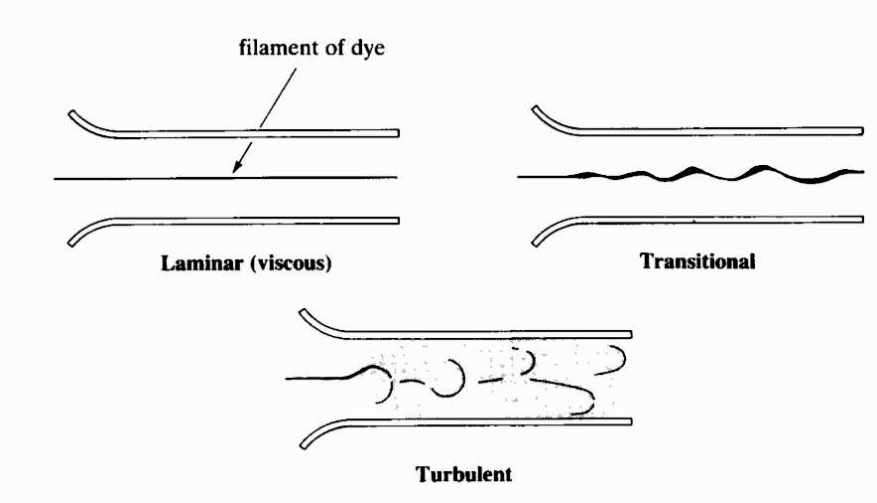

Figure 2.5: Reynolds' experiment (after Chadwick and Morfett 1998)

This allowed the identification of three distinct phases:

Viscous or laminar - in which the fluid may be considered to flow in discrete layers with no mixing

Transitional - in which some degree of unsteadiness becomes apparent.

Turbulent - in which the flow incorporates an eddying or mixing action. The motion of a fluid particle within a turbulent flow is complex and irregular, involving fluctuations in velocity and direction (Chadwick and Morfett, 1998).

From his experiments, Reynolds found that the onset of turbulence was a function of fluid velocity, viscosity and a typical dimension (length scale). This led to the formation of Reynolds Number (Re, dimensionless):

$$Re = \frac{\rho u l}{\mu} = \frac{u l}{\nu} \tag{2.1}$$

Where:

l is a length scale (the pipe diameter for pipe flows)

u is the mean fluid velocity for the characteristic flow

μ is the dynamic viscosity of the fluid, $= \nu \ / \ \rho$

ρ is the fluid density

ν is the kinematic viscosity of the fluid

Reynolds number represents a ratio of inertia and viscous forces (Chadwick and Morfett, 1998) allowing for any two flows to be compared in this manner. Within pipe flow:

'for Re < 2000, laminar flow exists (500 for open channels);

for 2000 < Re < 4000, the flow is transitional;

for Re > 4000, the flow is turbulent (1-2000 for open channels)'

However these values should be regarded as a rough guideline only. Some experiments have detected Laminar flows for Re > 4000 (Chadwick and Morfett, 1998).

2.4 Mixing in Turbulent Flows

Three main processes govern solute mixing:

Advection - the bodily movement by an imposed flow regime

Diffusion - at molecular level, is movement by random fluctuations (Brownian motion). Often small scale random turbulent fluctuations are considered to be analogous to diffusion and termed turbulent diffusion.

Dispersion - the combination of advection and diffusion.

Figure 2.6 shows the velocity profile in an open channel and the introduction of an instantaneous line source of tracer. It can be seen from the downstream tracer profile that the tracer nearest the channel boundary (bed) moves more slowly than that at the surface. The parabolic shape of the downstream profile is due to differential advection. The horizontal spread however is primarily caused by turbulent diffusion. Dispersion in pipe flow is usually similar to this example.

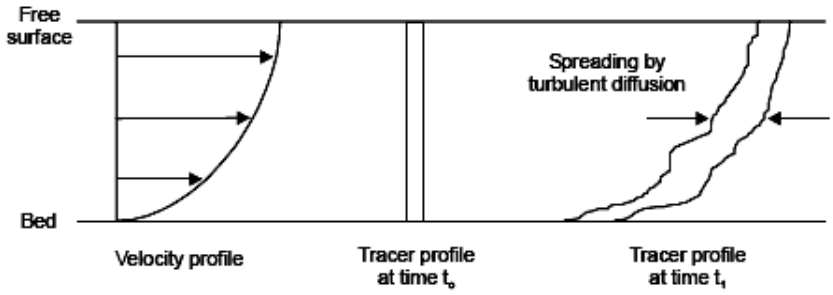

Figure 2.6: The effects of differential advection and turbulent diffusion (after Rutherford 1994)

2.4.1 Solute Transport Modelling

A number of solute transport models can be used to analyse longitudinal dispersion for laboratory, field and simulated data. A dispersion or mixing coefficient is then usually obtained. This literature review considers the method of moments, the ADE and ADZ model.

2.4.2 Method of Moments

The moments of a given distribution can be expressed as:

$$M_0 = \int_{-\infty}^{\infty} c(x,t)dc \tag{2.2}$$

$$M_1 = \int_{-\infty}^{\infty} xc(x,t)dx \tag{2.3}$$

$$M_2 = \int_{-\infty}^{\infty} x^2 c(x,t) dx \tag{2.4}$$

These and the following properties may easily be evaluated:

Area

$$A = M_0 \tag{2.5}$$

Centroid

$$\mu = \frac{M_1}{M_0} \tag{2.6}$$

Variance

$$\sigma^2 x = \frac{M_2}{M_0} - \mu^2 \tag{2.7}$$

Variance can also be evaluated by calculating the second moment of the distribution about the centroid:

Variance

$$\sigma^2 x = \frac{M_{2\mu}}{M_0} \tag{2.8}$$

2.4.2.1 Frozen Cloud Approximation

The frozen cloud approximation is used to convert between concentration-time and concentration-distance relationships when:

$$\frac{x}{u} >> \frac{D}{u^2} \tag{2.9}$$

Where:

x Distance

u Cross sectional mean velocity

D Dispersion coefficient

An assumption is made that 'no longitudinal dispersion occurs during the time taken for tracer to pass a sampling site' (Rutherford, 1994).

Using the frozen cloud approximation where t_1 and t_2 are times at which spatial variances are measured it can be shown that:

$$D = \frac{1}{2}\frac{d\sigma_x^2(t)}{dt} = \frac{1}{2}\frac{\sigma_x^2(t_2) - \sigma_x^2(t_1)}{t_2 - t_1} \tag{2.10}$$

Hence to evaluate the longitudinal mixing coefficient from a temporal moment (definitions are shown in figure 2.8):

$$D = \frac{1}{2}u^2\frac{d\sigma_t^2(x)}{dt} = \frac{u^2}{2}\frac{\sigma_t^2(x_2) - \sigma_t^2(x_1)}{t_2 - t_1} \tag{2.11}$$

2.4.3 Fickian Model of Longitudinal Dispersion

2.4.3.1 Taylor's Analysis

When a source of tracer is initially introduced its shape is largely governed by the velocity distribution across the channel width. The advective zone is closest to the source and is where the velocity distribution has the most influence. Within this zone, the tracer profile becomes negatively skewed (i.e. the rising limb is shorter than the falling limb, (Rutherford, 1994)) shown in figure 2.7.

'Theoretical and experimental work by Taylor in pipe flow (Taylor 1953, 1954) *indicates that at some point downstream from the source an equilibrium becomes established between transverse velocity shear (which promotes longitudinal dispersion) and transverse diffusion (which counteracts longitudinal dispersion).'* (Rutherford, 1994)

After this point the longitudinal variance of the cross-sectional averaged tracer increases linearly with time and the skewness introduced in the advective zone begins to decay, eventually returning to a Gaussian distribution. This is known as the equilibrium zone. Fick's law, equation 2.12 (derived by Fick in 1855, (Rutherford, 1994)), may be used in the equilibrium zone to model the cross-sectional averaged concentration of a tracer cloud.

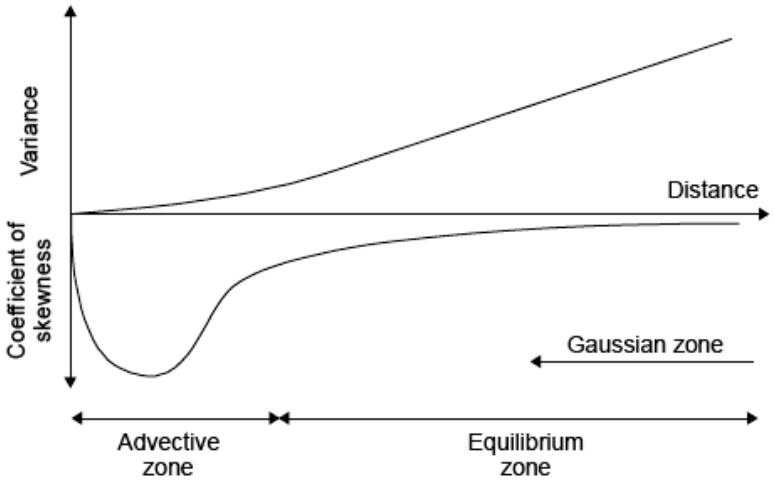

Figure 2.7: Fickian model predictions of how the variance and coefficient of skewness of a concentration profile differs with distance (after Rutherford 1994)

$$\frac{\delta S}{\delta t} + V_x \frac{\delta S}{\delta x} = K_x \frac{\delta^2 S_a}{\delta x^2} \tag{2.12}$$

Where:

S_a Cross-sectional averaged tracer concentration

V_x Cross-sectional averaged velocity

K_x Longitudinal dispersion coefficient

If V_x and K_x are constant then the solution to equation 2.12 is:

$$S_a(x,t) = \frac{M}{A\sqrt{4\pi K_x t}} exp\left[-\frac{(x - V_x t)^2}{4K_x t}\right] \tag{2.13}$$

Where:

M Mass of tracer injected at $x = 0$ and $t = 0$

A Cross sectional area of the channel

Equation 2.4.3.1 is known as the Taylor Solution (Rutherford, 1994).

2.4.4 Routing Procedures

Routing procedures may be used to predict temporal profiles from a temporally distributed input. Two methods are proposed by Rutherford (1994); 'The Frozen Cloud Method' and the 'Hayami Solution'. Comparison of the two methods shown in Rutherford (1994) highlights more skewed results by using the Hayami solution.

2.4.4.1 The Frozen Cloud Routing Procedure

Details of the frozen cloud approximation are listed in section 2.4.2.1. Although the approximation is not entirely accurate as longitudinal dispersion continually occurs, the error introduced is negligible. Therefore the frozen cloud approximation is still considered robust for longitudinal dispersion analysis. The following equation can be used to route temporal concentration profiles:

$$S_a(x_2,t) = \int_{\tau=-\infty}^{\infty} \frac{S(x_1,t)V_x}{\sqrt{4\pi K_x(\bar{t}_2-\bar{t}_1)}} exp\left[-\frac{V_x^2(\bar{t}_2-\bar{t}_1-1+\tau)^2}{4K_x(\bar{t}_2-\bar{t}_1)}\right] d\tau \qquad (2.14)$$

$S(x_1,t)$	Observed concentration as a function of time at site 1 (located at x_1)
$S(x_2,t)$	Observed concentration as a function of time at site 2 (located at x_2)
$\bar{t}_1$ & $\bar{t}_1$	Mean time of passage at sites 1 and 2 respectively.

This method (shown in figure 2.8) effectively takes each individual upstream element of the temporal concentration distribution and advects it downstream by a fixed amount whilst also spreading it (assuming a Gaussian distribution). By combining the downstream distributions the downstream concentration profile can be obtained.

Rutherford (1994) highlights four important points about the routing procedure:

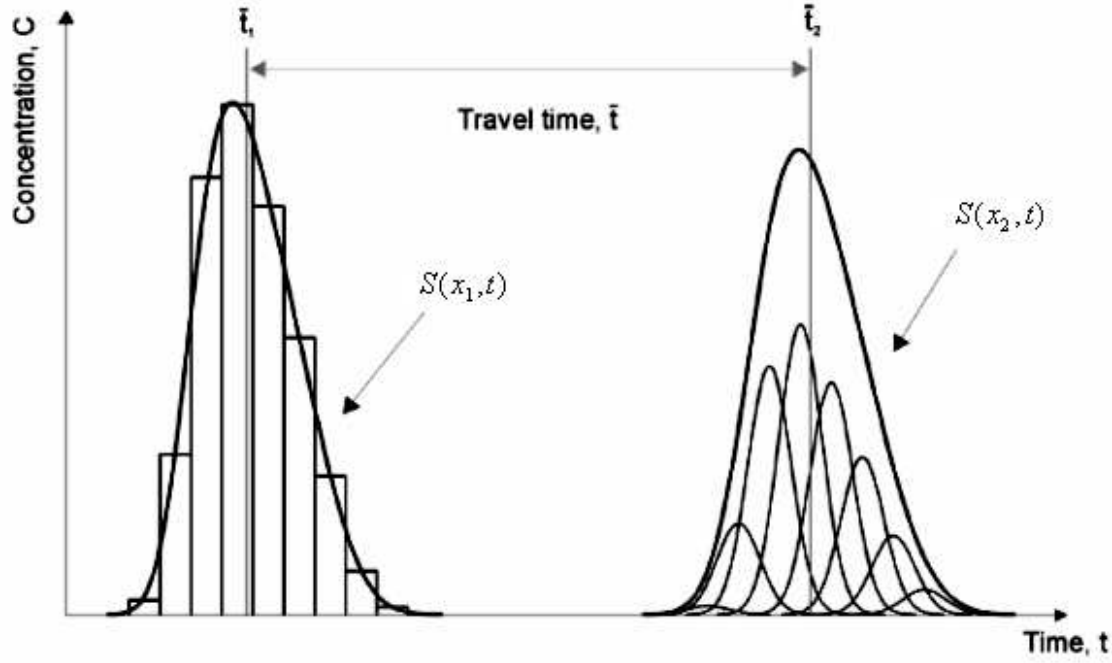

Figure 2.8: Example of the ADE Frozen Cloud Routing Procedure (Rutherford, 1994)

- *'Site 1 must be outside of the advective zone*
- *The entire concentration versus time profile including the leading edge and long tail, must be captured*
- *Tracer loss must be negligible*
- *The routing procedure gives reach-averaged values of V_x and K_x'*

2.4.5 The Cells in Series (CIS) model

The CIS model (figure 2.9) *'represent a river reach by a sequence of sub-reaches (hereafter called cells) which flow into each other'* (Rutherford, 1994). Within the CIS model each cell is assumed to be well mixed and the concentration of a conservative tracer is governed only by the inflow concentration, and the residence time of the cell. A river reach is modelled using a series of these cells where the outflow of one cell becomes the inflow of the next.

The CIS model has two main flaws; it does not output a skewed tracer profile which is often observed in natural channels (Stefan and Demetracopoulos, 1981),

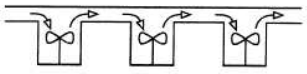

Figure 2.9: Representation of a CIS Model

and in sewerage systems (Guymer and O'Brien, 2000). Secondly, the number of cells determines both the rate of dispersion and travel time. These parameters cannot be varied independently which restricts the applicability of the model (Rutherford, 1994). Due to these flaws it has limited applicability within the scope of this document despite remaining popular in Chemical Engineering (continuously stirred tank reactor models) (Rutherford, 1994).

2.4.6 The Aggregated Dead Zone (ADZ) Model

Beer and Young (1984) introduced the ADZ model as a variant of the cells in series (CIS) model. The ADZ model has gained favour in the water engineering sector due to the quality of fit to observed data. The standard advective model can be modified to include a segregated mixing/retention zone:

$$\frac{\delta c}{\delta t} + u\frac{\delta c}{\delta x} = D\frac{\delta^2 c}{\delta x} + \Gamma_c(l - c) \tag{2.15}$$

Which describes the dispersion (D) within the main flow, and

$$\frac{\delta l}{\delta t} = \Gamma_l(l - c) \tag{2.16}$$

Describes the retention of a tracer within a dead zone where:

c, l	Concentration of tracer entering and leaving the dead zone respectively
Γ_c, Γ_l	Volumetric mass transfer coefficient in the main channel and dead zone respectively

If the Fickian dispersion coefficient K was zero, dispersion would still take place due to the retention within the storage zone (figure 2.10). Under zero dispersion

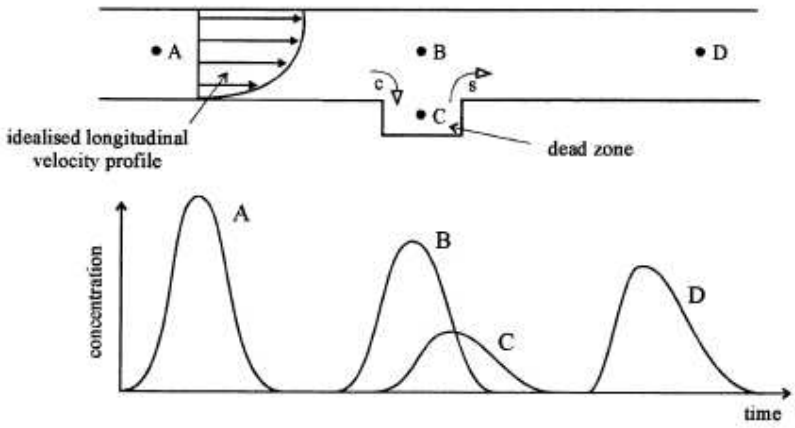

Figure 2.10: Idealised ADZ Model (after Rutherford (1994))

conditions traces A and B would remain unchanged. However, K would still be altered due to the effects of trace C. With this assumption *'It is postulated that a cell length can be found in which the river tracer concentration is governed by a first-order model. Within this cell it is assumed that the complex interaction of dead zones can be approximated by a single aggregated dead zone element. The main difference from the CIS model is that a pure time delay is introduced into the input concentration which allows advection and dispersion to be decoupled'* (Rutherford, 1994). To utilise this model for an entire reach the tracer must be advected through the reach prior to entering the dead zone. This can be done by entering a pure time delay into the input concentration term.

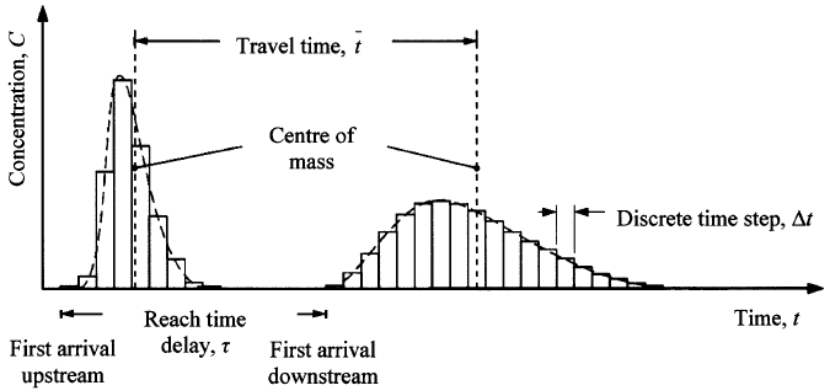

Figure 2.11: Discretised concentration time distributions

2.4.7 Residence Time Distribution (RTD)

The RTD of a flow system can be obtained via physical experiments or simulated using CFD. In CFD this is done using numerical models such as the discrete phase model. The RTD of a system shows the prevailing mixing as each form (of mixing) has a characteristic shape. Plug, piston, pipe and mixed flows as well as dead zones are common types of flow encountered by both hydraulic and chemical engineers. The responses of these flows to an instantaneous pulse injection are shown in figure 2.12.

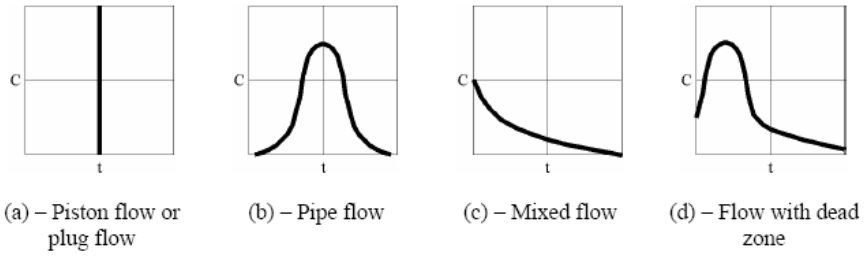

Figure 2.12: RTDs of typical flows (after Danckwerts, 1958)

However, these responses are to instantaneous upstream injections. In laboratory experiments (unlike CFD) it is not possible to create an instantaneous, well mixed injection. Guymer and Stovin (2011) have shown that RTDs can be derived from laboratory data using a technique termed deconvolution. The response of a system to an instantaneous unit impulse of dye can be derived from its response to a non-instantaneous upstream concentration profile. The Maximum Entropy Deconvolution technique is described in section 2.4.8.

2.4.8 Maximum Entropy Deconvolution

'The input/output relationship of a system can be considered in terms of a convolution integral between the upstream concentration and the RTD' (Stovin *et al.*, 2010).

$$C(x_2, t) = \int_0^t C(x_1, t - \tau) \cdot E(\tau) d\tau \tag{2.17}$$

Where

$C(x_1, t)$ is the measured upstream input

$E(\tau)$, is the RTD

If $C(x_1, t)$ and $C(x_2, t)$ are measured it is possible to deconvolve the unknown RTD.

A number of methods exist for identifying $E(\tau)$. Madden *et al.* (1996) compares six different methods for determining a system input from a simulated concentration profile and RTD. For each of the five inputs tested, Maximum Entropy Deconvolution (based on Skilling and Bryan (1984)) was the most successful at replicating the input.

Maximum entropy deconvolution was successfully used by Hattersley *et al.* (2008) to investigate a cause of renal failure in Multiple Myeloma patients. The code used was later developed by Stovin *et al.* (2010) to identify the RTDs for a range of urban drainage structures before being used to develop a 1D mixing model for surcharged manholes (Guymer and Stovin, 2011).

The code itself seeks to maximise entropy, M_e:

$$M_e = -\Sigma \left(dlog \left(\frac{d}{m} \right) \right) \tag{2.18}$$

where:

$$m(n) = \frac{d(n-1) + d(n+1)}{2} \tag{2.19}$$

and d is the estimate for the RTD.

'Maximising M_e forces each point on the RTD to be as close as possible to its neighbours, and encourages the RTD to be smooth as would be expected for a natural system', Jones (2012). This is constrained by the R_t^2 goodness of fit parameter (Young *et al.*, 1980) which forces the predicted downstream concentration profile to be as close as possible to that of the measured profile.

Continuing work being undertaken at the University of Sheffield (Sonnenwald *et al.* (2011) and Sonnenwald (*in press*) aims to further refine deconvolution

techniques for use with urban drainage structures and includes an evaluation of the constraint measures applied (i.e. R_t^2).

2.4.9 Cumulative Residence Time Distribution

The RTD of a system may also be presented as a CRTD. As before, each type of flow has a characteristic shape of CRTD.

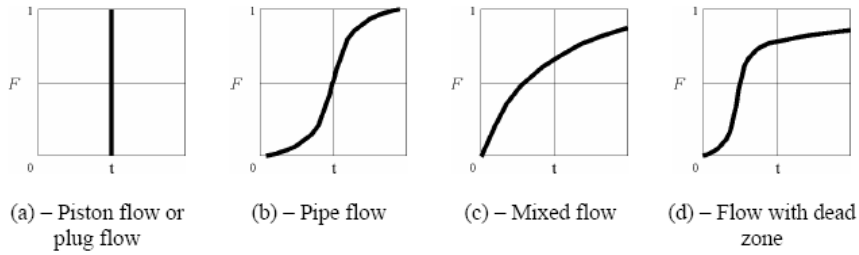

Figure 2.13: CRTDs of typical flows (after Danckwerts, 1958)

In hydraulic engineering CRTDs have been used to evaluate the performance of structures such as ponds and tanks using derived parameters (Adamsson *et al.*, 2003). Lau *et al.* (2008) investigated the validity of using CRTDs for scaling purposes, building on a suggestion by Danckwerts (1958); if two systems are geometrically similar and fulfil the principles of scaling, their CRTDs normalised with respect to nominal travel time (equation 2.4.9) will be identical.

$$t_{nominal} = V/Q \tag{2.20}$$

Where:

V Volume

Q Flowrate

2.5 Computational Fluid Dynamics (CFD)

'CFD is the analysis of systems involving fluid flow, heat transfer and associated phenomena such as chemical reactions by means of computer based simulation.' (Versteeg and Malalasekera, 2007)

2.5.1 Basic Principles of CFD

CFD codes allow for fluid flow problems to be tackled using numerical algorithms. These include the Finite Difference method, the Finite Element method and the Finite Volume method (the latter is used throughout this study).

Most commercial CFD packages include user interfaces to input problem parameters and examine the results. All codes therefore contain three main elements (Versteeg and Malalasekera, 2007):

- Pre-Processor
- Solver
- Post-Processor

2.5.2 Pre-Processor

A pre-processor (such as GAMBIT, provided by Fluent Inc.) allows for the user to input the geometry of a given problem i.e. axis, boundaries, inlets and outlets etc. before generating a grid; this is the sub division of the domain into a number of smaller cells (widely referred to as a mesh).

2.5.2.1 Mesh Quality

Mesh quality plays a significant role in the accuracy and stability of a CFD solution (FLUENT, 2005b). Different criteria for assessing mesh quality are used dependent on cell type (tetrahedral, hexahedral, polyhedral, etc.). Mesh quality can be examined using:

- Skewness *'defined as the difference between the shape of the cell and the shape of an equilateral cell of equivalent volume. Highly skewed cells can decrease accuracy and destabilize the solution'.*
- Aspect Ratio *'a measure of the stretching of the cell'.*
- Squish Index *'is computed for cells using the vector from the cell centroid to each of its faces and the corresponding face area vector. The worst cells will have a cell squish index close to 1, with better cells closer to 0'* (FLUENT, 2005b).

2.5.2.1.1 Flow-Field Dependency The effect of mesh quality is highly dependant on the flow field simulated. In regions of complex flows, with strong flow gradients, poor mesh quality (i.e. highly skewed cells), can be very damaging. However, in areas of quiescent flow the effects of such poor mesh elements is low. It is desirable to generate a high-quality mesh over the whole flow domain as prior knowledge of such areas of flow is not always possible.

Criteria utilised in this study for assessing mesh quality are presented in table 4.7.

2.5.3 Solver

Although there are three distinct numerical solution techniques, the finite volume method used in the most established codes will only be considered here-forth. *'In outline the numerical algorithm consists of the following steps:*

- *Integration of the governing equations of fluid flow over all the (finite) control volumes of the domain.*
- *Discretization - conversion of the resulting integral equations into a system of algebraic equations.*
- *Solution of the algebraic equations by an iterative method.'* (Versteeg and Malalasekera, 2007)

This process is shown schematically in figure 2.14.

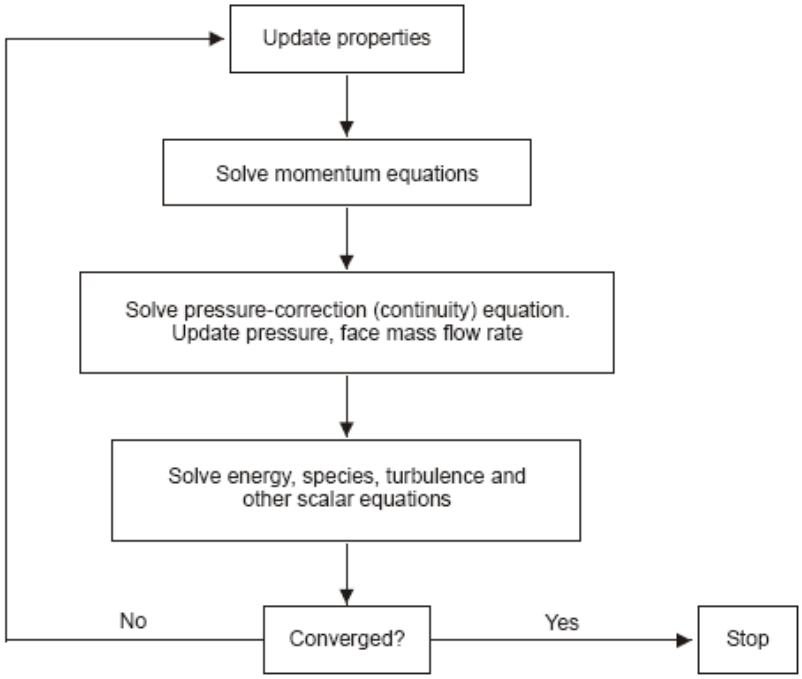

Figure 2.14: Overview of the Solution Method (after FLUENT 2005a)

2.5.4 Post Processor

Due to increased graphics capability of late, leading CFD packaged are increasingly developing data visualisation tools. These include (Versteeg and Malalasekera, 2007):

- Domain geometry and grid display
- Vector plots
- Line and shaded contour plots
- 2D and 3D surface plots
- Particle Tracking

As well as graphic based outputs, all codes produce alphanumeric outputs which can be easily imported into software such as Microsoft Excel and Mathworks Matlab.

2.5.4.1 Governing Equations of fluid dynamics

Within a domain the flow field can be predicted (if all boundary conditions are valid) by solving the governing equations of fluid dynamics:

- Conservation of Mass
- Conservation of Momentum
- The rate of change of energy is equal to the sum of the rate of heat addition to the rate of work done on a fluid particle (first law of thermodynamics). If heat transfer is not relevant to a given study, the energy equation can often be turned off.

2.5.4.2 Conservation of Mass

For an infinitesimally small fluid element:

Rate of increase of mass in fluid element = Net rate of flow of mass into fluid element

Numerically:

$$\frac{\partial \rho}{\partial t} + \frac{\partial(\rho u)}{\partial x} + \frac{\partial(\rho \nu)}{\partial y} + \frac{\partial(\rho w)}{\partial z} = 0 \tag{2.21}$$

In equation 2.21, the first term represents the rate of change in time of the density (mass per unit volume), obviously for an incompressible fluid (a liquid) the density is constant and equation 2.21 can be simplified further (Versteeg and Malalasekera, 2007):

$$\frac{\partial u}{\partial x} + \frac{\partial \nu}{\partial y} + \frac{\partial w}{\partial z} = 0 \tag{2.22}$$

2.5.4.3 Conservation of Momentum

Rate of increase of momentum of fluid particle = Sum of forces on fluid particle
Newton's second law.

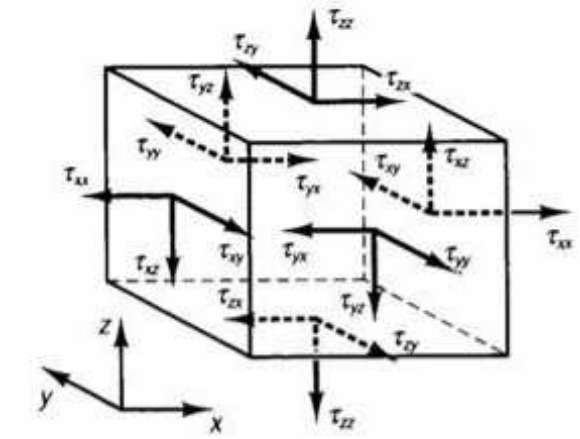

Figure 2.15: Stress component on three faces of a fluid element (Versteeg and Malalasekera, 2007)

'First we consider the x-components of the forces due to pressure p and the stress components. The net force acting in the x-direction is the sum of the force components acting in that direction on the fluid element.'

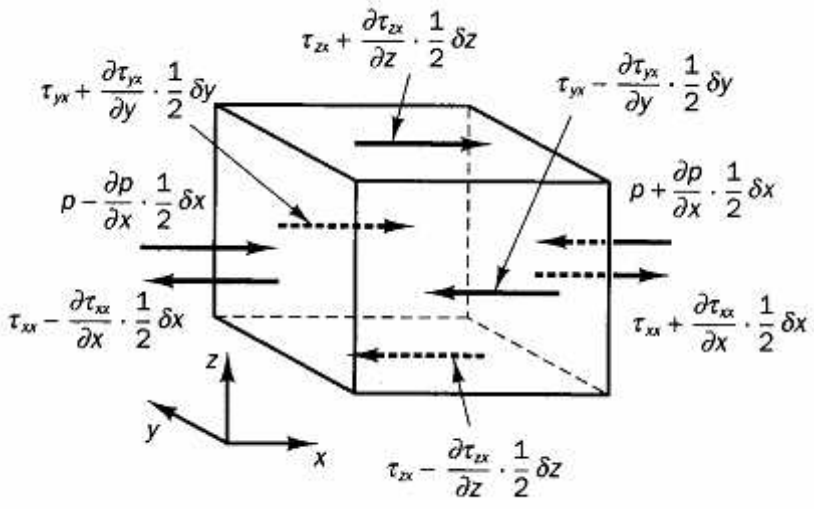

Figure 2.16: Stress components in the x-direction (Versteeg and Malalasekera, 2007)

The x-component of the momentum equation is found *'by setting the rate of change of x-momentum of the fluid particle equal to the total force in the x-direction on the element due to surface stresses plus the rate of increase of x-momentum due to sources'* (Versteeg and Malalasekera, 2007):

$$\rho\frac{Du}{Dt} = \frac{\partial(-p+\tau_{xx})}{\partial x} + \frac{\partial\tau_{yx}}{\partial y} + \frac{\partial\tau_{zx}}{\partial z} = S_{Mx} \tag{2.23}$$

2.5.5 Turbulent Flow Calculation

Turbulent eddies (with a wide range of time and length scales) interact in a complex manner. In some engineering applications turbulence is favourable; in others it is less so. However, due to this there has been a significant amount of research carried out in order to develop numerical methods of modelling its effects (Versteeg and Malalasekera, 2007).

- Turbulence models for Reynolds-averaged Navier-Stokes (RANS) equations - these focus on the mean flow field and effects of turbulence on the mean flow properties. The Navier-stokes equations (section 2.5.5.1) are time averaged leading to additional terms in the flow equations which are modelled with turbulence models such as the two equation k-ϵ (section 2.5.6.1).

- Large eddy simulation (LES) - Tracks the behaviour of large eddies and uses spatial filtering (of the unsteady Navier-Stokes equations) to reject small eddies. A 'sub-grid' scale model represent the effect of the rejected eddies on the mean flow field. LES modelling requires unsteady equations to be solved thus increasing computational demands. However, it should be noted that LES modelling is only double the computational expense of a RANS based Reynolds Stress Model (RSM) approach for a much finer flow field resolution.

- Direct numerical simulation (DNS) - *'these simulations compute the mean flow and all turbulent velocity fluctuations'* (Versteeg and Malalasekera, 2007).

In Civil Engineering the mean flow field (macro flow features) is usually of the greatest concern (rather than the micro flow features resolved by alternatives such as LES). Previous CFD based studies on manholes (Lau, 2008), showed a RANS based approach to be in strong agreement with laboratory based PIV data. Grimm (2003) also used a RANS based approach whilst investigating a modelling methodology for solute transport in pipes. Coroneo *et al.* (2011) investigated the effect of numerical issues on the RANS-based predictions of single phase stirred tanks and states *'the most widely accepted conclusion is that adequate values are generally to be expected for the predicted mean flow quantities, while much less confidence must be put on the calculated turbulent quantities and related phenomena'*, the latter part is confirmed within Aubin *et al.* (2004). Therefore, in studies such as this, where the mean flow field is of the greatest interest, a RANS approach appears applicable.

2.5.5.1 Navier-Stokes Equations

The equations governing the motion of an incompressible Newtonian fluid are known as Navier-Stokes equations and can be written in vector notation (for a homogeneous fluid, Niño and Tamburrino (2004)) as:

$$\rho\frac{D\vec{v}}{Dt} = \rho\frac{\partial\vec{v}}{\partial t} + (\vec{v}\cdot\bigtriangledown)\vec{v} = -\bigtriangledown\hat{p} + \mu\bigtriangledown^2\vec{v} \tag{2.24}$$

where:

ρ is the fluid density

μ is the dynamic viscosity

D/Dt is the material or total derivative

$\vec{v}$ is the velocity vector

$\hat{p}$ is the piezometric pressure, including pressure and gravitational force terms:

$$\hat{p} = p + \rho g h \tag{2.25}$$

where:

p is the thermodynamic pressure

g denotes acceleration due to gravity

h is a vertical axis defined opposite to gravity

Equation 2.24 contains an unknown for each velocity component of $\vec{v}$ as well as one corresponding to the thermodynamic pressure, p. To close the number of equations required to solve a given flow problem, the continuity equation (which is derived from the mass conservation principle) needs to be considered (Niño and Tamburrino, 2004).

For an incompressible fluid, the continuity equation reduces to:

$$\bigtriangledown \cdot \vec{v} = 0 \tag{2.26}$$

This is a linear equation. Tensor notation can be conveniently used to visualize the terms of the governing equations; three coordinates are considered: (x_1; x_2; x_3), relating to the three components of the velocity vector (u_1; u_2 ; u_3). For example, the component of equation 2.24 in direction x_i, for a homogeneous fluid, can be shown as (Niño and Tamburrino, 2004):

$$\frac{\partial u_i}{\partial t} + u_j \frac{\partial u_i}{\partial x_j} = -\frac{1}{\rho}\frac{\partial \hat{p}}{\partial x_i} + \nu \frac{\partial^2 u_i}{\partial x_j \partial x_j} \tag{2.27}$$

where:

ν is the kinematic viscosity

In tensor notation, the continuity equation reduces to:

$$\frac{\partial u_j}{\partial x_j} = 0 \tag{2.28}$$

In equations 2.27 and 2.28 the sub-index j implies summation over j = 1, 2 and 3.

2.5.5.2 Reynolds Averaging

The Navier-Stokes equations (section 2.5.5.1), are valid in both laminar and turbulent flows. However, when a flow becomes turbulent, the velocity becomes unstable with quasi-random characteristics (Versteeg and Malalasekera, 2007), even during steady flow conditions (section 2.3). Velocity fluctuations in the flow arise due to the presence of turbulent eddies or vortices. These eddies transfer energy (in a process described as 'turbulent energy cascade') in a highly efficient manner (negligible dissipation) to smaller eddies (Niño and Tamburrino, 2004). Limitations due to the Kolmogorov's scale (which represents the smallest turbulent eddy within the flow) and 'Nyquist Criterion', imposes a large restriction on the discrtetization of a grid to be used for numerical simulation; grid size must be smaller than half of Kolmogorov's scales which poses a practical limitation due to the computational power required to calculate a solution at such a fine resolution (Niño and Tamburrino, 2004). Due to this a number of alternative models for simulating turbulent flows have been developed. Section 2.5.5 demonstrates that, for Civil Engineering purposes, where the mean flow field behaviour is if paramount interest, a RANS based approach is valid. RANS modelling of turbulence is based upon modelling the quasi-random fluctuations statistically. As these fluctuations relate to roughly 15% of the mean flow velocity it can be argued that *'it is more interesting to know the behaviour of the mean flow rather than that of the fluctuations from the computation'* (Niño and Tamburrino, 2004). Ensemble averaging is used on the Navier-Stokes equations to extract the behaviour of the mean flow field from that of the turbulent fluctuations. A large number of repetitions of a given turbulent flow (subject to the same boundary conditions) are used to extract the average flow properties (for each time step). The following derivation is presented fully in (Niño and Tamburrino, 2004).

Using the ensemble averaging procedure, an instantaneous flow velocity x_i, can be decomposed into a mean value, $\overline{u}_i$ where:

$$u_i = \overline{u}_i + u'_i \tag{2.29}$$

Where the over-bar represents the ensemble average and u'_i represents a fluctuation.

For pressure:

$$\hat{p} = \overline{\hat{p}} + \hat{p}' \tag{2.30}$$

This is then used to decompose the Navier-stokes equations, followed by ensemble averaging them over the turbulence. Equation 2.27 and 2.28 are modified by multiplying by u_i. The resultant equation is added to equation 2.27:

$$\frac{\partial(\overline{u}_i + u_i')}{\partial t} + \frac{\partial((\overline{u}_j + u_j')(\overline{u}_i + u_i'))}{\partial x_j} = -\frac{1}{\rho}\frac{\partial(\overline{\hat{p}} + \hat{p}')}{\partial x_i} + \nu\frac{\partial^2(\overline{u}_i + u_i')}{\partial x_j \partial x_j} \tag{2.31}$$

Taking the ensemble average of equation 2.31 (considering that $\overline{\overline{a}} = \overline{a}$ and $\overline{a}' = 0$), for any variable, a, gives:

$$\frac{\partial \overline{u}_i}{\partial t} + \frac{\partial(\overline{u}_j\overline{u}_i + \overline{u_j'u_i'})}{\partial x_j} = -\frac{1}{\rho}\frac{\partial \overline{\hat{p}}}{\partial x_i} + \nu\frac{\partial^2 \overline{u}_i}{\partial x_j \partial x_j} \tag{2.32}$$

The ensemble average continuity equations results to:

$$\frac{\partial \overline{u}_j}{\partial x_j} = 0 \tag{2.33}$$

Finally, multiplying this equation by $\overline{u}_i$ gives:

$$\frac{\partial \overline{u}_i}{\partial t} + \overline{u}_j\frac{\partial \overline{u}_i}{\partial x_j} = -\frac{1}{\rho}\frac{\partial \overline{\hat{p}}}{\partial x_i} + \nu\frac{\partial^2 \overline{u}_i}{\partial x_j \partial x_j} - \frac{\overline{u_i'u_j'}}{\partial x_j} \tag{2.34}$$

The term $\overline{u_i'u_j'}$ does not equal zero, as in general the velocity fluctuations are correlated. The fact that the cross-correlation $\overline{u_i'u_j'}$ with $i \neq j$ is not zero, suggests that turbulence is not entirely random, but has structure. These correlations represent turbulent fluxes of momentum and are known as turbulent (or Reynolds) stresses:

$$\tau_{tij} = -\rho\overline{u_i'u_j'} \tag{2.35}$$

According to Stokes law for Newtonian fluids, the viscous stresses of the mean flow are given by:

$$\tau_{vij} = 2\mu\epsilon_{ij} = \mu(\frac{\partial \overline{u}_i}{\partial x_j} + \frac{\partial \overline{u}_j}{\partial x_i}) \tag{2.36}$$

Where ϵ_{ij} represents the deformation tensor. The total stress within a turbulent flow can be expressed as:

$$\tau_{ij} = \tau_{vij} + \tau_{tij} = \mu(\frac{\partial \overline{u}_i}{\partial x_j} + \frac{\partial \overline{u}_j}{\partial x_i}) - \rho\overline{u_i' u_j'} \tag{2.37}$$

Therefore, equation 2.34 can be expressed as:

$$\frac{\partial \overline{u}_i}{\partial t} + \overline{u}_j \frac{\partial \overline{u}_i}{\partial x_j} = -\frac{1}{\rho}\frac{\partial \overline{\tilde{p}}}{\partial x_i} + \frac{1}{\rho}\frac{\partial \tau_{ij}}{\partial x_j} \tag{2.38}$$

The problem of random fluctuations is not concluded from averaging the Navier-Stokes equations; instead they appear as Reynolds stresses (i.e. there is no one set of equations to describe the behaviour of the mean flow). This is the well documented 'turbulence closure problem' (Niño and Tamburrino, 2004). Therefore, the RANS methodology relies on adding additional (external) equations in order to 'close' these equations and model the Reynolds Stresses. These models, and their limitations are discussed further within section 2.5.6.

2.5.6 Turbulence Models

To compute turbulent flows with Reynolds Averaged Navier-Stokes (RANS) equations, turbulence models are necessary to predict Reynolds stresses and scalar transport terms. In order to be widely useful, turbulence models must be simple, accurate and economical to run. Existing turbulence models can be classified by the additional number of transport equations that need to be solved (as well as the RANS flow equations, Versteeg and Malalasekera (2007)).

No. of extra equations	Name
0	Mixing length model
1	Spalart-Allmaras model
2	k-ϵ model
	k-ω model
7	Algebraic stress model
	Reynolds stress model

Table 2.2: Extra equations required by RANS turbulence models (after Versteeg and Malalasekera 2007)

2.5.6.1 The k-ϵ turbulence model

The k-ϵ turbulence model has become widely used in computational modelling (Chadwick and Morfett, 1998). It depends upon two parameters; turbulent kinetic energy (k) and turbulent dissipation rate (ϵ). Computational models therefore contain two equations to establish the rate of change of k and ϵ. The equations can be expressed as (Versteeg and Malalasekera, 2007):

Rate of change of k or ϵ + Transport of k or ϵ by convection =

Transport of k or ϵ by diffusion + Rate of production of k or ϵ

- Rate of destruction of k or ϵ

Or algebraically:

$$\frac{\partial(\rho k)}{\partial t} + div(\rho k U) = div\left[\frac{\mu_t}{\sigma_k} grad k\right] + 2\mu_t S_{ij} \cdot S_{ij} - \rho\epsilon \tag{2.39}$$

$$\frac{\partial(\rho \epsilon)}{\partial t} + div(\rho \epsilon U) = div\left[\frac{\mu_t}{\sigma_\epsilon} grad \epsilon\right] + C_{1\epsilon}\frac{\epsilon}{k} 2\mu l S_{ij} \cdot S_{ij} - C_{2\epsilon}\rho\frac{\epsilon^2}{k} \tag{2.40}$$

Where:

S_{ij} Mean Strain Rate

μ_t Turbulent kinematic viscosity

C_μ Empirical Constant 0.09

σ_k Empirical Constant	1.00
σ_ϵ Empirical Constant	1.30
$C_{1\epsilon}$ Empirical Constant	1.44
$C_{2\epsilon}$ Empirical Constant	1.92

The empirical constants shown, are as given by Versteeg and Malalasekera (2007). The k-ϵ model is widely used and highly validated (Versteeg and Malalasekera, 2007) for certain flows, requiring no need for case by case adjustments of the model constants, performing particularly well in confined flows. As this is widely applicable to many potential uses in industry its popularity is apparent. Despite of the success of the model under these conditions it has only moderate agreement in unconfined flows. Reportedly the model does not perform well in weak shear layers and drastically over predicts the spreading rate of axis-symmetric jets in stagnant surroundings (Versteeg and Malalasekera, 2007). This weakness may be apparent in the 'above threshold' surcharge condition where the flow is dominated by an axis-symmetric jet surrounded by stagnant (or gently recirculating) flow.

Development of the equations behind the k-ϵ model are presented in Niño and Tamburrino (2004).

2.5.6.2 The Renormalisation k-ϵ Turbulence Model (RNG)

The RNG turbulence model includes a random forcing function in the Navier-Stokes equation. *'This removes small scales of motion from the governing equations by expressing their effects in terms of larger scale motions and a modified viscosity'* (Versteeg and Malalasekera, 2007). The two governing equations for the RNG k-ϵ turbulence model are similar to that of the standard k-ϵ model:

$$\frac{\partial(\rho k)}{\partial t} + div(\rho k U) = div\left[\frac{\mu_t}{\sigma_k} grad k\right] + 2\mu_t S_{ij} \cdot S_{ij} - \rho\epsilon \tag{2.41}$$

$$\frac{\partial(\rho \epsilon)}{\partial t} + div(\rho \epsilon U) = div\left[\frac{\mu_t}{\sigma_\epsilon} grad \epsilon\right] + C_{1\epsilon} * \frac{\epsilon}{k} 2\mu_l S_{ij} \cdot S_{ij} - C_{2\epsilon}\rho\frac{\epsilon^2}{k} \tag{2.42}$$

However a new strain dependent function 2.43 is introduced which leads to *'the smaller destruction of k, reducing k and, eventually, the effective viscosity. As a result, in rapidly strained flows, the RNG model yields a lower turbulent viscosity than the standard k-ϵ model. Thus, the RNG model is more responsive to the effects of rapid strain and streamline curvature than the standard k-ϵ model, which explains the superior performance of the RNG model for certain classes of flows.'* (FLUENT, 2005a).

$$C_{1\epsilon}* = C_{1\epsilon} - \eta \left(\frac{\frac{1-\eta}{\eta_0}}{1 + \beta\eta^3} \right) \tag{2.43}$$

$$\eta = \frac{(2S_{ij}S_{ij})^{\frac{1}{2}k}}{\epsilon} \tag{2.44}$$

Where:

S_{ij} Mean Strain Rate

C_μ Empirical Constant 0.0845

σ_k Empirical Constant 1.39

σ_ϵ Empirical Constant 1.39

$C_{1\epsilon}$ Empirical Constant 1.42

$C_{2\epsilon}$ Empirical Constant 1.68

(Versteeg and Malalasekera, 2007)

Within the manhole volume the core jet can be thought of as a semi-confined; Zhu and Shih (1994) modelled confined jets in a cylindrical duct using three turbulence models. The k-ϵ RNG model appeared to offer no improvement over the standard k-ϵ turbulence model under these flow conditions. However, a Realizable form of the RSM model consistently outperformed both k-ϵ models, and consistently captured the main flow structures.

2.5.6.3 The k-ϵ Realizable Model

The k-ϵ Realizable model has two main differences when compared to the standard k-ϵ model (FLUENT, 2005a).

- A new formulation for turbulent viscosity.
- A new transport equation for dissipation rate.

The full transport equations can be found in FLUENT (2005a).

'The term realizable means that the model satisfies certain mathematical constraints on the Reynolds stresses, consistent with the physics of turbulent flows. Neither the standard k-ϵ model nor the RNG k-ϵ model is realizable. An immediate benefit of the realizable k-ϵ model is that it more accurately predicts the spreading rate of both planar and round jets. It is also likely to provide superior performance for flows involving rotation, boundary layers under strong adverse pressure gradients, separation, and recirculation' (FLUENT, 2005a).

According to FLUENT (2005a) both the k-ϵ RNG and k-ϵ Realizable models have shown large improvements over the standard model where flows include strong streamline curvature, vortices and rotation (all encountered in the highly complex flows within a surcharged manhole). However, due to the relative recency of the k-ϵ Realizable model, it is not yet apparent under which circumstance it consistently outperforms the k-ϵ RNG model. Shih *et al.* (1995) and Kim *et al.* (1999) show the k-ϵ Realizable model to out-perform other k-ϵ models when flows are separated or contain complex secondary flow features (such as the secondary recirculations seen within manholes in 'below threshold' conditions).

Pattamatta and Singh (2012) investigated the capabilities of thirteen turbulence models available in FLUENT for heated wall jet flow. Although heat transfer has little relevance to this study, the results of the various turbulence models were firstly examined using their velocity profiles and jet spreading rate for the inner region of the jet (this study included a comparison with lab data). Pattamatta and Singh (2012) concludes that *'The near wall velocity profile captured using the Realizable k-ϵ (RKE) (model) with enhanced wall treatment (EWT) shows the best agreement with the experimental data as compared to the other models'.*

2.5.6.4 The Reynolds Stress Model (RSM)

The Reynolds stress model (RSM) is the most elaborate (RANS) turbulence model provided within FLUENT (requiring seven additional transport equations to be solved in 3D, FLUENT (2005a)).

The RSM model accounts for effects of streamline curvature, swirl, rotation and changes in rapid strain rate more rigorously than other more simple (one and two equation) models. Thus, it is more likely to represent complex flows well. However, the model still relies on a set of assumptions made to the transport equations. These equations can be derived by taking moments of the exact momentum equation. However, closing the equations relies on a number of modelling assumptions that are thought to compromise the accuracy of the RSM model (Launder *et al.*, 1975, FLUENT, 2005a).

Furthermore, *'The RSM might not always yield results that are clearly superior to the simpler models in all classes of flows to warrant the additional computational expense. Use of the RSM is a must when the flow features of interest are the result of anisotropy in the Reynolds stresses'* FLUENT (2005a). Feng *et al.* (2011) carried out numerical simulations of swirling flows with different turbulence models. In this study the RSM model out-performed the k-ϵ RNG model in replicating the flow experienced during laboratory tests. However, both models were out performed by the k-ϵ Realizable model in Pattamatta and Singh (2012), when simulating near-wall jets (this is highly applicable to flow conditions within a manhole).

2.5.7 Modelling Near Wall Turbulence

A wall is the most common boundary encountered in confined fluid problems (Versteeg and Malalasekera, 2007). Due to the no-slip condition that must be satisfied at the wall the velocity field is affected. Close to the wall or boundary (inner sub-layer), turbulent eddies barely exist and the flow is dominated by viscous stress. Towards the outer part of the near-wall area (log-law layer) large gradients in mean velocity are caused by the production of turbulent kinetic energy. According to FLUENT (2005a) *'The near-wall modelling significantly impacts the fidelity of numerical solutions, in as much as walls are the main*

source of mean vorticity and turbulence. After all, it is in the near-wall region that the solution variables have large gradients, and the momentum and other scalar transports occur most vigorously. Therefore, accurate representation of the flow in the near-wall region determines successful predictions of wall-bounded turbulent flows.' As most turbulence models are valid only for turbulent flows far from the wall region, it is necessary to consider how to adjust these models to be suitable for wall-bounded flows. Numerous experiments have shown that the near-wall region can be largely subdivided into three layers (FLUENT, 2005a):

- *viscous sublayer - the flow is almost laminar, and the viscosity plays a dominant role in momentum and heat or mass transfer.*
- *log-law layer - the effects of molecular viscosity and turbulence are equally important*
- *fully-turbulent layer - turbulence plays a major role.*

Figure 2.17 demonstrates these three divisions.

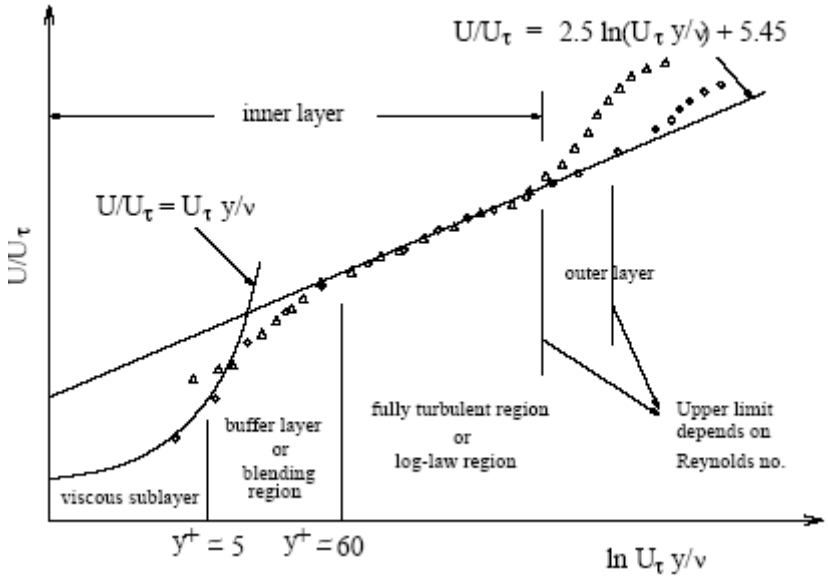

Figure 2.17: Subdivisions of the Near-Wall Region (after FLUENT 2005a)

2.5.7.1 Wall Functions vs. Near-Wall Model

Two approaches are used to model near wall turbulence. The first of these two methods uses 'wall functions' to effectively bridge the viscosity-affected region between the wall and the fully turbulent zone. This method does not require the turbulence models to be altered. The second approach modifies the models by resolving the mesh all the way to the wall boundary (including the viscous sublayer). These two approaches are shown in figure 2.18.

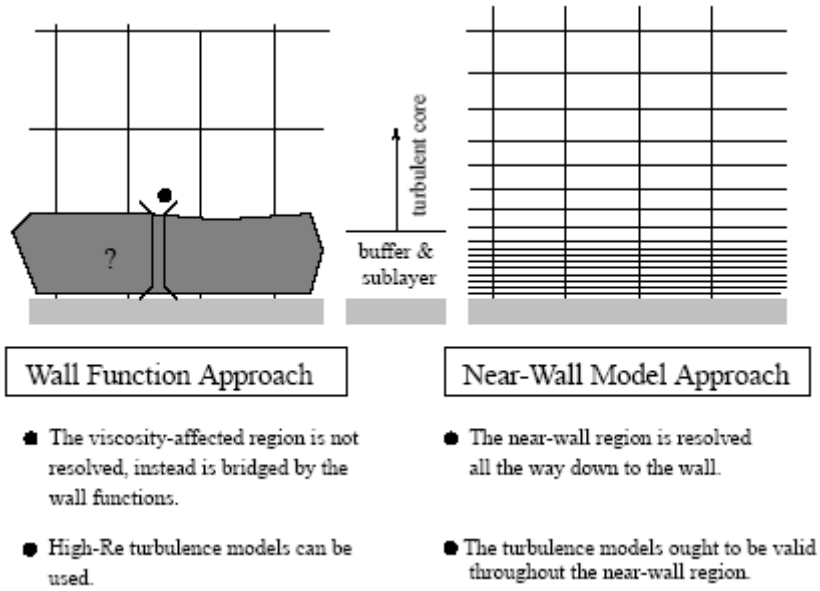

Figure 2.18: Near-Wall Treatments in FLUENT (after FLUENT 2005a)

Both of these approaches are available within the FLUENT CFD software. However, wall functions have two distinct advantages. Due to the reduced number of near wall cells, computational time is vastly reduced compared to the near-wall model approach. Secondly, empirical data such as wall roughness can be considered. One stipulation of the wall function approach is that the centroid of the near wall cell should be located within the log-law layer, this equates to $30 < y^+ < 300$ (FLUENT, 2005a), where y^+ is a non-dimensional distance from the wall given by:

$$y^+ = \frac{u^* y}{v} \tag{2.45}$$

where

u* is the shear velocity

y is the distance from the wall

Two variants of the wall function are included within FLUENT, details of these can be found in the user manual.

2.5.8 FLUENT

Like most large scale commercial CFD code FLUENT uses the Finite Volume method. The methodology used for pre-processing, solution and post-processing is the same as that set out in section 2.5.1. A full description of the capabilities of the software can be found in the FLUENT 6.2 user manual (FLUENT, 2005a). FLUENT and GAMBIT were both selected for use in this study due to the expertise that already exists within the University of Sheffield, however the principles documented above are relevant to all commercially available CFD software.

2.5.9 Discretization Scheme

Grimm (2003) validated a discretization scheme for modelling dye traces through a pipe. This is shown in 2.3.

Pressure	PRESTO
Pressure velocity coupling	SIMPLE
Momentum	Second order upwind
Turbulent kinetic energy	Second order upwind
Turbulent dissipation	Second order upwind
Reynolds stress	Second order upwind

Table 2.3: Discretization Scheme (Grimm, 2003)

Further details on discretization can be found in the FLUENT user manual (FLUENT, 2005a), and discussion within Grimm (2003) and Lau *et al.* (2008).

2.5.10 Modelling Multiphase Flows

'A large number of flows encountered in nature and technology are a mixture of phases. Physical phases of matter are gas, liquid, and solid, but the concept of phase in a multiphase flow system is applied in a broader sense. In multiphase flow, a phase can be defined as an identifiable class of material that has a particular inertial response to and interaction with the flow and the potential field in which it is immersed. For example, different-sized solid particles of the same material can be treated as different phases because each collection of particles with the same size will have a similar dynamical response to the flow field.' (FLUENT, 2005a)

Multiphase flow can be grouped into three categories:

- Gas-liquid or liquid-liquid flows
- Gas-solid flows
- Liquid-solid flows

The first of which (Gas-liquid) is relevant to this study and can be identified as:

- bubbly flow: discrete gaseous or fluid bubbles in a continuous fluid
- droplet flow: discrete fluid droplets in a continuous gas
- slug flow: large bubbles in a continuous fluid
- stratified/free-surface flow: immiscible fluids separated by a clearly-defined interface

Currently within FLUENT two approaches for the numerical calculation of multiphase flows exist; the Euler-Lagrange approach and the Euler-Euler approach. A qualitative assesment of the two approaches for modelling gas/liquid flows can be found in Sokolichin *et al.* (1997), where (dependent on discretization scheme) results were comparable.

2.5.10.1 Euler-Lagrange approach

The Euler-Lagrange approach tracks a large number of particles through the calculated flow field, it is therefore recommended within the FLUENT user documentation for use predicting sprays or fuel combustion but not for free surface prediction where the volume fraction of the second phase may not be minimal.

2.5.10.2 Euler-Euler approach

2.5.10.2.1 The Eulerian Model The Eulerian Model is recommended for use with bubble columns, risers, particle suspension, and fluidized beds (FLUENT, 2005a).

2.5.10.2.2 The Mixture Model The mixture model is recommended for use with particle-laden flows with low loading, bubbly flows, sedimentation, and cyclone separators. The mixture model can also be used without relative velocities for the dispersed phases to model homogeneous multiphase flow (FLUENT, 2005a).

2.5.10.2.3 The VOF (Volume of Fluid) Model The VOF model is recommended for use with free-surface flows, filling, sloshing, the motion of large bubbles in a liquid, the motion of liquid after a dam break, the prediction of jet break-up (surface tension), and the steady or transient tracking of any liquid-gas interface (i.e. a free water surface) (Hirt and Nichols, 1981, FLUENT, 2005a). The VOF model relies on the modelled phases not inter-penetrating. Each time an additional phase is added within the mode a phase volume fraction is added to the computational cell. With a control cell all of the volume fractions sum to unity (FLUENT, 2005a).

- $\alpha_q = 0$ the cell is empty of the qth fluid
- $\alpha_q = 1$ the cell is full of the qth fluid
- $0 < \alpha_q < 1$ the cell contains the interface between the qth fluid and one or more other fluids

(FLUENT, 2005a)

'Based on the local value of α_q, the appropriate properties and variables will be assigned to each control volume within the domain'.

The VOF model can therefore be used to predict the location of a free surface within an open channel or any hydraulic structure. Used in conjunction with the species model the VOF model can also be used to model multiple species under these conditions. As the free surface is predicted by the VOF model it is unnecessary to artificially impose a 'rigid (or fixed) lid' on a structure at an estimated free surface level (Lau *et al.*, 2008).

Kouyi *et al.* (2011) used a steady, 3D VOF CFD model to optimise the location of a water depth sensor in a dual overflow system consisting of two CSOs. However, the VOF discretization scheme used was not detailed. Liu *et al.* (2002) shows the VOF model to be capable of reproducing much more complex surface conditions than those encountered within manholes; flow over a semicircular weir. Numerical results from this study agree well with laboratory data.

Three spatial discretization schemes available within FLUENT (for use with the VOF model) are the Modified High Resolution Interface Capturing (HRIC), Geometric Reconstruction (GEO-reconstruct) and Compressive Interface Capturing Scheme for Arbitrary Meshes (CICSAM). These are discussed below:

2.5.10.2.4 Modified HRIC For multiphase VOF modelling, upwind schemes are not suitable due their diffusive nature (FLUENT, 2005a). *Central differencing schemes, while generally able to retain the sharpness of the interface, are unbounded and often give non-physical results'* (FLUENT, 2005a). FLUENT uses a modified version of the HRIC scheme to overcome these two issues. The modified HRIC scheme is a *'composite NVD scheme that consists of a non-linear blend of upwind and downwind differencing'* (FLUENT, 2005a).

2.5.10.2.5 Geometric Reconstruction The GEO-Reconstruct scheme uses standard interpolation schemes available within FLUENT when a cell is completely filled with an entire phase. When the cell is near an interface (i.e. partially full) the GEO-reconstruct scheme is utilised.

'The geometric reconstruction scheme represents the interface between fluids using a piecewise-linear approach. In FLUENT this scheme is the most accurate and is applicable for general unstructured meshes' (FLUENT, 2005a).

The GEO-reconstruct scheme is derived from Youngs (1982) and works by calculating the position of a linear interface relative to the centre of each partially full cell. After this, *'The second step is advecting the amount of fluid through each face using the computed linear interface representation and information about the normal and tangential velocity distribution on the face. The third step is calculating the volume fraction in each cell using the balance of fluxes calculated during the previous step'* (FLUENT, 2005a).

The GEO-reconstruct scheme requires a time-dependent solution.

2.5.10.2.6 Compressive Interface Capturing Scheme for Arbitrary Meshes CICSAM, based on Ubbink (1997), is a high resolution differencing scheme. The CICSAM scheme is recommended for use when there is a high ratio of viscosity between the modelled phases. Within FLUENT, CICSAM is only available as an explicit scheme. FLUENT (2005a) suggests that the CICSAM scheme is capable of producing results, equivalent in sharpness to that of the GEO-Reconstruct scheme.

Each scheme is recommended by FLUENT based on the type of flow to be modelled. This is discussed (and investigated) further in section 4.3.

2.5.11 The Species Model

One way of modelling solute transport in FLUENT is to utilise the Species Model which has the same form as the ADE equation. However, there is no 'dispersion coefficient', instead there is a diffusion coefficient. Like the governing equations of flow it is solved using discretization. The transport equation for species (k):

Rate of change of mass of species k +

Net rate of decrease of mass of species k due to advection

=

Net rate of increase of mass of species k due to diffusion +

Net rate of increase of mass of species k due to sources

$$\frac{\partial}{\partial t}(\rho Y_k) + \frac{\partial}{\partial x_i}(\rho u_i Y_k) = \frac{\partial}{\partial x_i}\left(\rho D \frac{\partial Y_k}{\partial x_i}\right) + \omega_k \tag{2.46}$$

This form of the equation has been simplified to allow for only one diffusion coefficient (Versteeg and Malalasekera, 2007). Grimm (2003) used the species model to investigate solute transport within a straight pipe. The species model can also be used to model chemical reactions as well as energy transfer. However, this is irrelevant when considering two non reacting species. Grimm (2003) found a time step of 0.01 s (20 iterations per time step) was needed to attain good agreement with laboratory solute trace data. FLUENT (2005a) recommends that the number of iterations per time step always remains as 20 for time step independent results.

The scalar transport equations (also the decomposed variants) behind the species model are presented in Niño and Tamburrino (2004).

2.5.12 Stochastic Particle Tracking

The particle tracking model is commonly used to simulate spray combustion systems in chemical engineering. It has been used in hydraulic engineering by numerous people to study sediment transport (Grimm (2003); Lau *et al.* (2008); Adamsson *et al.* (2003); Buxton (2002); Stovin and Saul (1998)), and presents an alternative to the species transport model for solute transport work. Particles are tracked by continuous succession of turbulent eddies superimposed on the mean flow of the fluid phase (Adeniji-Fashola and Chen, 1990). The simulation time required for an uncoupled particle tracking methodology is much less than the species transport model (in the order of ten times, Grimm (2003)). However, Grimm (2003) and Lau *et al.* (2008) both found the particle tracking method to under-predict the peak downstream concentration profiles of a monitored tracer. If the run-times are excessively high for models involving species transport the particle tracking method may present an alternative (Stovin *et al.*, 2008). Modelling parameters such as the Time Scale Constant (TSC) may allow

for an improvement in the over-estimation of peak concentrations. However, Lau (2008) suggests the model has a low sensitivity to this constant. When using the particle tracking method it is not straightforward to show spatial concentration distributions within the domain.

2.6 Previous Work on Urban Drainage Structures

2.6.1 Longitudinal Dispersion in Surcharged Manholes

Guymer and O'Brien (2000) began investigating solute transport in manholes in order to provide information that could be utilised by commercial sewerage system modelling software such as Infoworks (Wallingford Software) or MOUSETRAP (DHI Water and Environment). The study aimed to quantify dispersion due to surcharged manholes. The effect of a number of different configurations was then covered in later work by Guymer *et al.* (1998 and 2005a), Dennis (2000), Guymer and O'Brien (2000) and Saiyudthong (2003). These studies investigated the effects of:

- diameter
- step height
- change in pipe direction
- benching

on the mixing processes within manholes. These studies were based upon laboratory tracer experiments carried out in physical scale models. Upstream of the manhole (far enough to allow the dye to become fully mixed) a tracer dye (such as Rhodamine) was injected into the flow. Fluorometers either side of the manhole rig were then used in conjunction with data logging devices to record upstream and downstream temporal concentration profiles. These profiles were then analysed using standard moment analysis as well as the ADE and ADZ models. Generally an optimization procedure first proposed by Dennis (2000) was used to

determine model parameters. Model parameters determined using this optimization procedure *'were in better agreement than the results of the standard moment analysis'* (Dennis, 2000).

Common terminology used in previous manhole investigations is shown in figure 2.19.

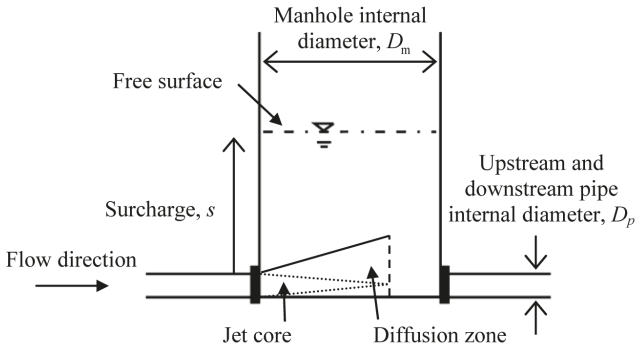

Figure 2.19: Common manhole terminology used in previous manhole investigations (after Lau (2008))

2.6.1.1 Manhole Diameter and Surcharge

Guymer *et al.* (2005a) studied the effects of manhole diameter on longitudinal dispersion in surcharged manholes. Four unbenched manholes were considered with D_M/D_p ratios of 4.55, 5.66, 6.82 and 9.09 (these relate to manhole diameters of 400 mm, 500 mm, 600 mm and 800 mm on an 88 mm diameter pipe) under a wide range of surcharge conditions. The study identified a surcharge level at which the solute transport characteristic of the manholes sharply altered; at low surcharge (pre-threshold, figure 2.20) the travel times varied linearly with surcharge, at high surcharge (post-threshold, figure 2.21) the travel times dropped to a low, constant level. This threshold was more pronounced for the manholes with high D_M/D_p ratios. The optimised ADE and ADZ model coefficient results showed travel time, dispersion coefficients and dispersive fraction for models with the same discharge and surcharge conditions to increase with manhole diameter. This is in agreement with theory. As the manhole diameter increases, so too does the volume of water available for mixing, therefore a larger manhole should experience more mixing. Reach time delay remained independent of the manhole

diameter. Stovin *et al.* (2007) suggested that the temporal concentration distributions observed at low surcharge showed solute experiences instantaneous mixing within the stored volume, whilst at high surcharge depths (figures 2.21 and 2.23), a large proportion of the tracer is advected through the manhole, experiencing little mixing. Some is retained in the upper surcharge volume, which acts as a dead zone. Guymer *et al.* (2005a) suggests the change between hydraulic regimes occurs at a threshold surcharge level (s') of $0.258D_m$. Figure 5.3 does not show a secondary peak (thought to be caused by recircualtion) identified later in this study (shown in figure 5.3), this is likely due to fluorometer noise and/or cut-off techniques.

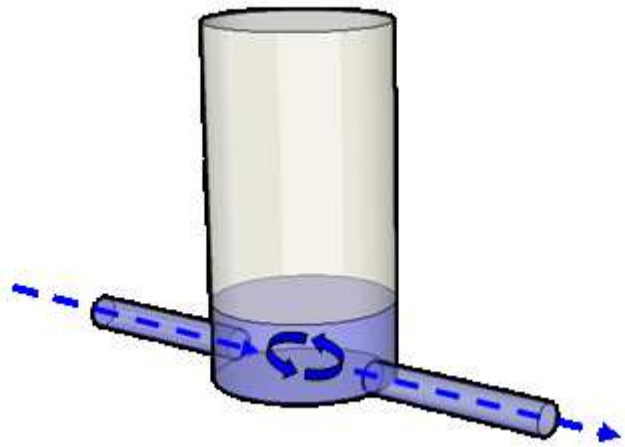

Figure 2.20: Low surcharge (pre-threshold) hydraulic regime in a manhole

The study determined trends in parameter values for the ADE and ADZ models for discharge and surcharge level (for the four manholes used). It was suggested that, as per the original aim, these model parameters could be used in water quality models to improve temporal and spatial water quality predictions. However, it was also noted that the laboratory results were limited to the range of configurations and hydraulic conditions used in the experiments. Guymer *et al.* (2005a) also noted that the results obtained may have only been applicable to the specific scale of the manholes studied, as the scalability of the model parameters was not clearly understood. Lau *et al.* (2008) specifically addressed the issue of scalability.

Lau *et al.* (2008) measured energy loss coefficients and temporal concentration

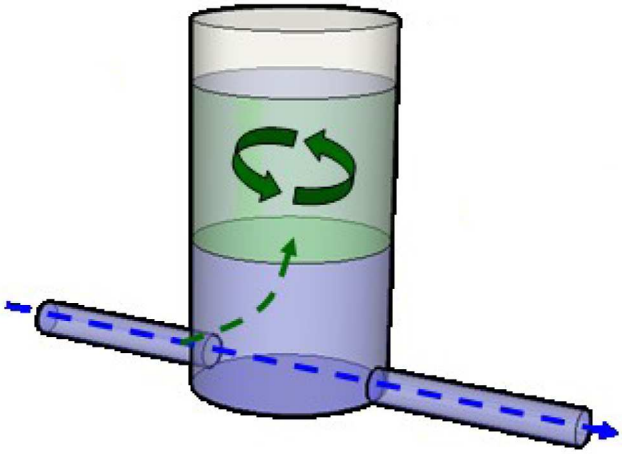

Figure 2.21: High surcharge (post-threshold) hydraulic regime in a manhole

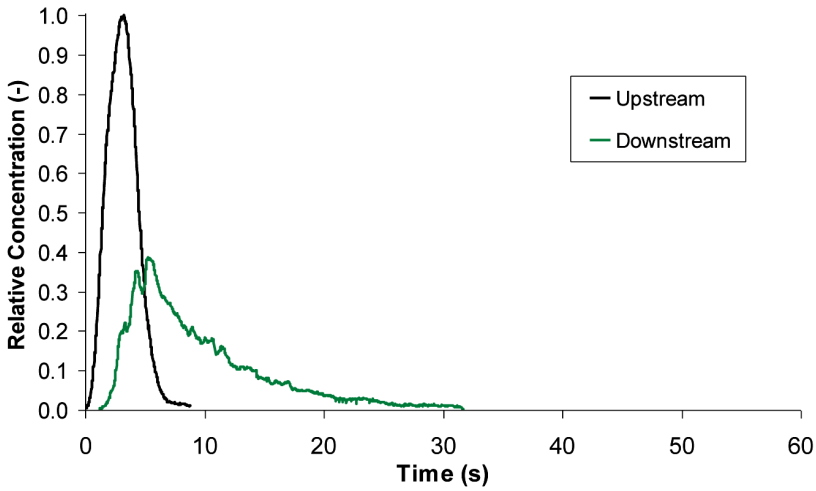

Figure 2.22: Example of tracer temporal concentration distributions in the scale manhole study (Q = 0.35 l/s; S = 1.25; Pre-threshold) (Lau et al.*, 2008)*

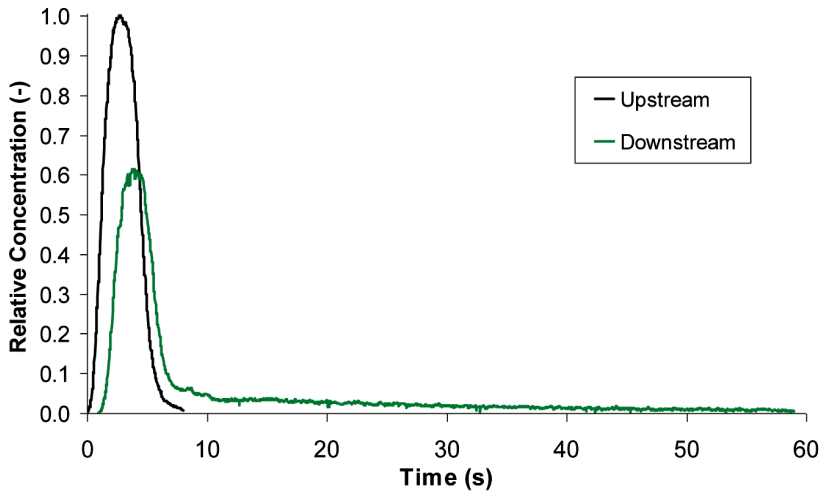

Figure 2.23: Example of tracer temporal concentration distributions in the scale manhole study (Q = 0.35 l/s; S = 3.33; Post-threshold) (Lau et al.*, 2008)*

distributions. These exhibited a sharp transition between pre-and post threshold surcharge ratios (S, equation 2.47) of between 2.0 and 2.5 (in agreement with Guymer *et al.* (2005a).

$$S = \frac{s}{D_p} \tag{2.47}$$

s Surcharge

D_p Pipe Diameter

Lau (2008) showed that the parameters for the ADE and ADZ models are not scalable as they appeared to be sensitive to the upstream temporal concentration distributions. This issue is particularly significant when the models do not provide a good fit to the measured concentration profiles. It was also noted that the determined model parameters are only applicable where the upstream conditions match that for which the parameters were originally derived. Due to this Temporal Concentration Profiles (TCP) and Cumulative Temporal Concentration Profiles (CTCP) were investigated as an alternative means of characterizing mixing processes within the manhole. Two distinct CTCPs, one for each of the two hydraulic regimes (pre and post threshold) were observed by Lau (2008).

Lau (2008) carried out a particle image velocimetry experiment (PIV) with the main aim of validating CFD manhole simulations. The work focussed on the time averaged velocity for the five planes of illumination under the pre and post threshold hydraulic conditions. To validate the PIV measurements of the time averaged velocity pipe flow, measurements were cross-referenced with Laser Induced Fluorescence (LIF) images. Verification of the PIV data was obtained on both the vertical and horizontal planes.

Lau *et al.* (2008) proposed that the scale-independent solute transport behaviour of manholes can be characterised by just two dimensionless CRTDs (normalised by the nominal residence time, equation 2.4.9); one for pre-threshold (low surcharge) and the second for post-threshold (high surcharge) hydraulic conditions. Results showed that geometric scaling laws may be used to characterise the flow regime, and to identify the threshold surcharge depth.

Guymer and Stovin (2011) used maximum entropy deconvolution (section 2.4.8) to generate CRTDs from previous laboratory data sets (over 800 individual solute traces). The resultant CRTDs did not collapse onto the two curves identified by Lau *et al.* (2008). This was attributed to cut-off techniques, and was especially prevalent in the high surcharge condition where recirculations are small. Subsequent scaling of the CRTDs using the known mass-balance factors allowed for two CRTDs to be derived; one for low, and one for high surcharge levels. Dimensionless CRTDs were shown to be transferable to different manhole-to-pipe diameter ratios.

2.6.1.2 Higher Order solute Transport Modelling

Guymer *et al.* (2005a) showed that the first order ADE and ADZ models did not fully describe the observed mixing processes in the laboratory experiments. However the optimisation procedure first presented by Dennis (2000) allowed for an improvement in the determination of these parameters. It was thought that the first order ADE model could not properly account for the large dead zone found in the manholes and the resulting impact on the mixing processes. It was suggested that *'two parallel ADZ cells, once cell describing the solute passing directly through the manhole and the other for the storage effects of the surcharged volume, would improve the accuracy of predictions'.* Guymer and

Dutton (2007) used higher order solute transport models to analyse temporal concentration profiles obtained from manhole laboratory data. Previous studies using the two parameter ADE and ADZ models did not accurately represent the downstream concentration profiles, and thus the models utilised were not fully representative. Therefore higher order solute transport models were needed to improve the accuracy of predicting the skewed downstream distributions caused by the dead zone. Guymer and Dutton (2007) showed the Hart transient storage model to better predict the skewed downstream traces in comparison to the first order ADE and ADZ models. Saiyudthong (2003) used the two cell technique of the first order ADZ model which provided a significant improvement over the single cell ADZ model. However, according to Lau *et al.* (2008): *'the models are not implemented in sewerage system models because of their complexity. There are no general rules to link the parameter values to physical properties of the system'.*

2.6.1.3 Benching

Benching is used in a manhole to provide a secure and flat surface for personnel to access the chamber, it is also designed to prevent flooding on the benching surface during dry weather flow (DWF) and to prevent the deposition of solids (Butler and Davies, 2004). Dennis (2000) studied the impact of benching in a manhole with a 1.5 D_p step height. He concluded that, with full pipe depth benching, *'the response of the manhole to the tracer experiments was highly comparable to that of a straight pipe'.* Saiyudthong (2003) also investigated the effect of benching on longitudinal mixing within a manhole. The manhole was benched to half pipe depth and also contained a change in pipe direction. Results showed that in most cases benching reduced mixing, this was most significant at low angles of deflection. At higher deflective angles it was hypothesised that the change in flow direction was too sharp and that the incoming flow passed over the channel and therefore mixed with the storage. As there was more interaction between the inflow and the stored volume of water, more mixing occurred in these cases (deflection $> 30°$).

2.6.1.4 Change in Direction

Saiyudthong (2003) examined the effects of a change in pipe direction on the longitudinal mixing in surcharged manholes. A 388 mm diameter manhole was considered with four different angles of deflection (0°, 30°, 60°, 90°) in both benched and unbenched manholes. The sharp transition previously mentioned in section 1.12.1.1 was shown using the ADZ model in the unbenched cases. As the deflection angle increased so too did the threshold level. This trend was not exhibited in the benched manhole ADZ data. No explanation was provided. It was concluded that an increase in deflection angle would result in more mixing within both the benched and unbenched manholes. This increase in mixing was caused by a greater interaction between the inlet jet and the dead zone leading to a greater transfer of tracer (Sonnenwald *et al.*, 2011).

2.6.1.5 Step Height

Dennis (2000) investigated five different step heights and their effects on longitudinal dispersion in a surcharged manhole. The study utilised a 388 mm manhole and step heights of 0 D_p, 0.5 D_p, 1 D_p, 1.5 D_p and 2.0 D_p. The study showed that the degree of mixing within the manhole increased with step height. It was theorised that this was due to a greater interaction between the incoming jet and the storage volume (dead zone). This led to a greater transfer of solute tracer to the dead zone and the remaining flow. Travel time, dispersion coefficient and dispersive fraction exhibited an approximately linear relationship with step height. However reach time delay did not. All model parameters were independent of surcharge depth and exhibited no obvious transitions in the solute transport characteristics. Lau *et al.* (2008) suggests that this might be due to Dennis (2000) only considering high levels of surcharge.

2.6.2 CFD Based Studies

Stovin (1996) presents probably the earliest CFD-based investigation into sewer system hydraulics and pollutant transport, focussing on sediment deposition in storage chambers. It has subsequently been built upon by a range of other studies.

Jarman *et al.* (2007) provides a good overview.

2.6.2.1 Combined Sewer Overflows (CSO)

Section 2.2.1 highlights the need for CSOs. Two similar studies have been undertaken using CFD to replicate the complex flow fields found in hydrodynamic separators. Harwood and Saul (2001) used the RSM turbulence models to simulate the flow fields for a 'Storm King'. Particle tracking was used to determine the retention efficiency of the structure. The results were validated against measurements from a full scale physical model. The CFD simulations were found to replicate the retention efficiency and the swirling nature of the flow field. Tyack and Fenner (1999) carried out a similar study to predict the flow field in a 'Grit King'. In these simulations the RNG k-ϵ turbulence model was used. The predictions made using CFD showed close agreement with experimental velocity data. Although most studies (lab and CFD) relating to solute and sediment transport in urban drainage systems have considered only steady conditions, Stovin *et al.* (2002a) proposed a methodology for the evaluation of the fine sediment separation efficiency of storage chambers. CFD was used to simulate the flow field within a 2D CSO as a result of a time varying inflow. Instantaneous 'snapshots' of the flow field were taken for use with the particle tracking method. The VOF model was used to track the position of the free surface. A hysteresis behaviour was detected, with efficiency being enhanced as the chamber was emptying compared to filling. At the time this was undertaken it was believed that simulating a larger more complex (3D) structure would be too computationally demanding with a 2D CSO run requiring 'several days' simulation. Kouyi *et al.* (2011) used a steady, 3D VOF CFD model to optimise the location of a water depth sensor in a dual overflow system consisting of two CSOs. However, the VOF discretization scheme used is not detailed. No comment is made on the sharpness of the air-water interface under steady modelling conditions.

2.6.2.2 Manholes

Asztely and Lyngfelt (1996) used CFD to predict energy loss in a simplified manhole under surcharged conditions. The manhole was modelled using a plane of symmetry on the central pipe axis as well as a fixed lid approximation (i.e. not

a free surface model). Good correlation was shown between the CFD predictions of energy loss coefficient and laboratory measurements published by Lindvall (1984). The standard k-ϵ turbulence model was also used by Dennis (2000) and Saiyudthong (2003) to predict the flow field and energy loss within step (or drop) manholes (which incorporate a vertical drop to connect sewers with different invert levels) and manholes with a change in pipe direction, the conclusion of which was that the computed energy loss coefficients were consistently smaller than laboratory results. This may be due to insufficient consideration of the modelling parameters such as grid resolution and refinement as well as selection of an appropriate turbulence model. No consideration was given for the use of CFD for solute transport predictions within Dennis (2000) and Saiyudthong (2003), (Lau *et al.*, 2008). Lau *et al.* (2008) carried out a detailed investigation of CFD modelling for surcharged manholes with the aim to develop a standard modelling protocol for manhole simulations through parametric studies of the modelling options. A 218 mm diameter manhole was simulated under pre and post threshold conditions to allow for the use of lab based validation data. The parametric studies undertaken are shown in table 2.4:

Parametric Studies	Objectives
Grid refinement	Identification of the mesh density required to obtain a grid independent flow field solution so that the errors associated with grid resolution, arise from interpolation between neighbouring grid points, are minimised
Spatial discretization scheme	Identification of appropriate schemes to minimise truncation error and obtain stable solutions
Turbulence model	Identification of appropriate turbulence models to reduce the numerical errors caused by RANS turbulence model
Solute transport model	Identification of appropriate solute transport models

Table 2.4: Parametric studies considered and the aims of each study (Lau et al.*, 2008)*

These led to a number of suggestions for a standard modelling protocol (Lau *et al.*, 2008):

- QUICK and PRESTO discretization schemes are recommended for manhole simulations
- The extra computational expense required by the RSM did not lead to improved predictions about the mean flow field
- The RNG k-ϵ turbulence model is recommended for manhole simulations
- The particle tracking technique and the species model exhibited highly comparable predictions when the same flow field was used for prediction. Due to the increased run time required for the species model, the particle tracking method is recommended for solute transport predictions.

The proposed modelling protocols were highlighted as an appropriate compromise between accuracy and computational efficiency. Lau *et al.* (2008) investigated the effect of surcharge, discharge and geometrical scale for manholes using the standard modelling protocols listed above. The study showed that the degree of jet deviation in the flow field under pre-threshold conditions was a function of surcharge conditions. Jet deviation was low with an increasing surcharge ratio and disappeared completely when the surcharge level increased beyond the threshold. Post-threshold, the flow field remained independent of surcharge. A comparison between the CFD models and the lab based studies showed the numerical models to prematurely predict the occurrence of the transition (at a surcharge ratio (S) of 2.05). Lau *et al.* (2008) suggested that *'When more advanced computational resources becomes available, the manhole simulations should be repeated using two phase modelling to account for the effects of the free surface. The results could be used to assess the effects of the fixed lid assumption on the flow field and solute transport predictions. In addition, Large Eddy Simulation (LES) or a coupled LES/RANS modelling approach* (Turnbull, 2003) *should be considered.'* To the best of the author's knowledge no previous work has been carried out to quantify dispersion in time dependent flows with a free surface model (such as the VOF model).

2.6.2.3 Pipes

Grimm (2003) utilised CFD to predict the flow field and solute transport in a 10 m straight pipe. Numerous runs were carried out in order to verify the flow field

and the solute transport predictions by comparing them with published lab data (Guymer and O'Brien, 2000). Through this validation a number of parameters to which the models were sensitive were identified.

- Species transport model parametric study - predictions were found to be sensitive to the choice of spatial and temporal discretization scheme, and to the size of the time step. The options that resulted in robust predictions for both the mean travel time and dispersion were identified (Grimm, 2003).
- Discrete phase model parametric study - was shown to be computationally efficient and that consistent predictions were attainable. The prediction of the mean travel time was inaccurate (Grimm, 2003).

When validating the species transport model the predicted variation in longitudinal dispersion coefficient with discharge showed the same linear trend as the theoretical equation proposed by Taylor (1954). However, the simulated data consistently under predicted the measured Guymer and O'Brien (2000) values. In conclusion, a defined methodology for modelling solute transport through a pipe was created which had previously not existed (Stovin *et al.*, 2002a).

2.6.2.4 Ponds and Reservoirs

Various CFD studies (Ta and Brignal, 1998; Wood et al., 1998; Shilton 2000; Salter et al., 2000) have been carried out in ponds and reservoirs because of fears about the operating performance, due to short circuiting effects. These studies have allowed for a better understanding of the residence time characteristics of these structures. However, due to a lack of proper validation these studies have been severely limited.

2.6.2.5 Sewer Invert Traps

Solids are an increasing problem in combined sewer systems in developed countries due to increasing urbanisation and a growing population (Stovin *et al.*, 2005). Sediment deposits in sewer systems can lead to many problems. This may impair the function of the sewer and could lead to problems such as blockages or

premature operation of CSOs due to insufficient capacity. One solution is the use of sewer invert traps. These aim to remove problematic solids before build-ups occur. Buxton (2002) developed a CFD modelling approach for the prediction of the sediment retention performance of in-sewer invert traps. Numerical predictions were compared with laboratory particle image velocimetry (PIV) flow field data and sediment trapping performance data. The study showed high sensitivity to the selection of turbulence model with regards to predicting secondary circulations in a trapezoidal channel. The sediment retention performance was also found to be highly sensitive to the initial parameters for the particle tracking model.

2.6.2.6 Storage Chambers

Online and offline storage chambers are an integral part of urban drainage systems. By providing extra storage within the system the number and magnitude of CSO spills can be reduced. Stovin (1996) used CFD to predict flow fields and sediment retention efficiency in a storage chamber. Flow field predictions were validated against laboratory flow field data and were shown to be in reasonable agreement. Sediment retention efficiency was examined in two ways; one approach *'was based on the concept of a critical bed shear stress for deposition'*. The particle tracking model was also used to obtain a statistical distribution of sediment destinations. A number of different geometric and hydraulic configurations were used to evaluate the differences in the retention efficiencies shown by these two methods. This was taken further by Stovin *et al.* (1999) where the particle tracking model was used to predict the gross solids separation efficiency in six storage chambers. The critical bed shear stress approach detailed above was further developed by Adamsson *et al.* (2003) creating a user-defined boundary condition for use with the particle tracking model to determine the destination of particles within a storage chamber. This was validated against measured data and was proven to be superior to the standard modelling parameters. Dufresne *et al.* (2007) used Particle Image velocimetry (PIV) and acoustic Doppler velocimetry to measure the 3D mean velocity and the turbulent kinetic energy in transversal planes of a storm-water tank. Measurements were then compared to the simulated results of a VOF CFD model and were said to be in good agreement. However, goodness of fit was not quantified. PIV was suggested as a good

way of measuring three-dimensional velocity flow fields (as used by Lau (2008)).

2.6.2.7 Storm Tanks

Storm tanks are designed to provide extra storage during a storm event before discharging to a neighbouring water course. A design method using CFD for the optimum retention of solids was developed by Kluck (1997). The method aimed to achieve optimum retention of solids. The particle tracking model was implemented by Ta (1999) to examine the retention efficiency of suspended particles in a rectangular storm tank under unsteady conditions. Lau *et al.* (2004) evaluated the performance of different geometrical configurations of storm tanks by comparing their retention time and short circuiting parameters found using a number of 2D CFD models. The particle tracking model was used to predict the retention time distributions for the models. This shows the particle tracking model to be capable of representing the solute transport characteristics of an urban drainage structure such as a storm tank (or manhole).

2.6.2.8 Gully Inlet

Djordjević *et al.* (2011) investigated the interactions between surface flood flow in urban areas and the flow in below ground drainage systems (sewer pipes and manholes) using an experimental rig; a full scale gully structure with inlet grating connected to an 8 m^2 surface area. Below the surface, an outfall pipe connected to a tank allowed for surcharge conditions to be imposed (i.e. the gully to over-top).

A three-dimensional CFD VOF representation of the laboratory rig is also presented showing comparisons of CFD modelling (OpenFOAM) results (free-surface position) with observed experimental results. Djordjević *et al.* (2011) suggests the surface position predicted by the CFD is a 'good fit'. However, the goodness of fit is not quantified. Detailed description of governing equations, turbulence models, numerical modelling procedures and mesh generation are not presented. Galambos *et al.* (submitted) intends to contain all such information.

Snapshots of an unsteady (VOF) flow simulation presented indicate that the model is capable of simulating complicated (rapid surcharge) flow situations and

producing qualitatively realistic results. The meshing scheme used for this simulation appears to be unstructured.

2.6.2.9 Hydrodynamic Vortex Mixer

Fink and Andoh (2011) outline the development process of a custom non-powered vortex mixer from initial concept through preliminary CFD models (to determine fitness for purpose) to the ultimate testing of the actual constructed unit in-situ. An unstructured tetrahedral meshing scheme (500,000 cells) was used for the vortex mixer. The RSM model was used to represent turbulence.

Results included assessment of path-lines, velocity profiles and predictions of sludge concentrations (using an introduced scalar). Sludge concentrations for the CFD model and in-situ unit were shown to be in high agreement (0.04% error). As the introduction of a scalar (to represent sludge) effectively integrates with the flow field this suggests the unstructured mesh and corresponding flow field (and turbulence models) represented the flow within the vortex mixer well.

Fink and Andoh (2011) concludes that the in-situ unit works as designed.

2.6.2.10 Hydrodynamic Separator

Pathapati and Sansalone (2009) presents a stable, grid independent representation of a hydrodynamic separator. CFD results were validated with data from a scale laboratory rig using the relative percentage difference between model and measured data (particles separated, less than 10% difference). The standard k-ϵ turbulence model was used as *'the full RSM, Realizable and Renormalized k-ϵ models tested, did not suggest any improvement that might warrant the increased computational power and time'*.

2.6.2.11 Junctions

Mignot *et al.* (2011) validated a 3D CFD model of flow structures in junctions, using experimental velocity data (profiles and contours of magnitude) giving confidence for extending the use of the numerical model post validation.

2.7 Conclusions

The use of CFD to model components of urban drainage systems is now reasonably well established (Jarman *et al.*, 2007), although all of the key studies that have focussed on pollutants (sediment or solute) have been restricted to steady state hydraulics for which the position of the free surface could be directly imposed.

Stovin *et al.* (2002b) have presented a preliminary 2D study to asses the feasibility of modelling time-dependent flows using the two phase VOF model.

The present study will extend this work to consider the situation in surcharged manholes, where an interesting transition (first identified by Guymer *et al.* 2005a) occurs between two distinctly different hydraulic regimes as a function of surcharge depth ($s' = 0.258D_m$). Recent work on solute transport in manholes (Lau *et al.*, 2008) identified significant limitations to the use of the two-parameter ADE and ADZ models in this context. As an alternative, the use of the dimensionless CRTD was advocated, which was shown to provide a more complete and scalable model. The proposed time-dependent work will build upon this finding.

Current manhole work is limited to unrealistically high D_M/D_p ratios; the research also aims to explore the existence of the hydraulic threshold in low D_M/D_p manholes.

Due to previous work carried out by Lau (2008), Guymer and O'Brien (2000) (The University of Sheffield) and Jones (2012) (The University of Warwick), a large amount of data already exists pertaining to surcharged manholes. This includes laboratory PIV (mean flow field), fluorometer data (which can be manipulated into other forms) and CFD (mean flow field, solute traces etc.). This data is invaluable for potential validation work and was used throughout this study to compliment the investigations herein. A summary of this data may be found in appendix 2.

Chapter 3

Preliminary Investigations

3.1 Introduction

A number of preliminary investigations were undertaken in advance of the main programme of simulations and analysis. There were two specific purposes for these investigations. The first was simply to gain operational familiarity with the CFD modelling tools, and to develop an appreciation of the key issues and considerations involved. The second purpose was more directly to influence the selection of scenarios and parameters to be included (or excluded) from the main experimental programme. In the absence of any restrictions on time and computational resources, a CFD-based investigation into the solute transport characteristics of surcharged manholes subjected to time-dependent inflows and intermittent solute injections would require full 3D simulations of large numbers of manhole configurations subjected to a wide range of time-dependent inflow conditions and periodic solute injections. Ideally such a study would also include comprehensive sensitivity analyses to consider mesh-independence, the influence of turbulence model choice and a range of parameters that influence the solute transport modelling approaches (species or discrete phase). Both Grimm (2003) and Lau (2008) found the species model to offer a slight improvement in replicating the initial peak of solute trace data. Due to this improvement and the need to use a coupled method for representing solute within the flow field (for unsteady conditions), the species model was considered initially over the alternate discrete-phase. The dis-

crete phase model also includes coupling. However FLUENT (2005a) suggests it is intended for use where the continuous phase flow pattern is impacted by the discrete phase.

Given the necessarily finite nature of the work, it was very important to refine the experimental programme such that useful outcomes might efficiently be derived, maximising the confidence in the conclusions and the generic value of the outcomes. The preliminary tests were therefore also designed to address the following questions:

- Are 3D simulations required?
- Are time-dependent simulations (and thus species modelling) required and/or practical?
- Are time-dependent, 3D simulations required?

These questions were addressed through a logical progression of model scenarios, beginning with a 2D pipe flowing full, and progressing via a 2D free-surface CSO model to full 3D free-surface manhole simulations. These preliminary investigations are discussed in sections 3.2, 3.3 and 3.4 respectively. Section 3.2 also includes the development of a methodology for identifying a dispersion coefficient under unsteady conditions. Finally, section 3.5.3 reflects on whether the computational expense associated with fully coupled time-dependent flow and solute transport simulations is justified, through consideration of the relative time-scales associated with solute transport and hydraulic regime transitions in the context of surcharged manholes. Table 3.1 shows an overview of the models investigated.

	2D Pipe Flowing Full	2D Free Surface CSO	3D Free Surface Manhole
Free-surface	No	Yes	Yes
Steady	Yes	No	No
Unsteady	Yes	Yes	Yes
Solute	Yes	Yes	No
Turbulence Model	k-ϵ RNG	k-ϵ RNG	k-ϵ RNG

Table 3.1: Overview of Preliminary Investigations

3.2 CFD Modelling of Solute Transport in a 2D Pipe Flowing Full

3.2.1 GAMBIT Methodology

Previous investigations of dispersion within a laboratory pipe set-up at The University of Sheffield utilized a 0.024 m diameter Perspex pipe (Lau, 2008). It was therefore decided that a mesh would be generated to represent the same pipe to allow for comparison against existing laboratory data. The mesh generation was undertaken using GAMBIT meshing software which is supplied with the FLUENT CFD software. The properties of the generated mesh were as follows:

- 2D
- 10 m in length
- 0.012 m radius
- Axis symmetrical problem (See figure 3.1)
- ≈18,000 Cells
- Maximum cell aspect ratio in accordance with user documentation (FLUENT, 2005a)

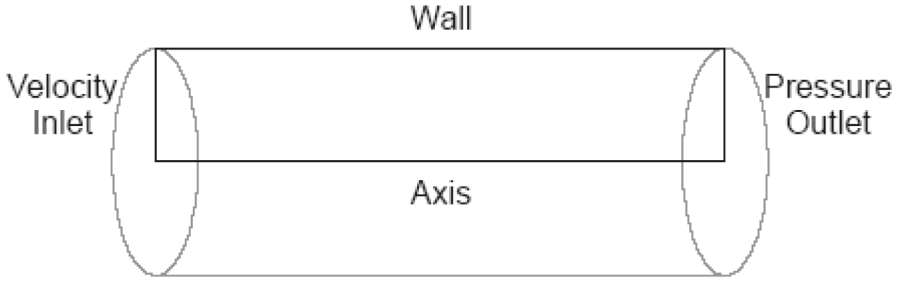

Figure 3.1: Axis Symmetrical Boundary Conditions

3.2.2 FLUENT Methodology

3.2.2.1 Ensuring a fully developed flow solution

To ensure a fully converged flow solution before inputting any dye traces, a velocity was set normal to the pipe inlet. The residuals were then monitored until they converged ($1x10^{-5}$). The velocity profiles at the pipe outlet (10 m), as well as the turbulent intensity and dissipation rate (ϵ) were then read in as a user defined profile at the pipe inlet, before the process was repeated. A sample velocity distribution ($\overline{u}$ = 0.6 m/s) is shown in figure 3.2 reflected around the x-axis (as in the axis symmetrical solver).

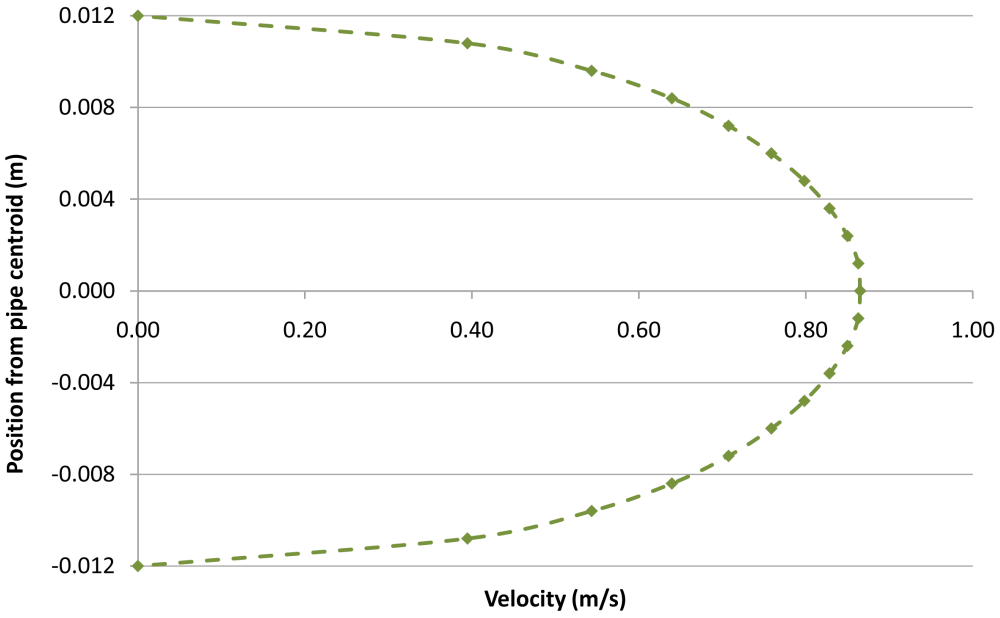

Figure 3.2: An axis symmetrical velocity distribution created using FLUENT (Q = 0.33 l/s)

This process resulted in the flow solution converging (on visual inspection) within 0.1 m of the pipe inlet.

The k-ϵ RNG turbulence model was used throughout all preliminary studies following recommendations by Lau (2008). The double precision solver was also used for all studies requiring the species model (section 3.2.2.2). A laboratory derived roughness of 4×10^{-5} (Perspex) was used for all walls. For preliminary investigations mesh independence was not considered.

3.2.2.2 Modelling Tracer Species

In order to model 'dye traces' through the pipe using the species model, a new tracer fluid, based on water, was created and then added to the mixture template along with water. The labelling used in the CFD model allows the user to add any number of unique tracer species, whereas lab tests are usually limited to one tracer at a time (because traces can only be distinguished on the basis of physical properties). However, this may be overcome with the use of fluorescent input tracers. In accordance with Grimm (2003) and FLUENT (2005a), the second order upwind discretization scheme was utilised throughout all preliminary simulations. Once a converged flow solution was reached in steady conditions (residuals lower than 1×10^{-5}), the flow and turbulence equations were turned off (this is termed cold or uncoupled processing) reducing the computational expense of enabling the species model (and therefore unsteady conditions). Typically this allowed for full ($> 99.9\%$) mass recovery within a few hours (this is estimated as 10 times more efficient than coupled processing (Grimm, 2003)). A time step of 0.01 s was used with 20 iterations per time step based on findings by Grimm (2003) and recommendations by FLUENT (2005a).

To ensure full mixing of input tracer the pipe was split into four 2.5 m reaches, each being monitored at the start and the end. A square, 1 second long inlet trace was passed through the pipe and the concentration (area weighted average mass fraction of species) was monitored at each cross-section.

Dispersion was calculated using the method of moments (section 2.4.2) for each reach, the results of which are shown in figure 3.3, for a steady flow simulation.

It can be seen from figure 3.3 that the dispersion becomes constant after the first 2.5 m reach. The slight increase in dispersion in the final reach (7.5-10 m) is due to monitoring directly on a pressure outlet. In all subsequent simulations the monitors were placed slightly before this outlet.

3.2.2.3 Modelling Multiple Tracer Species

To confirm the robustness of the methodology used in 3.2.2.2, a simulation was carried out to monitor 3 overlapping pulses of dye through the pipe.

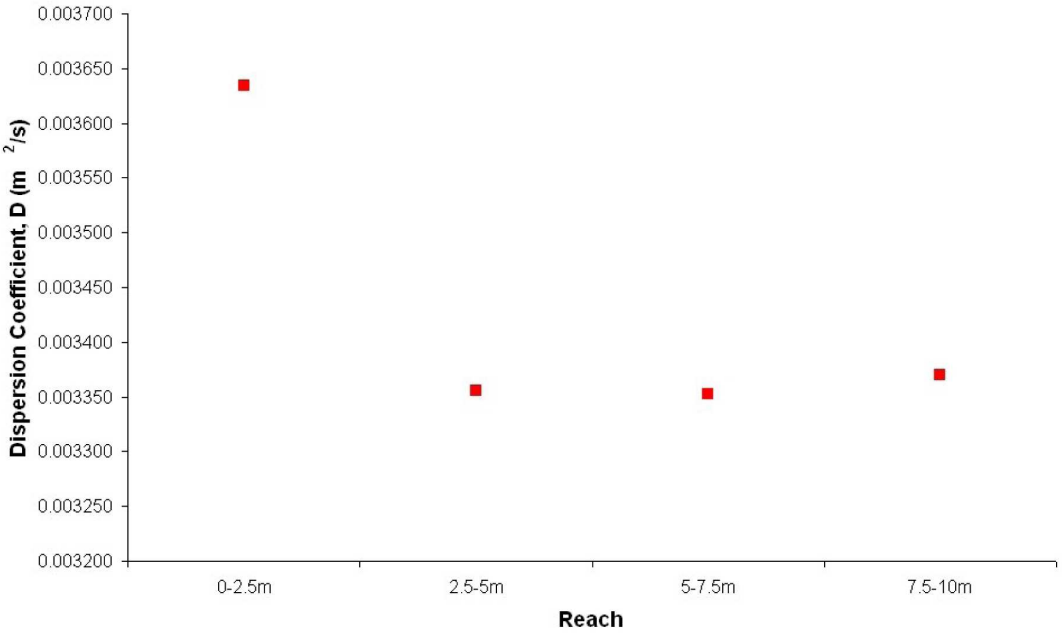

Figure 3.3: Dispersion between four 2.5 m reaches (Q =0.5 l/s)

The dashed traces shown in figure 3.4 were monitored at the mid-point in the pipe length, whereas the solid traces were measured just before the pressure outlet. Colours link the monitored traces.

It can be seen that (in figure 3.4 and table 3.2) each trace has experienced the same amount of dispersion, thus proving that the previous simulation (3.2.2.2) was robust and that the multiple trace modelling 'experimental' procedure used is consistent.

Tracer	Length (m)	Travel Time (s)	u (m/s)	Dispersion Coefficient D (m^2/s)
1	5	4.5085	1.1	0.003362
2	5	4.5082	1.1	0.003363
3	5	4.5080	1.1	0.003367

Table 3.2: Multi injection summary results

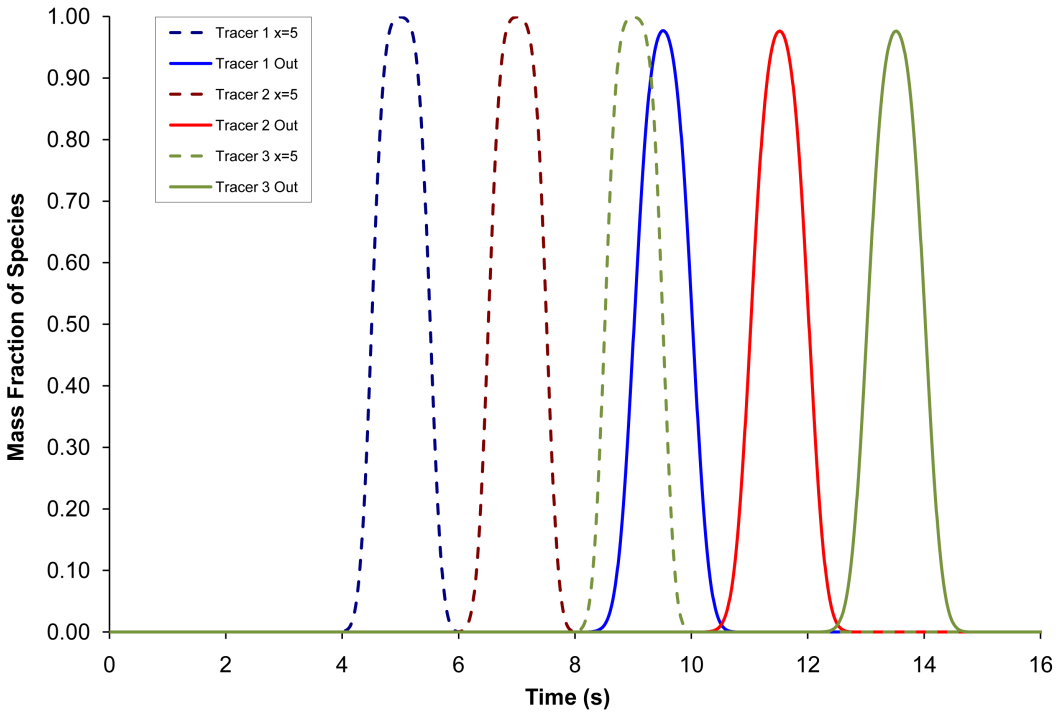

Figure 3.4: Monitored traces using multiple injections (Q = 0.5 l/s)

3.2.3 Steady Flow Dispersion Investigation

Utilising the primary methodology developed, a representative range of fully turbulent flows was selected to investigate dispersion within the 2D pipe under steady conditions, these are shown in table 3.3.

3.2.4 Steady Flow Results

As per the previous two simulations, a converged flow solution was developed using the method detailed in 3.2.2.1 for a range of inlet velocities from 0.6 m/s to 1.8 m/s (the corresponding flow rates are shown in table 3.3). A 1 s square inlet trace was then monitored between two points within the pipe (5 m and 7.5 m from the inlet) and then analysed using the method of moments. It can be seen from figure 3.5 that, as the velocity within the pipe increases, dispersion increases linearly, as per Taylor (1954).

u (m/s)	Q (m^3/s)	Q (l/s)	Re
0.6	0.00027	0.27	14400
0.7	0.00032	0.32	16800
0.8	0.00036	0.36	19200
0.9	0.00041	0.41	21600
1.0	0.00045	0.45	24000
1.1	0.00050	0.50	26400
1.2	0.00054	0.54	28800
1.3	0.00059	0.59	31200
1.8	0.00081	0.81	43200

Table 3.3: Flow rates and velocities used for pipe FLUENT simulations

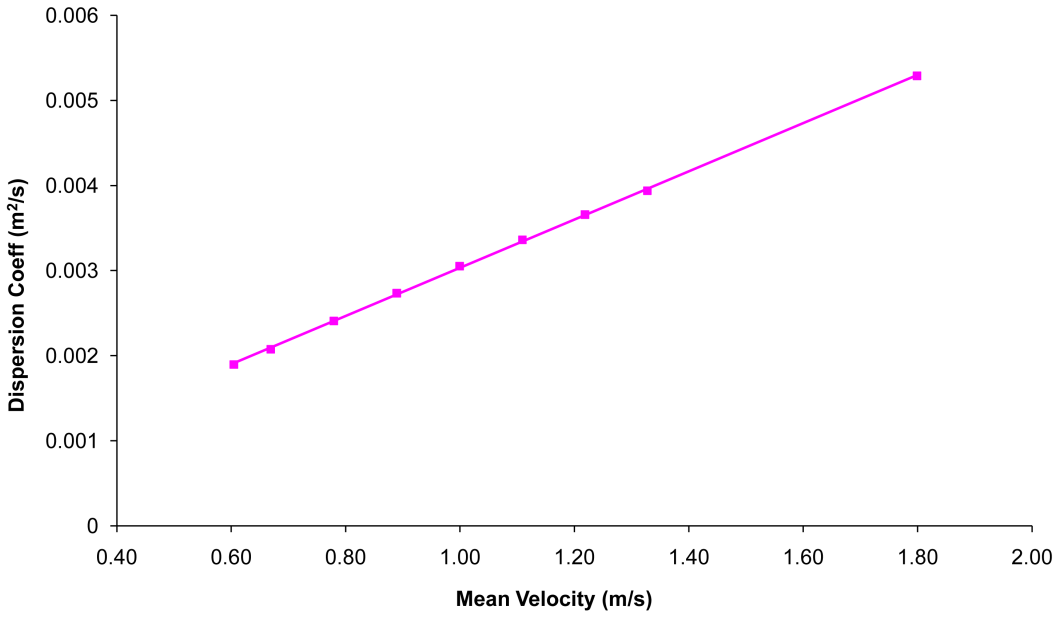

Figure 3.5: Steady state dispersion coefficients

3.2.5 Unsteady Flow Conditions

Steady state conditions are not overly relevant to the majority of hydraulic structures as they often experience dynamic storm events, which in turn cause acceleration and deceleration within the flow field and changes in depth/level of surcharge. In order to better understand potential phenomena caused by these changing flows, the pipe model was subjected to a series of unsteady flow conditions. The following sections describe a series of feasibility studies aimed at confirming that the FLUENT CFD software can be used to generate solute trace data under unsteady flow conditions, and to develop appropriate procedures of analysing the output data.

3.2.5.1 Idealised Hydrograph Methodology

Commonly urban drainage structures experience storm events which can be represented within the software by using an inflow profile or hydrograph. In order to minimise the run time of the unsteady simulation a shortened inflow hydrograph with duration of 20 seconds was chosen. Inlet velocity profiles were input as previously detailed (3.2.2) and a journal file was created (FLUENT, 2005a) which allowed a stepped hydrograph profile (figure 3.6) to be input.

A series of 1 s square pulses was input over the entire length of the hydrograph (figure 3.7). This was done in such a manner as to achieve traces that had experienced the rising limb of the hydrograph, the crest and the falling limb to enable the effects of accelerating and decelerating flows to be seen. Figure 3.7 shows traces corresponding to monitors positioned at 5 m and 7.5 m.

3.2.5.2 Idealised Hydrograph Results - Cumulative Time

The average velocity for a given tracer was calculated using the reach length and the travel time (shown in figure 3.8).

$$\overline{u} = \frac{\overline{t}_{ds} - \overline{t}_{us}}{x} \tag{3.1}$$

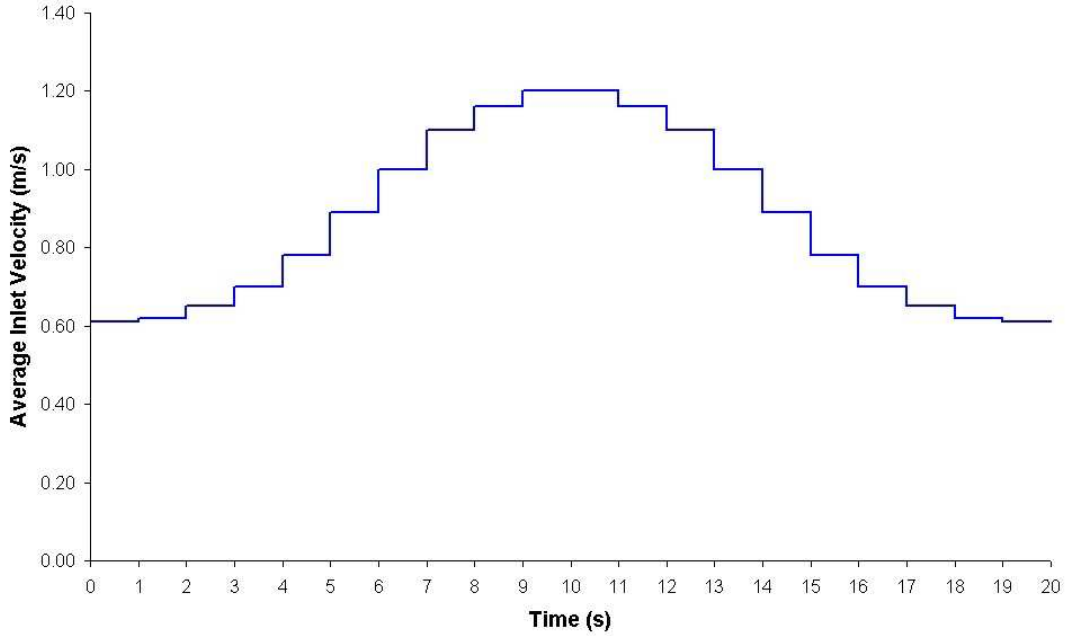

Figure 3.6: Idealised Stepped Hydrograph

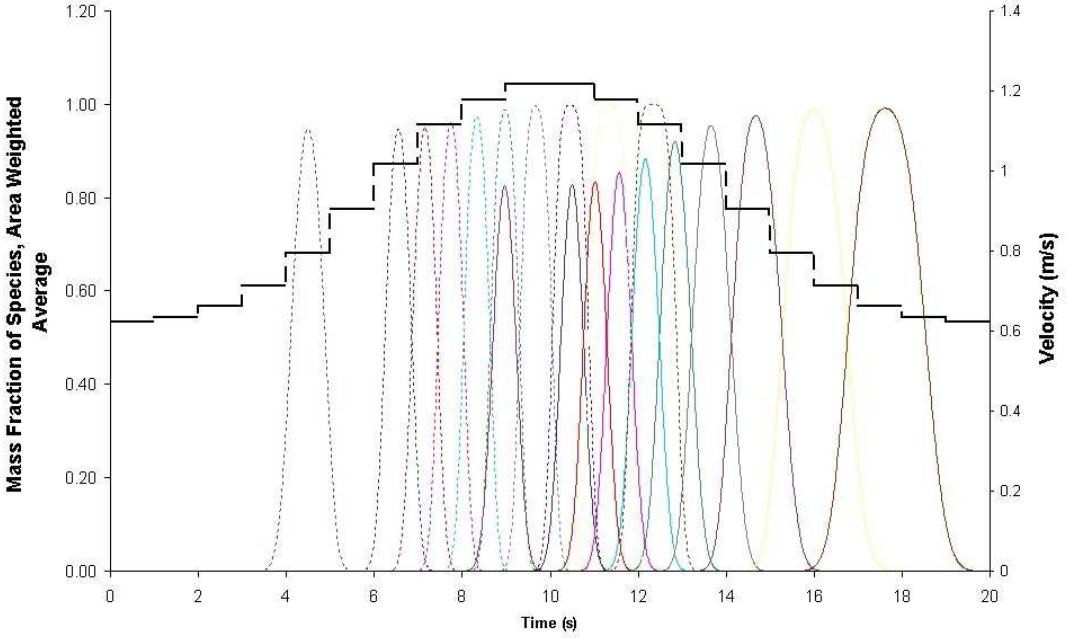

Figure 3.7: Monitored Traces corresponding to the inflow hydrograph shown in figure 3.6, dashed lines were monitored at 5 m from the inlet, solid lines were monitored at 7.5 m from the inlet (the input mean velocity is also shown)

where:

- x distance between monitoring locations (m)
- $\bar{t}_{us}$ upstream time for centroid of distribution (s)
- $\bar{t}_{ds}$ downstream time for centroid of distribution (s)

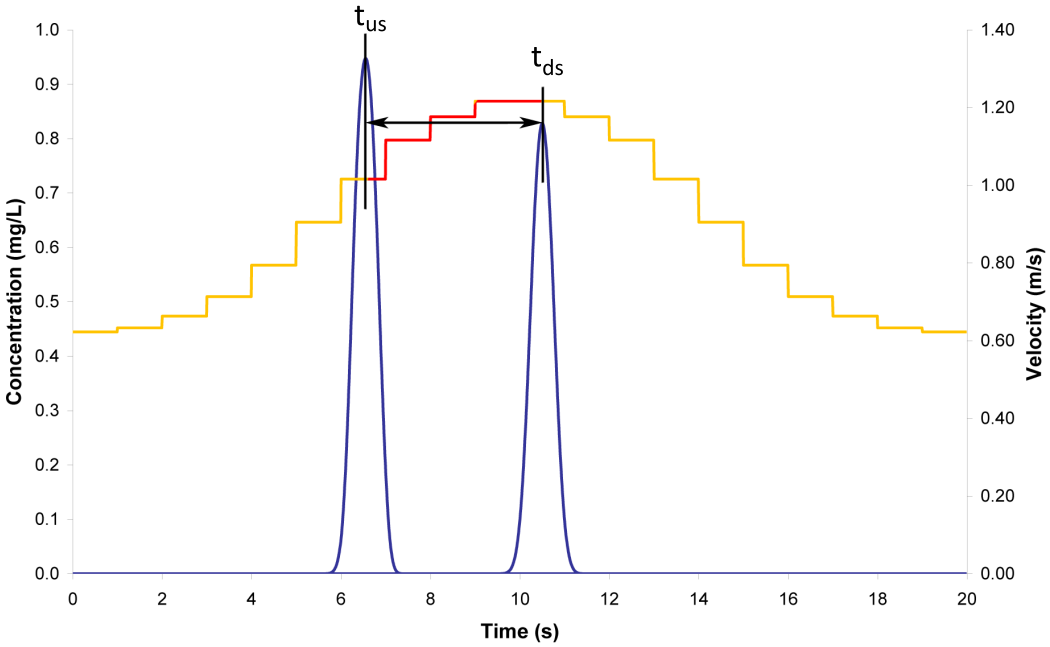

Figure 3.8: Classifying average velocity; the velocity experienced by the modelled solute is shown in red

Dispersion was calculated as per the previous investigations (using equation 3.2). The results (figure 3.9) highlighted an anomaly; a trace that had experienced the majority of the falling limb resulted in a negative dispersion coefficient. This was due to the upstream monitored pulse experiencing a much greater volume of flow than the downstream pulse, thus compressing the second distribution. Simple temporal moment analysis applied to concentration data with respect to time assumes that flow rate is constant. Strictly, however, it is a mass flow rate, therefore requiring concentration · Q to give comparable loads. This temporal moment analysis is therefore inapplicable for unsteady conditions.

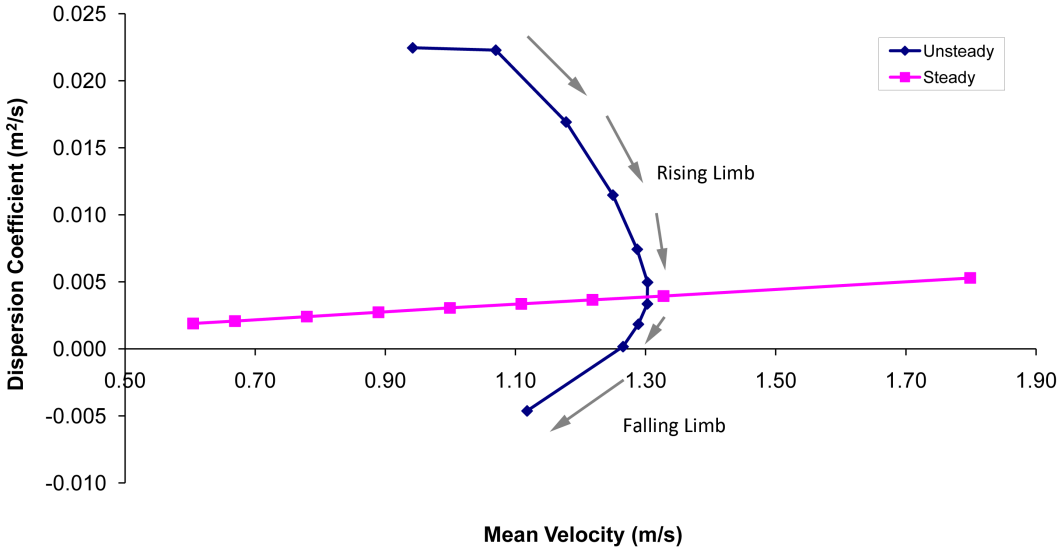

Figure 3.9: Comparison of dispersion under both steady and unsteady conditions carried out with respect to cumulative time

3.2.5.3 Analysis of Dispersion in Time-Dependent Problems

Due to the observations detailed above it was necessary to devise an approach to quantify dispersion in unsteady conditions (equation 3.2 is used in steady conditions). Equation 3.3 was therefore formulated (see appendix 1) for full derivation).

$$K = \frac{u^2}{2} \cdot \frac{{\sigma_t}^2(x_2) - {\sigma_t}^2(x_1)}{t_2 - t_1} \tag{3.2}$$

$$K = \frac{1}{2}\left(\frac{x \cdot Q}{vol}\right)^2 \left(\frac{1}{Q} \cdot \frac{d{\sigma^2}_{vol}}{dvol}\right) \tag{3.3}$$

Where:

K	dispersion coefficient
dvol	change in cumulative discharge
σ^2	variance

In equation 3.3, dispersion is calculated relative to cumulative discharge (volume

of flow), rather than time. This ensures that the spread is quantified with respect to the same 'parcel' of water, even if the specific flowrate varies in time. To validate equation 3.3, the initial steady state results were re-analysed with respect to cumulative flow. Results are shown in table 3.4.

u (m/s)	Eq 3.2	Eq 3.3	Error
0.6	0.002076	0.002076	1.03E-15
0.7	0.002408	0.002409	-3.54E-16
0.8	0.002734	0.002734	1.72E-15
1.0	0.003053	0.003053	1.09E-16
1.1	0.003363	0.003363	2.50E-15
1.2	0.003658	0.003658	4.77E-17
1.3	0.003939	0.003939	2.60E-15

Table 3.4: Dispersion coefficients for steady state data analysed with respect to time and cumulative flow

The error column clearly shows that there is no significant difference in calculated dispersion for these two approaches. Therefore, equation 3.3 was applied to the results obtained from the idealised hydrograph simulation.

3.2.5.4 Idealised Hydrograph Results - Cumulative Discharge

Figure 3.10 shows the results originally presented in figure 3.9 re-analysed according to equation 3.3 (arrows indicate whether a 'trace' lies on the rising or falling limb). Figure 3.10 shows the greatest dispersion on the rising limb (with dispersion exceeding that of a similar velocity simulation under steady conditions). As the flows begins to reach a maximum velocity, level off and then start decelerating, a change can be seen in the monitored dispersion. For a similar average velocity on the falling limb the dispersion is less than that experienced over the same average velocity on the rising limb, this trend continues until the levels of dispersion converge back to steady state.

In order to further investigate the effects of acceleration and deceleration on dispersion it is necessary to isolate the two. In this way an input trace will only experience one of the two processes. Section 3.2.5.5 describes an experiment to measure dispersion under a range of steady acceleration conditions.

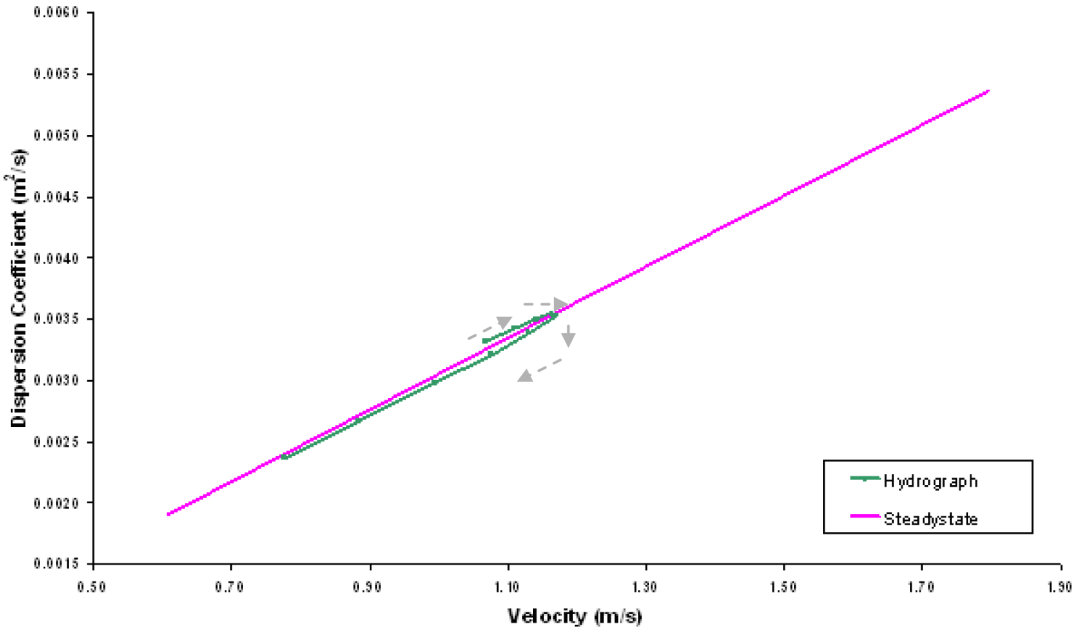

Figure 3.10: Enhanced levels of dispersion shown by the hydrograph simulation when compared to steady state

3.2.5.5 Idealised Rising Limb Methodology

The rising limb of the hydrograph was modelled with an extended flat lead-in and a similar tail. The aim of the lead-in and the tail was to allow more than one pulse to pass through the model whilst still effectively under steady state flow conditions. Each section of the rising limb had a duration that allowed at least 3 pulses to pass through the model. Another pulse was added at each change in acceleration. These pulses are represented in figure 3.11 as purple lines with the start and end marked for clarity.

The velocity profile for the rising limb simulation is also shown in figure 3.11. Note that in this case the transitions are not stepped, but smooth (specified using an input velocity equation within a journal file).

3.2.5.6 Idealised Rising Limb Results

As per section 3.2.5.4, dispersion was quantified using a method of moments with respect to cumulative discharge.

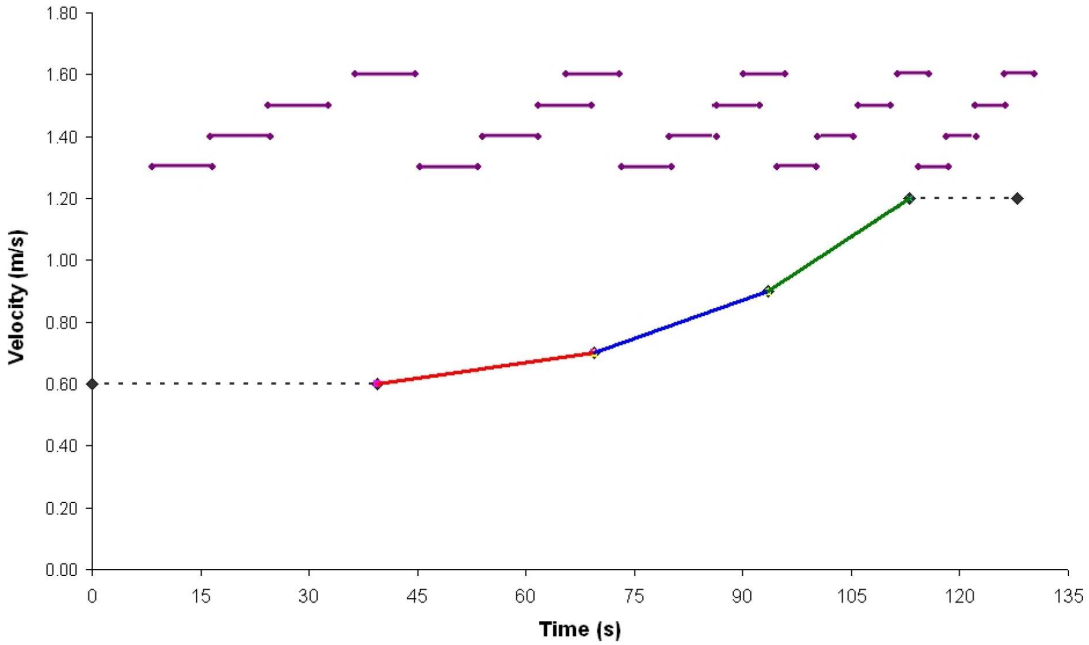

Figure 3.11: Rising limb velocity profile and overlaid dye traces

The results (figure 3.12) appear to show similar levels of dispersion to the initial steady state simulation, however they are not identical. The rising limb simulation is in agreement with the steady state data initially (the lead in), it then exhibits enhanced levels of dispersion before returning to steady conditions (the tail). The magnitude of the monitored enhanced dispersion is small (max 2% enhancement with respect to steady flow).

3.2.5.7 Idealised 'Large Step' Methodology

As section 3.2.5.6 did not exhibit a greater amount of dispersion than observed in the idealised hydrograph simulation, a more obvious change in flow conditions was investigated. The pipe model was subjected to two different large velocity steps, one from 0.6-1.2 m/s and the other from 0.6-1.8 m/s. As in all previous simulations a number of square inlet pulses were input to the model and monitored between two fixed positions (5 m and 7.5 m from the inlet). The dispersion coefficient was then calculated using the method of moments with respect to cumulative flow as detailed in section 3.2.5.3.

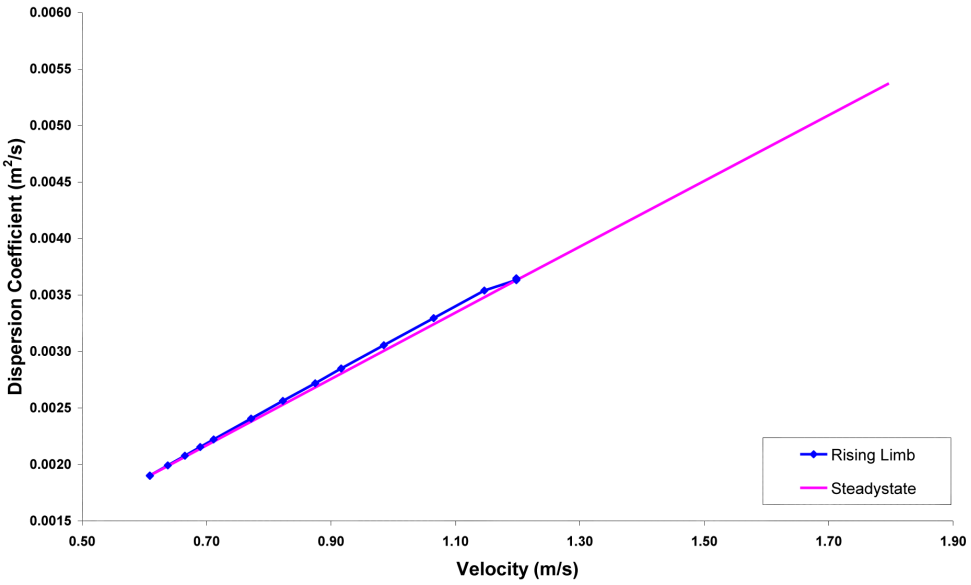

Figure 3.12: Rising limb dispersion results

3.2.5.8 Idealised 'Large Step' Results

It can be seen (figure 3.13) that for both 'steps' the dispersion is greater (maximum 2.5% and 3.5% respectively) than for that of the steady state simulations. The trend lines deviate from the steady state up until the point at which the effects of the step have passed and the flow solution re-converges to a steady state solution (thus showing the model is robust).

3.2.5.9 Flow Velocities

Due to the differences between the hydrograph and the rising limb simulation it was necessary to confirm whether FLUENT (and the modelling methodology) was accurately representing the flow field after each 'step', as immediate convergence of the flow field to the 'new' velocity profile would not be realistic.

Figure 3.14 shows the velocity at a given radial distance from the pipe axis whilst the pipe experiences the 0.6-1.2 m/s step at time 1000 ms. It can be seen that near the pipe axis (the centre of the pipe), the velocity increases to a magnitude greater than the step maximum, conversely near the pipe boundary the velocity is reduced until the boundary layer reforms and equilibrium is reached. During

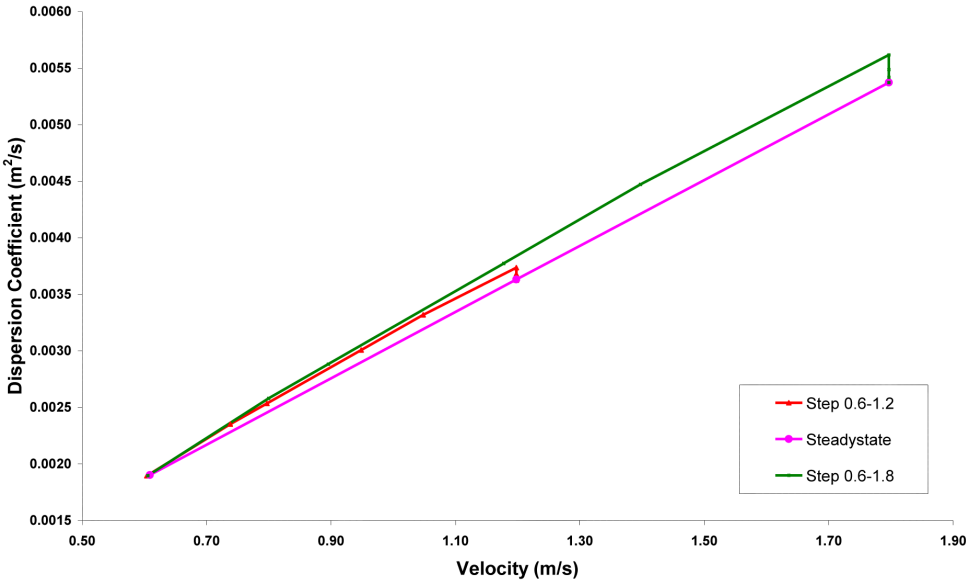

Figure 3.13: Dispersion over two large velocity steps

this process the average velocity remains constant. This shows that the flow solution does not re-converge to steady state immediately after the large change in velocities experienced. This may account for the increased dispersion.

3.2.6 Conclusions

Figure 3.15 summarises the dispersion results for the preliminary investigations in a pipe. Section 3.2.5.5 and figure 3.15 have shown FLUENT to be a robust modelling tool which represents the flow field accurately in unsteady conditions (in a range of scenarios). It allows for full recovery of any injected species whilst also allowing for multiple unique species to be injected simultaneously, unlike lab based studies. Initial results led to a method of quantifying dispersion with respect to cumulative discharge (see appendix 1), this was validated against results obtained under steady conditions.

Despite figure 3.15 highlighting interesting phenomena associated with increased / decreased dispersion due to unsteady conditions, the magnitude of this enhancement is fairly small (maximum 3.5%). The impact of unsteady conditions on dispersion within a pipe is minor and should not be investigated further. However, it is likely that in more hydrodynamic structures such as manholes these effects may be larger and of greater importance.

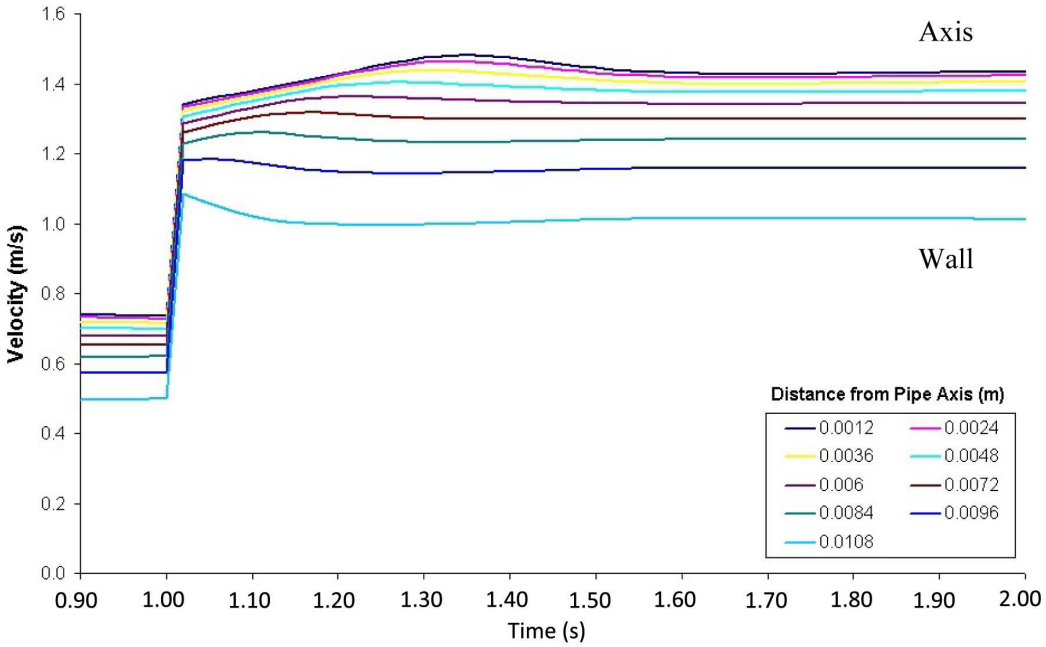

Figure 3.14: Velocity of flow at varying distances from the modelled pipe axis

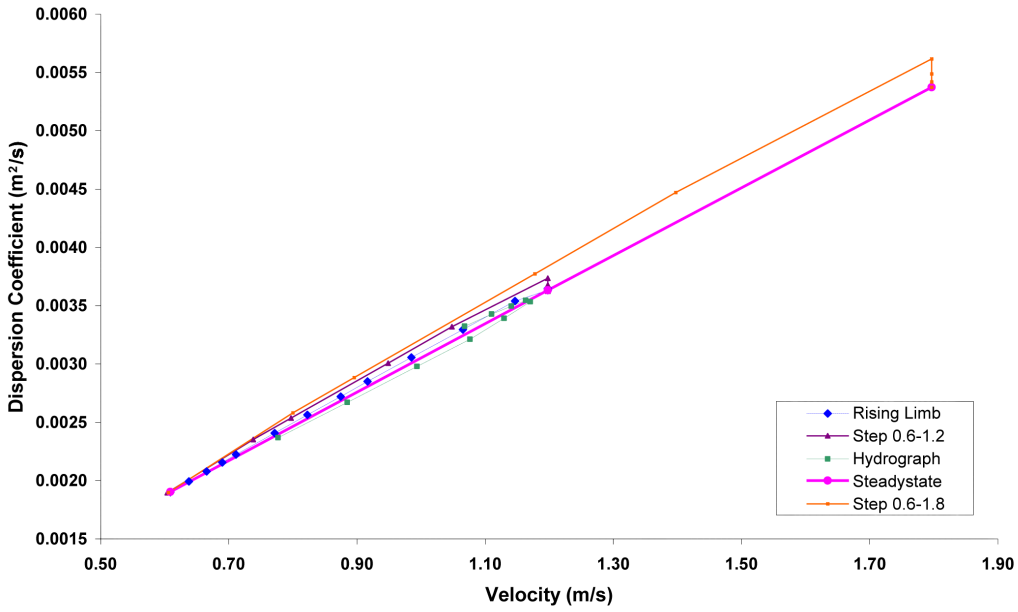

Figure 3.15: 2D Unsteady Primary Investigations of Solute Tracer Dispersion

3.3 CFD Modelling of Solute Transport in a 2D CSO

3.3.1 Methodology

The preliminary studies showed FLUENT did not require an excessive amount of computational power or time to reach a converged solution for a 2D pipe flowing full in unsteady conditions. However, before progressing to a more complex 3D system it was important to check whether the same would be true for a free surface, time dependent model. A simple representation of a Combined Sewer Overflow (CSO) used by Stovin *et al.* (2002b) was selected and meshed in 2D using GAMBIT meshing software. The CSO (showing in figure 3.16) contained an inflow pipe, overflow and continuation pipe as well as a baffle wall. Wall roughness and turbulence modelling options from the previous preliminary studies were used within the solver.

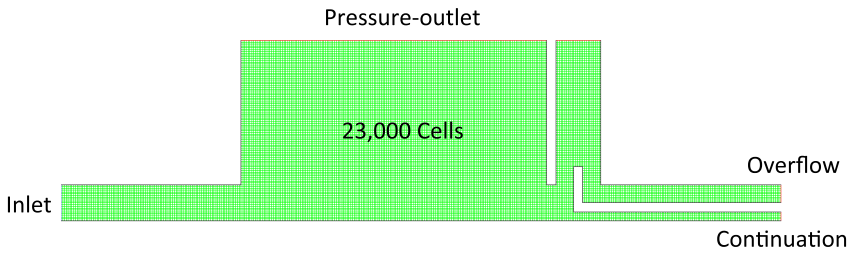

Figure 3.16: 2D CSO mesh and boundaries

A user defined temporal inlet velocity profile (figure 3.17) was used to control the velocity of the fluid entering the CSO at the inlet. Constant velocity values were defined across the entire inlet face. The volume of fluid (VOF) model within FLUENT was used to determine the position of the free surface as the CSO filled, spilled and emptied.

As for all other simulations thus far, the species model was also activated to allow for the injection of 'tracer'. In this case it was necessary to first create a mixture containing air and water to allow the VOF (modified HRIC) model to define the interaction between the two (and hence the free surface) before altering

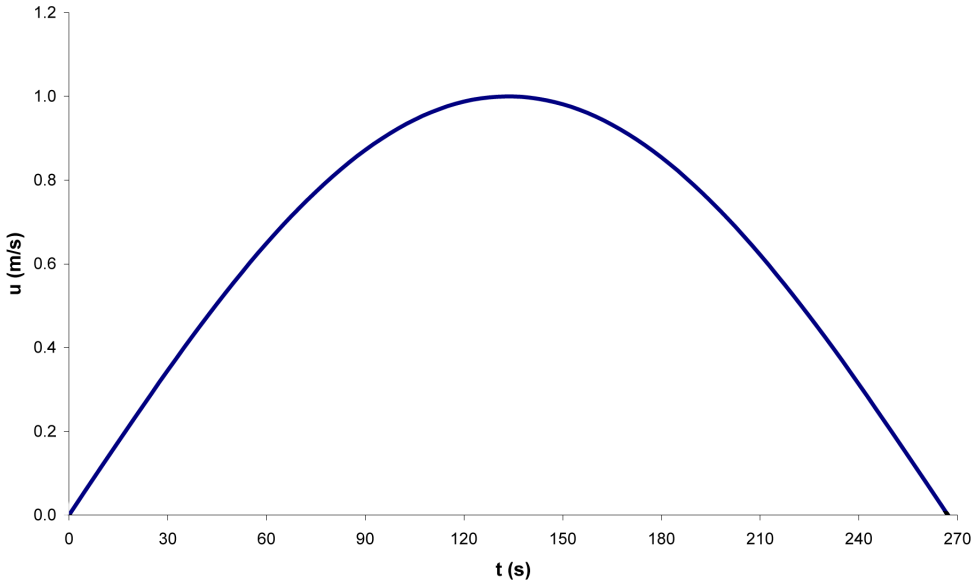

Figure 3.17: Inflow hydrograph used with the 2d CSO model

the mixture template to add-in solute tracer. Dye tracer was input at the inlet as a square trace, temporarily replacing all fluid at this boundary with tracer. Monitors were placed to measure the mass fraction (effectively concentration) of the tracer species at the inlet, overflow and outlet. A visual representation of the free surface was also output at regular intervals throughout the inflow hydrograph, this allowed the user to check for any large irregularities in the flow field that may potentially have arisen due to having multiple models enabled.

The simulation was carried out at a time step of 0.01 s and 20 iterations per time step (maximum) in order for the flow solution to converge at each individual time step and prevent model divergence.

This hydraulic simulation represents work undertaken by Stovin *et al.* (2002b). However, no previous work combining VOF with the species model for solute transport has been reported.

3.3.2 Results

Figure 3.18 shows the resultant mass fractions (section 2.5.10.2.3) at a range of time intervals throughout the inflow profile. The mixture phase (in this case tracer and water) is shown in red. Air is shown in blue. The remaining colours

represent a mixture between the two, with bright green showing a 50:50 mix of the two phases. It can be seen that the model, fills, spills and empties as expected. This model required 24 hours of computational time (approximately 10 times more than the previous, uncoupled preliminary pipe study).

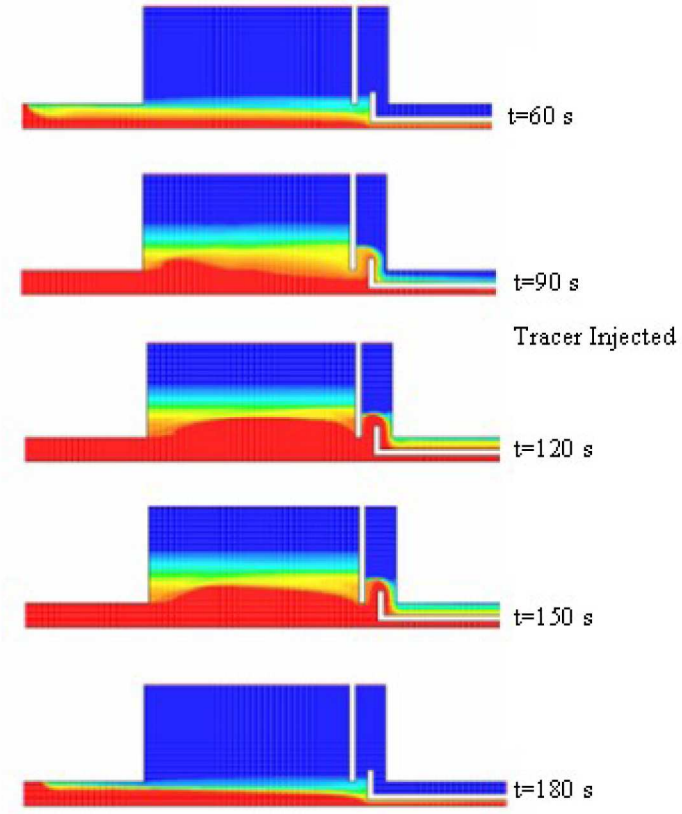

Figure 3.18: 2D CSO during a modelled storm event. Red represents 100% water, blue represent 0%.

Solute transport injections also show the model to fill and spill, with injected solute being recovered on both the continuation and overflow outlets (figure 3.19). A high mass recovery (>99%) confirms the robustness of the model.

3.3.3 Conclusions

The run time for this simulation was in the order of 6 days, which is positive for future (more complex) 3D models. However, the interface shown in figure 3.18 is not sharp enough to easily identify the position of the free surface. This aspect was of concern, and future studies therefore specifically looked at identi-

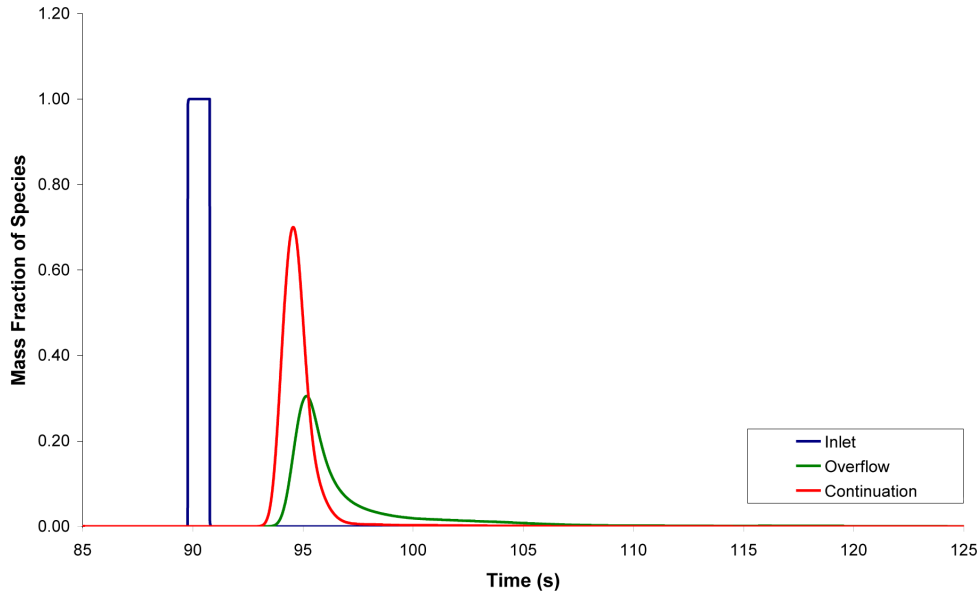

Figure 3.19: Results from injecting a square pulse during a storm event at t = 90 s

fying modelling options and mesh refinement strategies in order to improve the resolution of the free surface (section 4.3).

3.4 CFD Modelling of a 3D Manhole in Unsteady Conditions

3.4.1 Introduction

The previous investigation showed that it was feasible to model both unsteady conditions and solute tracer, in a 2D model (without excessive computational expense). To expand that further it is necessary to look towards 3D modelling (allowing for a better representation of urban drainage structures i.e. manholes). As detailed in section 2.6.2.2, Lau (2008) used the 'Fixed Lid Assumption' to artificially impose the position of the free surface within a manhole. However, as further work it was recommended that:

'When more advanced computational resources becomes available, the manhole simulations should be repeated using two phase modelling to account for the effects of the free surface. The results could be used to assess the effects of the fixed lid

assumption on the flow field and solute transport predictions.'

This is can be investigated even in steady flow conditions. Due to the continuing development at The University of Sheffield of 'Iceberg', part of the White Rose Grid Computing resource, it was possible to investigate this suggestion further. This constant improvement in technology allows for increases in speed in all aspects of CFD models considered within this study.

3.4.2 Methodology

A mesh was generated (figure 3.21) using an alternate scheme to those examined by Lau (2008) (following recommendations from a FLUENT engineer) to create a representation of his 'scale', 218 mm diameter manhole (on a 24 mm pipe). By intersecting two cylinders to form the 'pipe' and 'central' sections of the manhole, the number of skewed elements were significantly reduced (from approximately 1% down to 3×10^{-4} %). This required 8 cells to be specified as triangular (figure 3.21) at each corner point where the volumes intersect. The Quad-pave Cooper scheme was used to mesh these volumes, with the total number of cells equal to 500,000.

The model was sized as per Lau (2008) (figure 3.20) with the inlet placed $20D_p$ upstream of the upstream fluorometer and the outlet, $5D_p$ beyond the downstream fluorometer. The model boundary conditions were specified as per Lau; velocity-inlet and pressure-outlet, with the top of the model also defined as a pressure outlet. The remaining surfaces (by default) are specified as walls (roughness equal to 1×10^{-5}m). To ensure the free surface would fill past the hydraulic threshold identified by Guymer *et al.* (2005a) (0.258 D_M), a pressure head (200 Pa) was applied at the outlet of the model.

Lau (2008) carried out a detailed parametric study of modelling options within FLUENT to develop a protocol with which to converge his 'Scale Manhole' simulations. These were used for the preliminary investigations (table 3.5).

The implicit modified HRIC scheme used for preliminary modelling of a 2D CSO failed to offer a clearly resolved, free surface position despite recommendations within the FLUENT manual. Therefore, the Geo-reconstruct scheme was selected as an alternative candidate (FLUENT, 2005a) for the nature of the flow to be

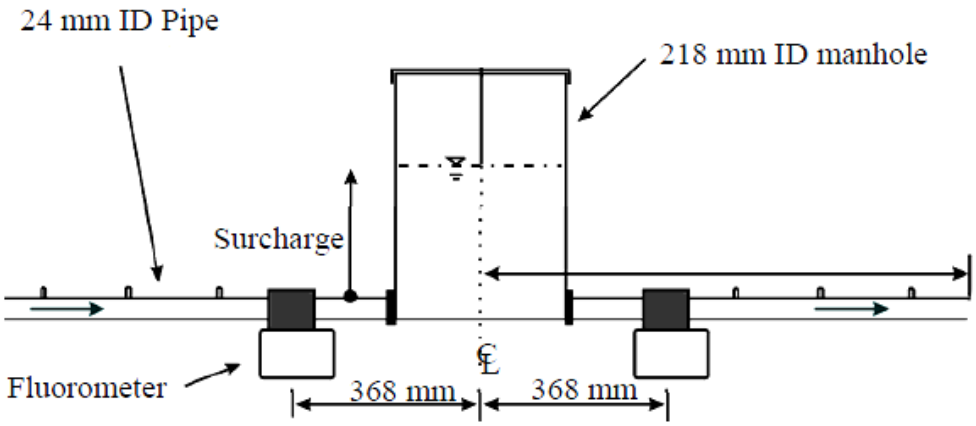

Figure 3.20: Schematic of the 218 mm diameter scale manhole (after Lau (2008))

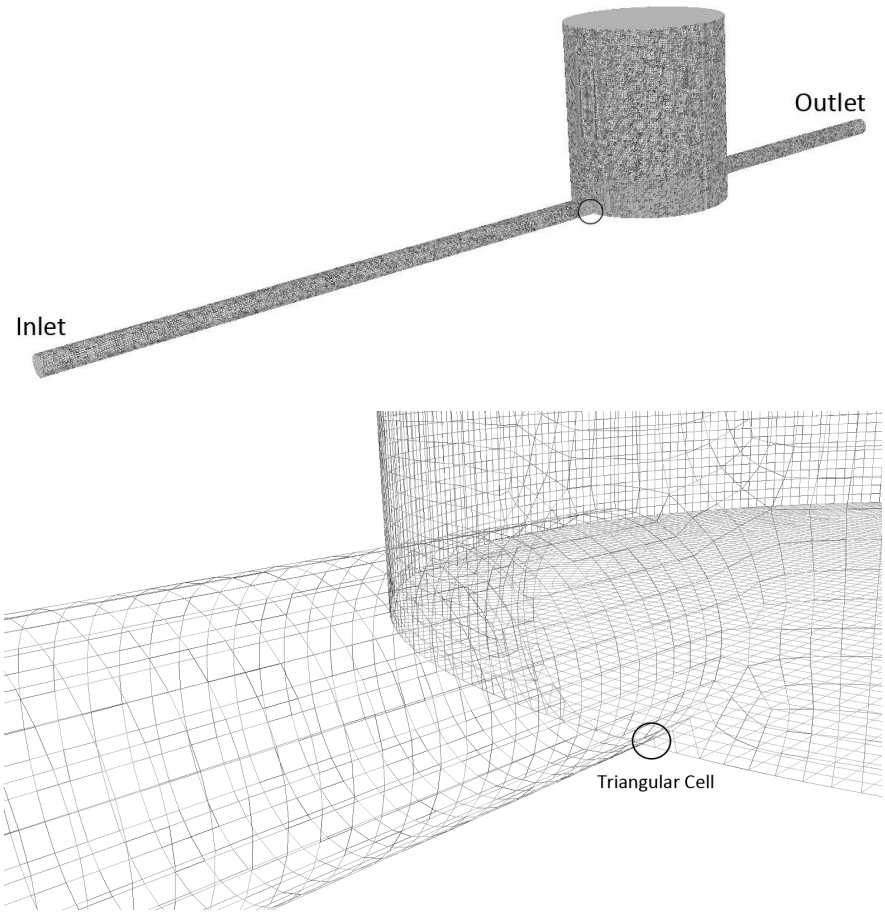

Figure 3.21: Schematic of the 218 mm diameter manhole mesh with zoomed in section showing triangular cells

Parameter		Value
Spatial discretisation scheme	*Pressure*	PRESTO
	Momentum, Turbulence	QUICK
	Velocity-pressure coupling	SIMPLEC
Turbulence model		RNG k-ϵ

Table 3.5: Standard Modelling Protocol for Manhole Simulations (after Lau 2008)

modelled.

The model was initialised with the free surface patched at pipe full depth to save unnecessary computational expense and with a flowrate of Q = 0.35 l/s (used by Lau (2008)). A time step of 0.001 s and 20 iterations per time step was required to prevent model divergence. Decreasing either parameter often led to divergence in FLUENT. This would occur after a large amount of time and resulted in much wasted computational effort.

3.4.3 Results

The final flow solution presented in figure 3.22 required 28 days to model 120 seconds of flow without the addition of the highly computationally demanding species model (the cost of which increases with the addition of extra unique tracer species). However, it can be seen (figure 3.22) that the interface between air and water is sharp and greatly improved compared to the Modified HRIC scheme used previously (figure 3.18).

The solution also exhibits the two flow regimes identified by Guymer *et al.* (2005a) and replicated by Lau (2008). Initially the jet is highly asymmetric (below, or pre-threshold, $s = 0.2291D_m$, figure 3.22a) and gradually straightens (above, post-threshold, $s = 0.2429D_m$, figure 3.22q). However, its behaviour is more transitional than previous studies have noted. Due to this, it is not possible to accurately define a precise 'threshold'. However, the transition occurs below the 0.258 D_M suggested by Guymer and O'Brien (2000). Although it was possible to create a converged, 3D model of a filling manhole, due to the small time step (0.001 s) required for stability it was deemed infeasible to conduct solute modelling in such conditions. Due to this the following section aims to assess whether fully-coupled flow/solute transport calculations are necessary to represent the

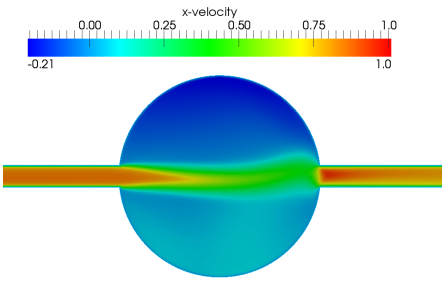

(a) CHP, $t = 97$ s

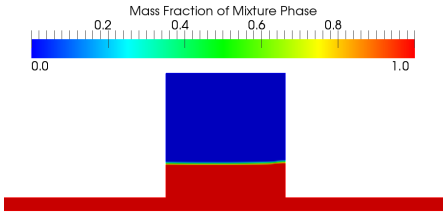

(b) CVP, $t = 97$ s, $s = 0.2291 D_m$

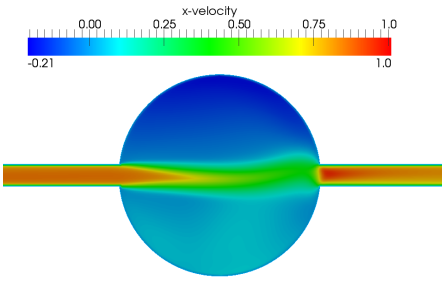

(c) CHP, $t = 98$ s

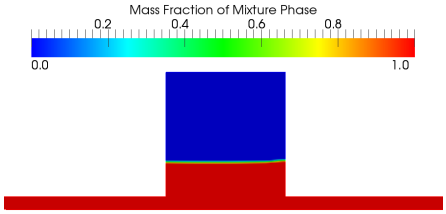

(d) CVP, $t = 98$ s, $s = 0.2323 D_m$

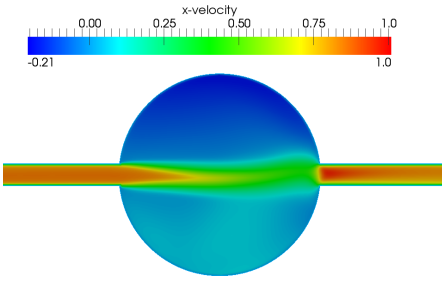

(e) CHP, $t = 99$ s

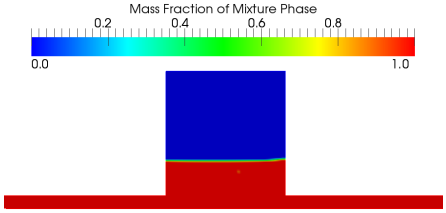

(f) CVP, $t = 99$ s, $s = 0.2350 D_m$

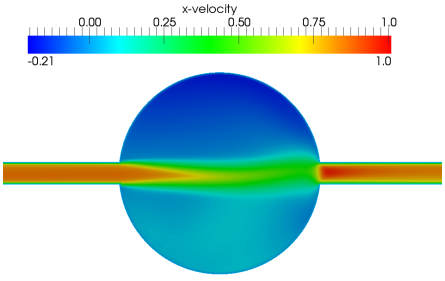

(g) CHP, $t = 100$ s

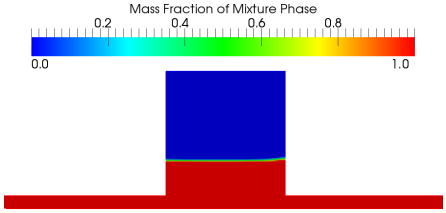

(h) CVP, $t = 100$ s, $s = 0.2372 D_m$

Figure 3.22: Contours of x-velocity and Mass Fraction in a filling 218 mm diameter manhole

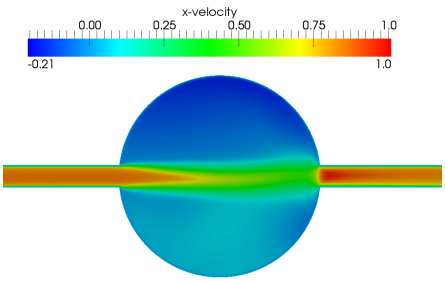

(i) CHP, $t = 101$ s

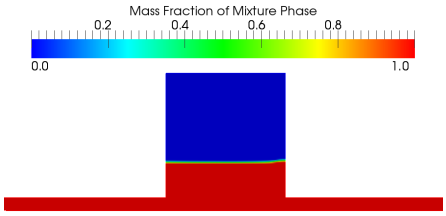

(j) CVP, $t = 101$ s, $s = 0.2391 D_m$

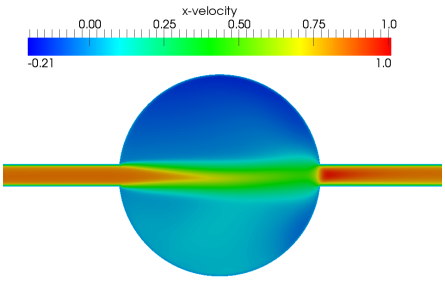

(k) CHP, $t = 102$ s

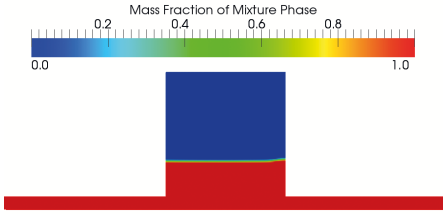

(l) CVP, $t = 102$ s, $s = 0.2407 D_m$

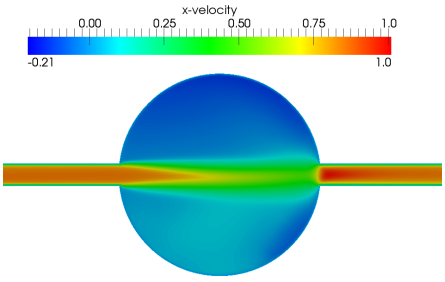

(m) CHP, $t = 103$ s

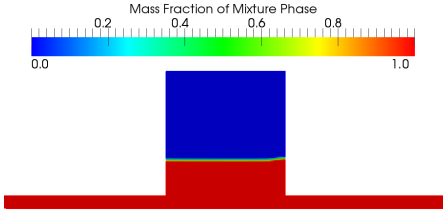

(n) CVP, $t = 103$ s, $s = 0.2418 D_m$

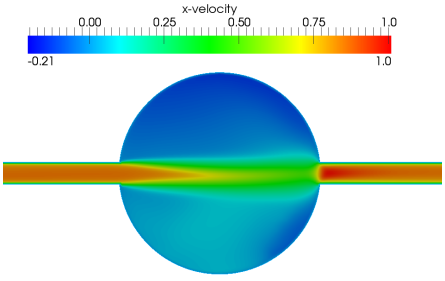

(o) CHP, $t = 104$ s

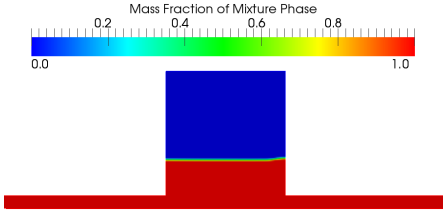

(p) CVP, $t = 104$ s, $s = 0.2426 D_m$

Figure 3.22: Contours of x-velocity and Mass Fraction in a filling 218 mm diameter manhole

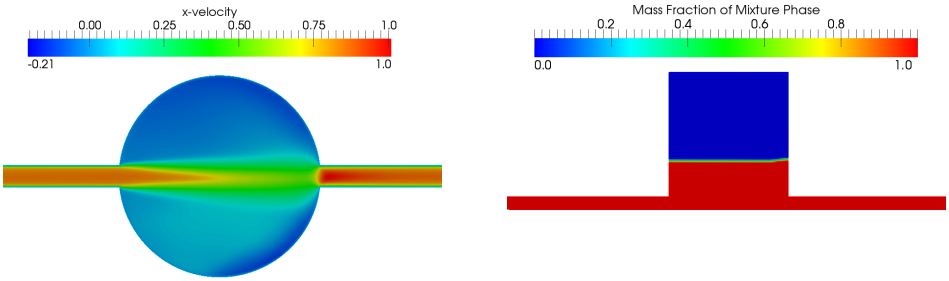

(q) CHP, $t = 105$ s (r) CVP,$t = 105$ s, $s = 0.2429D_m$

Figure 3.22: Contours of x-velocity and Mass Fraction in a filling 218 mm diameter manhole

behaviour of manholes subjected to unsteady inflow conditions.

3.5 One Dimensional Modelling of Manholes in Unsteady Conditions

3.5.1 Introduction

From an engineering perspective, the need or desirability for explicitly modelling time-dependent solute transport phenomenon is influenced by the relative time-scales operating to control the hydraulic (and hydrodynamic processes) relative to the solute travel times. If the solute travel times are relatively slow, such that the system may experience significant changes in hydraulic state whilst the solute passes through it, then coupling between the hydraulic and solute models is likely to prove critical. Conversely, if the solute residence time is short relative to the time-scale of hydraulic changes, then a pseudo steady modelling framework may be justified. In other words, time-dependent hydraulic simulations may be combined with simplified solute transport models, using the relevant hydraulic state as the solute enters the system to predict the anticipated exit temporal concentration profile.

3.5.2 Working Hypothesis

In this section indicative solute travel times will be considered alongside realistic estimates of hydraulic regime change times to establish whether there is a real need for fully-coupled solute transport modelling in this context. Stovin *et al.* (2007) and Lau (2008) have proposed a two-regime solute transport model for surcharged manholes, presented in the form of two normalised CRTDs within Guymer and Stovin (2011). The theoretical CSTR model (equation 3.4, (Levenspiel, 1958)) can also be considered; it corresponds to an idealised (well mixed) exponential CRTD (similar to that of the below-threshold condition). All three CRTDs are shown in figure 3.23.

$$MF = 1 - e^{(-t/[V/Q])} \tag{3.4}$$

Where

MF Mass Fraction

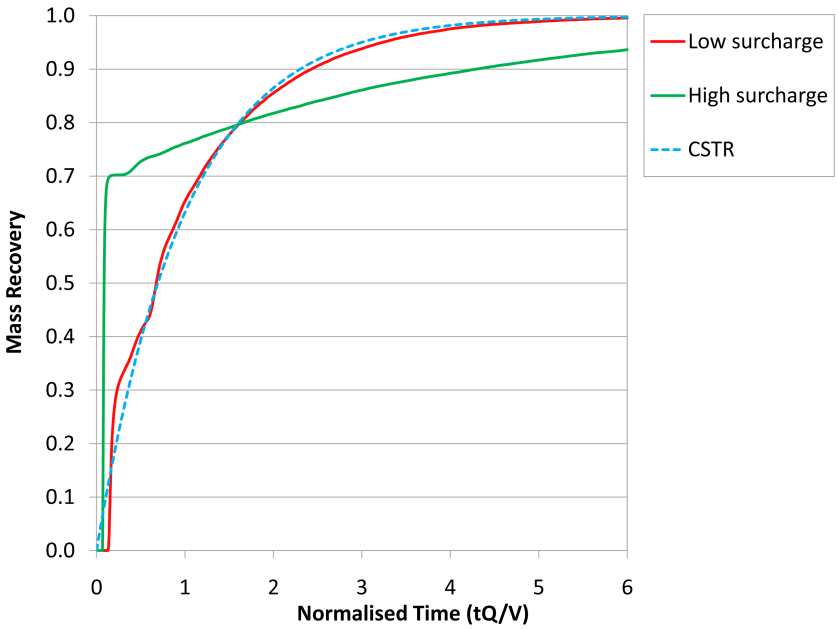

Figure 3.23: Low, high and CSTR normalised CRTDs

Consider two manholes; Lau's 218 mm diameter scale manhole and also a full-scale manhole (D_P= 750 mm, D_M= 1200 mm), both under surcharge conditions

of $s = 0.5D_p$ (below threshold) and $s = 4D_p$ (above threshold), with two flowrates respectively (0.5 l/s, 50 l/s). T_{10}, t_{50} and t_{90} values for each scenario are presented in table 3.6.

For the laboratory-scale system, expected t_{50} travel times range from 0.27 to 7.17 seconds, with the highest t_{90} equal to 49.27 seconds. For the full-scale systems the worst-case t_{50} and t_{90} travel times are 67 and 466 seconds. This is the same order of magnitude as one sewer network simulation model time step (typically 5-10 mins)

This shows that although sewer system hydraulics are time-dependent they are rarely 'dynamic'. They are characterised by gradual filling and emptying processes (typically over 30 mins to several hours) rather than small scale shock effects. Data from an Ilkley catchment Infoworks model shows that during both the 2M 60 and M5 60 design storms, the depth of flow within a manhole increases at a maximum rate of approximately 0.027 m/min.

The 3D free-surface manhole simulations of the 218 mm system suggested that the transition occurred over a real-time period of 10 seconds, much less than one typical model time step. During this period, the manhole surcharge increased by only 3 mm. In the majority of cases the expected travel times can be judged large when compared to the transitional 'threshold' region. Due to this, it may be concluded that it is unnecessary to model unsteady conditions, as it becomes of greater importance to accurately model which flow regime persists in the manhole at a given surcharge level. This will dictate the mixing characteristic encountered by solute.

3.5.3 Discussion

Section 3.4.3 highlighted several practical limitations associated with the implementation of fully-coupled flow models for surcharged manholes. However, section 3.5.2 provided evidence to support a pseudo-steady simulation approach in which time-dependent hydraulic modelling may be combined with the application of 'suitable' CRTD models to represent instantaneous solute transport behaviour. Table 3.6 highlights a further critical point. It demonstrates that for the CRTD model to be applied in the context of a surcharged manhole, it is dependent upon

			Configuration Specific Values (s)				
			0.024	0.024	0.75	0.75	D_p (m)
			0.218	0.218	1.20	1.20	D_M (m)
			0.012	0.096	0.375	3.00	s (m)
			0.0013	0.0045	1.2723	4.2412	V (m^3)
Model	Percentile	Normalised (tQ/V)	0.0005	0.0005	0.05	0.05	Q (m^3/s)
CSTR	t_{10}	0.10	0.27	0.90	2.54	8.48	
Idealised exponential model	t_{50}	0.70	1.88	6.27	17.81	59.38	
	t_{90}	2.20	5.91	19.71	55.98	186.61	
Pre-threshold model	t_{10}	0.15	0.40	1.34	3.82	12.72	
(below threshold)	t_{50}	0.80	2.15	7.17	20.36	67.86	
	t_{90}	0.95	2.55	8.51	24.17	80.58	
Post-threshold model	t_{10}	0.10	0.27	0.90	2.54	8.48	
(above threshold)	t_{50}	0.10	0.27	0.90	2.54	8.48	
	t_{90}	5.50	14.78	49.27	139.96	466.53	

Table 3.6: Indicative travel times (s) for laboratory and field-scale manhole systems Configuration-specific values (s)

whether the depth of surcharge is above or below the threshold, as two alternative CRTD models have been previously identified. The idealised CSTR model does not provide a good approximation to either of these, reflecting the complex mixing processes that have been described elsewhere. The critical question then becomes, how do we know which hydraulic regime we are in, i.e. which is the relevant CRTD model to apply? Previous authors (Guymer *et al.*, 2005a) have suggested that the threshold between these two regimes may be related to surcharge/manhole diameter, but critically, there is no existing data for realistic D_M/D_p ratios. Guymer *et al.* (2005a) examined D_M/D_p ratios between 9.1 and 4.4 and found the threshold behaviour to be most evident in the largest manhole ($D_M/D_p = 9.1$). At $D_M/D_p = 4.4$ (the smallest case) a step in travel time is hard to identify. These observations therefore led to a focus on identification of the threshold as a function of D_M/D_p. The use of a pseudo-steady modelling approach has been justified.

3.6 Conclusions

The FLUENT CFD software has been shown to be a robust modelling tool for characterising solute transport within complex flow fields under unsteady inflow conditions. Multiple, overlapping traces provide a significant advantage over laboratory studies. However, the complexity of 3D unsteady free-surface models combined with species modelling (for solute transport) would lead to problems with simulation complexity (section 3.4.3) and computational time requirements that were judged ultimately to be impractical. Section 3.2.6 demonstrated that the impact of unsteady conditions on dispersion within a pipe is minor. Section 3.5.2 also suggested that solute travel times in manholes are small relative to the time-scales associated with the underlying hydraulics/hydrodynamics of the sewer/manhole system. Hence the decision was made that the remainder of the thesis should focus on accurately identifying CRTDs/threshold depths for a more representative range of D_M/D_p values than had previously been considered. A method for evaluating dispersion coefficients under time-varying conditions has been proposed and validated using steady flow data.

Chapter 4

CFD Validation and Sensitivity Analysis

4.1 Introduction

Previous work studied the effects of manhole diameter on longitudinal dispersion in surcharged manholes. A surcharge level at which the solute transport characteristics of the manholes sharply altered was identified; at low surcharge (termed 'pre-threshold') the travel times varied linearly with surcharge, at high surcharge (termed 'post-threshold') the travel times dropped to a low constant level. Subsequent research focused on a 218 mm manhole (Lau, 2008), using laboratory PIV to validate CFD-based simulations of the flow fields. The study included a parametric study of turbulence and other modelling options. The k-ϵ Realizable turbulence model (recommended for use with jets (FLUENT, 2005a), was not considered and all tests were carried out using a fixed lid assumption (a slip free wall to represent the free surface) limiting the work to steady conditions. The fixed-lid models generated by Lau (2008) were able to replicate laboratory solute trace data well (returning high goodness of fit values, $R_t^2 > 0.974$).

CFD allows for insight into the flow field within a given structure as well as enabling the generation of its solute transport characteristics via the use of available models (including the discrete phase (particle tracking), and species transport

models). Using existing laboratory PIV and solute trace data, discussion will be made upon modelled primary (flow field visualisation) and secondary (quantitative flow field error analysis, discrete phase and species CRTDs) validation data for three turbulence models (RSM, k-ϵ RNG and k-ϵ Realizable), in both low (below or pre-threshold), and high surcharge (above or post-threshold) conditions. Further validation is presented in the form of convolved downstream solute traces and goodness of fit parameters.

The same validation techniques are also applied to free surface models (which remove the need to make assumptions regarding the 'fixed lid'). Qualitative discussion of the air-water interfaces generated by three Volume of Fluid (VOF) models (Modified HRIC, Cicsam and Geo-reconstruct)are presented, followed by a final VOF representation of the two validation cases studied by Lau (2008) and the corresponding flow fields. Secondary validation is presented in the form of solute trace based CRTDs. These are used to generate convolved downstream solute traces (from a known upstream laboratory injection), allowing the goodness of fit to be calculated and hence the acceptability of the examined model to be evaluated.

In this chapter, structured mesh flow fields are presented for each turbulence model (alongside PIV laboratory flow fields) and qualitatively discussed. Methods of evaluating error in these flow fields are then presented and discrepancies between the three turbulence models studied are presented.

Models for representing solute within FLUENT (discrete phase particle tracking and species transport) are evaluated, including an independency study on the number of particles required for use with the discrete-phase model. These are used to generate CRTDs which are compared with laboratory derived CRTDs allowing for the performance of each solute model (and turbulence model) to be evaluated further. Sensitivity of the discrete-phase model to the Time Scale Constant (TSC) is presented followed by convolution of measured laboratory traces allowing for quantitative comparison of goodness of fit (using R_t^2).

Free-surface modelling is then considered for three Volume of Fluid (VOF) schemes and an evaluation of the sharpness of the air-water interface is presented. Qualitative and quantitative analysis is presented in the same manner as per the fixed-lid models allowing for a direct comparison of the performance of

each method of representing the free-surface.

Following this, unstructured meshing is presented with a full mesh independency study for both validation cases investigated by Lau (2008).

4.2 Structured mesh

4.2.1 218 mm manhole (0.35 l/s, S = 1.17 S = 3.27)

Two representations of the laboratory set-up shown in figure 4.1 were generated using GAMBIT meshing software (figure 4.2). The 218 mm diameter manhole (studied by Lau (2008)) was modelled between the upstream and downstream fluorometer locations for both below (s = 1.17 D_p) and above threshold (s = 3.27 D_p) surcharge conditions (figure 4.3). Upstream of the first (upstream) fluorometer, 20 D_p of pipe was added to allow for injected species to become fully mixed. After the downstream fluorometer 5 D_p of pipe was added to address issues of monitoring on a boundary. The geometry was then filled with a 'Quad-Pave', 'Cooper' uniform mesh with a similar number of cells (300,000 and 500,000 respectively) to mesh independent models studied by Lau (2008). As these models are directly comparable with those studied by Lau (2008) (in terms of velocity gradients, scale and mesh size), the mesh independency study carried out previously by Lau (2008) (where a range of grid densities were evaluated) is still valid. The inlet was set as a 'velocity-inlet' whereas the outlet was specified as a 'pressure-outlet'. The top of the manhole model was specified as a separate 'wall'. This allows it to have different (zero) frictional properties to other walls within the model. Remaining boundaries were specified as 'wall' (by default).

Solutions were generated using FLUENT 12. A fully developed pipe flow profile (Q = 0.35 l/s, derived from a separate periodic pipe model) was input at the inlet of the manhole models. All boundary and solver conditions remained the same across the fixed lid manhole models (excluding the turbulence model). The turbulence models evaluated were the k-ϵ Renormalization Group (RNG), k-ϵ Realizable and the Reynolds Stress Model (RSM). Boundary roughness (equal to 1×10^{-5}) derived from laboratory Perspex pipe tests (Lau (2008)) was utilised for the walls. The top (fixed lid) of the model was specified as having zero boundary

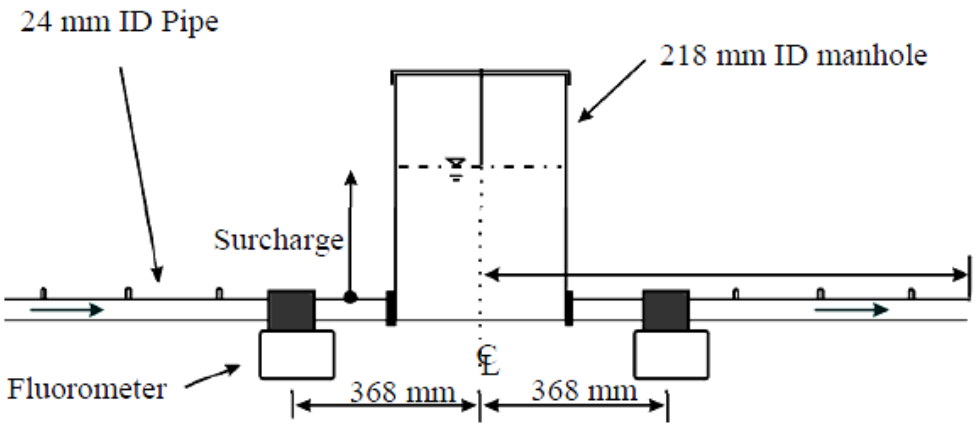

Figure 4.1: Schematic of the 218 mm diameter scale manhole (after Lau (2008)

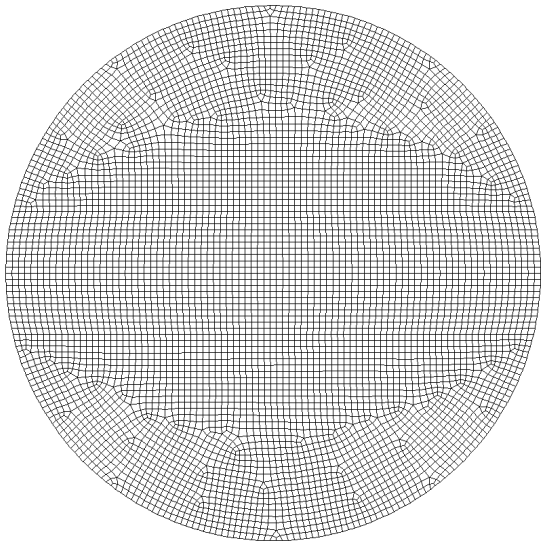

Figure 4.2: Cells on the top face of the structured meshes

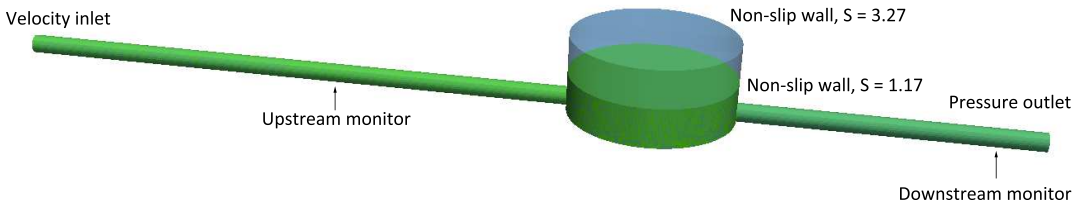

Figure 4.3: Schematic of the 218 mm diameter manhole CFD model, both surcharge conditions (S = 1.17; S = 3.27) are shown

roughness to represent the free surface.

4.2.1.1 Sensitivity of flow field to turbulence model

The Central Vertical Plane and Central Horizontal Plane (CVP and CHP) through the manhole were selected for primary validation purposes as they clearly show the amount of modelled jet dissipation as well as the recirculation effects present on both planes. Figure 4.4 compares the measured PIV and simulated fixed-lid CFD flow fields for the low-surcharge (pre-threshold, s = 1.17 D_p) condition.

Lau (2008) identified the common over-estimation of jet length attributed to the homogeneous k-ϵ RNG model (figures 4.4b and 4.4d). However, the RSM provides a more accurate degree of jet dissipation (figures 4.4e and 4.4g) and is in closer agreement with the PIV data (figures 4.4a and 4.4c). It can also be seen that the less computationally expensive k-ϵ Realizable model (figures 4.4f and 4.4h) is in close agreement with both the PIV and therefore also the RSM model. A small recirculation zone shown in the PIV data, neighbouring the outlet to the manhole, is poorly represented in all cases. The RSM solution appears to model this recirculation to a greater degree, although it is not successful in replicating the reverse current shown in the PIV results (figures 4.4a and 4.4c).

Figure 4.5 shows the CVP and CHP for the high surcharge (post-threshold, S = 3.27) fixed lid manhole models. Both the k-ϵ RNG and k-ϵ Realizable models appear to offer a good representation of laboratory data, both in jet length and

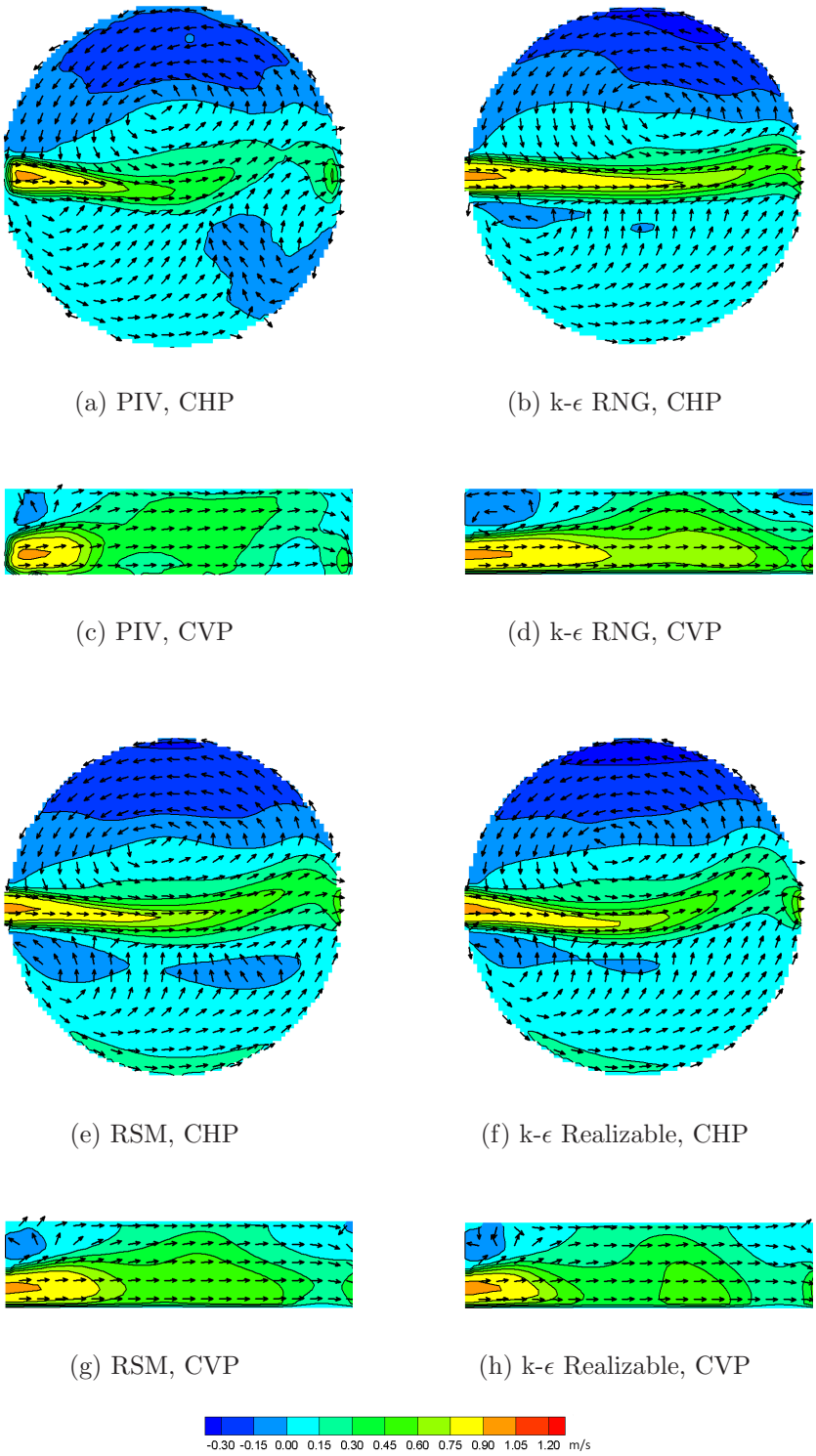

(a) PIV, CHP

(b) k-ϵ RNG, CHP

(c) PIV, CVP

(d) k-ϵ RNG, CVP

(e) RSM, CHP

(f) k-ϵ Realizable, CHP

(g) RSM, CVP

(h) k-ϵ Realizable, CVP

Figure 4.4: CHP and CVP flow fields for a 218mm manhole (Q = 0.35 l/s, s = 1.17D_p, below threshold) for PIV data (measured, Lau (2008)) and the three turbulence models considered (contours coloured by longitudinal velocity, vectors indicate flow direction)

vertical recirculation. However, the RSM model appears to underestimate the length of the jet's high velocity core (figures 4.5e and 4.5g).

4.2.1.2 Quantifying error in flow fields

The PIV/CFD comparisons presented in section 4.2.1.1 highlight specific discrepancies between the flow fields generated by each turbulence model evaluated. However, they give no indication as to whether the magnitude of these discrepancies is large enough to warrant a given model's exclusion from further investigation. This section will present quantitative error analysis.

The PIV data sets previously presented were captured on a different grid to that of the CFD results. It was therefore necessary to interpolate the CFD results onto the same grid for comparison (using Tecplot). A regularly spaced square grid (equivalent in size to D_M) with 10,000 points was placed over both the CVP (aligned with the manhole invert) and CHP (centred over the manhole volume). The CHP and CVP for this region are shown in appendix 3. Each data set was then subsequently interpolated onto this common grid. The vectors shown in figures such as 4.4, have an 'index skip' applied due to the large number of data points available. However, they represent regular positions on the common grid. Although the PIV grid was of lower resolution than the CFD model (and hence should minimise any skewing of the data), this process will invariably introduce some uncertainty into the validation results presented (Stovin *et al.* (2008b)).

Stovin *et al.* (2008b) showed that using a spatial distribution of differences to evaluate the accuracy of a flow field was not sufficient, as it did not allow for differences in the sign of a velocity vector to be identified. This approach allowed underestimations of the flow field to be confused with areas of reversed flow (and vice versa). Thus two equations for use when validating a CFD based study were presented (equations 4.1 and 4.2).

$$\%u_{diff} = \left| \frac{u_{CFD} - u_{PIV}}{u_{PIV}} \right| \times 100 \tag{4.1}$$

$$\%u_{diff} = \left| \frac{u_{CFD} - u_{PIV}}{\overline{u}} \right| \times 100 \tag{4.2}$$

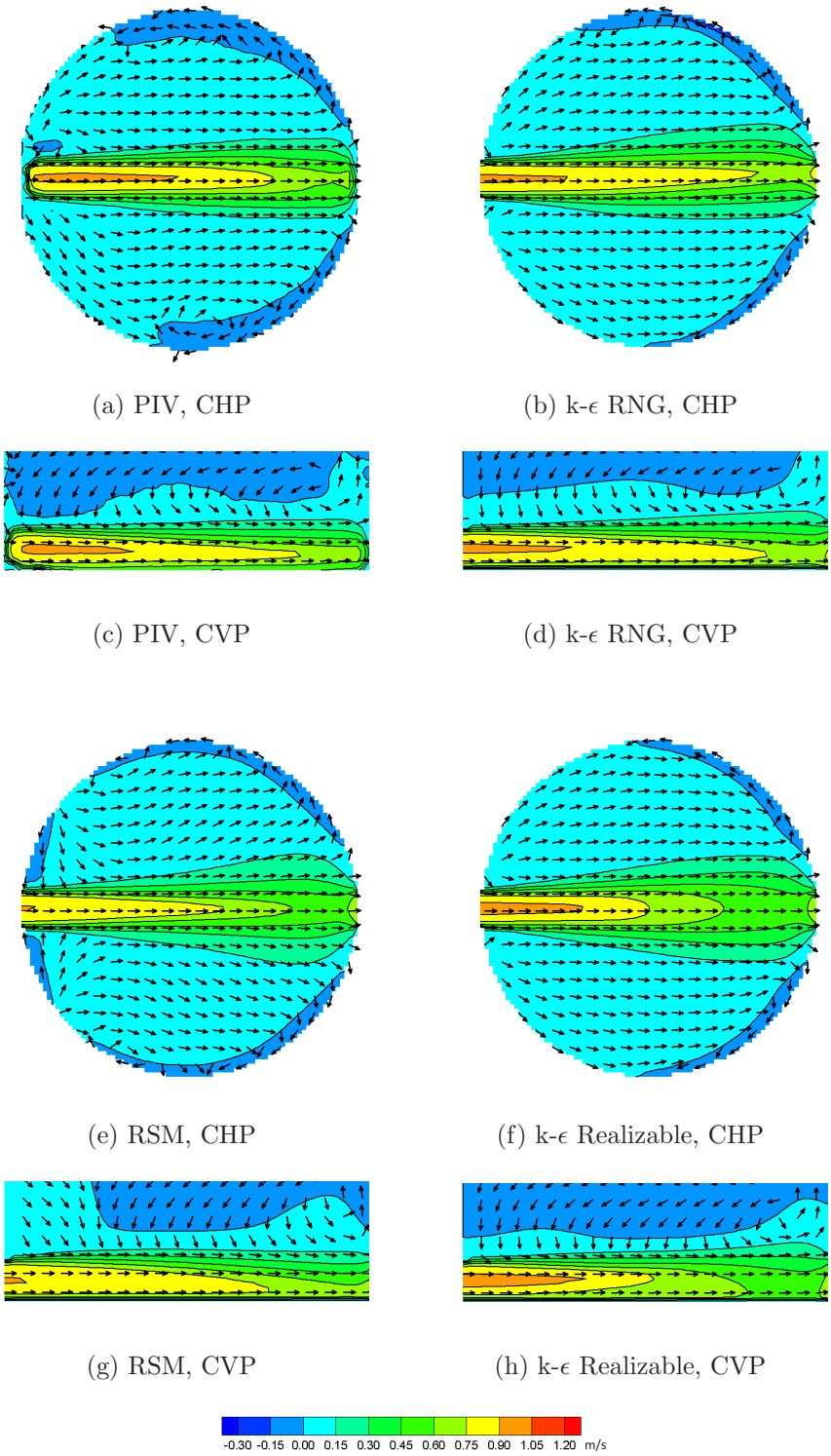

(a) PIV, CHP

(b) k-ϵ RNG, CHP

(c) PIV, CVP

(d) k-ϵ RNG, CVP

(e) RSM, CHP

(f) k-ϵ Realizable, CHP

(g) RSM, CVP

(h) k-ϵ Realizable, CVP

Figure 4.5: CHP and CVP flow fields for a 218mm manhole (Q = 0.35 l/s, s = 3.27D_p, above threshold) for PIV data (measured, Lau (2008)) and the three turbulence models considered (contours coloured by longitudinal velocity, vectors indicate flow direction)

Where:

u_{CFD} is the velocity at a given point according to CFD data

u_{PIV} is the velocity at a given point according to PIV data

$\overline{u}$ is the mean velocity through the inlet pipe

Equation 4.1 relates the difference in velocity to the local u-velocity (on a point-by-point basis). Stovin *et al.* (2008b) comments that *'This approach may exaggerate the significance of differences associated with low flow regions (where u_{PIV} tends to zero'*. Equation 4.2 addressed this issue by normalising the differences with respect to the mean flow velocity ($\overline{u}$). However, it was suggested that this may trivialise differences that occur in the regions of flow outside of the core jet.

Due to the associated shortfalls of each equation they are in fact, complementary. Both have therefore been used to examine the flow fields generated by the three turbulence models evaluated by this study in both surcharge conditions (S = 1.17; S = 3.27). As per section 4.2.1.1, the CHP and CVP have been selected as they capture the dominant flow feature (jet) well. Selection of the mean velocity will determine where errors apply. Here, the mean velocity through the pipe was used. However, it would be possible to use other measures of mean velocity.

Under low surcharge conditions (S = 1.17) equation 4.1 shows the k-ϵ RNG model to vastly overestimate the jet length (figures 4.6a and 4.6c). This is a well known flaw of the model and was encountered by Lau (2008) and Bennett *et al.* (2011). The highest error appears to be in the very tip of the jet and the neighbouring recirculation zone (top right).

Equation 4.2 (figures 4.6b and 4.6d), thought to trivialise errors in areas outside of the core jet, also exhibit similar results, highlighting large differences in the flow field away from the jet whilst also highlighting the characteristic over representation of the jet itself (on both planes).

Equation 4.1 (figures 4.6e and 4.6g), shows the RSM to produce a much more accurate representation of the flow field with the main jet being replicated well. However, the main point of difference is the secondary recirculation zone to the right of the outlet, which was also described in section 4.2.1.1. On the CVP

(figure 4.6g) the largest error is close to the manhole outlet. This may be due to errors within the PIV data, as it was not known where the boundary for these measurements ceased.

Equation 4.2 (figures 4.6f and 4.6h), also confirms that the RSM turbulence model produces a good representation of the PIV flow data. The largest discrepancies are within the jet itself, overestimating its length.

Equation 4.1 (figures 4.6i and 4.6k), shows the newly-evaluated k-ϵ Realizable model to yield similar results to that of the RSM model (figures 4.6e and 4.6g), whilst by its nature offering a lower computational expense. The largest errors are once again in the secondary recirculation zone previously highlighted in section 4.2.1.1. These are similar to that encountered by the RSM model in magnitude. However, their location is slightly different.

Equation 4.2 (figures 4.6j and 4.6l), again shows the k-ϵ Realizable model to yield similar results to that of the RSM model (figures 4.6f and 4.6h). However, the magnitude of the errors exhibited is lower. The CVP (figure 4.6l) shows an improvement in the accuracy of the core jet suggesting the newly-evaluated k-ϵ Realizable model offers a real alternative to the RSM model in low surcharge conditions.

Under high surcharge conditions (S = 3.27) equation 4.1 shows the k-ϵ RNG model to represent the core jet well (figures 4.7a and 4.7c). Maximum errors are encountered in the small recirculation zones at the outer edges of the manhole volume and at the upper edge of the jet on the CVP. The CVP (figure 4.7c) shows a large error on the model top. This may be due to uncertainties in the PIV data boundaries and/or limitations associated with the fixed-lid assumption.

Equation 4.2 (figures 4.7b and 4.7d), shows only minor errors, the largest of which are close to the inlet and outlet to the central manhole volume. Once again, this may be due to boundary measurement uncertainties (see also Lau (2008)).

Equation 4.1 shows the RSM model to represent the CHP well (figure 4.7e). However, errors are evident in the small recirculation zones at the edge of the manhole. The CVP (figure 4.7g) shows a discrepancy in the re-circulatory zone neighbouring the inlet to the manhole volume. This error is not apparent in any of the other model results.

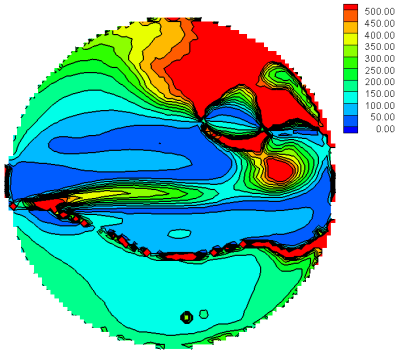

(a) Eq. 4.1, k-ϵ RNG, S = 1.17, CHP

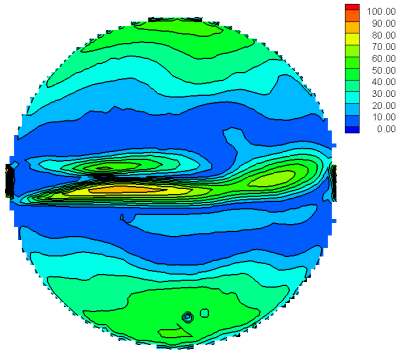

(b) Eq. 4.2, k-ϵ RNG, S = 1.17, CHP

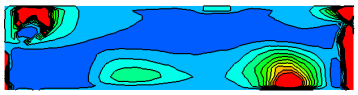

(c) Eq. 4.1, k-ϵ RNG, S = 1.17, CVP

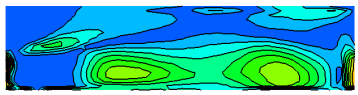

(d) Eq. 4.2, k-ϵ RNG, S = 1.17, CVP

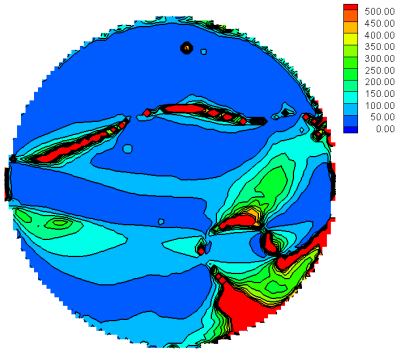

(e) Eq. 4.1, RSM, S = 1.17, CHP

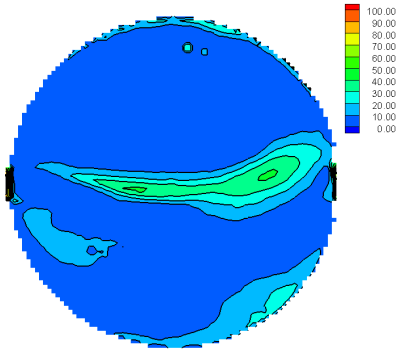

(f) Eq. 4.2, RSM, S = 1.17, CHP

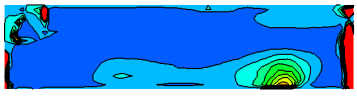

(g) Eq. 4.1, RSM, S = 1.17, CVP

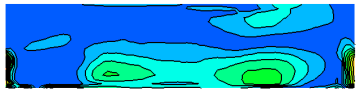

(h) Eq. 4.2, RSM, S = 1.17, CVP

Figure 4.6: Contours of percentage error (equations 4.1 and 4.2) in the below threshold (S = 1.17; Q = 0.35 l/s) 218 mm manhole model

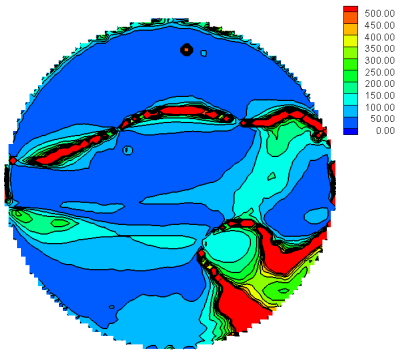

(i) Eq. 4.1, k-ϵ Realizable, S = 1.17, CHP

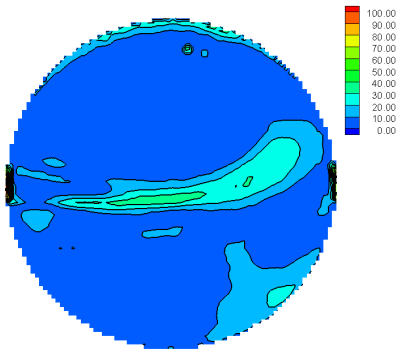

(j) Eq. 4.2, k-ϵ Realizable, S = 1.17, CHP

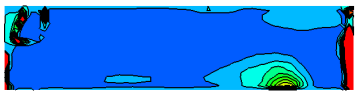

(k) Eq. 4.1, k-ϵ Realizable, S = 1.17, CVP

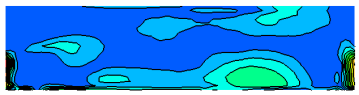

(l) Eq. 4.2, k-ϵ Realizable, S = 1.17, CVP

Figure 4.6: Contours of percentage error in the below threshold (S = 1.17; Q = 0.35 l/s) 218 mm manhole model

Equation 4.2 (figures 4.7f and 4.7h), shows the RSM model to only exhibit minor errors on both planes considered.

Equation 4.1 (figures 4.7i and 4.7k), shows the k-ϵ Realizable model to yield similar results to that of the other models considered. However, small errors ($< 50\%$) are more prolific in the area surrounding the central jet. Once again, errors are encountered in the re-circulatory zones at the edge of manhole.

Equation 4.2 (figures 4.7j and 4.7l), shows the k-ϵ Realizable model to yield errors in the regions closest to the edge of the jet. This is likely due to its increased spreading rate (FLUENT, 2005a) over representing the jet dissipation.

Although section 4.2.1.2 highlights local discrepancies between the flow fields, it is still hard to judge which model performs best. The k-ϵ Realizable turbulence model replicates the results of the PIV, and the more computationally demanding RSM model well and thus appears advantageous under low surcharge conditions. However, in high surcharge conditions it is out-performed by the k-ϵ RNG model; this may be due to the nature of the flow (i.e. dominated by a core jet) as swirling/circulatory flows are not present.

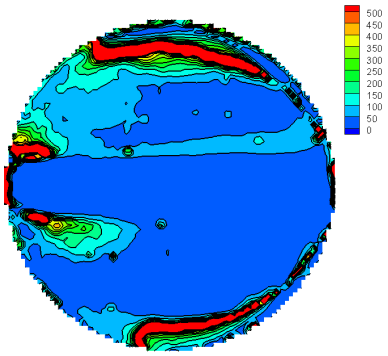

(a) Eq. 4.1, k-ϵ RNG, S = 3.27, CHP

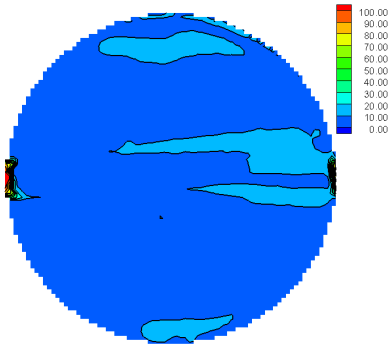

(b) Eq. 4.2, k-ϵ RNG, S = 3.27, CHP

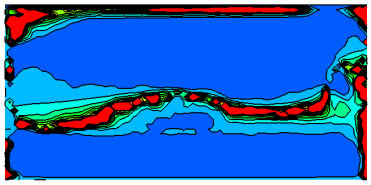

(c) Eq. 4.1, k-ϵ RNG, S = 3.27, CVP

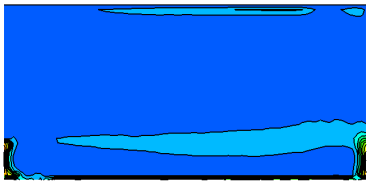

(d) Eq. 4.2, k-ϵ RNG, S = 3.27, CVP

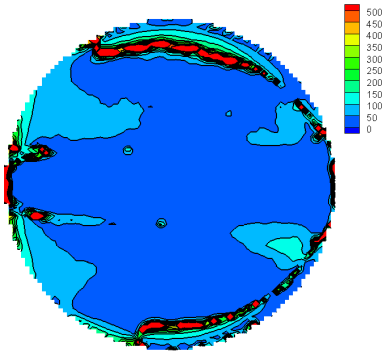

(e) Eq. 4.1, RSM, S = 3.27, CHP

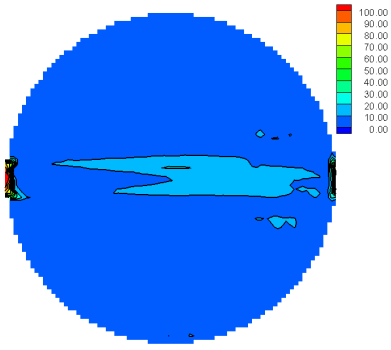

(f) Eq. 4.2, RSM, S = 3.27, CHP

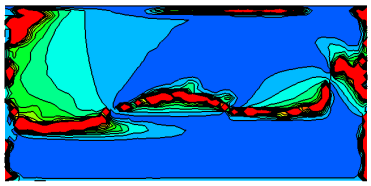

(g) Eq. 4.1, RSM, S = 3.27, CVP

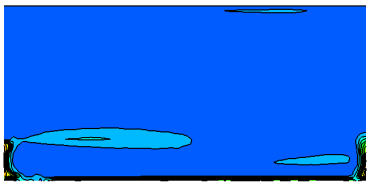

(h) Eq. 4.2, RSM, S = 3.27, CVP

Figure 4.7: Contours of percentage error (equations 4.1 and 4.2) in the above threshold (S = 3.27; Q = 0.35 l/s) 218 mm manhole model

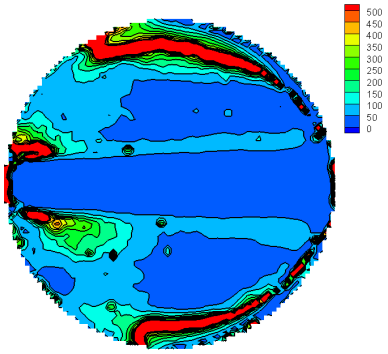

(i) Eq. 4.1, k-ϵ Realizable, S = 3.27, CHP

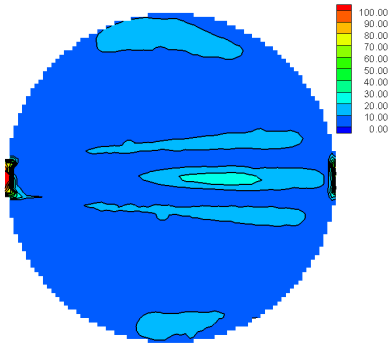

(j) Eq. 4.2, k-ϵ Realizable, S = 3.27, CHP

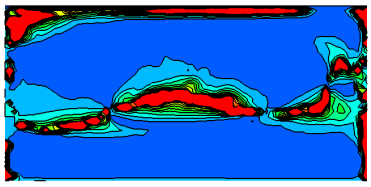

(k) Eq. 4.1, k-ϵ Realizable, S = 3.27, CVP

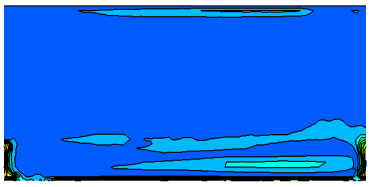

(l) Eq. 4.2, k-ϵ Realizable, S = 3.27, CVP

Figure 4.7: Contours of percentage error (equations 4.1 and 4.2) in the above threshold (S = 3.27; Q = 0.35 l/s) 218 mm manhole model

Lau (2008) demonstrated that solute traces could be used to identify the hydraulic threshold first reported on by Guymer and O'Brien (2000) in a CFD model. Solute transport characteristics of a structure represent the integration of the whole flow field and thus may describe the whole hydrodynamic process better than error plots (Guymer and Stovin, 2011).

4.2.1.3 Large sample particle-tracking validation

Sections 2.5.11 and 2.5.12 discuss the relevant models for representing solute transport within FLUENT. Unlike the Species model, stochastic particle tracking relies on a predictable action (mean flow field) and a random event (turbulence, modelled stochastically). Due to this, it is necessary to investigate the number of particles to input in order to be within an acceptable error of the mean behaviour.

To do this, the discrete phase model was enabled for both validation cases studied

by Lau (2008) (D_M = 218 mm, D_p = 24 mm, S = 1.17; S = 3.27). All modelling parameters were the same in both surcharge conditions including the turbulence model (k-ϵ Realizable). The k-ϵ Realizable was chosen as it represented the low surcharge condition well (section 4.2.1.2) and did so more efficiently than the k-ϵ RSM model.

A large (600,000) discrete-phase particle sample was created by increasing the 'Number of tries per cell'. This sample was then sub-sampled at increasing sample size (with an increase of 100 particles) until it reached that of the 'complete sample'. The maximum number of steps was set to the maximum allowable in FLUENT (1×10^9) to ensure completion of each particle track.

An acceptable error was set as a percentage (1%) of the 'complete sample' mean travel time and a Matlab script was created in order to identify the sample size at which the error was within acceptable bounds. Figures 4.8 and 4.9 show the mean travel time for each sample size (each of which was repeated), for each surcharge level. The green and red lines show the upper and lower acceptability bounds respectively.

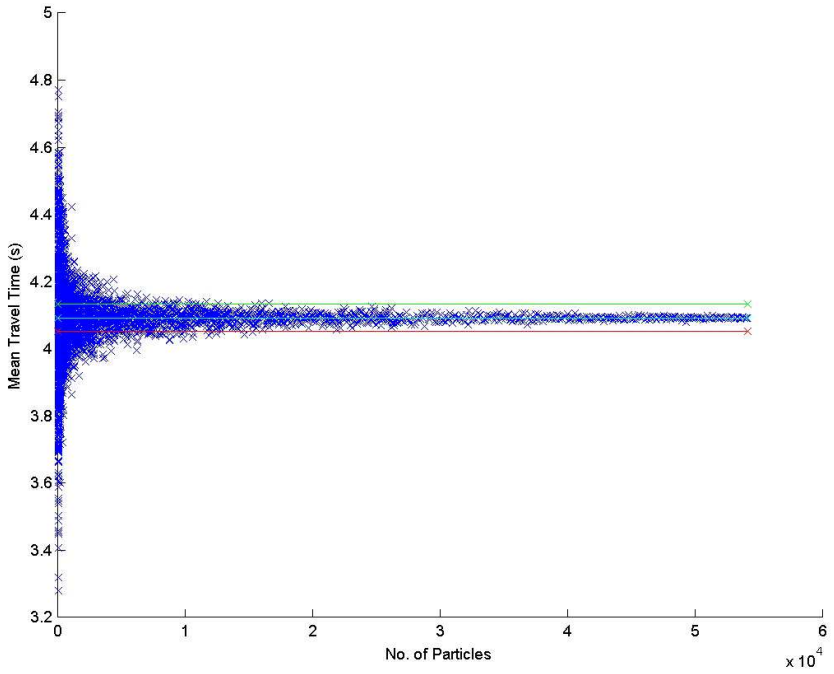

Figure 4.8: Mean Travel Time for Increasing Sample Size in the low surcharge (S = 1.17) validation case

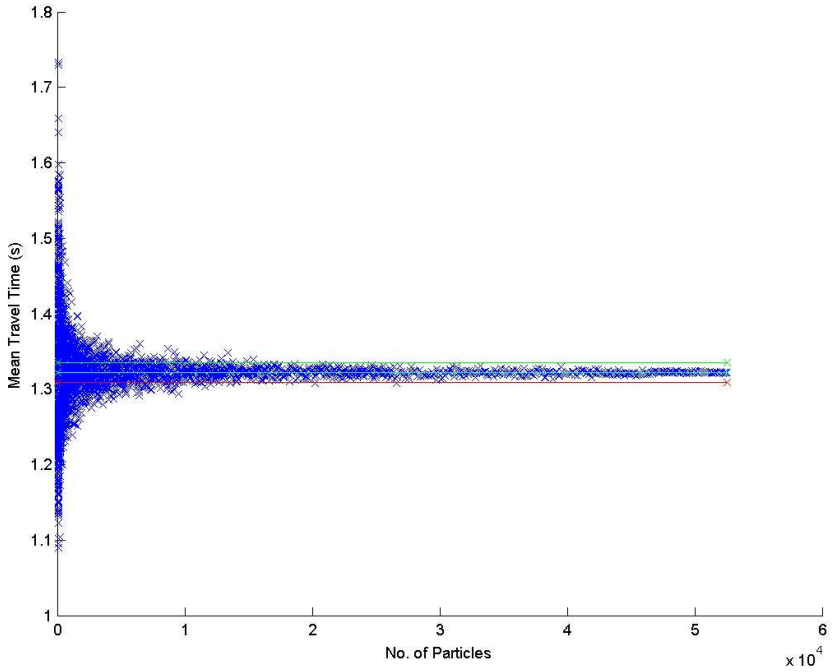

Figure 4.9: Mean Travel Time for Increasing Sample Size in the high surcharge (S = 3.27) validation case

Figures 4.10 and 4.11 show the relationship between the percentage error parameter and the number of particles required to produce a mean travel time within those bounds (for each of the validation cases). The relationship shown highlights the additional computational expense of reducing the acceptable error below 0.5%.

The Matlab code output the number of particles required to achieve an 'acceptable' mean travel time when compared with that of the complete sample, the results of which are shown in table 4.1 for the acceptable error value of 1%.

	S = 1.17	S = 3.27
Travel Time (s)	4.09	1.32
Error Value	1 %	1 %
No. of Particles Required	18100	24900

Table 4.1: Acceptable number of particles for an error of $< 1\%$ *in mean travel time*

The standard deviation was also calculated for each sub sample (Figures 4.12 and 4.13). This was compared to the standard deviation of the 'complete sample'.

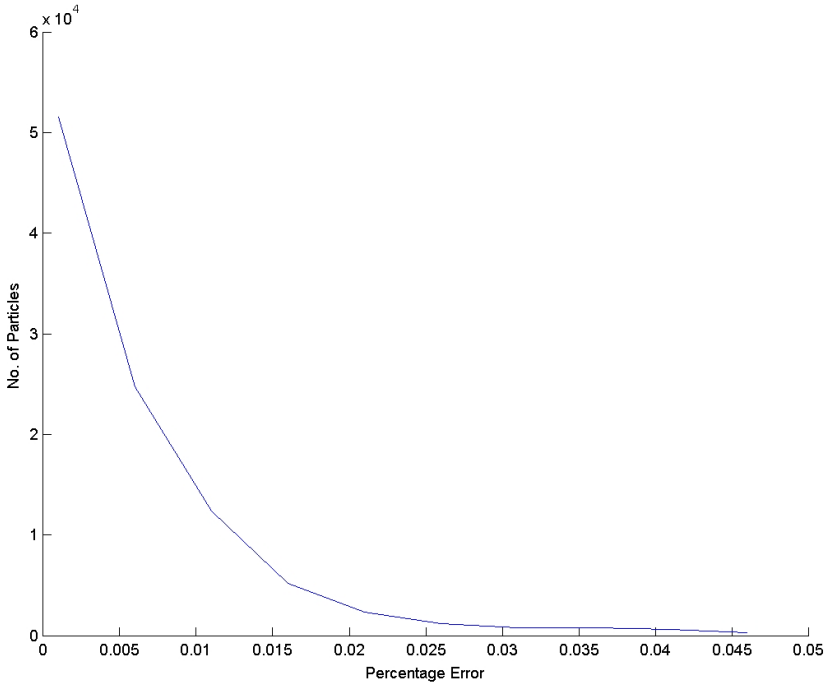

Figure 4.10: The number of particles required to fall within a set acceptable error parameter (S = 1.17)

Again, an acceptable percentage error was set (1%) and the Matlab code was used to determine at which sample size the standard deviation became within the defined bounds (the results of which are shown in table 4.2).

	S = 1.17	S = 3.27
Travel Time (s)	4.09	1.32
Error Value	1 %	1 %
No. of Particles Required	25400	43500

Table 4.2: Acceptable number of particles for a standard deviation of $< 1\%$ in mean travel time

The 10^{th} and 90^{th} percentiles of each sub-sampled distribution were computed within the Matlab code in order to classify the shape of the distribution for a given sample size. The relationship between the percentiles and sample size was the same as that of the standard deviation and the mean travel time. Therefore it offered no further insight into an acceptable number of particles to be used. However, it does show that either mean travel time or standard deviation are a representative parameter for determining an acceptable number of particles to be

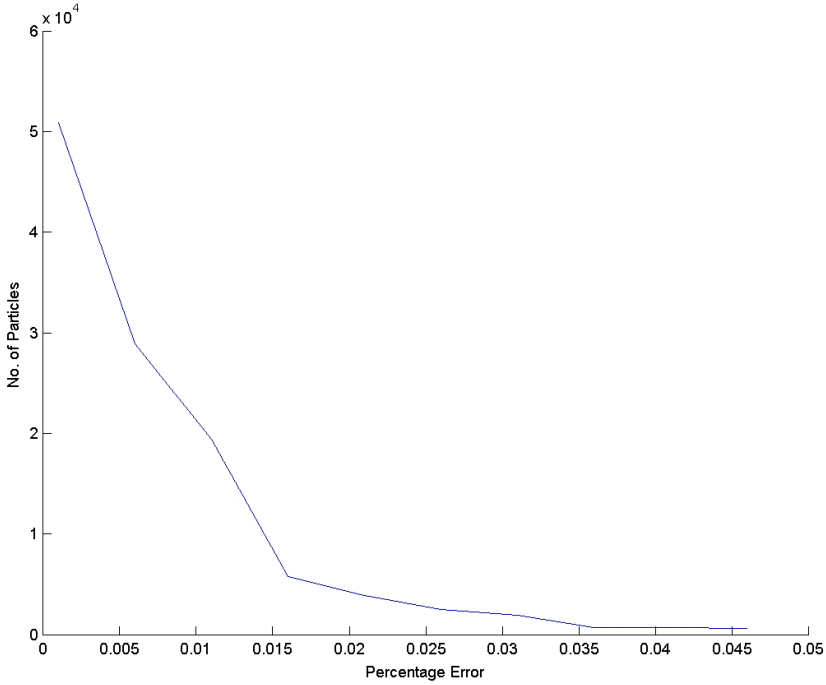

Figure 4.11: The number of particles required to fall within a set acceptable error parameter (S = 3.27)

input as the smaller samples did not offer an erroneously shaped distribution.

Often the input face (or surface) used for discrete phase modelling will not have a clean multiple of the required number of particles to fit within the acceptability bounds presented previously. However, by using at least the number of particles suggested in table 4.1 and 4.2, an acceptability boundary of 1% can be reached. Tables 4.1 and 4.2 show the 60,000 particles input by Lau (2008) to fall within the 1% accuracy bounds (for both mean travel time, and standard deviation). As using the standard deviation error to dictate the number of particles for input gave the greatest number whilst still remaining computationally feasible, a minimum number of particles as shown in table 4.2 was used for all further discrete phase modelling. A summary of the final discrete-phase modelling parameters is shown in table 4.3.

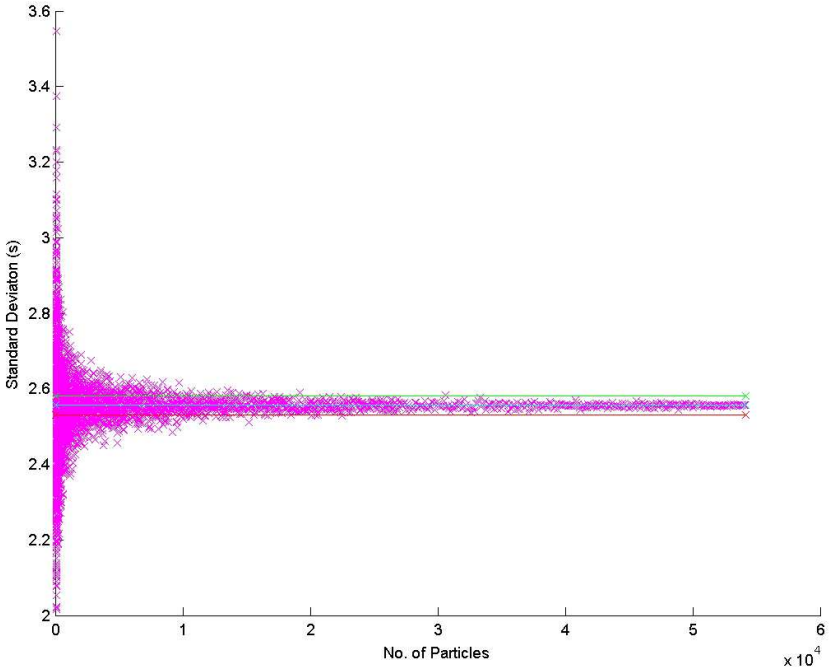

Figure 4.12: Standard Deviation for Increasing Sample Size in the low surcharge (S = 1.17) validation case

Parameter	Setting / Value
Solute:	
Model	Uncoupled particle tracking
Discrete random walk	Yes
No. of particles	$> 45,000$
Particle density	998.2 kg/m^3 (as per water)
Particle size	1×10^{-6} (uniform)
Injection	from surface (inlet)
Max no. of steps	1×10^{9} (maximum)

Table 4.3: Validated parameters for modelling solute in CFD manhole model simulations

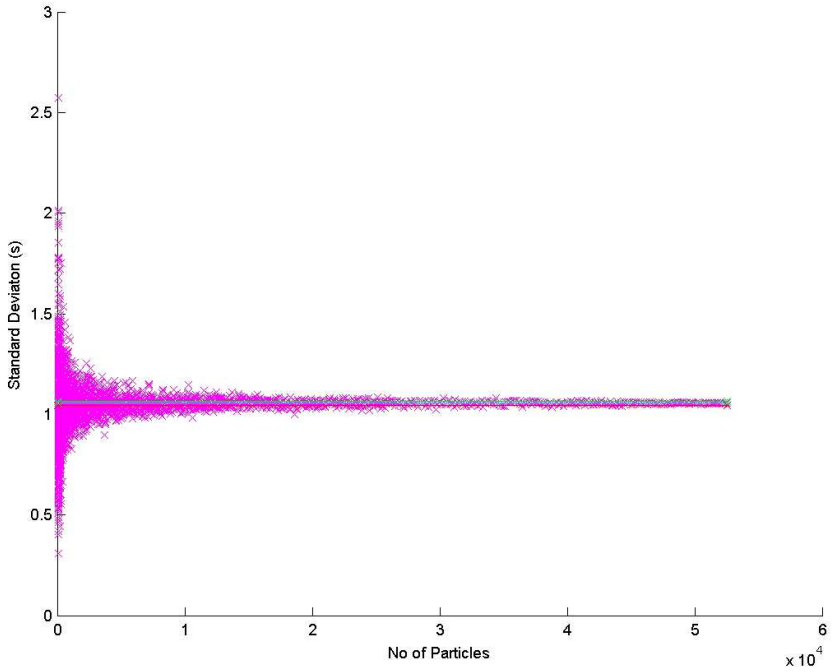

Figure 4.13: Standard Deviation for Increasing Sample Size in the high surcharge (S = 3.27) validation case

4.2.1.4 CRTDs

Using the validated particle tracking methodology (table 4.3), and the Species model method (section 3.3) in conjunction with deconvolution techniques (section 2.4.8), cumulative retention time distributions (CRTDs) were generated for each of the solute modelling options (each for three turbulence models), under both surcharge conditions (validation cases, S = 1.17, S = 3.27).

It can be seen that in low surcharge (pre-threshold) conditions (figures 4.14 and 4.15) all models correspond well with solute trace derived laboratory CRTD results. The RSM and k-ϵ Realizable models offer the closest fit in both short-circuiting (characterised by the initial fast mass recovery) and recirculation (characterised by the tail portion of the CRTD). The characteristic over-estimation of jet length in the k-ϵ RNG model can be seen by the poor fit to the initial mass recovery due to the initial steep limb in the particle tracking results. The species model offers a better fit to this section of the CRTD (for the k-ϵ RNG turbulence model).

In post-threshold surcharge conditions (figure 4.16) an accurate model of both small scale re-circulations and jet dissipation is vital to replicate the observed flow conditions. The majority of the injected mass (particles and species) are recovered rapidly due to the strong short circuiting jet effects, whilst the remaining solute recirculates throughout the volume. All models considered replicate this shape (and thus the general flow field) well. However, the amount of mass initially recovered varies by 20% of the total and the amount of recirculation also differs. Discussion of the two solute models used is presented in section 4.2.1.5.

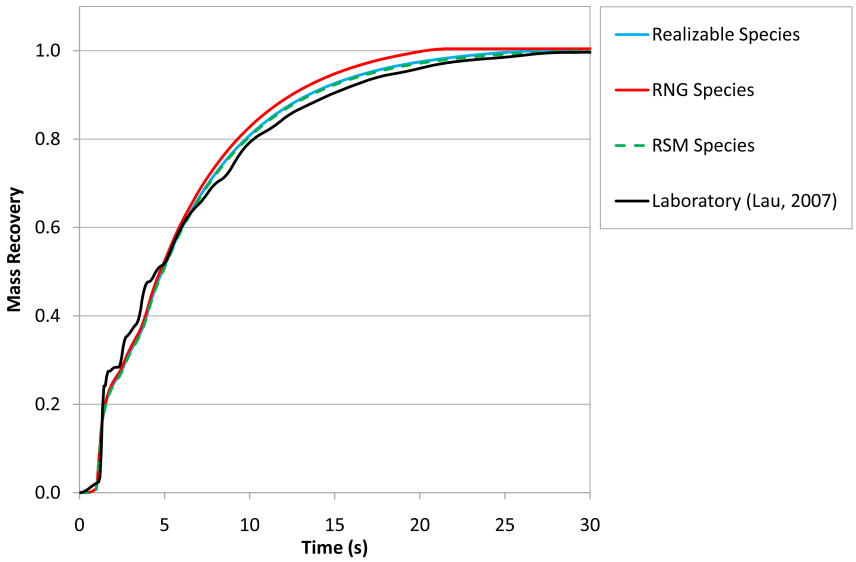

Figure 4.14: CRTDs for the low surcharge (S = 1.17) validation case generated using the species model and deconvolution techniques compared to laboratory results Lau (2008)

4.2.1.5 Particle Tracking and Species Modelling

Grimm (2003), Lau (2008) and Stovin *et al.* (2008a) found that the species model and particle tracking model generated similar solute transport predictions. However, the species model does offer better results than the particle tracking model when used with the k-ϵ turbulence model (figures 4.14 and 4.15). Ultimately, the computational time required for the particle tracking model to run was much less (in the order of ten times) and it was therefore deemed advantageous. Figure 4.15 confirms that all particle tracking results (in low surcharge conditions) offer predictions that are in close agreement with the laboratory data.

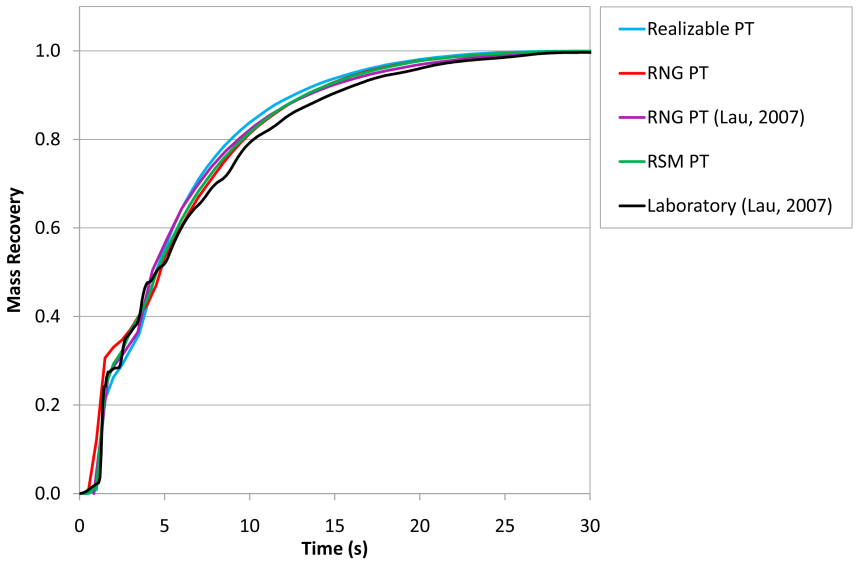

Figure 4.15: CRTDs for the low surcharge (S = 1.17) validation case generated using the discrete phase model compared to laboratory results Lau (2008)

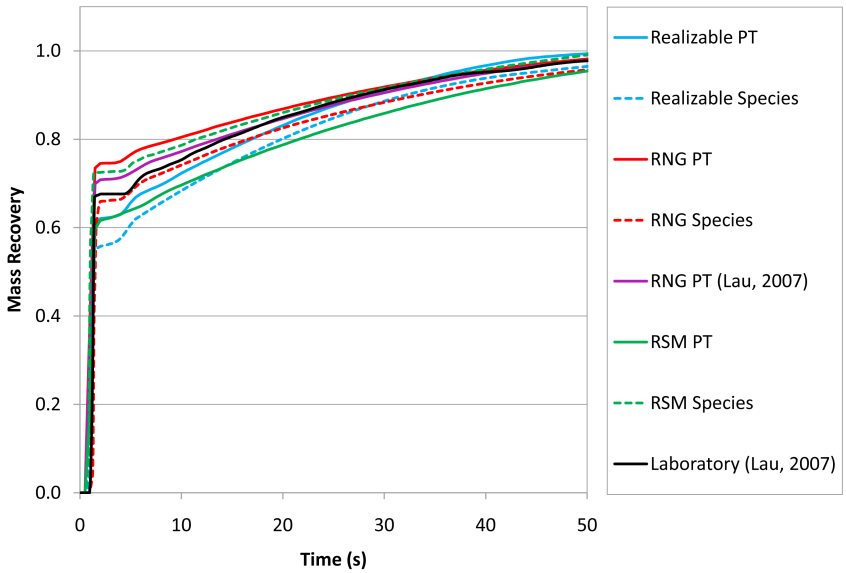

Figure 4.16: CRTDs for the high surcharge (S = 3.27) validation case generated using the species and discrete phase models compared to laboratory results Lau (2008)

In high surcharge (post-threshold) conditions the model CRTDs differ (whilst still representing the characteristic shape well). The initial amount of mass recovery varies by 20% of the observed, and the rate of recovery of mass (due to recirculation) on the tail portion of the CRTDs also varies. However, there is not a systematic difference in the behaviour of either model.

Utilising the discrete phase particle tracking model over the species transport model would offer a significant saving in model run time. Therefore, it is advantageous to exploit this possible saving by aiming to refine the model further. It would also exclude the need to use deconvolution techniques (section 2.4.8), and any associated uncertainty, as the discrete phase model directly represents an instantaneous injection.

Due to the nature of the flow conditions (circulatory/swirling) in the low surcharge (pre-threshold) condition the k-ϵ RNG model is unsuitable for further consideration. The k-ϵ Realizable model has been shown to reliably replicate PIV laboratory results similar to that of the RSM (in low surcharge conditions). However, in high surcharge conditions, it over estimates the spreading of the dominant jet. Despite this, it offers a significant improvement in simulation time over the RSM model. Therefore, it is advantageous to further refine the k-ϵ Realizable model.

4.2.1.6 Time Scale Constant sensitivity

The Discrete Random Walk (DRW), or 'eddy lifetime' model within the discrete phase particle tracking model relies on a Gaussian distributed random velocity fluctuation, and a Time Scale Constant (TSC). This TSC dictates how long a modelled particle remains within an eddy (FLUENT, 2005a). Using this TSC it is possible to enhance the fit of modelled solute transport data to that of the laboratory results independent of the flow field.

In low surcharge (pre-threshold) conditions the discrete phase modelling results showed an extremely low sensitivity to the TSC. However, in high surcharge (post-threshold) conditions, decreasing the TSC from its default value of 0.15 allowed for an improved fit with laboratory data. A value of 0.10 enabled the initial mass recovered due to the short circuiting effects to be increased whilst

still enabling a good fit with the tail (recirculation) portion of the CRTD (figure 4.18). Due to this improvement it is possible to adopt the discrete-phase particle tracking model with enhanced levels of accuracy.

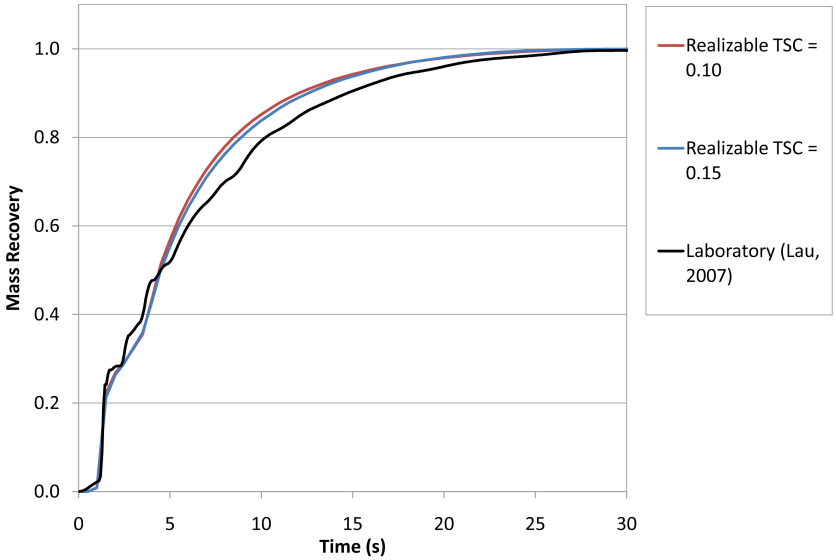

Figure 4.17: Sensitivity of the low surcharge ($S = 1.17$) validation case to the time scale constant

4.2.1.7 Convolution

Guymer and Stovin (2011) used convolution (superposition) to quantify the goodness of fit of a one-dimensional mixing model for surcharged manholes. A downstream laboratory trace was compared to a modelled downstream trace (from the same upstream laboratory input). The goodness of fit was calculated using R_t^2 (Young *et al.*, 1980). Thus, to quantify the goodness of fit of the k-ϵ Realizable modelling results, an upstream (measured) laboratory trace was convolved with the RTD to generate a downstream concentration profile as described above (figure 4.19) and the goodness of fit was quantified via R_t^2 values.

In the low surcharge (pre-threshold, figure 4.19a) surcharge condition R_t^2 equated to 0.959. Comparatively, in the high surcharge (post-threshold, figure 4.19b) surcharge condition, the R_t^2 value was calculated to be 0.997, which shows a higher level of agreement due to the lack of secondary peak shown in the downstream pre-threshold surcharge condition (also identified in Stovin *et al.* (2008a)). Although

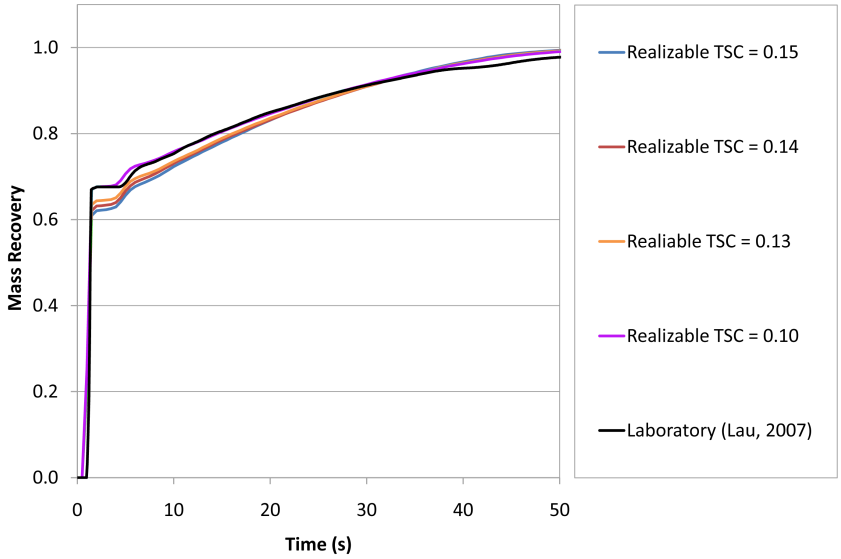

Figure 4.18: Sensitivity of the high surcharge (S = 3.27) validation case to the time scale constant

the appearance of a secondary peak was initially thought of as a shortfall of the CFD model (Lau (2008)), it may in fact highlight errors in the laboratory data (currently in use for validation). Jones (2012) identified the secondary peak in recent laboratory studies similar (D_M = 388 mm; D_p = 50 mm) to that of Lau (2008).

The fixed-lid assumption appears to replicate the solute transport of the manhole (in the two validation cases evaluated by Lau (2008)) to an acceptably high level. However, Lau (2008) suggested *'When more advanced computational resources becomes available, the manhole simulations should be repeated using two phase modelling to account for the effects of the free surface. The results could be used to assess the effects of the fixed lid assumption on the flow field and solute transport predictions'*. The next section will therefore present data corresponding to VOF modelling. Two phase (VOF) modelling is also required for time dependent modelling.

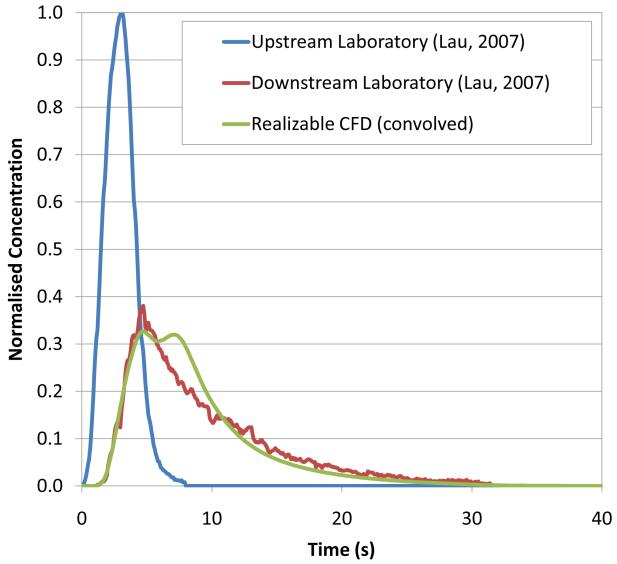

(a) S = 1.17, $R_t^2 = 0.959$

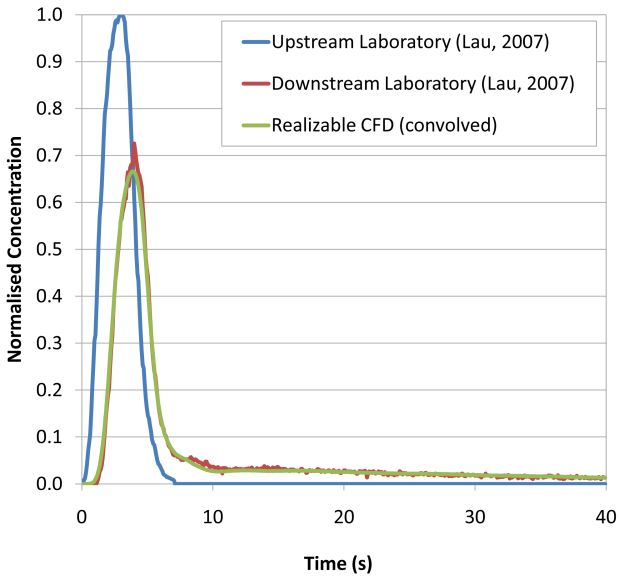

(b) S = 3.27, $R_t^2 = 0.997$

Figure 4.19: Comparison of convolved downstream traces with measured laboratory data (Lau (2008)) under both surcharge cases (S = 1.17; S = 3.27)

4.3 Explicit free-surface modelling

Although section 3.6 concluded that simulation of unsteady flow problems was ultimately impractical (due to time restrictions and computational resources), it is still feasible to use pseudo-steady conditions to generate a free-surface model with an unsteady solver. The implicit HRIC scheme was shown to replicate a pseudo-unsteady condition (section 3.3). However, the air-water interface was poorly resolved. In order to improve the resolution of the interface, other (explicit) models were investigated. These included the Modified HRIC, Cicsam and Geo-reconstruct schemes (detailed in section 2.5.10.2.3).

The high surcharge 218 mm manhole geometry (shown in figure 4.3) was modified for use with the VOF model (detailed in section 2.5.10.2.3). The top of the model was specified as a pressure outlet (instead of a non-slip wall). No pressure was applied at the outlet of the model at this stage.

The model was initialised as an empty manhole (no water) and allowed to converge (0.01 s time step; 20 iterations per time step) to the point at which continuity (Q = 1 l/s) had been reached (figure 4.20) and the residuals were less than 1×10^{-4} (this was reduced by an order of magnitude from preliminary investigations in an attempt to minimise solution time). Excluding the VOF scheme, all turbulence (k-ϵ Realizable) and modelling options remained constant, as per section 4.2.

Non-iterative time advancement was examined as a method of reducing solution time (as recommended by FLUENT (2005a)). However, it was found to require a similar number of iterations and offered no real benefit. This is likely due to the chosen time step (0.01 s) already being appropriate, following recommendations by Grimm (2003).

4.3.1 The sharpness of the free surface air-water interface

Resultant flow interfaces (on the CVP) are shown in figures 4.21 to 4.23. According to FLUENT (2005a) *'the CICSAM scheme or the modified HRIC scheme can be computationally inexpensive when compared to the geometric reconstruction*

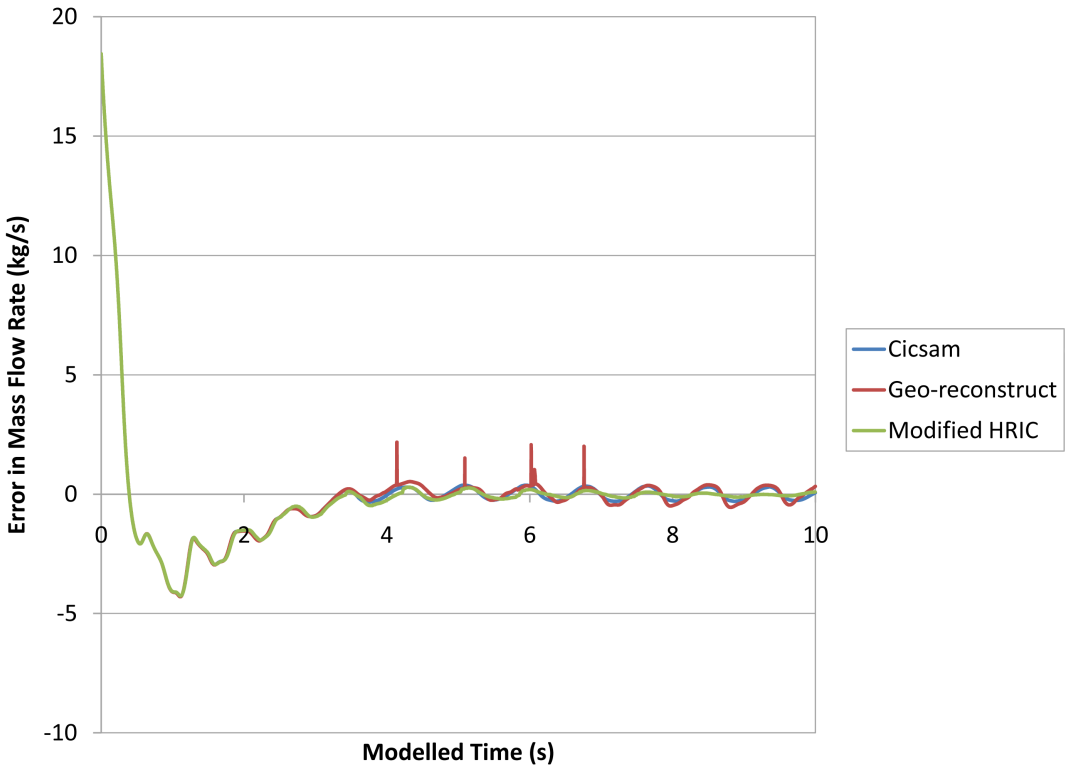

Figure 4.20: Convergence demonstrated using the error in continuity (mass flow rate) for the three VOF schemes evaluated

scheme'. This was confirmed and is shown in table 4.4. However, it can be seen that the Modified HRIC scheme produces a poorly resolved flow interface (figure 4.21). The size (or spread) of the interface would make it difficult to ascertain its exact location. Also, laboratory visualisations show the interface to be relatively clean (i.e. no spray). This does not fit with the Modified HRIC predictions. Furthermore, Wacławczyk and Koronowicz (2008) found the CICSAM scheme to outperform the Modified HRIC scheme when predicting the sloshing of water in a rectangular tank.

According to FLUENT (2005a) *'The CICSAM scheme gives interface sharpness of the same level as the geometric reconstruction scheme and is particularly suitable for flows with high viscosity ratios between the phases'*. The Cicsam scheme (figure 4.22) appears to only offer a slight improvement on results from the Modified HRIC scheme.

However, FLUENT (2005a) recommends use of the Geo-reconstruct scheme for jet breakup (both surcharge conditions are dominated by jet dissipation). It can

be seen (figure 4.23) that this scheme offers by far the sharpest air-water interface and a vast improvement over the other two models evaluated (under the same mesh conditions). Entrained air can be seen in the model results. It is thought that this is due to the initial filling of the volume and will not be present under pseudo-steady conditions. Özkan *et al.* (2007) shows the results of a code-to-code comparison of VOF methods; only interface reconstruction leads to *'physically sound and consistent results'*. Liu *et al.* (2002) showed the VOF model, in conjunction with the Geo-reconstruct scheme to be capable of accurately predicting the flow over a semicircular weir. However, this focussed on velocity profiles and the resolution of the air-water interface is not shown.

Due to the increased sharpness of the air-water interface in this section, the Geo-reconstruct model was adopted for further, free-surface investigation.

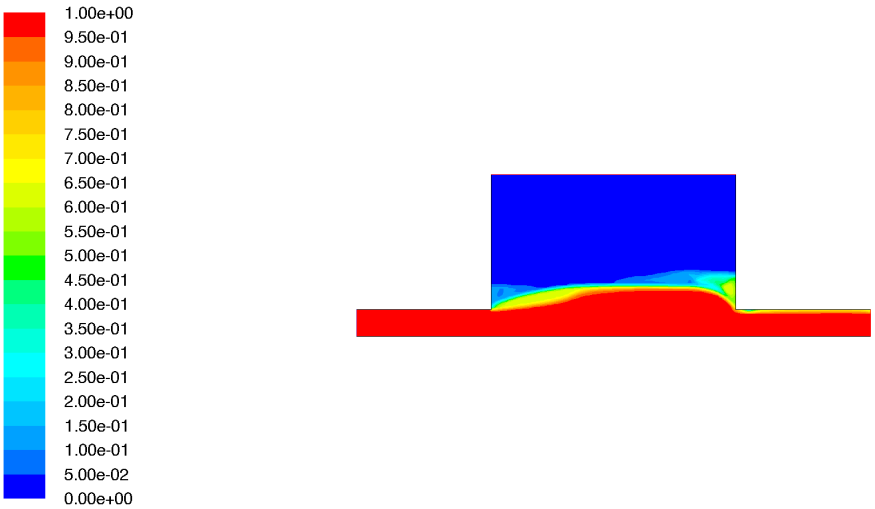

Figure 4.21: Contours of phase on the CVP generated using the Modified HRIC VOF scheme, red represents 100% water, blue represents 100% air. The free surface is defined as a 50:50 split, coloured green

	Cicsam	Geo-reconstruct	Modified HRIC
No of iterations	65148	89962	35622

Table 4.4: No. of iterations required for convergence of the error in mass flow rate

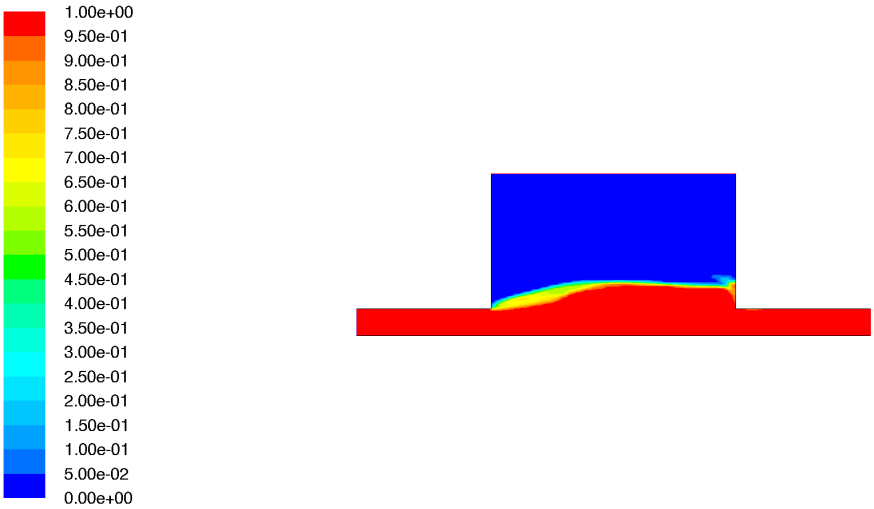

Figure 4.22: Contours of phase on the CVP generated using the Cicsam VOF scheme, red represents 100% water, blue represents 100% air. The free surface is defined as a 50:50 split, coloured green

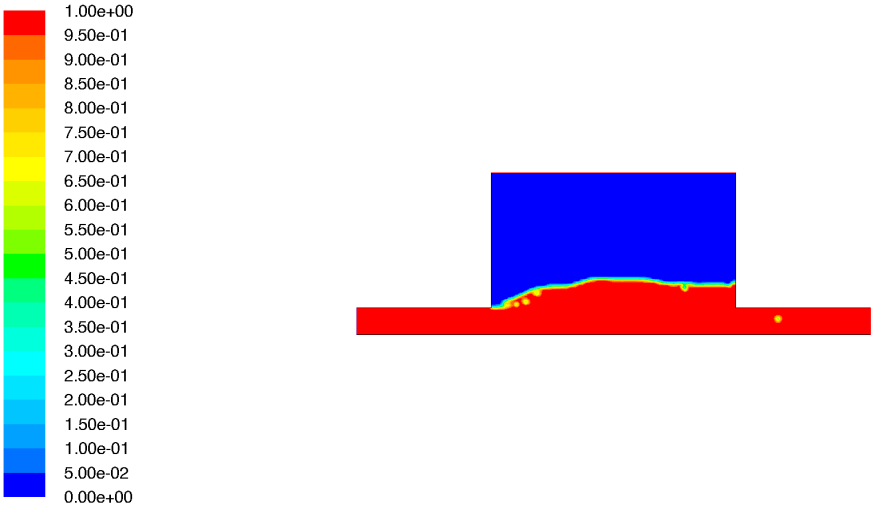

Figure 4.23: Contours of phase on the CVP generated using the Geo-reconstruct VOF scheme, red represents 100% water, blue represents 100% air. The free surface is defined as a 50:50 split, coloured green

4.3.1.1 VOF Validation

To compare the results of the VOF, free-surface model with the fixed-lid manholes already evaluated, the S = 3.27 218 mm manhole mesh was modified. The top of the model was extended upwards from the high surcharge condition boundary (allowing for a total possible surcharge level of S = 3.5).

Outlet pressures (calculated using $p = \rho g h$) of 510.9 Pa (S = 1.17) and 1005.3 Pa (S = 3.27) were applied at the model outlet. The Geo-reconstruct VOF scheme was used for the volume fraction and the k-ϵ Realizable model was used for the turbulence. The models were converged (0.01 s time step; 20 iterations per time step) to residuals of 1×10^{-4}.

4.3.1.2 Judging convergence of a steady solution in unsteady conditions

During the solution stage it was necessary to judge convergence of the pseudo-steady solution in unsteady conditions (in order to minimise computational time). Convergence per time step would not indicate that steady conditions had been reached, only that the time step was small enough to represent the flow field changes without diverging. Therefore, to monitor the development of the flow field, 10 positions around the manhole centre were chosen (figures 4.24 and 4.25). At each of these points, x and y velocities were monitored as these represent the main features of the flow field (jet and recirculation respectively). The development of the flow field on the CHP can be seen in figure 4.26 (for the low surcharge condition), whilst the x and y velocities for all ten positions are shown in figures 4.27 to 4.30 (for both surcharge conditions).

Figure 4.26 shows that under low surcharge conditions the jet begins to pass through the manhole volume with increasing length (t = 3 s, t = 17 s), and then a recirculation begins that leads to an asymmetric jet (t = 23 s). This then stabilises (t = 30 s). This is also confirmed by examining the x velocities (figure 4.27). However, the y velocities (figure 4.28) do not show this clearly, appearing to stabilise at the point at which the recirculation begins (t = 17 s).

Under high surcharge conditions it can be seen (figures 4.29 and 4.30, that no

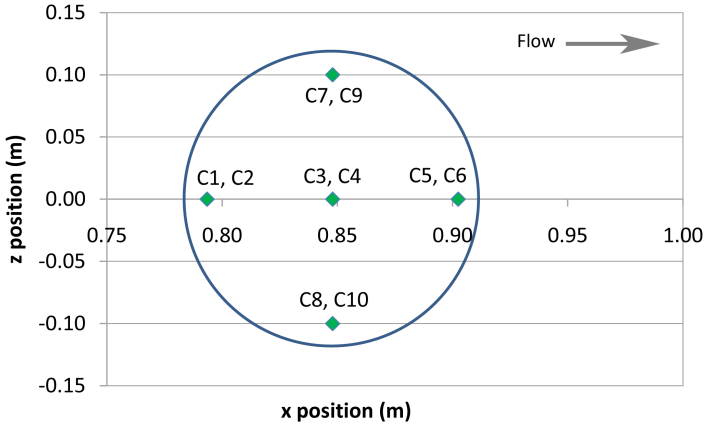

Figure 4.24: x and z values for 10 positions within the manhole volume used to monitor convergence of the flow field in pseudo-steady conditions (on the horizontal plane)

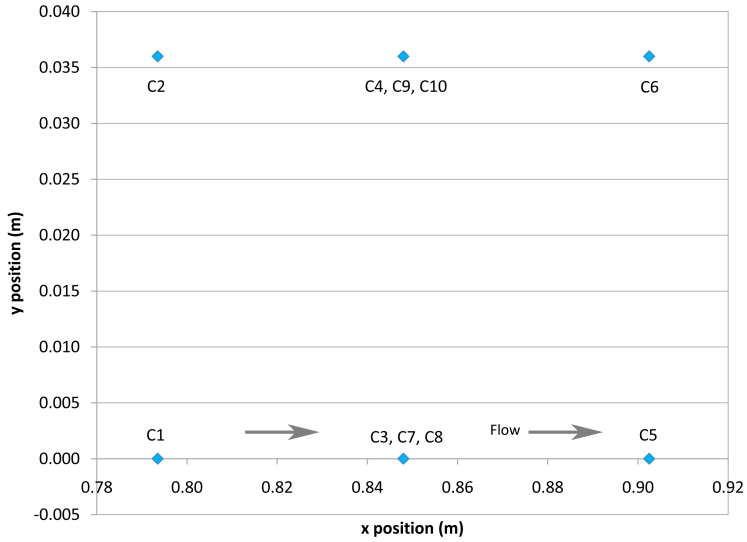

Figure 4.25: x and y values for 10 positions within the manhole volume used to monitor convergence of the flow field in pseudo-steady conditions (on the vertical plane)

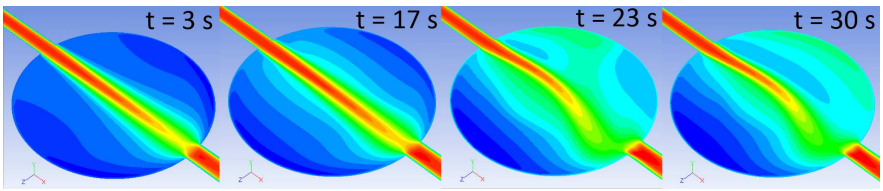

Figure 4.26: Development of the flow field (on the CHP) under pseudo-steady conditions

secondary recirculation begins and thus the model approaches 'steady' conditions without an obvious change in the x velocities.

The stabilization period appears not to be strongly dependent upon position within the manhole. Due to this C3, the mid manhole, mid pipe depth monitoring position was chosen for confirming whether the flow conditions were 'pseudo steady'.

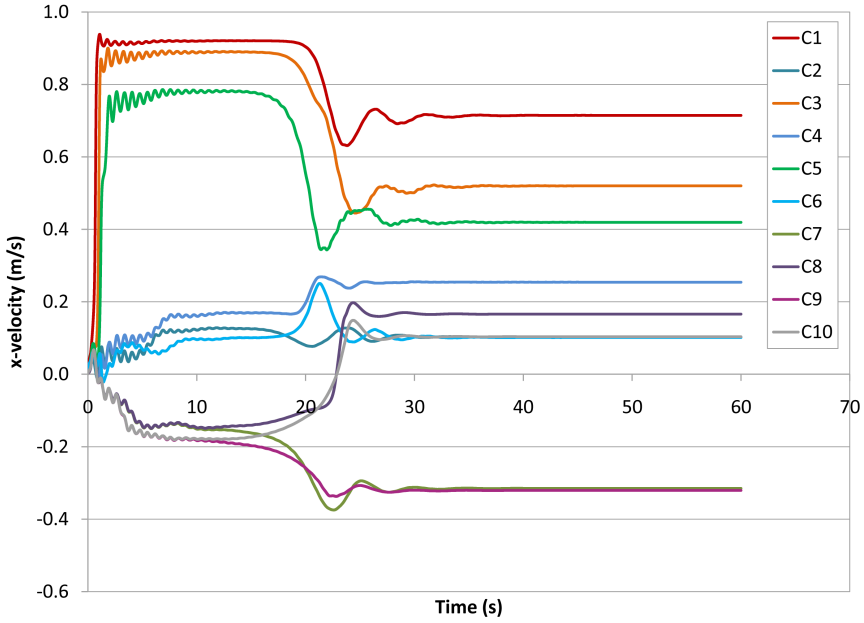

Figure 4.27: Convergence of x-velocity measured at the 10 monitoring points within the central manhole volume in low surcharge conditions (S = 1.17)

4.3.1.3 Converged VOF validation cases

Using the methodology set out in the previous sections, two final, fully converged pseudo-steady representations of the Lau (2008) validation cases were generated. Figures 4.31 and 4.32 show the clearly defined air-water interface on the CVP for S = 1.17 and S = 3.27 respectively. The free surface (air-water) interface was defined as a volume fraction = 0.5 (shown in green). The mean surcharge depth was calculated for both cases and found to be within 2% of the expected position.

Figures 4.33 and 4.34 show the flow fields for the CVP and CHP for the low and high surcharge (pre- and post-threshold) multiphase models. In low surcharge conditions (S = 1.17) the multiphase model accurately represents both the jet

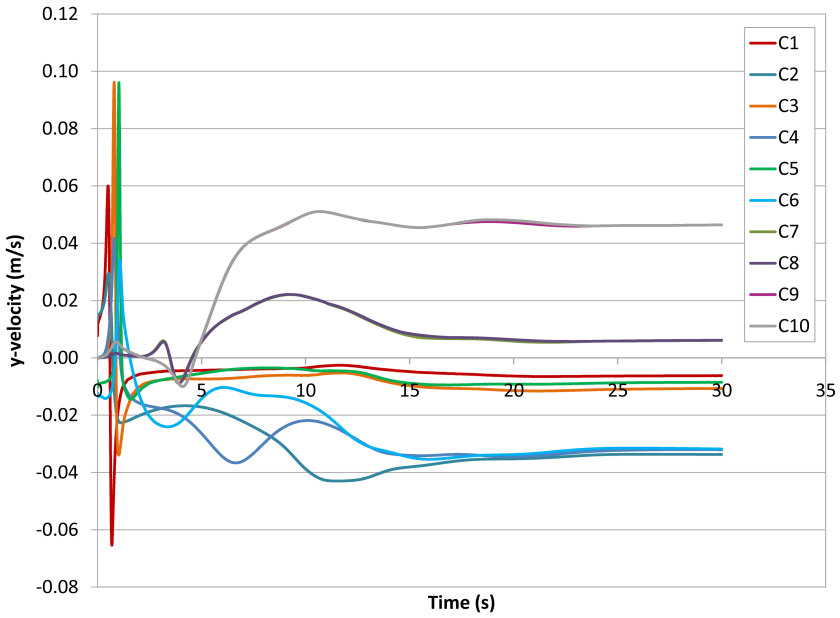

Figure 4.28: Convergence of y-velocity measured at the 10 monitoring points within the central manhole volume in low surcharge conditions (S = 1.17)

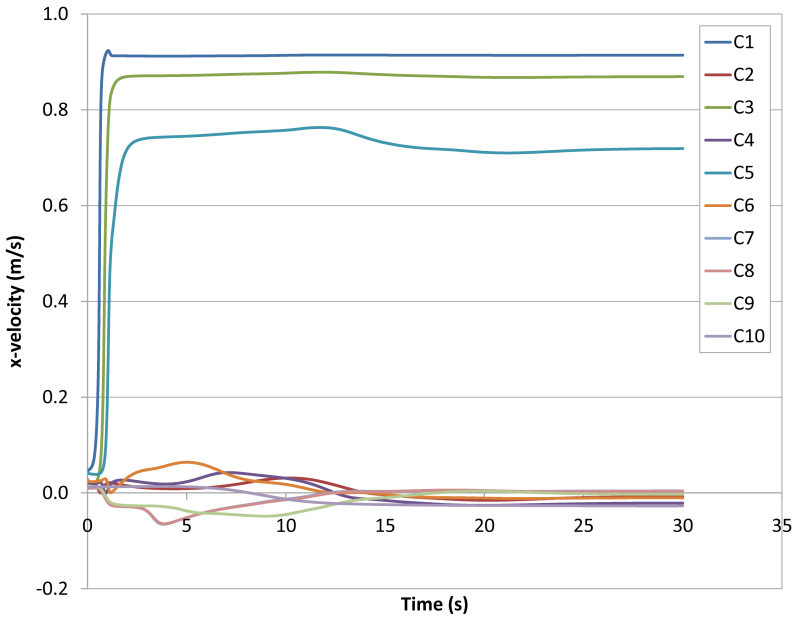

Figure 4.29: Convergence of x-velocity measured at the 10 monitoring points within the central manhole volume in high surcharge conditions (S = 3.27)

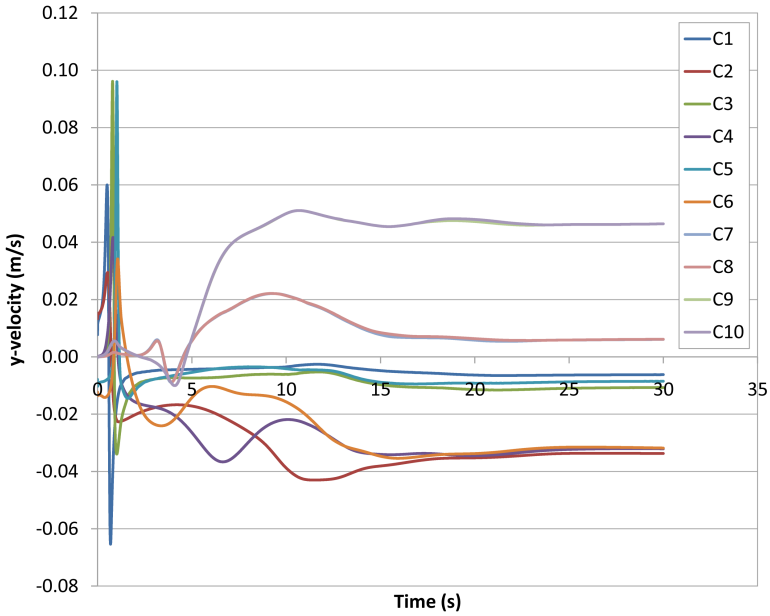

Figure 4.30: Convergence of y-velocity measured at the 10 monitoring points within the central manhole volume in high surcharge conditions (S = 3.27)

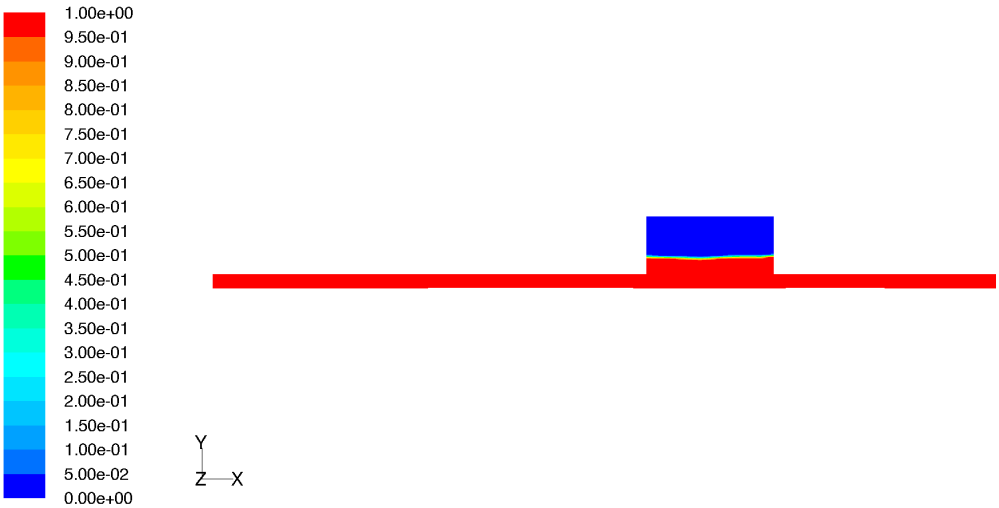

Figure 4.31: Contours of phase on the CVP generated using the Geo-reconstruct VOF scheme in converged pseudo-steady conditions (S = 1.17), red represents 100% water, blue represents 100% air. The free surface is defined as a 50:50 split, coloured green

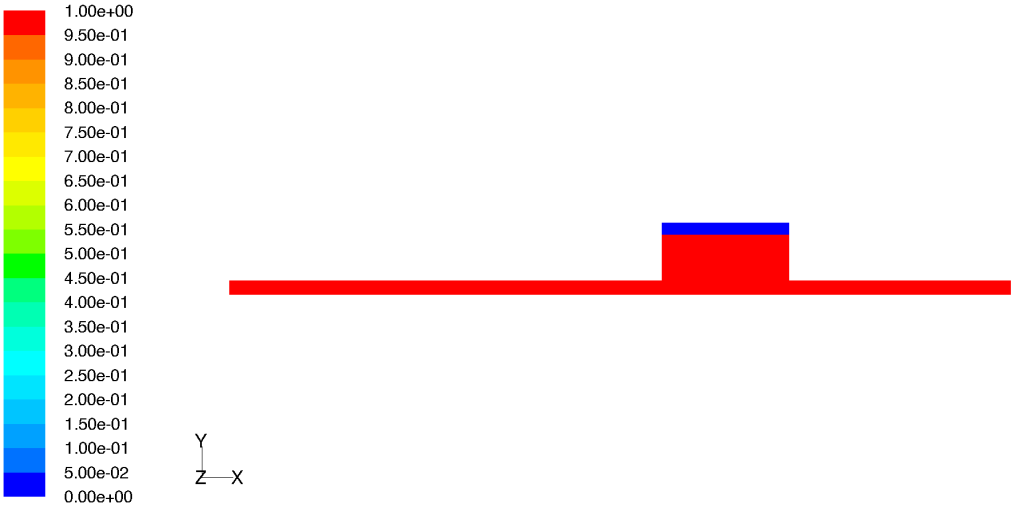

Figure 4.32: Contours of phase on the CVP generated using the Geo-reconstruct VOF scheme in converged pseudo-steady conditions (S = 3.27), red represents 100% water, blue represents 100% air. The free surface is defined as a 50:50 split, coloured green

dissipation and the recirculation zones to the same degree as in the fixed lid simulations (figure 4.33d). However, in post-threshold surcharge conditions the vertical recirculation is under represented. A high degree of secondary horizontal recirculation close to the outlet, not evident in the PIV and fixed lid models (figures 4.5a and 4.5f respectively), is also shown.

4.3.2 VOF Results - CRTDs

As per section 4.2.1.4, the CRTDs were generated using the validated discrete-phase particle tracking methodology (section 4.2.1.3). These are shown in figures 4.35 and 4.36 (low and high surcharge conditions respectively).

In low surcharge conditions (S = 1.17, figure 4.35), the initial mass recovered (due to the main jet) is greater ($\approx 10\%$) than that of the fixed-lid and laboratory results. The tail portion of the CRTD also exhibits a poor fit due to the increased time to recover the remainder of the input mass (i.e. over representation of the recirculation present).

In high surcharge conditions (S = 3.27, figure 4.36) the initial mass recovered is also over-estimated. However, the tail portion of the CRTD offers a relatively good fit to both the fixed-lid model and the laboratory data.

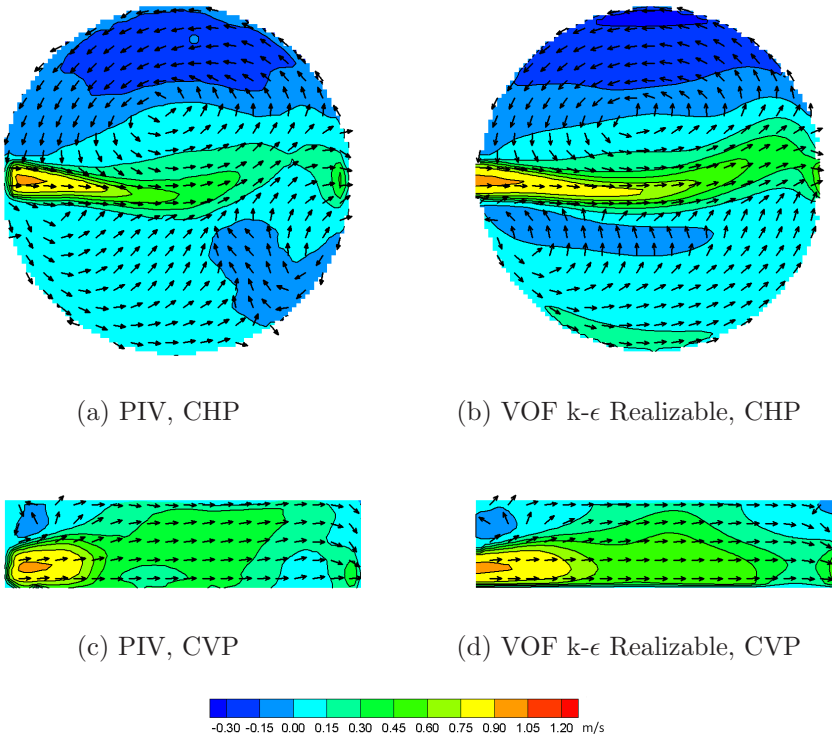

(a) PIV, CHP

(b) VOF k-ϵ Realizable, CHP

(c) PIV, CVP

(d) VOF k-ϵ Realizable, CVP

Figure 4.33: CHP and CVP flow fields for a 218 mm manhole (Q = 0.35 l/s, S = 1.17, below threshold) for the PIV (measured, Lau (2008)) and k-ϵRealizable Geo-reconstruct VOF model (contours coloured by longitudinal velocity, vectors indicate flow direction)

As per section 4.2.1.7, an upstream laboratory trace was convolved downstream using the CRTDs generated for the VOF models (see figure 4.37). This returned R_t^2 values of 0.973 (previously 0.959) and 0.980 (previously 0.997) respectively (S = 1.17; S = 3.27). Despite the apparent poor fit of the VOF model CRTD under low surcharge conditions, the goodness of fit is improved. It is thought that R_t^2 appears very sensitive to the goodness of fit surrounding the secondary peak. Under low surcharge conditions the VOF model (figure 4.35) appears to be in better agreement with the portion of the CRTD potentially representing this feature (immediately following the initial rapid, mass recovery). However, these parameters highlight how large differences in the CRTD have minor effects on the goodness of fit, with all models exhibiting a high level of fitness for purpose ($R_t^2 > 0.95$).

Figure 4.38 represents the differences between the VOF and fixed-lid model flow fields (S = 1.17; S = 3.27) generated using a modified version of equation 4.2;

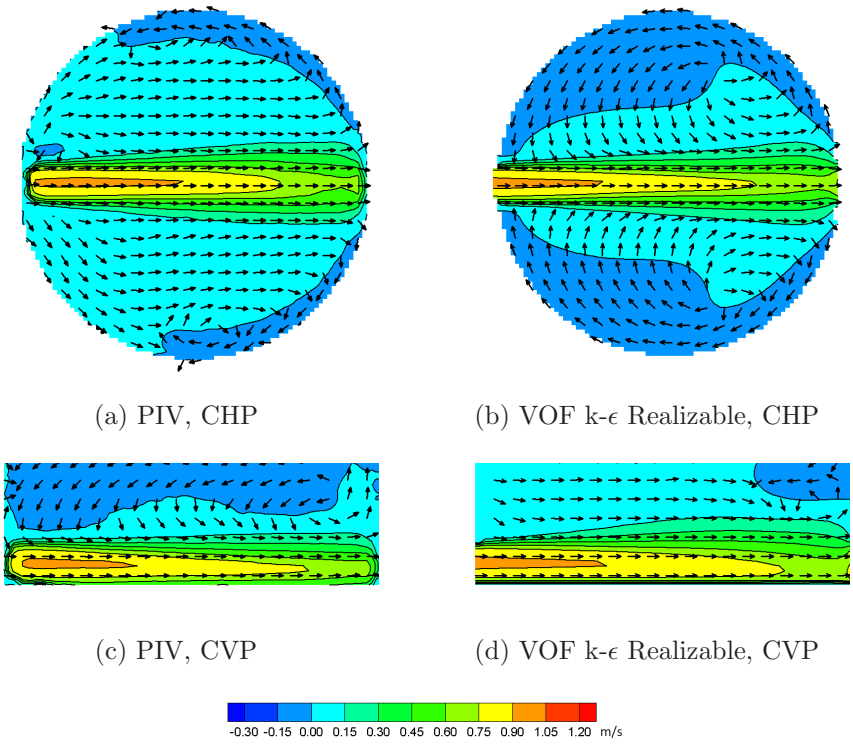

(a) PIV, CHP

(b) VOF k-ϵ Realizable, CHP

(c) PIV, CVP

(d) VOF k-ϵ Realizable, CVP

Figure 4.34: CHP and CVP flow fields for a 218mm manhole (Q = 0.35 l/s, S = 3.27, above threshold) for the PIV (measured, Lau (2008)) and k-ϵRealizable Geo-reconstruct VOF model (contours coloured by longitudinal velocity, vectors indicate flow direction)

equation 4.3.

$$\%u_{diff} = \left| \frac{u_{VOF} - u_{FIXED}}{\overline{u}} \right| \times 100 \tag{4.3}$$

u_{FIXED} is the velocity at a given point according to the fixed-lid model predictions

u_{VOF} is the velocity at a given point according to the VOF model predictions

Under low surcharge conditions (figures 4.38a and 4.38c), the largest errors can be seen surrounding the jet and also in the recirculation zones on the model edge, potentially explaining the enhanced level of fit to the laboratory PIV CRTD

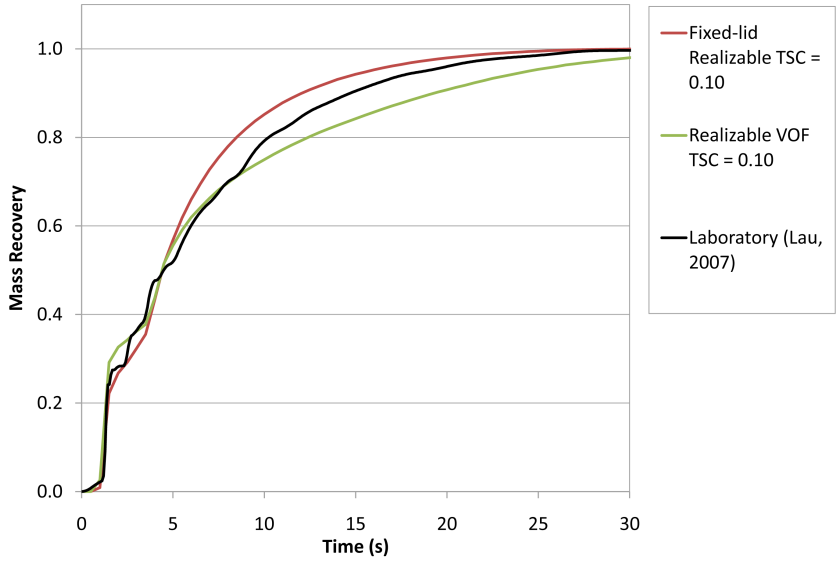

Figure 4.35: CRTDs for the fixed-lid and VOF Geo-reconstruct k-ϵ Realizable 218 mm manhole model under low surcharge conditions (S = 1.17) compared with laboratory data (Lau (2008))

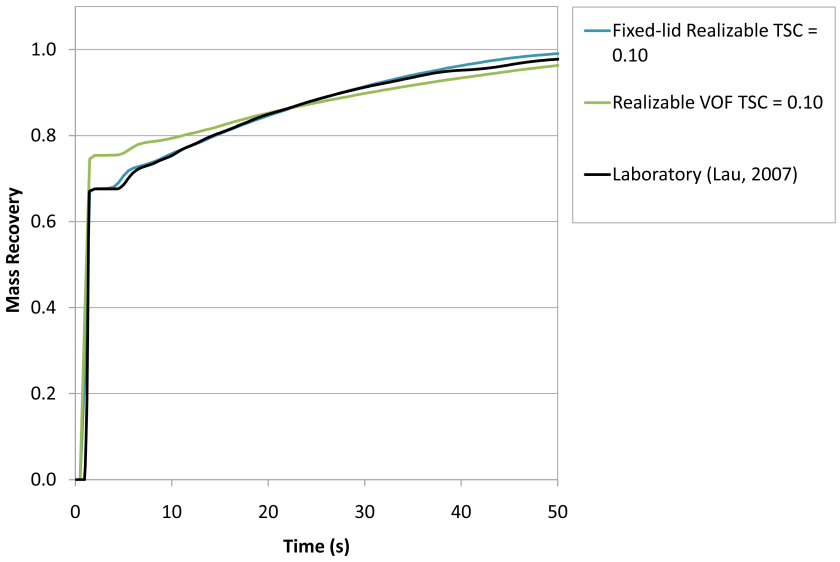

Figure 4.36: CRTDs for the fixed-lid and VOF Geo-reconstruct k-ϵ Realizable 218 mm manhole model under high surcharge conditions (S = 3.27) compared with laboratory data (Lau (2008))

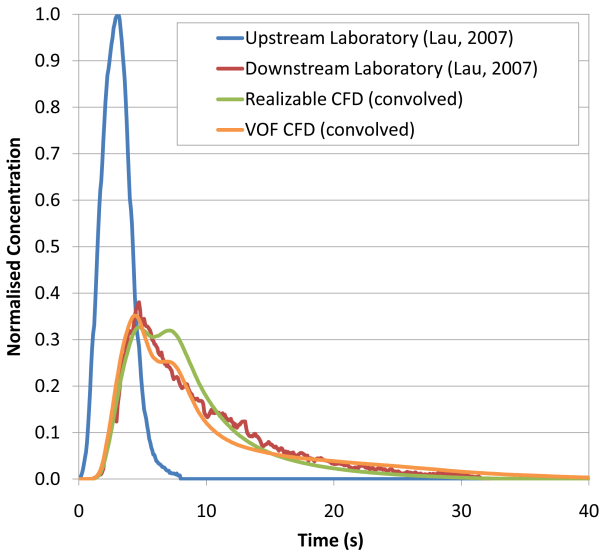

(a) S = 1.17

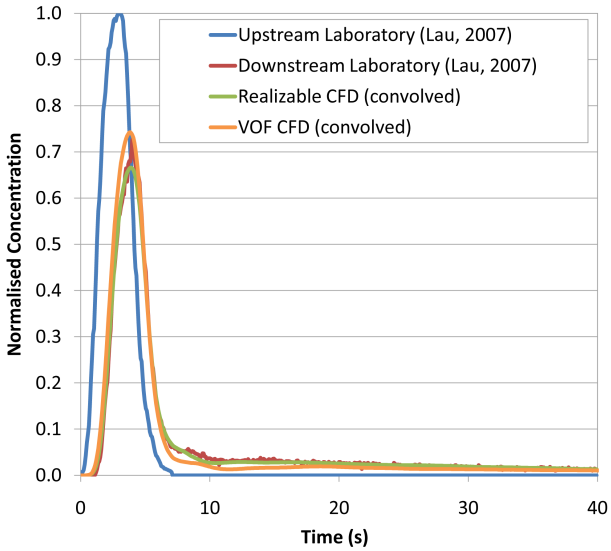

(b) S = 3.27

Figure 4.37: Comparison of a convolved Geo-reconstruct VOF downstream trace with the fixed lid model and laboratory data (Lau (2008)) for both surcharge conditions (S = 1.17; S = 3.27)

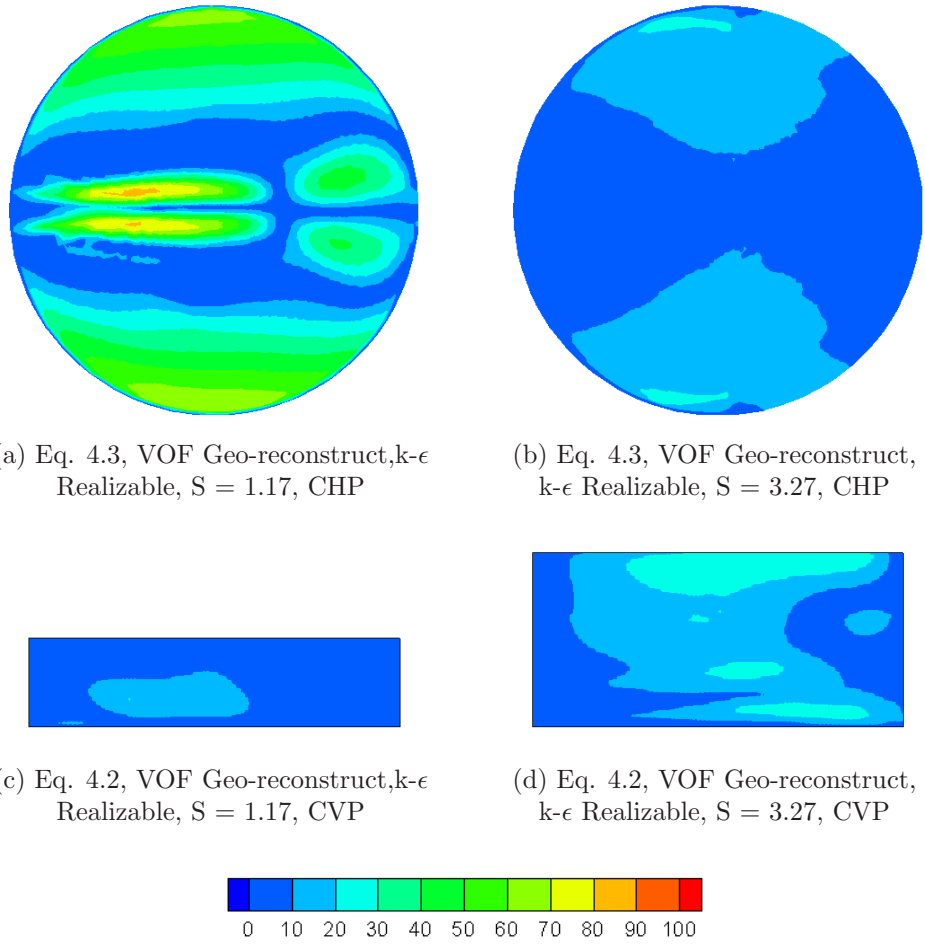

(a) Eq. 4.3, VOF Geo-reconstruct,k-ϵ Realizable, S = 1.17, CHP

(b) Eq. 4.3, VOF Geo-reconstruct, k-ϵ Realizable, S = 3.27, CHP

(c) Eq. 4.2, VOF Geo-reconstruct,k-ϵ Realizable, S = 1.17, CVP

(d) Eq. 4.2, VOF Geo-reconstruct, k-ϵ Realizable, S = 3.27, CVP

Figure 4.38: Contours of percentage error in the Lau (2008) validation cases (S = 1.17; S = 3.27), between the fixed lid and VOF k-ϵ Realizable models determined using equation 4.3

(which may be missing data correlating to the 'secondary peak' experienced by Jones (2012)).

Under high surcharge (S = 3.27) conditions, the zones of recirculation not evident in any other model are highlighted (figure 4.38b).

4.3.3 Conclusions

Whereas the fixed lid manhole models can be shown (from the primary validation) to offer a good fit to PIV data in both low and high surcharge conditions, the free surface VOF simulations appear less accurate. Due to time and computational

constraints it was not possible to converge the VOF models to the same residuals (errors defined in FLUENT e.g. continuity) as the fixed-lid. Residual errors were roughly one order of magnitude greater in the free surface models than the fixed lid (despite the solution being pseudo-steady). Therefore it may be possible to increase the number of iterations per time step (or decrease the time step interval) further to gain more accurate flow field results (i.e. residuals of the same order of magnitude).

Secondary validation shows that both the fixed lid and VOF models offer an acceptable level of fit ($R_t^2 > 0.95$) to laboratory solute trace data, despite clear differences in flow field representation. This may be due to factors other than the mean flow field governing the solute transport characteristics (such as turbulent intensity etc.) or other regions of flow, not considered directly in the validation of this work.

Both the RSM and k-ϵ Realizable turbulence models offer a good representation of laboratory flow field PIV data. However, the k-ϵ Realizable model inherently requires much less computational expense than the RSM, and is therefore preferable. Its characteristic greater jet dissipation seems to eliminate the k-ϵ RNG model's over representation of the jet effects identified by Lau (2008).

Volume of Fluid (VOF) free surface models can be shown to replicate similar solute transport characteristics to laboratory data. However, their flow fields appear to have certain limitations when compared to those derived under fixed lid conditions. Whilst the R_t^2 values suggest they are suitable for adoption, it cannot be certain that the models are truly representing the flow field behaviour. This is highlighted by the discrepancies shown between the fixed lid and VOF flow fields. Ultimately, the VOF (modelling the free-surface) offers no real gain in accuracy for an increased level of computational expense (and a decreased level of residual accuracy). For further investigations, the fixed-lid appears to offer a valid method for modelling a steady free-surface.

4.4 Unstructured Mesh Generation

So far, only structured meshes, highly similar to that of Lau (2008) have been considered. This removed the need for an additional grid independence study.

However, reliably developing the structured meshes considered in this study required a relatively large investment of time. Indeed many attempts to extend the meshing procedure (thus far validated) to additional geometries failed.

'The primary motivations for the development of unstructured grid technology are the potential for significant automation of the discretization process. In basic terms, speed (person hours and CPU time) and accuracy drive development. Unstructured grid generation techniques couple basic geometric building blocks with extensive geometric data to highly automate the grid generation process. In addition, the generalized data structures employed in these schemes permit the addition and removal of cells to maximize accuracy and minimize memory and CPU requirements' FLUENT (1994).

As the main aim of this study is to evaluate the solute transport characteristics of a wide range of manholes, under a large range of surcharge conditions, rapid grid generation is desirable. Due to this, unstructured representations of the validation cases (S = 1.17; S = 3.27) investigated by Lau (2008) were developed and a full grid independence study undertaken.

4.4.1 Grid independency methodology (replication of flow field, CRTDs)

As previously detailed (section 3.4.2), two cylinders were intersected to create the manhole (one 'pipe' and one 'central' volume). The fixed-lid assumption (and boundary conditions, i.e. zero slip top) were used. As the species model is no longer under consideration (and only an instantaneous input was desired), the additional inlet and exit pipe lengths were removed. Therefore, the model represented the laboratory set-up between the fluorometer positions (figure 4.1). By reducing the number of unnecessary cells, solution time is decreased.

The inlet face was meshed using the 'Tri-pave' scheme, and the remainder of the volume was filled using 'Tgrid' (with the inlet providing a source face). This produced tetrahedral cells throughout the volume.

This process was repeated for inlet cells sized 6 mm, 5 mm, 4 mm, 3 mm and 2.5 mm for both surcharge conditions (S = 1.17; S = 3.27). The resultant total

number of cells for each mesh is shown in table 4.5. The CHP for each mesh is shown in figure 4.39.

Grid Size (mm)	No. of Cells S = 1.17	No. of Cells S = 3.27	No. of Cells on the Inlet face	No. of Tries per cell
2.5	946713	1657219	164	205
3.0	590301	997058	124	403
4.0	282831	477061	72	694
5.0	138009	241577	42	1190
6.0	81794	137161	36	1389

Table 4.5: Acceptable number of particles for an error of $< 1\%$ *in mean travel time*

The solution was converged as per the structured meshes (residuals $< 1 \times 10^{-5}$), under steady conditions. The k-ϵ Realizable model was used to represent turbulence due to its performance in the unstructured validation cases. The number of cells on the inlet mesh face, (hence the number of particles required to comply with section 4.2.1.3) is shown in table 4.5. This maintains a level of accuracy across the 'solute' based testing. A time scale constant of 0.10 was used as for the structured k-ϵ Realizable cases. The least dense meshes (i.e. 6 mm spacing) were considered first.

4.4.2 Flow Fields

Inspection of the CHP velocity field showed that, at the lowest mesh resolutions (6 mm and 5 mm) the asymmetric nature of the flow field did not develop, despite the convergence criteria being met. Figure 4.40 shows a comparison between the flow field at 4 mm and 5 mm (under low surcharge conditions, S = 1.17), where the asymmetric jet can be seen only in the 4 mm case. Under high surcharge conditions (S = 3.27, figure 4.41) the dominant jet was well represented (even at the largest mesh spacing, 6 mm). This showed the low surcharge (below threshold) condition to be critical whilst evaluating mesh density.

It was not possible to draw any further conclusions by inspection alone as the more highly resolved flow field results were very similar. Therefore, solute testing was carried out.

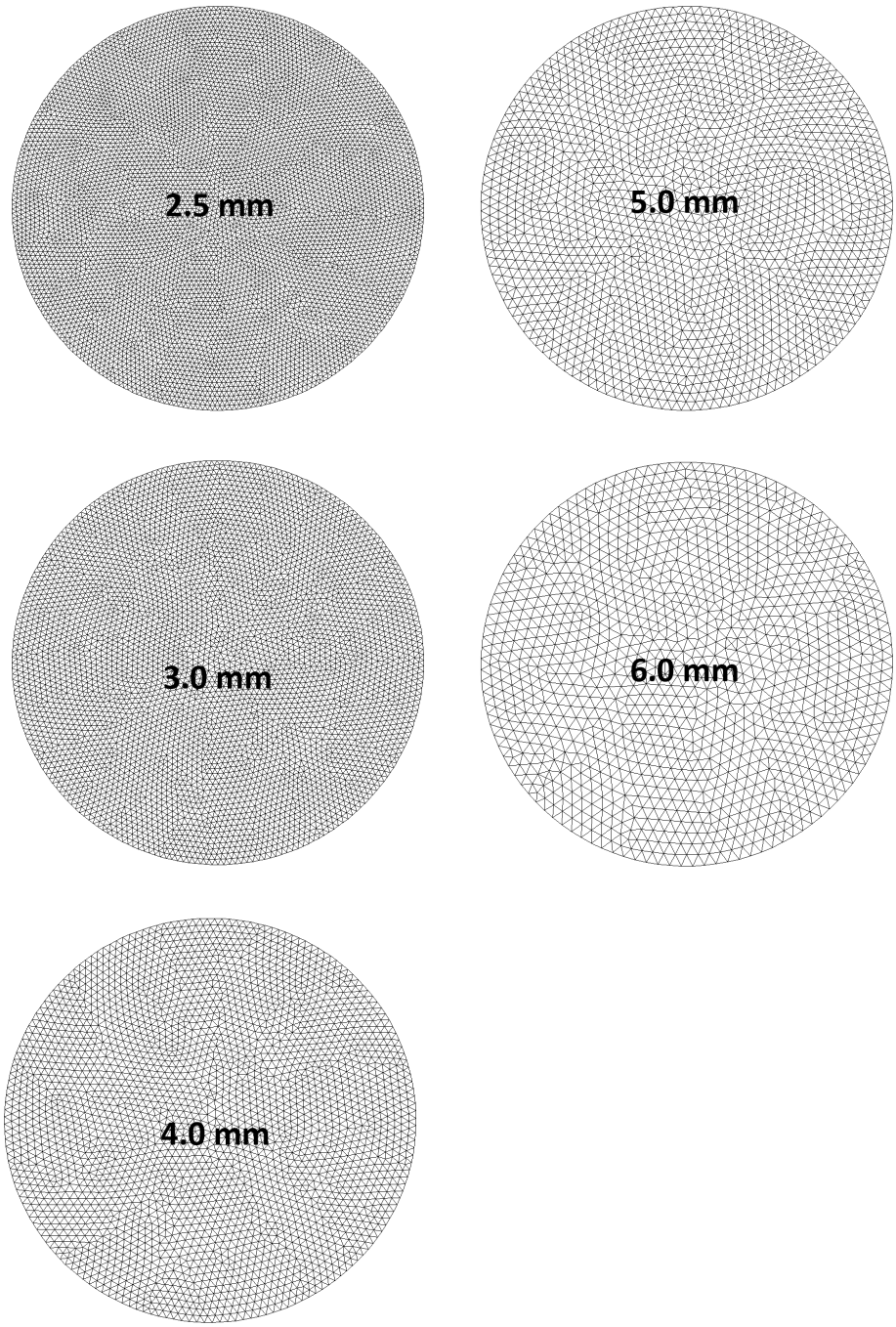

Figure 4.39: Unstructured tgrid meshes shown for the model top (for each grid size considered)

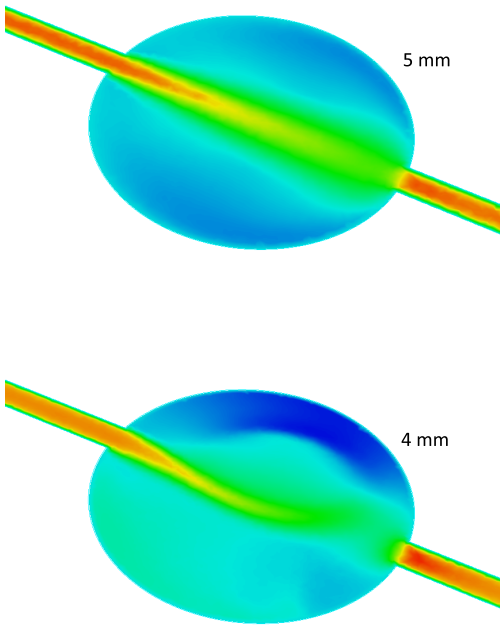

Figure 4.40: Contours of velocity on the CVP for the 5 mm and 4 mm grid interval under low surcharge (S = 1.17) conditions. The asymmetric nature of the expected flow field can only be seen in the 4 mm case

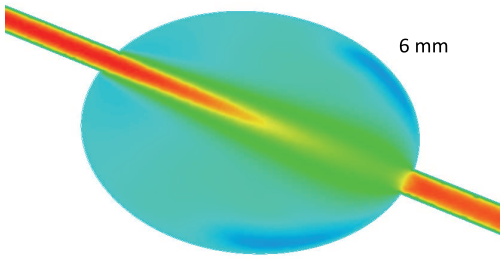

Figure 4.41: Contours of velocity on the CVP for the coarsest 6 mm grid interval evaluated under high surcharge (S = 3.27) conditions. The jet behaves as expected

4.4.3 CRTDs and Convolution

CRTDs were generated using the methodology described in section 4.2.1.4 (using the validated particle tracking methodology described in section 4.2.1.3). The number of particles input to each model complied with table 4.5 to maintain a level of accuracy in the discrete-phase solute modelling. Figure 4.42 shows the CRTDs for the mesh spacing considered further, all of which are in high agreement with the laboratory data (Lau, 2008) utilised to validate previous models.

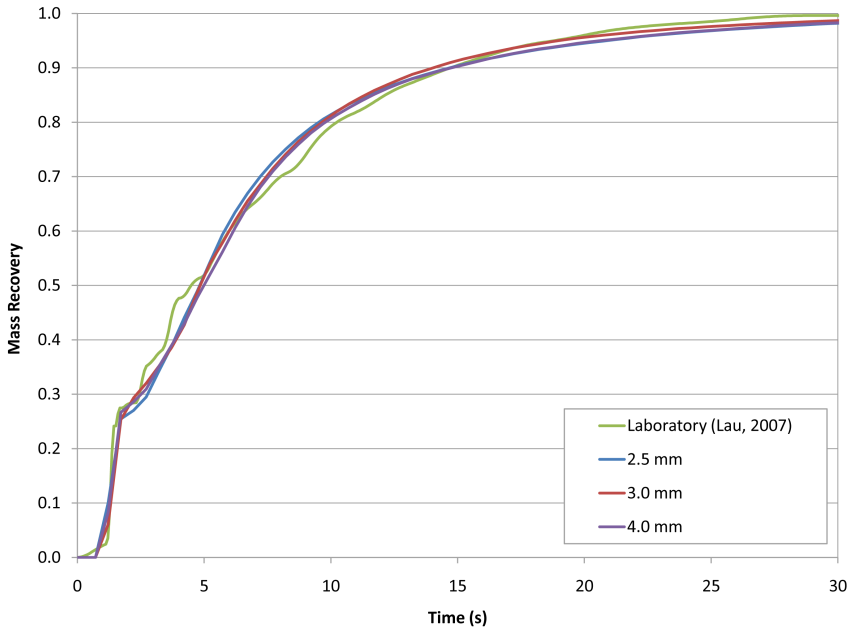

Figure 4.42: CRTDs for the low surcharge ($S = 1.17$) condition for mesh intervals capable of correctly displaying the asymmetric nature of the below threshold flow field, compared with laboratory data (Lau, 2008)

Using the CRTDs generated (for the low surcharge condition, deemed critical), a known (measured) upstream laboratory solute trace was convolved (Guymer and Stovin, 2011) to generate the downstream trace (as detailed in section 4.2.1.7), and compared to a known (measured) downstream laboratory trace (figure 4.43). The goodness of fit was then evaluated using R_t^2 (Young *et al.* (1980), table 4.6).

Table 4.6 suggests that all meshes evaluated are likely fit for purpose ($R_t^2 > 0.95$). However, the highest mesh resolution returns the lowest goodness of fit with with laboratory data. Once again, this can be linked with the appearance of an obvious secondary peak, not evident in the laboratory data. In more recent laboratory

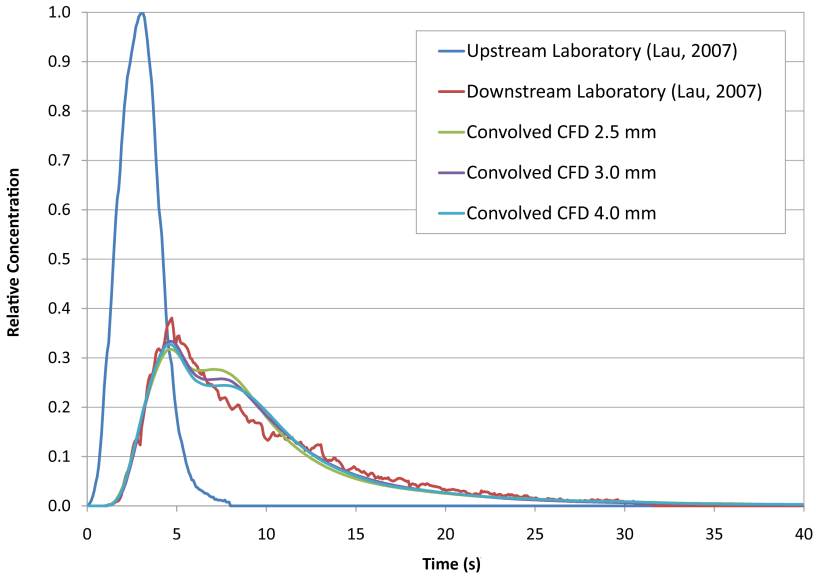

Figure 4.43: Convolved downstream traces for each grid interval capable of correctly displaying the asymmetric below threshold flow field compared to a measured laboratory trace (Lau, 2008)

Grid Size (mm)	R_t^2
2.5	0.974
3.0	0.983
4.0	0.980

Table 4.6: R_t^2 values for the mesh intervals capable of correctly displaying the asymmetric below threshold flow field

studies (Jones, 2012), this peak has been clearly identified. Jones (2012) found that it was necessary to add additional fluorometers surrounding the pipe (at equivalent monitoring locations, for a similarly configured manhole; D_M/D_p = 7.76) to achieve full mass recovery. This may explain the lack of secondary peak in the Lau (2008) laboratory data.

Standard practice for grid convergence is to go beyond the first appearance of a mesh-independent solution. This confirms that the solution has indeed stabilised and allows for a margin of error. Therefore, a mesh spacing of 3 mm was selected (rather than 4 mm) and the convolution process was repeated for the high surcharge (S = 3.27) condition (figures 4.44 and 4.45). Although figure 4.44 appears to show a relatively poor fit to the laboratory data (mainly in the tail portion of the CRTD), the convolved downstream trace (figure 4.45) is in high agreement ($R_t^2 = 0.994$).

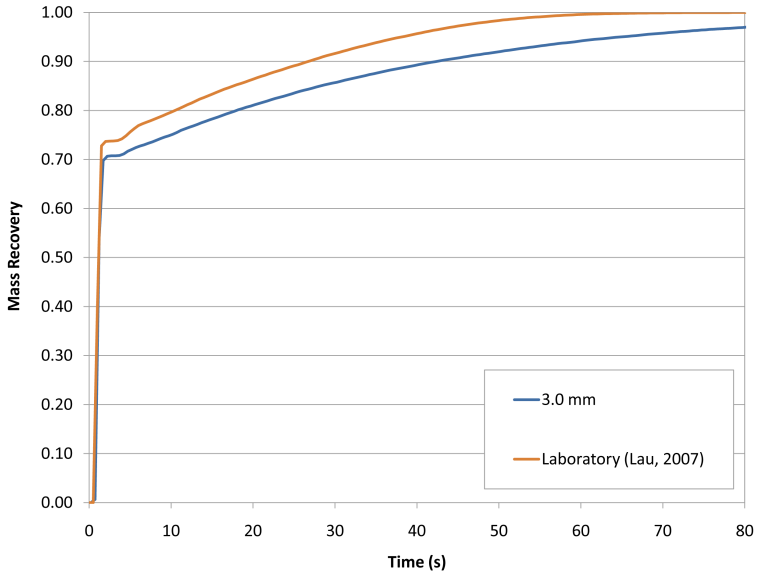

Figure 4.44: CRTDs for the 3 mm, high surcharge (S = 3.27) condition compared with laboratory data (Lau, 2008)

The structured models (based on Lau (2008) contained 300,000 and 500,000 cells (S = 1.17; S = 3.27) respectively. This is equivalent to an unstructured spacing of 4 mm. Thus, time gains in mesh generation, are lost in solution time. Despite this, unstructured meshing was adopted for further use due to its obvious advantages when meshing a large number of geometries (whilst still replicating laboratory solute trace data well under both surcharge conditions, $R_t^2 = 0.983$;

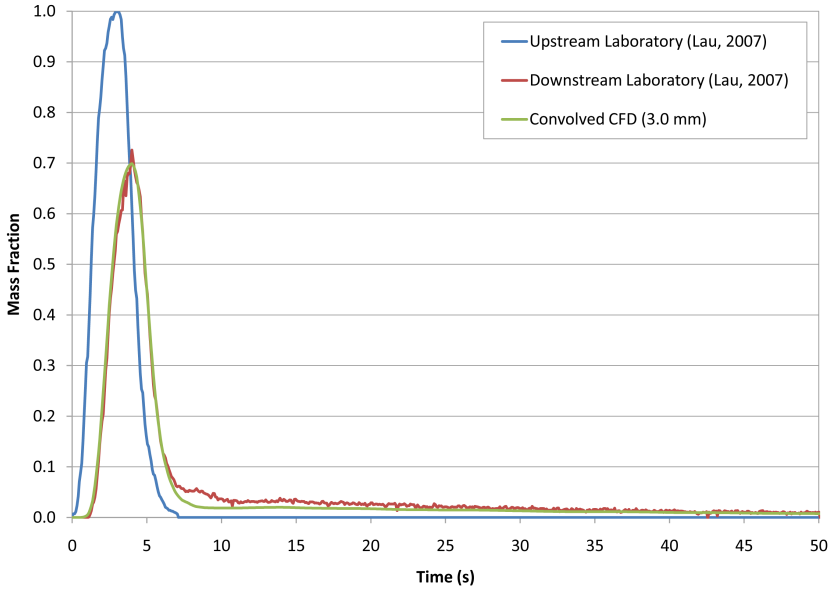

Figure 4.45: Convolved downstream traces generated using the 3 mm, high surcharge CRTD and laboratory data (Lau, 2008)

0.994 respectively). The structured meshes considered (after all sensitivity analysis, the results of which were applied to both mesh types) produced a comparable goodness of fit ($R_t^2 = 0.959$ and 0.997; S = 1.17, S = 3.27, respectively).

4.5 Conclusions

The k-ϵ Realizable turbulence model has been shown to reproduce laboratory based PIV flow fields and solute-trace derived CRTDs well under both surcharge conditions. It produced similar levels of agreement as the more computationally expensive RSM model (both models out-performed the k-ϵ RNG model used previously by Lau (2008)).

A large sample was used to determine the number of particles required for the stochastic Discrete Random Walk (DRW) model to return injection independent results. The results of which are shown in table 4.7.

The discrete-phase particle tracking model was chosen to model solute as its sensitivity to the Time Scale Constant (TSC) allowed for an improved goodness of fit with laboratory trace data (when convolved). Uncoupled particle tracking was

found to be roughly ten times more computationally efficient than the alternative species model.

An unstructured mesh independency study showed a grid spacing of 3 mm to be appropriate for producing mesh independent results.

Three VOF schemes were evaluated. The Geo-reconstruct scheme offered the sharpest air-water interface.

Structured fixed-lid and free-surface VOF (pseudo-steady) models were compared. The fixed-lid assumption was shown to be a valid way of representing the free-surface and ultimately offered better results for significantly less computational expense.

Table 4.7 contains a summary of the validated modelling parameters investigated and validated in this chapter. These settings will be used for all future manhole simulations considered by this study.

Parameter	Setting / Value
Mesh:	
Meshing Strategy	Unstructured, fixed-lid
Face Mesh	Tri-pave
Volume Mesh	Tgrid
Reference Face	Inlet
Inlet boundary	Velocity-inlet
Outlet boundary	Pressure-outlet
Top boundary	Wall (zero friction)
Wall boundary	Wall (Perspex)
Mesh interval	3 mm ($D_p/8$)
Skewness	< 0.85
Aspect Ratio	$0.45 \leq A_{ratio} \leq 1$
y^+ values	$30 < y^+ < 300$
Solver:	
Global Methodology	RANS
Pressure	PRESTO
Momentum terms	QUICK
Velocity-pressure coupling	SIMPLEC
Turbulence Model	k-ϵ Realizable
Gravity	Yes
Boundary wall roughness	0 m, 4×10^{-5} m
Near-wall treatment	Non-equilibrium wall functions (Kim and Choudhury, 1995)
Residuals	1×10^{-5}
Solute:	
Model	Uncoupled particle tracking
Discrete random walk	Yes
No. of particles	$> 45,000$
Particle density	998.2 kg/m^3 (as per water)
Particle size	1×10^{-6} (uniform)
Injection	from surface (inlet)
Max no. of steps	1×10^9 (maximum)
Time Scale Constant	0.10

Table 4.7: Validated parameters for meshing, solving and modelling solute in FLUENT manhole model simulations

Chapter 5

Further CFD Validation - Identification of the Threshold

5.1 Introduction

Chapter 4 presented a comprehensive approach to validating CFD manhole models, based on a combination of primary (flow field) and secondary (solute transport) validation. Primary validation was achieved through the direct comparison of modelled flow fields with laboratory PIV data originally collected by Lau (2008) in a 218 mm diameter laboratory manhole. This was done for two different surcharge depths, selected specifically because they were representative of the two contrasting hydraulic and solute transport regimes that have been previously observed in surcharged manholes. Secondary validation comprised comparisons between observed downstream solute traces and traces generated using simulated CRTDs derived from particle tracking.

Both the primary and secondary validation provided high levels of confidence in the CFD modelling protocol summarised in table 4.7. However, the validation only considered two specific surcharge depths for one specific flowrate for one size of manhole, 218 mm in diameter.

Previous studies (e.g. Stovin *et al.* (2010)) demonstrated two interesting phenomena associated with surcharged manholes:

- Normalised CRTDs have been shown to be independent of physical scale and flowrate;
- Solute trace data collected over a range of surcharge depths tend to exhibit a sharp transition between so-called pre- and post-threshold surcharge depths. This is indicated in the shape of the downstream trace and in various statistics that describe the mean travel time.

As was highlighted earlier (section 3.5.3) previous work has focused on manholes with unusually high D_M/D_p ratios, and the primary aim of this thesis is to utilise CFD modelling tools to explore the occurrence (or otherwise) of the hydraulic transition (or threshold) in lower (more realistic) D_M/D_p ratio manholes. However, before moving to these previously unconsidered configurations, it is appropriate to demonstrate that the CFD modelling tool can replicate these two key observations (scale-independence of CRTDs, and the identification of the hydraulic threshold) robustly.

For this, use will be made of new solute transport data generated within a parallel laboratory-based project undertaken at the University of Warwick (Jones, 2012). This project employed a 388 mm diameter manhole, effectively a scale version of the 800 mm and 218 mm manholes considered by Guymer *et al.* (2005a) and Lau (2008) respectively. The new set-up was expected to provide higher-quality solute transport data than the previous studies, and to generate new data corresponding to very low levels of surcharge and non-surcharged conditions. This project also generated new information on solute-transport in time-varying flows, which would have been deployed for validation of time-varying CFD models, had the decision not to proceed with this not been made during the feasibility phase of the current project (chapter 3).

In this chapter the steady-flow solute transport data collected by Jones (2012) will be used to provide confidence that the validated simulation tool is capable of generating normalised CRTDs that are comparable with the laboratory data, and that it is feasible to unambiguously identify the threshold depth from the CFD data. Section 5.2 provides a brief description of the laboratory system and explains how the CFD model was used to recreate the wide range of experimental surcharge depths and flowrates (30 independent configurations). Section 5.3 explains how the normalisation procedure was applied to generate CRTDs that

may be considered to be scale and flowrate independent. In section 5.4 the normalised CFD-derived CRTDs are presented and a discussion of their variation with respect to surcharge is provided. Section 5.5 explains the method adopted to determine the threshold depth from the CRTDs, and compares the CFD-based values with those determined in the laboratory.

5.2 388 mm Manhole

The experimental facility, shown in figure 5.1, *'comprised a 388 mm internal diameter un-benched Perspex manhole with vertically and horizontally aligned 50 mm internal diameter Perspex inlet and outlet pipes. The inlet and outlet pipes ran flush with the base of the manhole and were horizontal along the full 6.1 m length of clear acrylic pipework. The depth of water in the manhole was controlled with a sluice gate situated 2.9 m downstream of the manhole exit, allowing low and high-surcharge regimes to be studied at specific flow rates.'* Jones (2012).

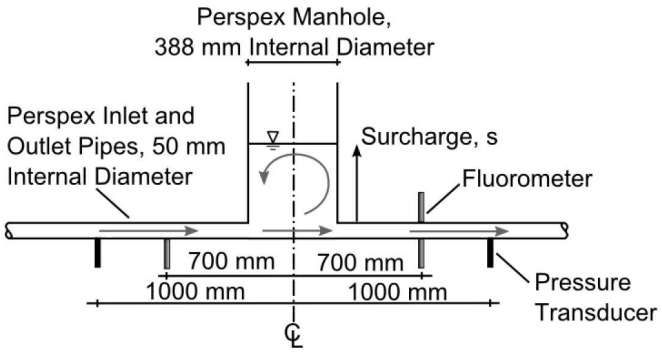

Figure 5.1: A schematic of the 388 mm diameter manhole laboratory set-up used by Jones (2012)

To save computational time it is unnecessary to model the laboratory set-up outside of the fluorometer positions. Therefore, (as in the unstructured 218 mm manhole models, section 4.4) two cylinders were intersected (the origin of the model was set as the centre of the manhole main volume, at mid pipe depth).

All mesh and solver conditions conformed to table 4.7 (effectively validated for a scale version of the 388 mm manhole). The number of cells on the inlet face was equivalent to that validated for similar velocity gradients in table 4.1. Fixed-lid meshes and converged solutions were generated for surcharge levels between S =

0.1 and S = 3.5 (s = 5 mm and s = 175 mm respectively, figure 5.2). For this manhole (D_M= 388 mm), the hydraulic threshold (s' = 0.258 D_M) is approximately equivalent to S = 2 (s = 100 mm). Therefore a wide range of surcharge conditions (above and below threshold) was modelled (figure 5.2). Three flow-rates (considered by Jones (2012)) were modelled for each surcharge condition, Q = 0.472 l/s; 0.972 l/s and 1.323 l/s.

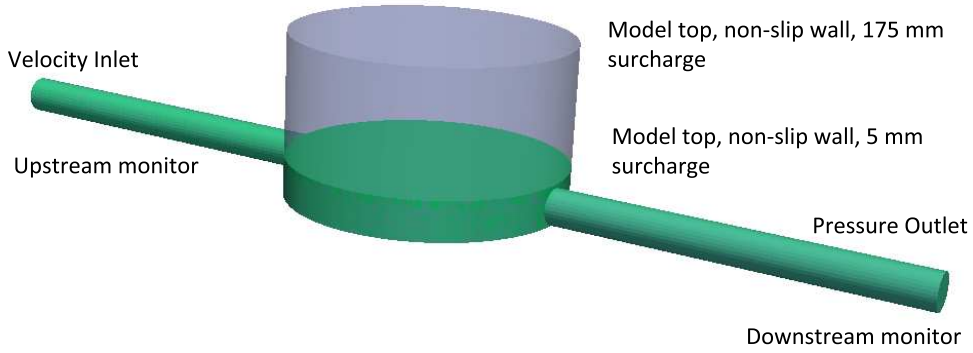

Figure 5.2: A schematic of the CFD geometry used to represent the 388 mm manhole investigated by Jones (2012) across the full range of surcharges considered

5.3 Normalisation Procedure

Thus far, only one flow-rate has been considered (chapter 4). However, in order to compare the three flow-rates first presented by Jones (2012) it is necessary to normalise the CFD solute transport results. This is undertaken as a three step process and is shown for the 388 mm manhole in figure 5.3.

Firstly, the RTD is gained via discrete-phase particle tracking (figure 5.3a). Secondly, a mean flow velocity assumption is made about the pipe sections of the model and the relevant travel time is deducted (figure 5.3b). This modified RTD is then normalised with respect to the nominal travel time of the manhole volume (V/Q, figure 5.3c).

Processing the data in this manner causes the RTDs (and CRTDs) to collapse into families of curves for each discharge. However, Guymer and Stovin (2011)

found CRTDs normalised in this way to be dependent of surcharge depth (i.e. exhibiting transitional behaviour); greater mixing was associated with the highest levels of surcharge below the hydraulic threshold. Above the hydraulic threshold the amount of short circuiting increased with surcharge depth. The CRTDs normalised using this procedure are presented and evaluated in section 5.4.

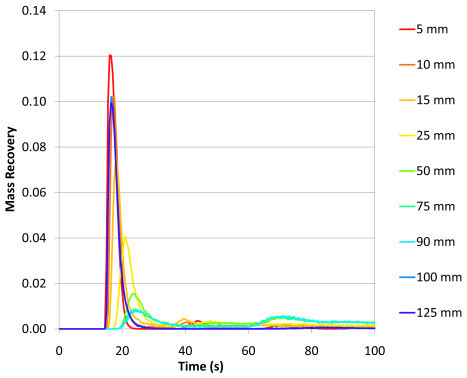

(a) RTDs for the 388 mm manhole

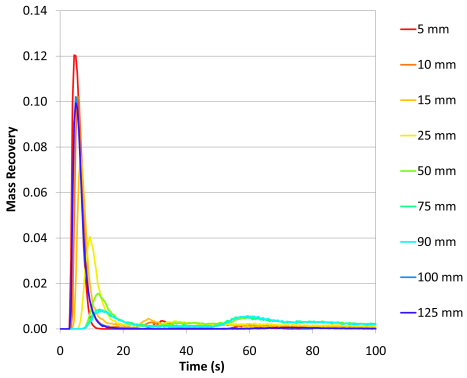

(b) RTDs for the 388 mm manhole with contributing pipe travel time removed

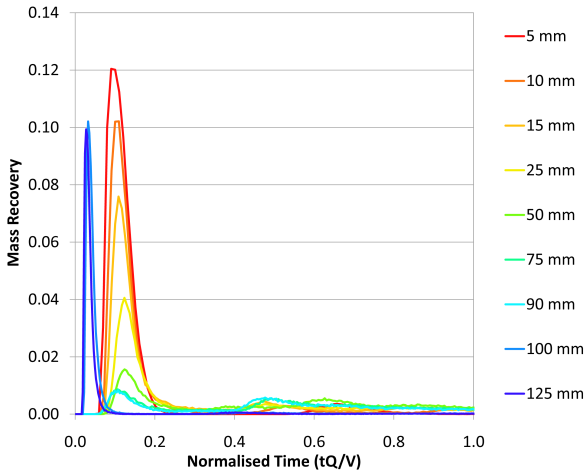

(c) RTDs for the 388 mm manhole with contributing pipe travel time removed, normalised using the nominal travel time (V/Q)

Figure 5.3: Normalisation procedure shown for the 388 mm manhole

5.4 CRTDs

Lau *et al.* (2008) proposed that the scale-independent solute transport behaviour

of manholes can be characterised by just two dimensionless CRTDs (normalised by the nominal residence time, equation 2.4.9); one for pre-threshold (low surcharge) and the second for post-threshold (high surcharge) hydraulic conditions. Normalised CRTDs for the 388 mm manhole (Q = 0.472 l/s, 0.972 l/s and 1.323 l/s) are shown in figures 5.4 to 5.6. As described by Guymer and Stovin (2011) clear grouping of curves can be seen. Under very low surcharge conditions (s = 5 mm, 10 mm) an above-threshold characteristic CRTD shape can be seen (this trace shape is out of character with previously described 'below threshold' behaviour, and is considered further in section 6.3.6). As surcharge increases (s = 15 mm, 25 mm, 50 mm, 75 mm) this systematically decays into the characteristic below threshold curve as presented in Guymer and Stovin (2011). At high surcharge (above threshold, s = 90 mm, 100 mm, 125 mm, 175 mm) levels, the CRTDs return to an above-threshold shaped curve.

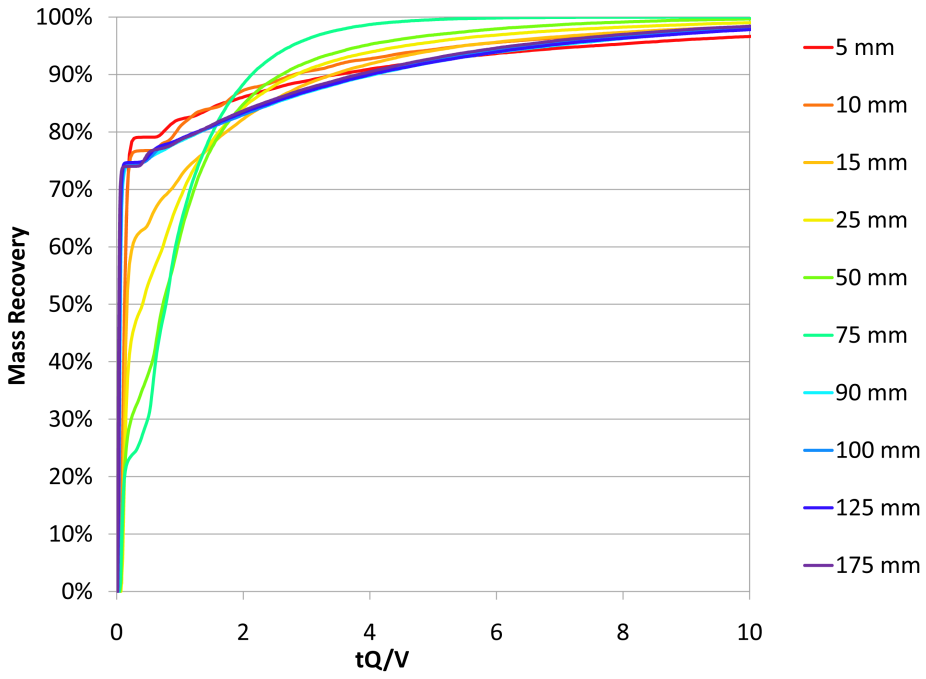

Figure 5.4: Normalised CRTDs for the 388 mm diameter manhole, Q = 0.472 l/s for the full range of surcharge conditions considered

It can be seen that the normalised CRTDs are independent of flow-rate, i.e. the same patterns are repeated in figures 5.5 and 5.6 for the two higher flowrates.

In order to integrate the solute transport behaviour of manholes within 1D models such as Infoworks, the procedure of identifying a change in hydraulic regime needs

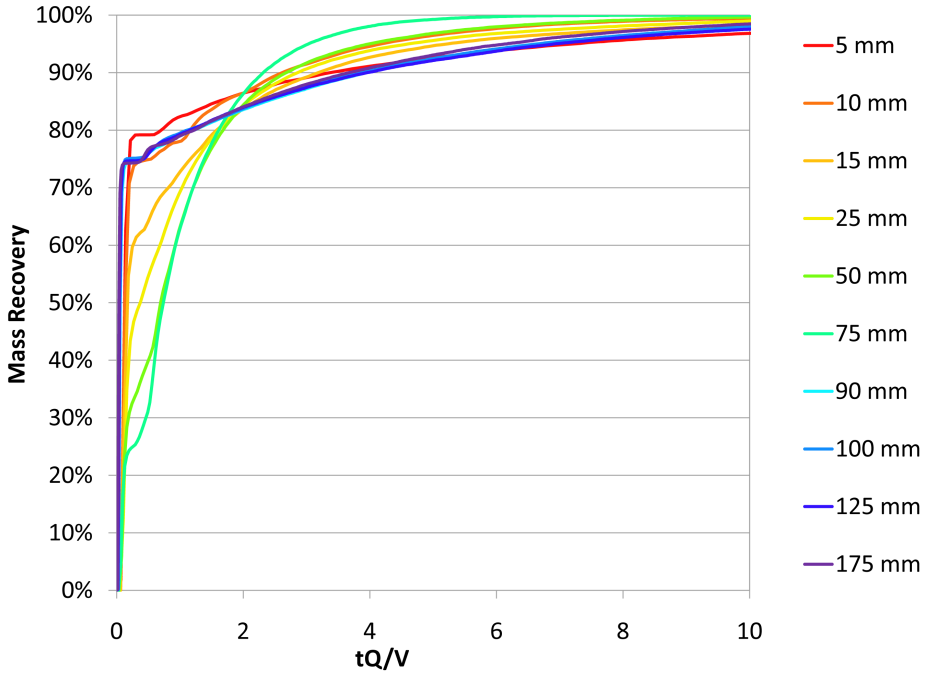

Figure 5.5: Normalised CRTDs for the 388 mm diameter manhole, Q = 0.972 l/s for the full range of surcharge conditions considered

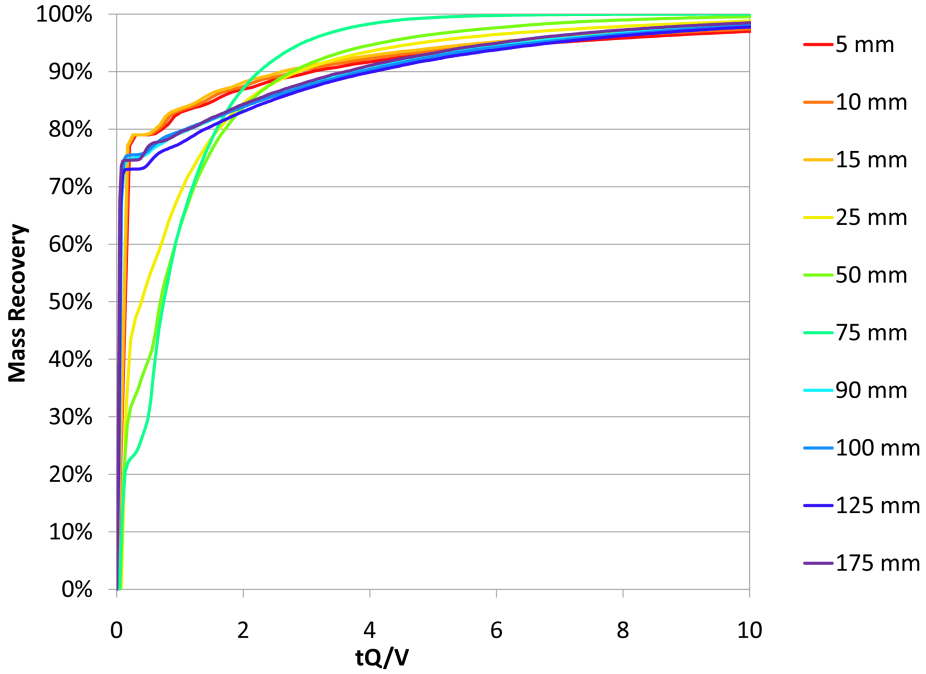

Figure 5.6: Normalised CRTDs for the 388 mm diameter manhole, Q = 1.323 l/s for the full range of surcharge conditions considered

to be automated. At this stage identification of the threshold relies solely on a (qualitatively-defined) change in the characteristic shape of the CRTD curves. By examining figures 5.4 to 5.6 the hydraulic threshold is located in this way between 75 mm and 90 mm surcharge (s = 0.19 D_M, s = 0.23 D_M, a lower level of surcharge than that identified by Guymer and O'Brien (2000)). The following section aims to identify a method for locating the threshold which is less reliant on subjective judgement.

5.5 Identifying the threshold location

5.5.1 Travel Times

Guymer and O'Brien (2000) used mean travel time ($\overline{t_2} - \overline{t_1}$) as an indicator of the hydraulic threshold. It could be seen that in low surcharge conditions the travel times increased up until a point (the hydraulic threshold) where they returned to a constant, low level. Therefore, the travel times were investigated as an objective means for locating the hydraulic threshold. However, figure 5.7 clearly shows no indication of the hydraulic threshold evident in the CRTDs. It is thought this is due to the discrete phase particle tracking model capturing the entirety of the modelled solute trace and therefore flattening the travel time/surcharge relationship. Large re-circulations cause a long tail and hence skew the mean travel time results towards the tail portion of the CRTD. Previous laboratory tests (Guymer and O'Brien, 2000; Lau, 2008 and Jones, 2012), all involved 'cut off' techniques to determine when the concentration of solute tracer (Rhodamine) fell below that of either the noise level or a percentage of the peak concentration, and hence failed to capture the entirety of the solute traces input.

5.5.2 Percentiles

Due to the findings of section 5.5.1, percentiles were investigated as an alternative means of locating the hydraulic threshold. Examining the normalised CRTDs (section 5.4) it can be seen that one of the main point of differences between the CRTD shapes is the initial mass recovery. Therefore, t_{10}, t_{20}, t_{30}, t_{40} and t_{50} were

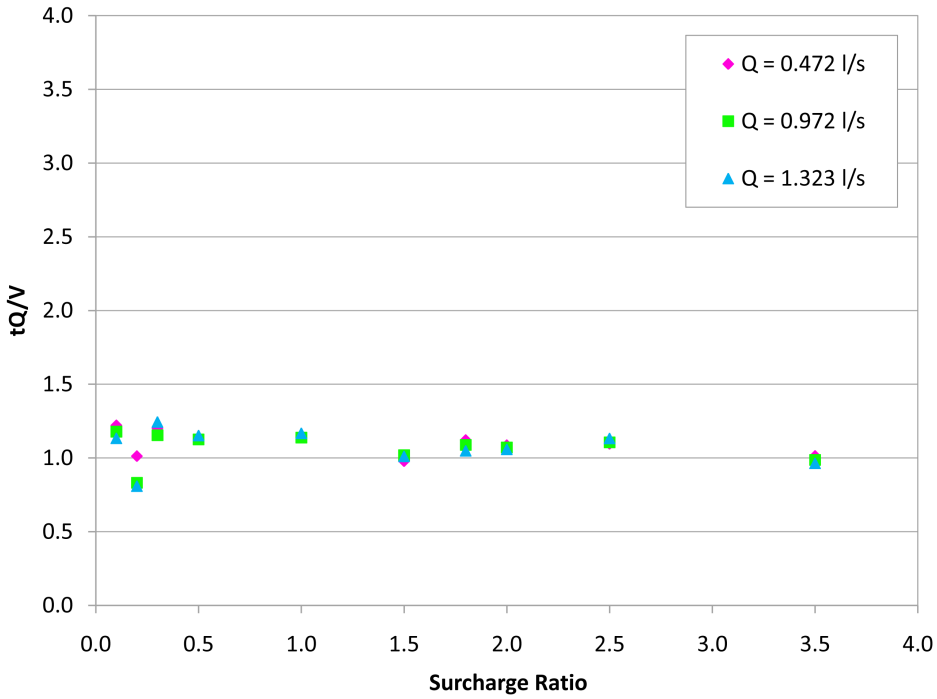

Figure 5.7: Travel times for the three flow-rates considered (Q = 0.472, 0.972 and 1.323 l/s) within the 388 mm diameter manhole

investigated for use in identifying the threshold location (in the D_M = 388 mm manhole, Q = 0.472 l/s), figure 5.8.

Figure 5.8 shows that t_{30}, t_{40} and t_{50} residence times clearly identify the existence of a hydraulic threshold (a large 'step'). These percentiles confirm findings by Guymer and O'Brien (2000). The $t_{30,40,50}$ times increase linearly as surcharge increases before returning to a low, constant level. The hydraulic threshold is located between 75 mm and 90 mm surcharge (s = 0.19 D_M, s = 0.23 D_M). This 'step' is most obvious using t_{50} as an indicator. Therefore, normalised t_{50} values were used to evaluate the CFD model's performance compared with laboratory data.

5.5.3 Threshold identification in the 388 mm manhole

Normalised t_{50} values were generated from discrete phase particle tracking results using the normalisation procedure detailed in section 5.3. These were then calculated for laboratory results recorded by Jones (2012) and are compared against

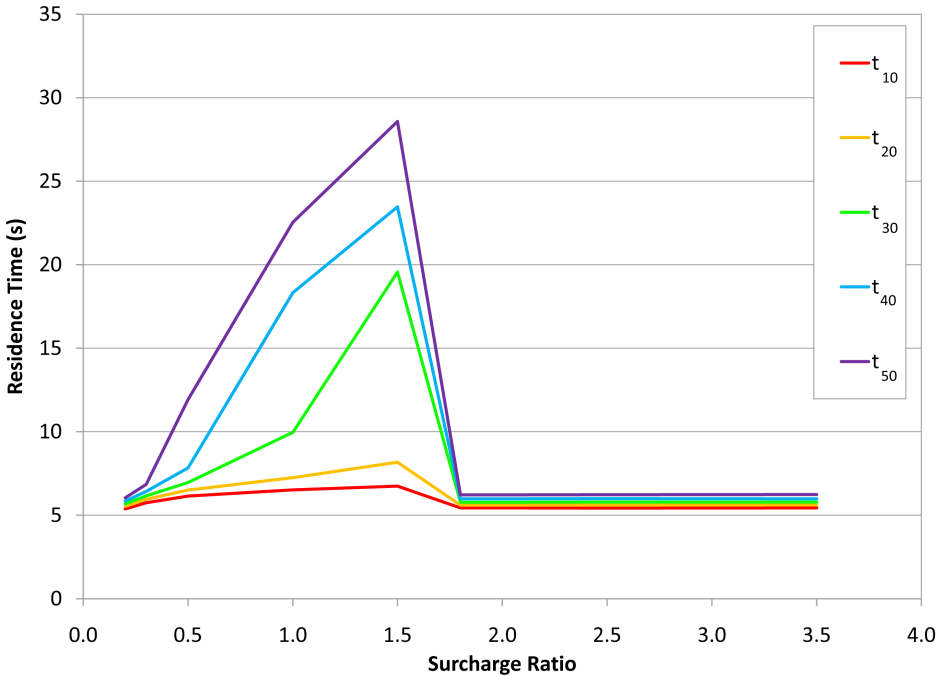

Figure 5.8: Residence times of percentiles considered as potential indicators of the hydraulic threshold (Q = 0.472 l/s)

the CFD data in figure 5.9a. Limits on the upper (0.258 D_M) and lower (0.2 D_M) boundaries for the threshold location suggested by Jones (2012) are also shown.

The CFD results show all flow-rates to collapse well. The CFD determined hydraulic threshold is also within the bounds suggested by Jones (2012). Both sets of results show the t_{50} time to increase as surcharge levels approach that of the lower threshold boundary (0.2 D_M). In the below-threshold region, a large step in t_{50} times can be seen, after which they return to a low, constant level. At the greatest below-threshold surcharge depths, the CFD results exhibit a slightly higher degree of mixing than that of the lab data. Once again, this could be due to laboratory cut-off techniques; discrete-phase particle tracking allows for 100% mass recovery. Particles that recirculate for a long periods of time skew the CFD CRTD (and hence the t_{50} value) towards its tail. Laboratory experiments can not feasibly hope to achieve full mass recovery and thus small amounts of trace in recirculatory zones can be ignored (e.g. due to background concentration levels or noise).

Under high surcharge conditions the laboratory and CFD predictions are in strong agreement.

Despite localised errors (just below the hydraulic threshold) in the solute transport results it can be seen that the CFD model accurately represents a hydraulic threshold as per the Jones (2012) laboratory data. Figure 5.9b contains the 800 mm case upon which the 388 mm manhole is based (found by Guymer and O'Brien (2000) to exhibit the hydraulic threshold most clearly), and the 218 mm (scale) validation cases evaluated by Lau (2008). It can be seen that the Guymer and O'Brien (2000) results are in agreement with the 0.258 D_M originally suggested and exhibit similar behaviour to that shown in figure 5.9a.

5.6 Conclusions

This chapter has shown the validated modelling scheme presented in table 4.7 to be capable of replicating solute trace data in another manhole geometry under three flow-rates and multiple surcharge conditions.

A normalisation procedure has been presented that allows for the comparison of CRTDs generated under different flow conditions. It shows three clear groupings of CRTDs; very-low surcharge (detailed further in section 6.3.6), below the threshold and above the threshold.

Percentiles have been evaluated as a way of identifying the hydraulic threshold location. It was found that t_{50} best indicates the appearance of a hydraulic threshold. Therefore normalised t_{50} was used to compare the CFD results with those generated by Jones (2012).

The hydraulic threshold was identified between 0.2 D_M and 0.258 D_M which was in agreement with Jones (2012). However, this was shown to be lower than the 0.258 D_M suggested by Guymer *et al.* (2005a).

Minor discrepancies between laboratory and CFD solute transport results in the highest below threshold surcharge conditions have been attributed to laboratory cut-off techniques.

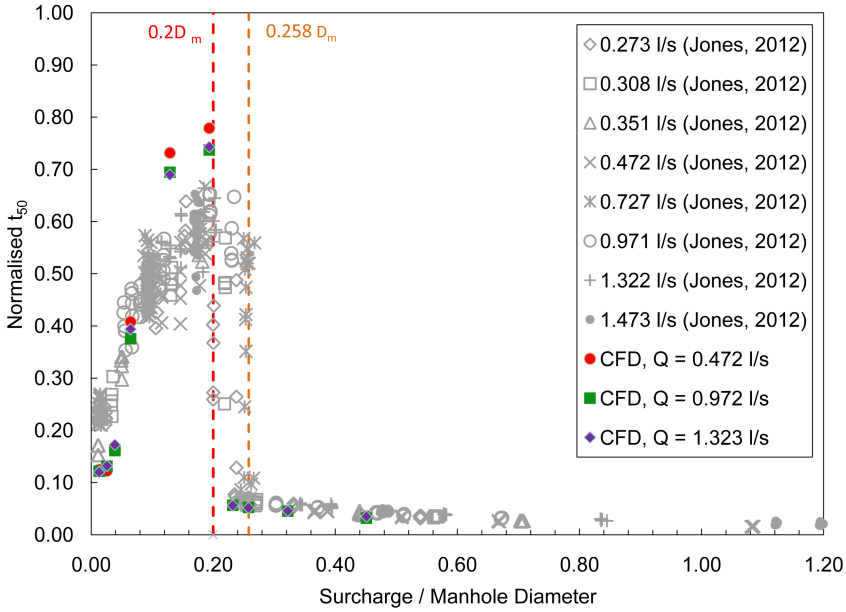

(a) Normalised laboratory (Jones, 2012) and CFD t_{50} results for the 388 mm manhole against surcharge/manhole diameter. Proposed upper and lower limits for the hydraulic threshold are shown.

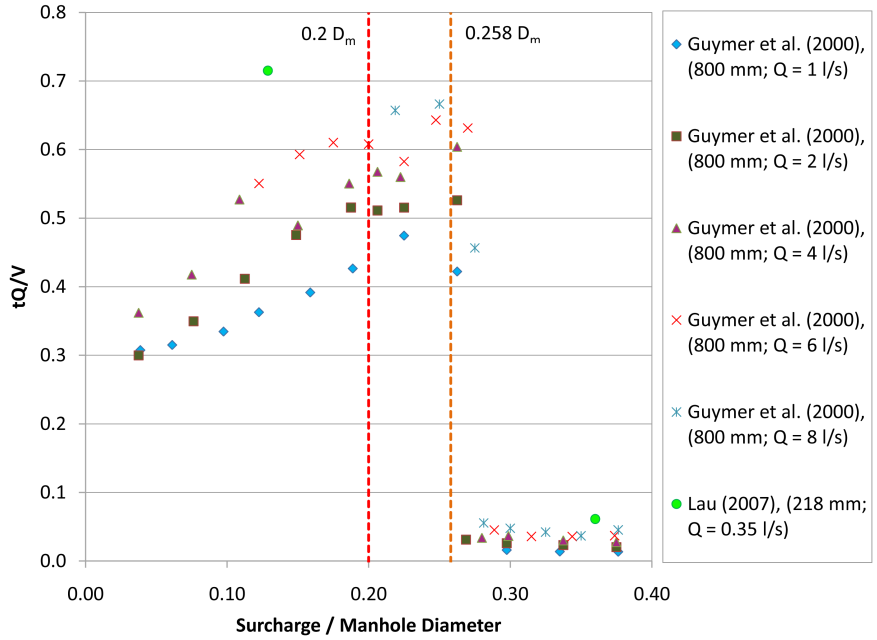

(b) Laboratory (Guymer and O'Brien (2000) and Lau (2008)) travel time results for the 800 and 218 mm diameter manholes (respectively) against surcharge/manhole diameter. Proposed upper and lower limits for the hydraulic threshold are shown.

Figure 5.9: Laboratory and CFD data identifying the threshold in the 218 mm, 388 mm and 800 mm manholes

Chapter 6

Identification of the threshold in low D_M/D_P surcharged manholes

6.1 Introduction

Guymer and O'Brien (1995) began investigating solute transport in manholes (section 2.6) in order to provide information that could be utilised by commercial sewerage system modelling software such as MOUSETRAP. The study aimed to quantify dispersion due to surcharged manholes. The effect of a number of different configurations was then covered in later work by Guymer and O'Brien (1996, 1998 and 2000), Saiyudthong (2003) and Guymer *et al.* (2005a). These studies investigated the effects of;

- diameter
- step height
- change in pipe direction
- benching

on the mixing processes within manholes. These studies were based upon laboratory tracer experiments carried out in physical scale models. Upstream of the manhole (far enough to allow the dye to become fully mixed) a tracer dye (such as Rhodamine) was injected into the flow. Fluorometers either side of the manhole rig (Figure 6.1) were then used in conjunction with data logging devices to record upstream and downstream temporal concentration profiles.

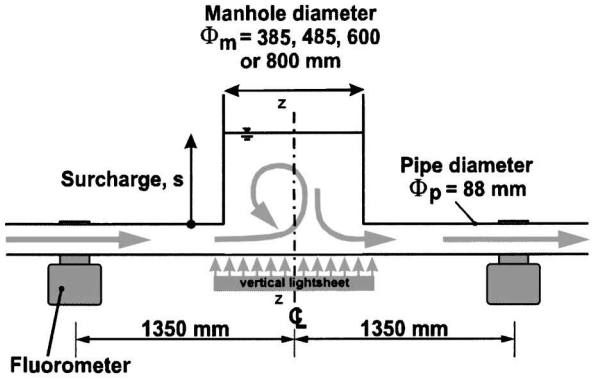

Figure 6.1: Laboratory setup used by Guymer and O'Brien (2000)

These profiles were then analysed using standard moment analysis as well as the ADE and ADZ models. Generally an optimization procedure first proposed by Dennis (2000) was used to determine model parameters. Model parameters determined using this optimization procedure *'were in better agreement than the results of the standard moment analysis'* (Dennis, 2000).

Guymer *et al.* (2005a) studied the effects of manhole diameter on longitudinal dispersion in surcharged manholes. Four unbenched manholes were considered with D_M/D_p ratios of 4.4, 5.5, 6.8 and 9.1 (these relate to manhole diameters of 385, 485, 600 and 800 mm with a fixed pipe diameter of 88 mm) under a wide range of surcharge conditions and flow rates.

The study identified a surcharge level at which the solute transport characteristic of the manholes sharply altered; at low surcharge (termed 'pre-threshold') the travel times varied linearly with surcharge, at high surcharge (termed 'post-threshold') the travel times dropped to a low, constant level. This threshold was more pronounced for the manholes with high D_M/D_p ratios. The existence of two distinctly different flow regimes was confirmed by Lau *et al.* (2007) using PIV techniques.

The optimised ADE and ADZ model coefficient results showed travel time, dispersion coefficients and dispersive fraction for models with the same discharge and surcharge conditions to increase with manhole diameter. This is in agreement with theory, as the manhole diameter increases, so too does the volume of water available for mixing.

The study determined sets of parameters for ADE and ADZ model coefficients, discharge and surcharge level for the four manholes used. It was suggested that, as per the original aim, these model parameters could be used in water quality models to improve temporal and spatial water quality predictions. However it was also noted that the laboratory results were limited to the range of configurations and hydraulic conditions used. Table 6.1 (adapted from 'Sewers for Adoption', Water Research Centre PLC (2006)) shows that the manhole D_M/D_p ratios investigated by Guymer and O'Brien (2000) may not be representative of those found in common sewer systems. The manhole D_M/D_p ratios shown in table 6.1 are all below the range considered by previous studies.

Largest pipe diameter (mm)	Manhole diameter (mm)	D_M/D_p
Less than 375	1200	Greater than 3.2
375 - 700	1500	4.00 - 2.14
750 - 900	1800	2.40 - 2.00
Greater than 900	Consult undertaker	NA

Table 6.1: Regularly encountered manhole sizings after 'Sewers for Adoption', Water Research Centre PLC (2006)

Albertson *et al.* (1950) showed that for a free jet, the core velocity is retained for a distance of $6.2D_p$, irrespective of pipe velocity (Figure 6.2). This equates to a distance of approximately 550 mm (with D_p= 88 mm), suggesting that for the larger manholes studied by Guymer *et al.*, *'assuming a free jet at the inlet, the core velocity would not be present at the outlet'*, (Guymer *et al.*, 2005a).

However, manholes with smaller D_M/D_p ratios (such as those shown in table 6.1) would retain the core jet velocity at the exit to the manhole. This may effect the strong asymmetric nature of the flow field below the hydraulic threshold ($0.258D_M$, Guymer *et al.* (2005a)). Figure 6.2 also shows the diffusion region of the jet. As Albertson *et al.* (1950) studied the discharge of a jet into an 'infinite volume' it is likely that the geometric constraints of the manhole will restrict the diffusion region.

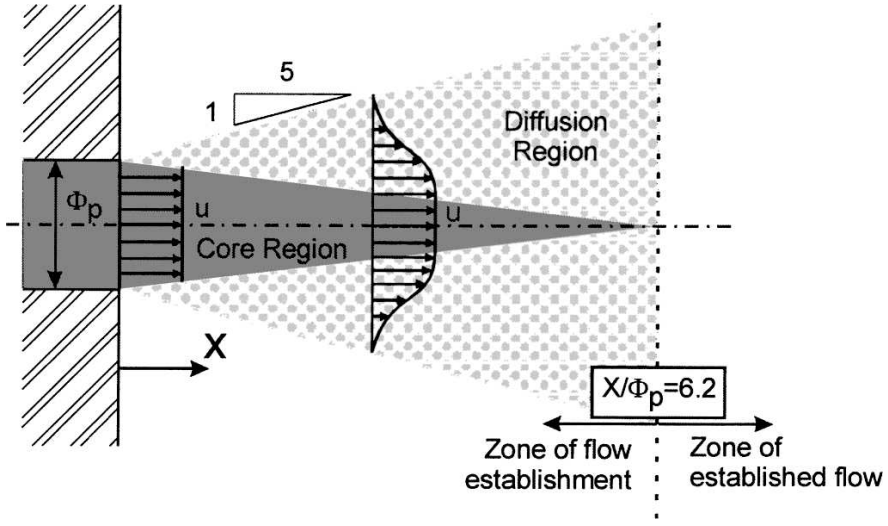

Figure 6.2: Velocity distribution and diffusion region in a circular free jet (after Albertson et al. *(1950))*

6.2 Methodology

Table 6.1 shows that the manholes considered by Guymer *et al.* (2005a) may not be representative of those found in real sewer systems. It is therefore necessary to investigate the effects of decreasing D_M/D_p ratios on the development of the two flow regimes. It is expected that below a ratio of $D_M/D_p = 6.2$ the high velocity core of the jet will be present at the exit to the manhole and that this will have an effect on the position or indeed appearance of the hydraulic threshold identified by Guymer *et al.* (2005a) and Lau (2008). Below $D_M/D_p = 5$ the diffusion region of the jet will also be constrained by the manhole geometry, likely effecting the flow conditions within the manholes.

6.2.1 Manhole Configurations

To investigate the effect of decreasing D_M/D_p ratios on the hydraulic threshold a range of new geometries need to be considered. However, initially by modelling the same configurations used by Guymer *et al.* (2005a) further validation into identifying the hydraulic threshold using CFD and of the validated modelling scheme detailed in chapter 4, can be gained.

By using a constant inlet pipe diameter (D_p) the meshing procedure and inlet

velocity profile can be simplified as these will remain the same (only requiring one velocity profile per flow rate). Guymer *et al.* (2005a) used D_p = 88 mm, therefore all new manhole configurations will be based around this, dictating the manhole diameters considered.

Below the D_M/D_p ratios investigated by Guymer *et al.* (2005a) further ratios of 3.5, 2.5, 2.0 and 1.5 were considered as well as the original ratios (9.1, 6.8, 5.5 and 4.4). To identify the presence of the hydraulic threshold within the different configurations it is necessary to model a wide range of surcharges. The surcharges investigated are shown in table 6.2 and cover a range from just above pipe full, s = 0.012 D_M, to s = 0.34 D_M. This upper limit is beyond the expected position (0.258 D_M) of the hydraulic threshold identified by Guymer *et al.* (2005a). All configurations modelled are shown in table 6.2.

6.2.2 Flowrates

Guymer *et al.* (2005a) investigated a range of flow rates from 1 l/s to 8 l/s. However, a large amount of scatter was present in the higher flow rates. The hydraulic threshold was most evident in the lowest flow rate (Q = 1 l/s) for all manholes investigated. Therefore, 1 l/s was chosen as well as a mid-range value of 4 l/s (which allows for the independency of threshold location and flow rate to be investigated). Due to the large number of configurations to be modelled, both flow rates were only used in the 800 mm manhole configurations.

6.2.3 Modelling Procedure

The validated modelling procedure set out in chapter 4 was used to generate fixed lid models of the manhole configurations detailed in table 6.2. A grid interval of $D_p/8$ was used for mesh generation (in accordance with table 4.1, for equivalent velocity gradients). This produced a set of converged flow solutions.

The converged flow field solutions were then inspected on both the Central Horizontal Plane (CHP) and Central Vertical Plane (CVP) for evidence of the hydraulic threshold (different flow regimes) for all surcharge conditions (examples are shown in section 6.3.1). It was then possible to use the validated particle

D_p (mm)	D_M (mm)	D_M/D_p -	Q (l/s)	s in mm for specific s/D_M ratios													
				0.012	0.025	0.038	0.080	0.130	0.155	0.180	0.190	0.200	0.220	0.270	0.293	0.327	0.340
88	800	9.1	1,4	10	20	30	64	104	-	144	-	160	176	216	235	661	272
88	600	6.8	1	7	15	23	48	78	-	108	114	120	-	162	-	-	204
88	485	5.5	1	6	12	18	39	63	-	87	92	97	-	131	-	-	165
88	385	4.4	1	5	10	15	31	50	60	69	-	77	-	104	-	-	131
88	308	3.5	1	4	8	12	25	40	-	55	-	62	-	83	-	-	105
88	220	2.5	1	3	6	8	18	29	-	40	-	44	-	59	-	-	75
88	176	2.0	1	2	4	7	14	23	-	32	-	35	-	48	-	-	60
88	132	1.5	1	2	3	5	11	17	-	24	-	26	-	36	-	-	45

Table 6.2: D_M/D_p manholes sizes and surcharges modelled

tracking methodology set out in section 4.2.1.3 to establish residence time distributions. Data from the particle tracking results was then analysed to first produce RTDs, CRTDs and finally normalised CRTDs allowing for more insight into the flow characteristics and any existence of a threshold. Results and analysis are shown in section 6.3.2

6.3 Results and Discussion

6.3.1 Flow Fields

Looking below the threshold, the converged flow field solutions were inspected on both the CHP and CVP for evidence of below-threshold behaviour for all surcharge conditions modelled per manhole. However, the majority of this data has been omitted for clarity. The results shown below are representative of the findings. The surcharge levels shown are in the region 'expected' to be below the hydraulic threshold ($s = 0.13\ D_M$).

Figures 6.3 (800 mm), 6.4 (600 mm), 6.5 (485 mm) and 6.6 (385 mm) clearly show the asymmetric flow field attributed to surcharge depths below the hydraulic threshold (previously termed 'pre-threshold'). In figure 6.7 the 308 mm manhole shows a slight deviation of the jet. However, the high velocity core passes directly to the manhole outlet, which is unlike the behaviour exhibited by the larger D_M/D_p manholes and suggests that the jet is partially restrained by the geometry of the manhole.

Figure 6.8 (200 mm), 6.9 (176 mm) and 6.10 (132 mm) show no obvious signs of an asymmetrical jet (below $D_M/D_p = 3.5$). The high velocity core of the jet passes directly towards the manhole outlet where the 'Vena Contracta' effect appears to be strong (containing the region of highest flow velocities). This suggests that the jet is fully restrained by the geometry of the manhole and the highly asymmetric (well mixed), below-threshold flow regime cannot be established.

As in section 4.4.2, the below threshold flow regime was deemed critical for identifying if the hydraulic threshold was present. As the D_M/D_p ratio decreases the flow field can be seen to tend towards that of the above threshold hydraulic con-

dition (dominated by short circuiting). Thus there is limited additional insight offered by the above threshold flow field results.

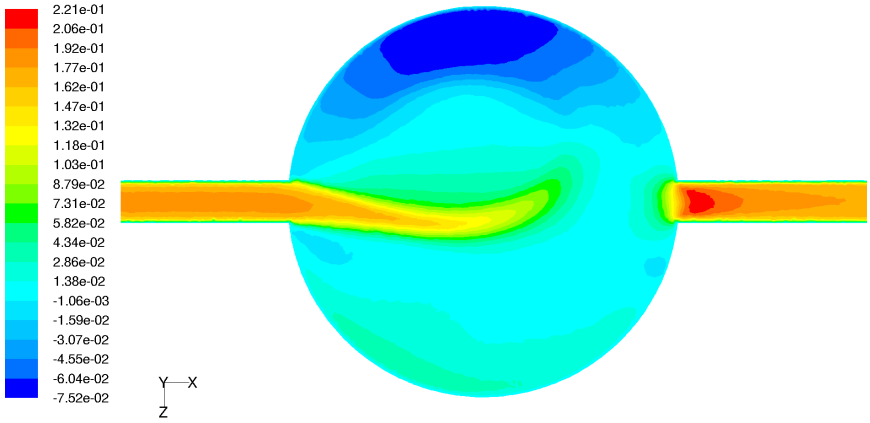

Figure 6.3: Contours of x-velocity, 800 mm diameter manhole, 88 mm diameter pipe, $D_M/D_p = 9.1$, $s = 0.13\ D_M$

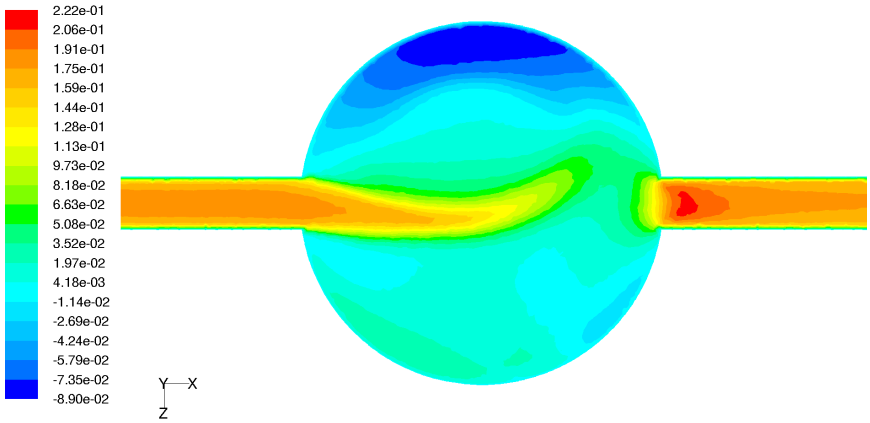

Figure 6.4: Contours of x-velocity, 600 mm diameter manhole, 88 mm diameter pipe, $D_M/D_p = 6.8$, $s = 0.13\ D_M$

6.3.1.1 Jet Direction

In the 485, 385 and 308 mm manhole flow fields (shown in Figures 6.5-6.7) the direction of the jet can be seen to differ from that of the other cases. Due to the unstructured nature of the mesh, it is not possible to ascertain whether this is due to the turbulence model or skewing based on the mesh. However, it is essentially random as shown in 4.2.1.4.

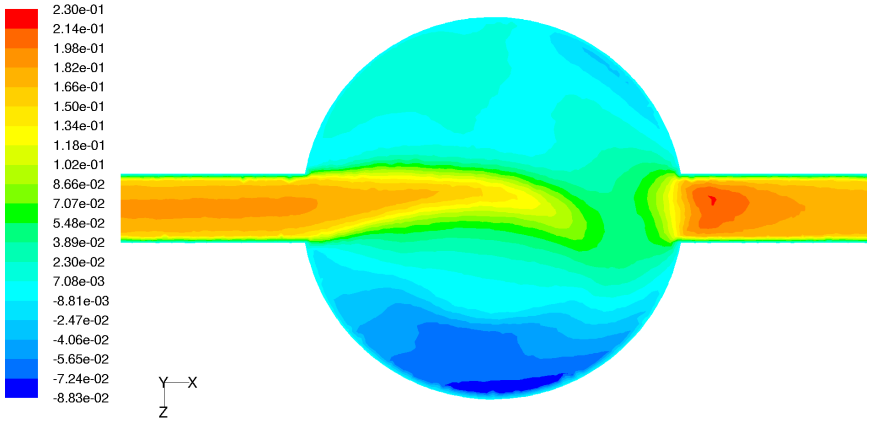

Figure 6.5: Contours of x-velocity, 485 mm diameter manhole, 88 mm diameter pipe, $D_M/D_p = 5.5$, $s = 0.13\ D_M$

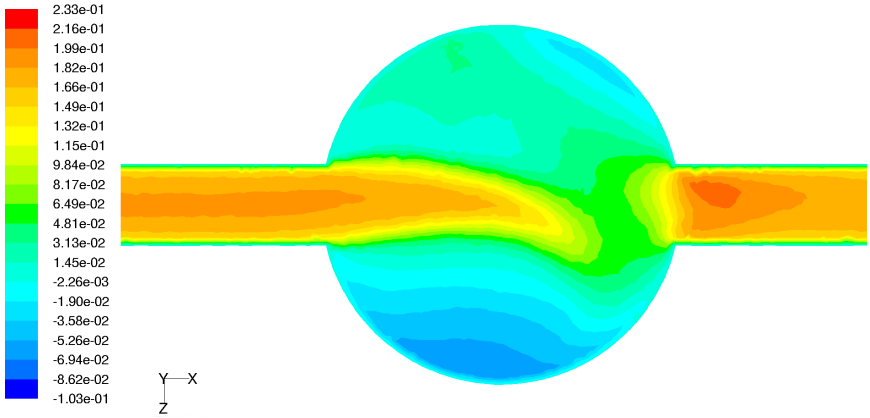

Figure 6.6: Contours of x-velocity, 385 mm diameter manhole, 88 mm diameter pipe, $D_M/D_p = 4.4$, $s = 0.13\ D_M$

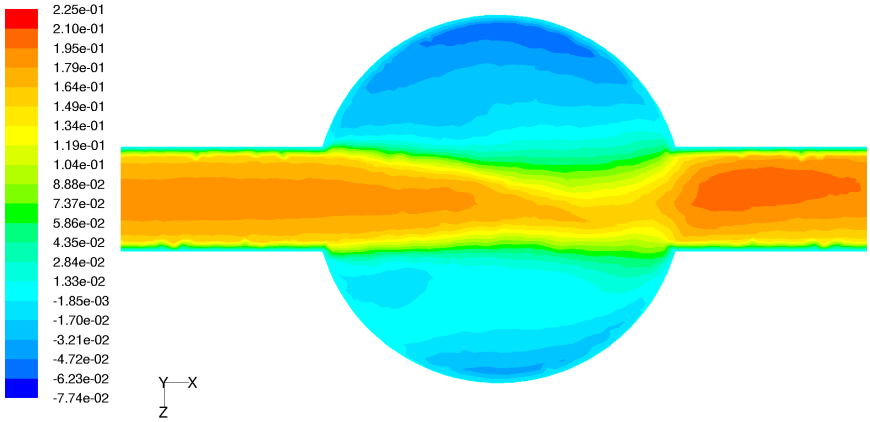

Figure 6.7: Contours of x-velocity, 308 mm diameter manhole, 88 mm diameter pipe, $D_M/D_p = 3.5$, $s = 0.13\ D_M$

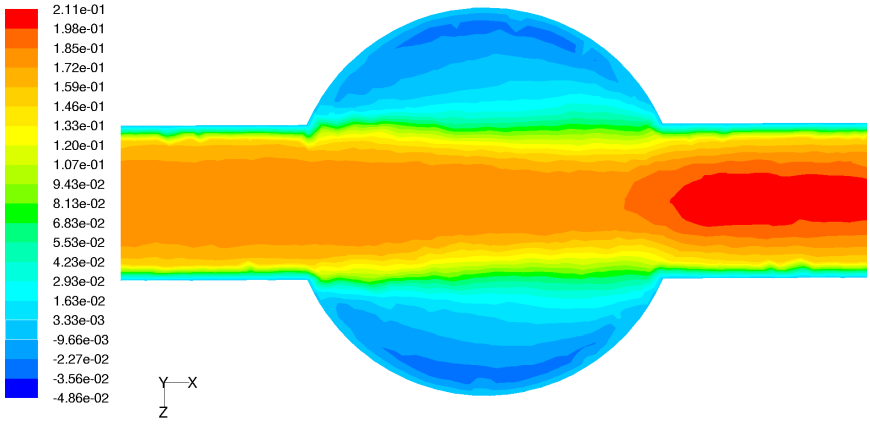

Figure 6.8: Contours of x-velocity, 220 mm diameter manhole, 88 mm diameter pipe, $D_M/D_p = 2.5$, $s = 0.13\ D_M$

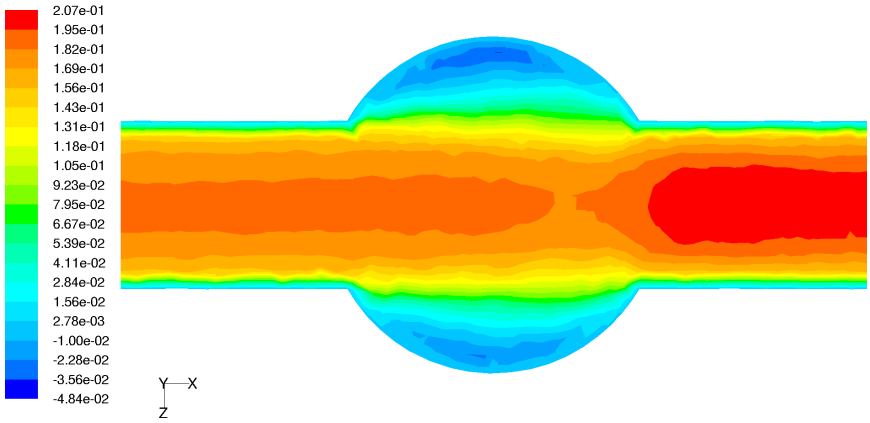

Figure 6.9: Contours of x-velocity, 176 mm diameter manhole, 88 mm diameter pipe, $D_M/D_p = 2$, $s = 0.13\ D_M$

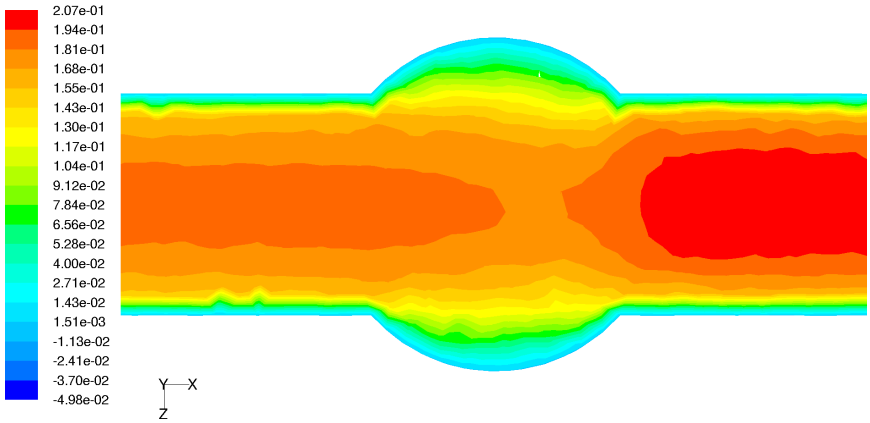

Figure 6.10: Contours of x-velocity, 132 mm diameter manhole, 88 mm diameter pipe, $D_M/D_p = 1.5$, $s = 0.13\ D_M$

6.3.2 RTDs and CRTDs

RTDs and CRTDs were produced using the discrete phase particle tracking methodology detailed in 5.3. More than sixty thousand neutrally buoyant particles were input into each model and their travel times recorded. This allowed for the rapid generation of RTDs and the respective CRTDs.

6.3.3 Normalised CRTDs

Considering all outcomes over the full set of surcharge depths, CRTDs were normalised with respect to the characteristic travel time for the manhole as detailed in section 5.3. The 176 mm and 132 mm ($D_M/D_p = 2$ and 1.5 respectively) manholes were not considered further as the flow fields presented in 6.3.1 exhibit no indicators of the hydraulic threshold.

The 800 mm manhole ($D_M/D_p = 9.1$) CRTDs presented in figure 6.11 show clear groupings of the previously identified flow regimes. At surcharge depths above the threshold (previously termed 'post-threshold') the CRTDs collapse well. However, below the threshold a systematic deviation of CRTD shape can be seen with the initial short circuiting indicated by the steep initial limb increasing as surcharge decreases (i.e. the least amount of short circuiting is evident with surcharge just below that attributed to the threshold). This is indicative of increased mixing within the manhole due to the highly asymmetric jet (shown in figure 6.3) and is in agreement with Guymer and Stovin (2011).

At very low surcharges (10-20 mm, not investigated by previous studies) a third grouping is present. Its characteristic CRTD shape is similar to that of the above-threshold flow regime. However, the steep initial limb (representing the short circuiting usually attributed to a dominant jet) is larger. This is followed by a 'stepped' gain in mass recovery (potentially due to a slight re-circulatory zone) and a long tail (usually indicative of a large dead-zone), similar to that of the above-threshold flow conditions.

The 600 mm manhole ($D_M/D_p = 6.8$) normalised CRTDs presented in figure 6.12 are similar to those of the 800 mm manhole. Clear grouping is evident above the threshold, with a systematic (transitional) deviation of shape below. The third,

very-low surcharge grouping is also present. However, it is arguably progressive.

The 485 mm manhole ($D_M/D_p = 5.5$) normalised CRTDs presented in figure 6.13 show similar behaviour to the 800 and 600 mm manholes. However, the steep initial limb of the CRTDs is always above 40% (double the minimum of the two prior examples). However, figure 6.3 does not show the high velocity core of the jet to be entering the manhole outlet.

The 385 mm manhole ($D_M/D_p = 4.4$) normalised CRTDs presented in figure 6.14 show evidence of the three groups (above-threshold, below-threshold and very-low surcharge) each indicative of their respective flow conditions. Once again, the initial mass recovery represented by the steep rising limb, is always greater than 50% which shows an increased short-circuiting effect with reduced D_M/D_p. This may be due to the decreasing volume available for full jet dissipation (Figure 6.2, $6.2D_p$, Albertson *et al.* (1950)).

The 308 mm manhole ($D_M/D_p = 3.5$) normalised CRTDs presented in figure 6.15 do not clearly show distinguishable grouping of the three regimes identified above. However, deviation of the CRTDs is systematic from high to very-low surcharge. The amount of short-circuiting has once again increased to greater than 70%. The corresponding flow field shown in Figure 6.7 shows the high velocity core of the jet to enter the manhole outlet, clearly showing it to be constrained by the geometry of the manhole itself. This is in agreement with the CRTDs presented.

The 220 mm manhole ($D_M/D_p = 2.5$) normalised CRTDs presented in figure 6.16 have very little difference in CRTD shape, which represents little difference in the flow fields relating to each CRTD. Initial mass recovery shown by the steep initial limb shows a similar amount ($> 80\%$) for all surcharge depths.

Further investigation and discussion of the flow condition described as 'very-low surcharge' within this section can be found in section 6.3.6.

6.3.4 Using t_{50} to define the threshold location

It was shown in section 5.5.2 that t_{50} can be used to locate a change in hydraulic regimes (i.e. a threshold). Guymer *et al.* (2005a) used travel times for a similar purpose. However, laboratory dye studies do not capture the entire input trace

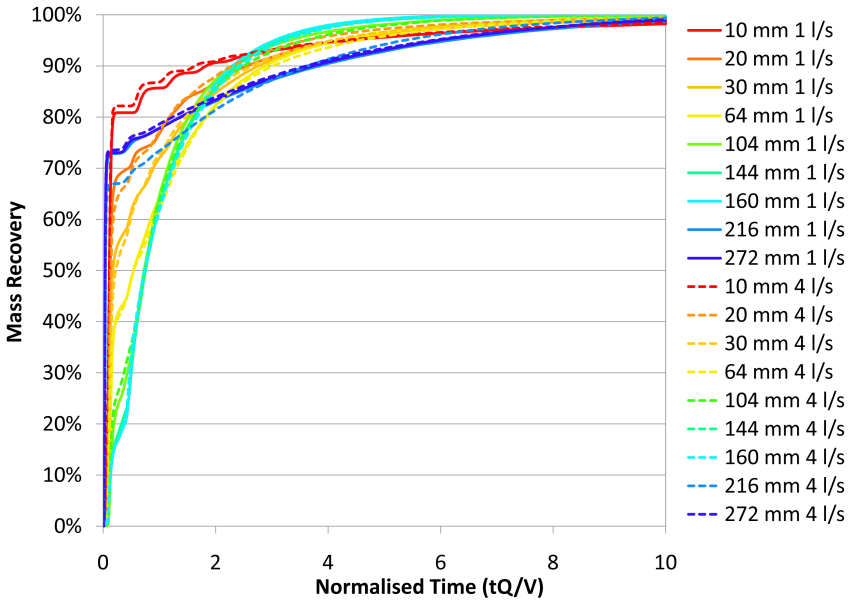

Figure 6.11: 800 mm diameter manhole normalised CRTDs

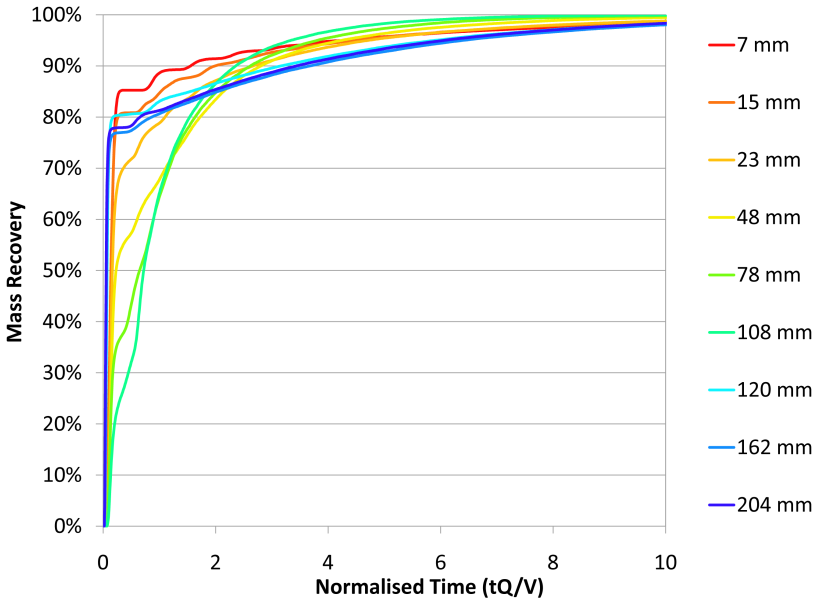

Figure 6.12: 600 mm diameter manhole normalised CRTDs

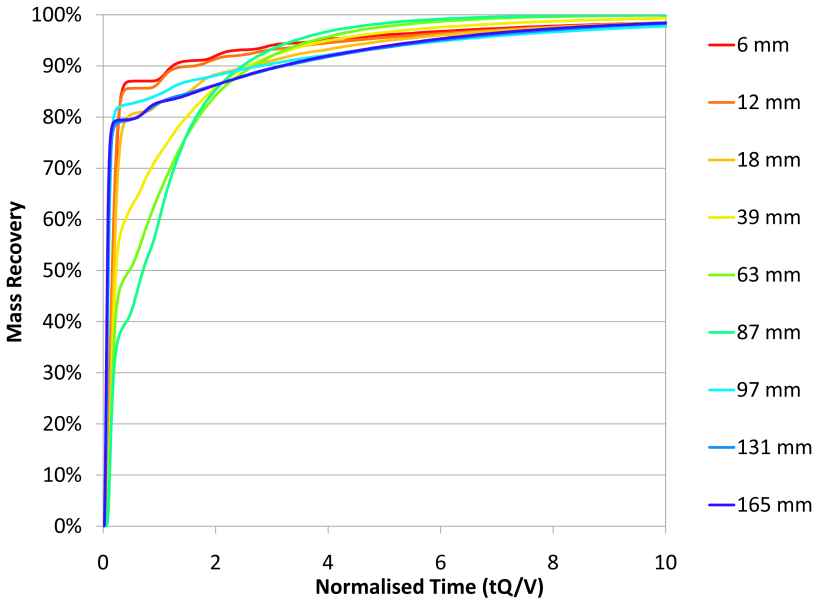

Figure 6.13: 485 mm diameter manhole normalised CRTDs

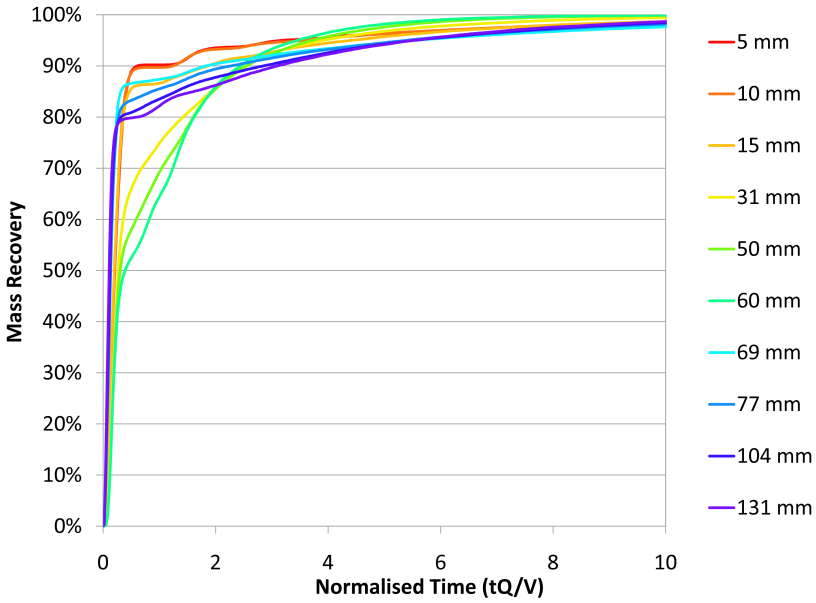

Figure 6.14: 385 mm diameter manhole normalised CRTDs

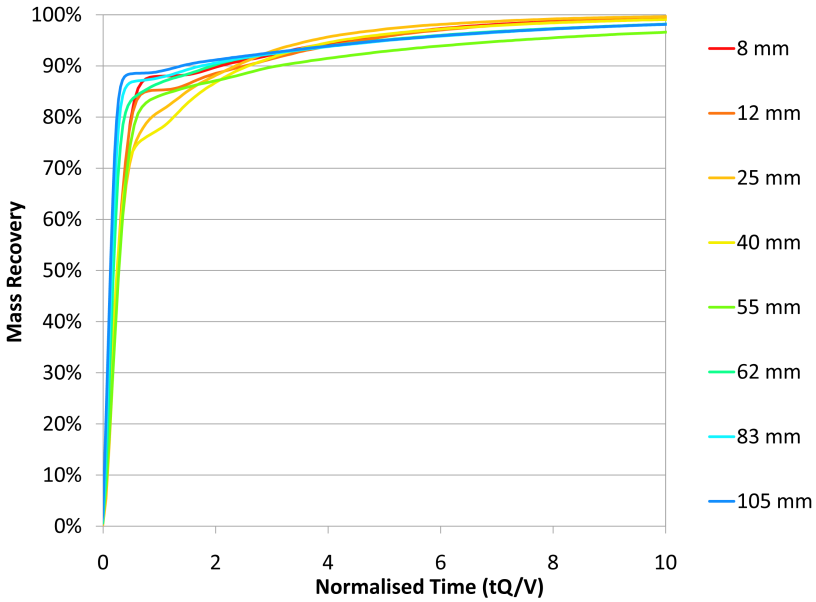

Figure 6.15: 308 mm diameter manhole normalised CRTDs

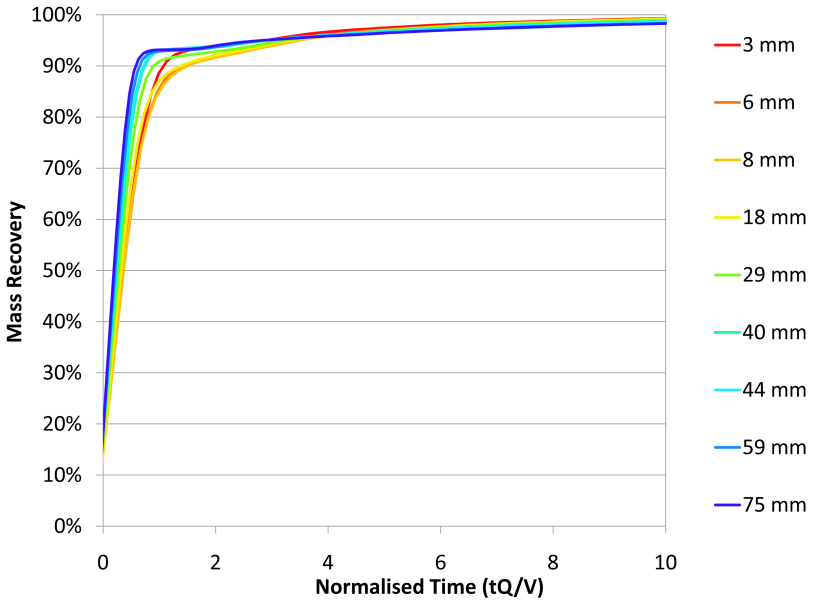

Figure 6.16: 220 mm diameter manhole normalised CRTDs

due to a combination of cut-off techniques and background fluorometer noise. CFD is capable of capturing the entire input trace (using particle tracking), thus mean travel times generated using this method are skewed towards the long tail of the trace, removing any indication of differing flow conditions between cases. Using t_{50} addresses this difference.

Figure 6.17 shows normalised t_{50} (section 5.3) against Surcharge Ratio (S). The 800 (Q = 1 and 4 l/s), 600, 485 and 385 mm manholes all exhibit a sharp step in normalised t_{50}s. These also exhibit the new hydraulic regime at very-low surcharge depths as indicated by the small amount of mixing present at the lowest surcharge depths. At these surcharge depths the t_{50}s are marginally greater than that of their corresponding high surcharge (above-threshold) counterparts. This may be down to a slight washing of the jet seen in laboratory tests.

Figure 6.17 shows that for the manholes that do exhibit a hydraulic threshold, the region below-threshold is transitional in nature (figures 6.20-6.23 show the flow field throughout this transitional zone an an 800 mm manhole). The 800 mm manhole shows a gradual transition from just below-threshold, steepening as the surcharge ratio decreases. The 600 mm manhole echoes this shape. However, the 485 mm manhole appears more linear in its variation. The 385 mm clearly shows the sharp step in t_{50} but its behaviour at below-threshold surcharge depths is similar to neither of the previous cases.

The 308 and 220 mm manholes do not exhibit a large step in t_{50} times, further confirming their lack of a hydraulic threshold (this is in agreement with sections 6.3.1 and 6.3.3). As the manhole volume available for mixing decreases (D_M/D_p decreases), the normalised t_{50} results tend towards that experienced by a pipe (i.e. plug flow).

Normalised t_{50}s for the 800 mm manhole are shown in figure 6.17 for both Q = 1 and 4 l/s. Results from both flow rates are nearly identical for all surcharge depths considered. This shows threshold location to be independent of flow rate.

The location of the threshold does not appear to be linked to a specific surcharge ratio (S, figure 6.17). Previously Guymer and O'Brien defined the threshold location as s' = 0.258 D_M. Therefore, figure 6.18 shows the relationship between normalised t_{50} and Surcharge / D_M. As before, the 800, 600, 485 and 385 mm manholes all show a large step in normalised t_{50}, whereas the 308 and 220 mm

manholes do not.

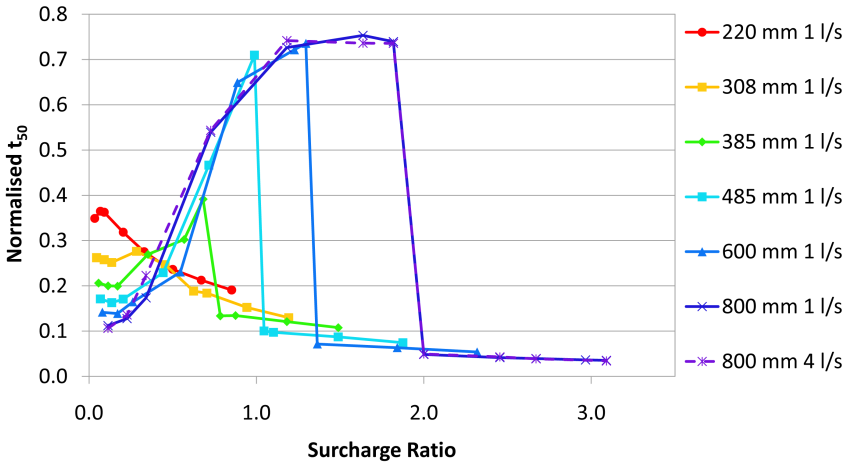

Figure 6.17: Surcharge ratio ($S = s/D_p$) shown against normalised t_{50}

The ratio at which the Albertson *et al.* (1950) 1:5 jet expansion theory would predict jet bridging to the outlet is shown in figure 6.18. The manholes with a D_M/D_p ratio greater than 5 (485, 600 and 800 mm diameter manholes) show a hydraulic threshold close to that of the Albertson *et al.* (1950) jet expansion limit. Below this limit, the 385 mm manhole ($D_M/D_p = 4.4$) also shows a step, indicative of a change in hydraulic regime (section 5.5.2). As the D_M/D_p ratio decreases, the surcharge required to cause a change in hydraulic regime also decreases. This is in agreement with the increased short circuiting identified in section 6.3.3; in below-threshold conditions the jet is partially constrained from fully diffusing due to the manhole geometry. Therefore, less surcharge is required to 'suppress' the jet into the short-circuiting flow condition exhibited in above-threshold flow conditions.

Figure 6.18 shows the location of the threshold to be roughly around that of the Albertson prediction for all cases where the manhole is large enough to allow for the full jet expansion region. The 800 mm manhole (and 388 mm manhole with a similar D_M/D_p ratio, shown in figure 6.18) threshold is the closest to this region. This is due to it being the closest representation of an 'infinite volume' within this study. Below this, as the volume decreases, the evidence of a threshold diminishes, with the two smallest cases showing no real indication of differing hydraulic regimes. As the volume available for mixing decreases, the normalised travel times tend towards that of a pipe (i.e. plug flow, figure 6.19).

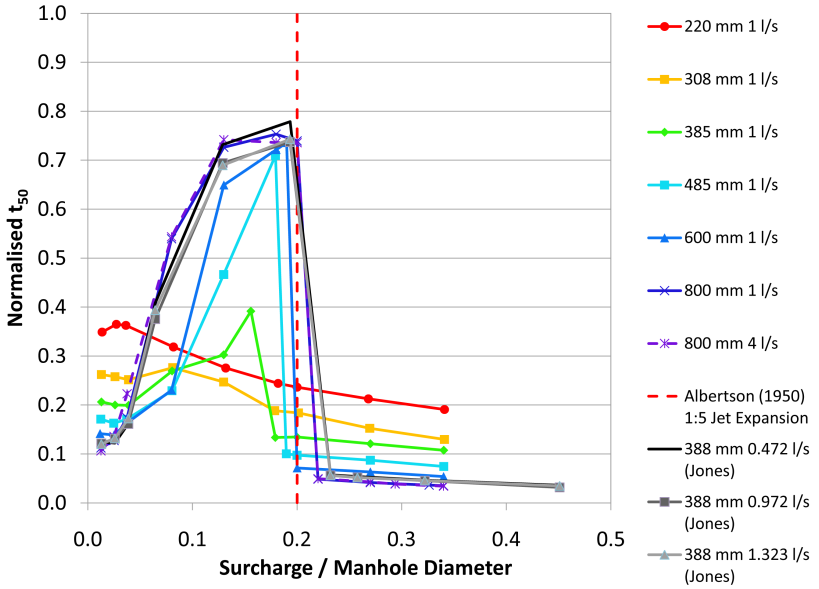

Figure 6.18: Normalised t_{50} against surcharge over D_M including 388 mm manhole results

Figures 6.20-6.23 show the flow fields corresponding to transitional, below threshold surcharge conditions on the CHP. The flow fields clearly demonstrate that an increasing level of surcharge leads to increasing asymmetry, less short-circuiting and more mixing (shown using t_{50}s in figure 6.18).

6.3.5 Comparison with Guymer *et al.* (2005a)

Figure 6.24 shows a comparison between the surcharge elevation related to the hydraulic threshold for all D_M/D_p manholes including those investigated by Guymer *et al.* (2005a). Where enhanced resolution was necessary, extra manhole configurations were added (shown previously in table 6.2). Hydraulic threshold s' limits correspond to that of the closest above and below threshold surcharge height for each D_M/D_p manhole modelled. There is no evidence of the high velocity core of the jet entering the manhole outlet at $D_M/D_p < 6.2$ (Albertson *et al.*, 1950). However, the results presented in section 6.3 are in close agreement with the Albertson *et al.* jet diffusion region. Figure 6.24 also shows the CFD generated results to be in closer agreement with Albertson *et al.* (1950) than the results presented by Guymer *et al.* (2005a). The threshold surcharge elevation is not shown for manholes with D_M/D_p less than, 4.4 as the present flow field and

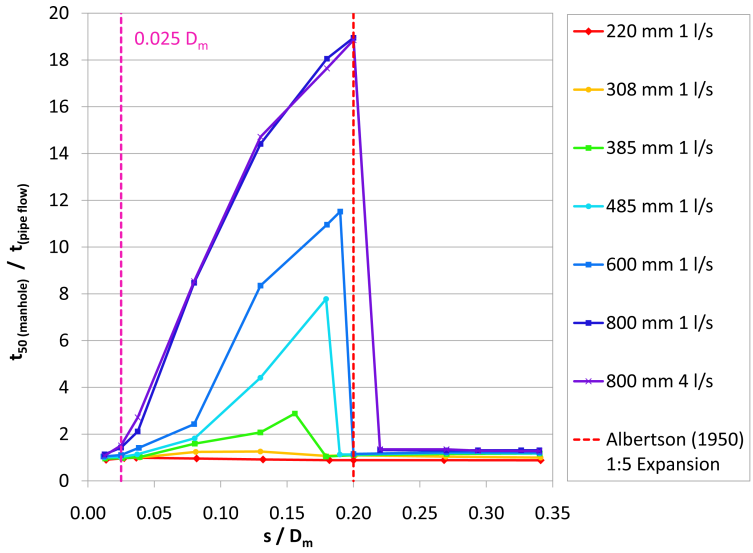

Figure 6.19: Surcharge over D_M against t_{50} normalised using pipe flow travel time

CRTD analysis showed no indication of its existence.

Table 6.3 shows the upper and lower limits of the threshold (S') as shown in figure 6.18. The threshold is defined between 3 and 13 mm accuracy (depending on manhole size) and can be approximated by:

$$s' = 0.2D_m \tag{6.1}$$

D_M (mm)	D_M/D_p (mm)	Q (l/s)	S' (low) (mm)	S' (high) (mm)	S'/D_M (low)	S'/D_M (high)	S'/D_M (mean)
385	4.4	1	60	69	0.16	0.18	0.17
485	5.5	1	87	92	0.18	0.19	0.18
600	6.8	1	117	120	0.20	0.20	0.20
800	9.1	1	163	176	0.20	0.22	0.21
800	9.1	4	163	176	0.20	0.22	0.21

Table 6.3: Upper and lower limits of the hydraulic threshold

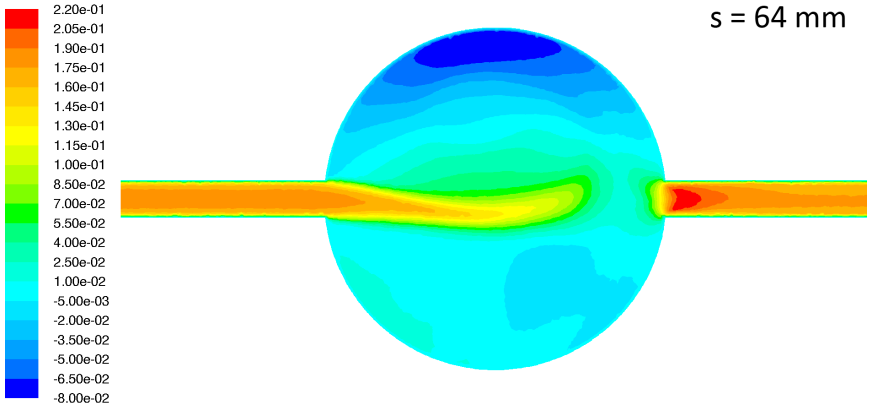

Figure 6.20: Contours of x-velocity, 800mm diameter manhole, $D_M/D_p = 9.1$, $s = 64$ mm

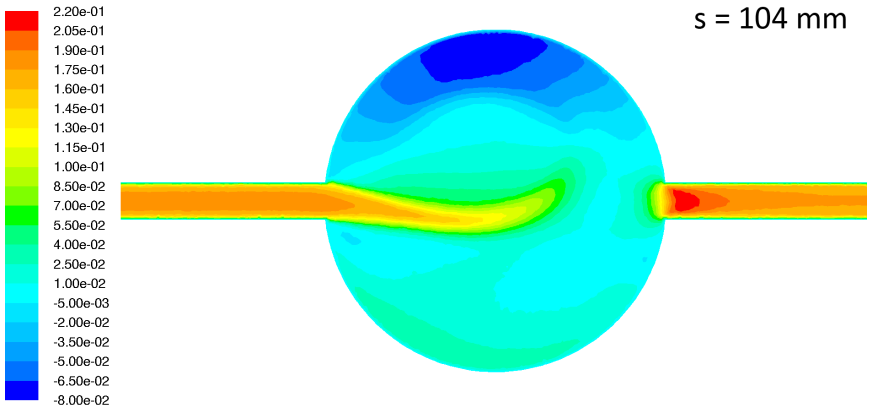

Figure 6.21: Contours of x-velocity, 800mm diameter manhole, $D_M/D_p = 9.1$, $s = 104$ mm

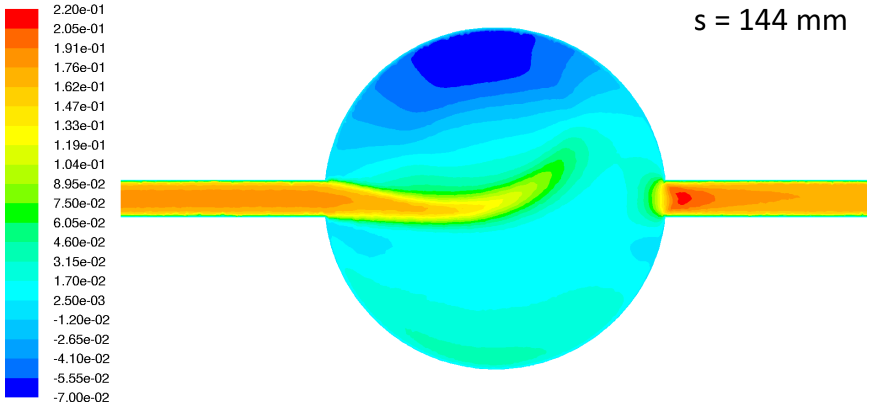

Figure 6.22: Contours of x-velocity, 800mm diameter manhole, $D_M/D_p = 9.1$, $s = 144$ mm

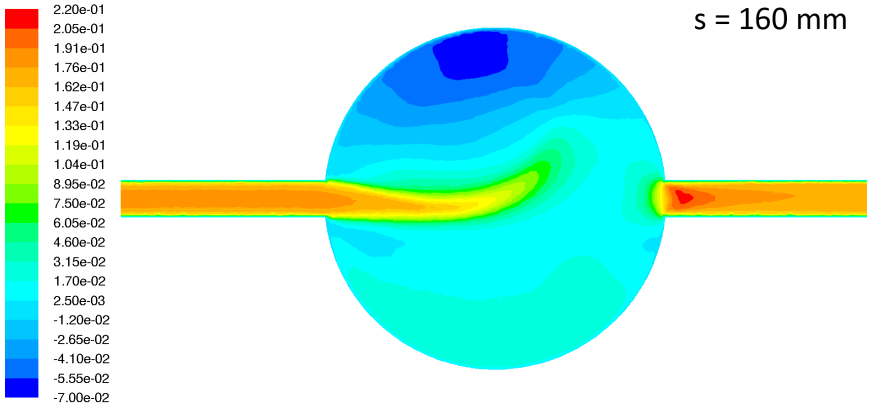

Figure 6.23: Contours of x-velocity, 800mm diameter manhole, D_M/D_p = 9.1, s = 160 mm

6.3.6 The very-low surcharge hydraulic regime

All previous work (Guymer *et al.* (2005a), Lau (2008), Stovin *et al.* (2010) and Guymer and Stovin (2011)) identified two hydraulic regimes. Evidence for an additional flow regime is present in CFD-generated flow fields (section 6.3.1), CRTDs (section 5.4, section 6.3.3 and figure 6.27) and t_{50} data (figure 5.9a and section 6.3.4).

Due to laboratory constraints, Guymer *et al.* (2005a) and Lau (2008) were unable to investigate very low surcharge conditions. Head loss across the laboratory manholes required the addition of a downstream syphon in order to attain below-threshold conditions. Thus very-low surcharge conditions were not investigated.

Figures 6.25 and 6.26 show very low surcharge conditions (s = 0.012 D_M) in the 600 and 800 mm manholes respectively. The jet passes directly to the manhole outlet. This would explain the larger amount of short-circuiting encountered in section 6.3.4 and figure 6.27. The resultant CRTDs are shown in figure 6.27 for each manhole at s = 0.012 and 0.025 D_M. All of the curves appear to have a shape similar to that of an above-threshold CRTD as noted in section 6.3.3. The two s = 0.025 D_M 800 mm manhole CRTDs do not collapse upon the others. This would suggest that s = 0.025 D_M is close to a change in hydraulic regime from that of very-low surcharge conditions to the asymmetric (well-mixed) flow exhibited in below-threshold conditions (figure 6.19). This lower-threshold of s = 0.025 D_M is in agreement with data presented in section 6.3.4.

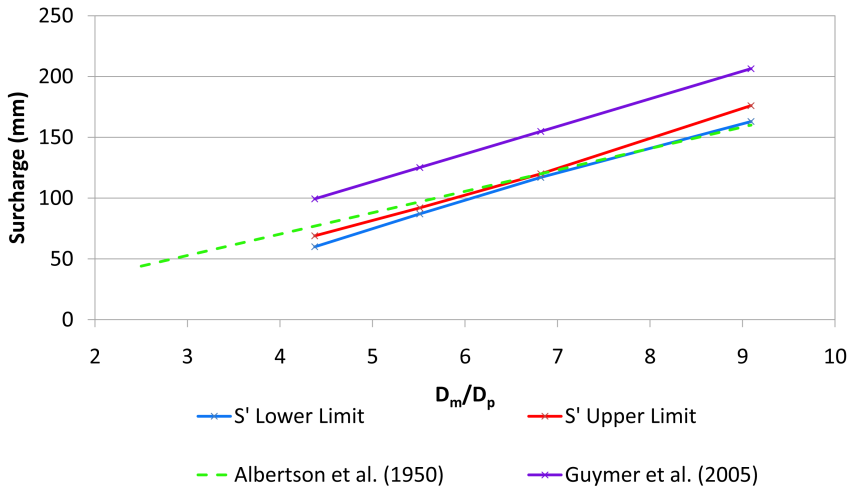

Figure 6.24: Threshold elevation with decreasing D_M/D_p ratio manholes compared with results from Guymer and O'Brien (2000) and Albertson et al. *(1950)*

Currently the very-low surcharge flow regime has only been identified using CFD. The laboratory setup used by Jones (2012) in 5.5.3 was used to generate tracer dye flow visualisations (using red food colouring) for each of the expected flow regimes. The results are shown in Figures 6.28 (very-low surcharge), 6.29 (below-threshold) and 6.30 (above-threshold).

Figure 6.28 clearly shows a similar flow field to figures 6.25 and 6.26. However, the incoming jet length appears shortened in visualisations. The jet fluctuated from side to side gently unlike above-threshold conditions where it was predominantly stable. This fits well with the stepped nature of the corresponding CRTD.

Figures 6.29 and 6.30 show that the lab visualisations were able to demonstrate the previously documented flow conditions and that it was possible to distinguish between the existing flow regimes, and the 'new' very-low surcharge condition.

6.3.7 Normalisation and mean pipe flow

Section 5.3 details the normalisation procedure used thus far. However, removing the travel time due to the pipe sections of the model can be carried out easily using CFD, as monitoring locations can be placed anywhere. This is unlike the laboratory where physical constraints of setup geometries and fluorometer re-

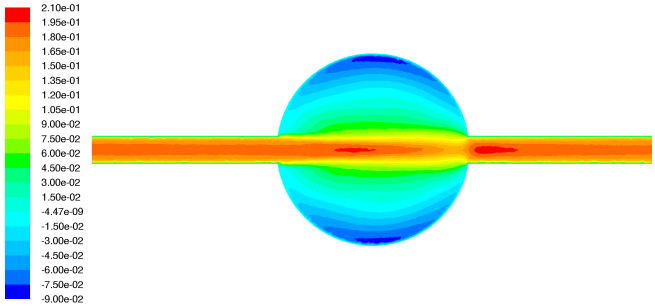

Figure 6.25: Contours of x-velocity, 600 mm diameter manhole, $D_M/D_p = 6.8$, $S = 0.012$

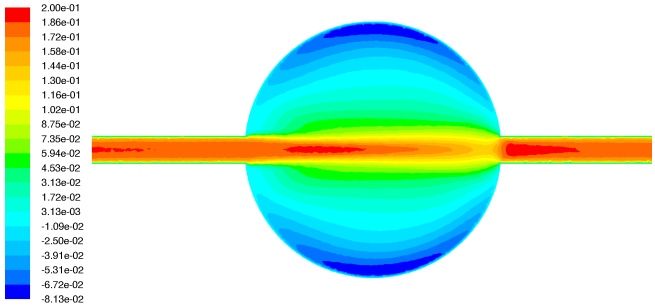

Figure 6.26: Contours of x-velocity, 800 mm diameter manhole, $D_M/D_p = 9.1$, $S = 0.012$

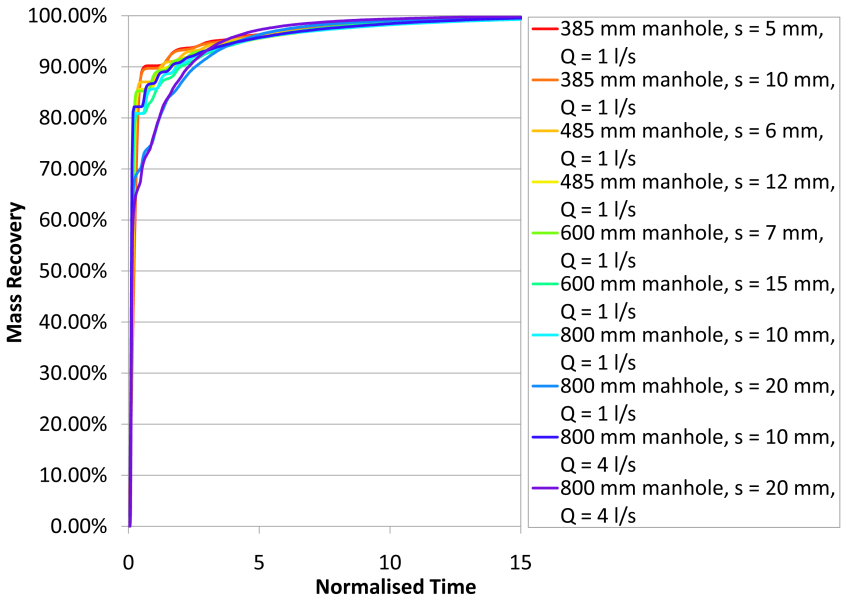

Figure 6.27: Normalised 'very low surcharge' CRTDs

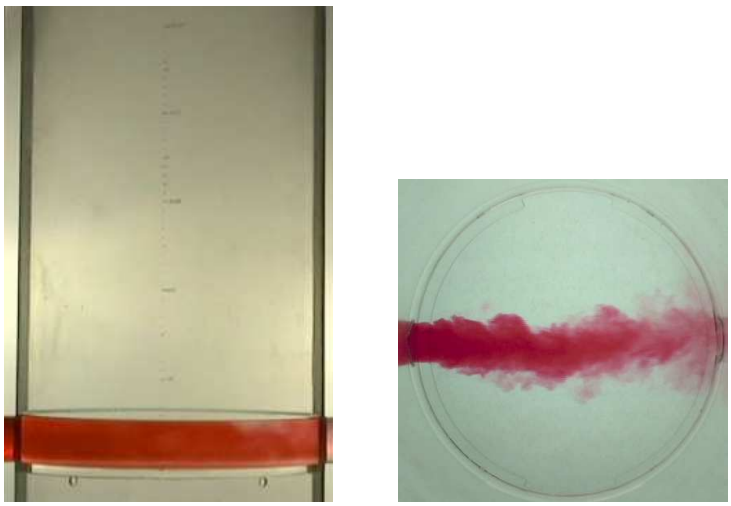

(a) CVP (b) CHP

Figure 6.28: A video screen shot of a laboratory dye trace experiment, s = 5 mm, Q = 0.3 l/s, D_M = 388 mm, D_p = 50 mm, D_M/D_p = 7.76

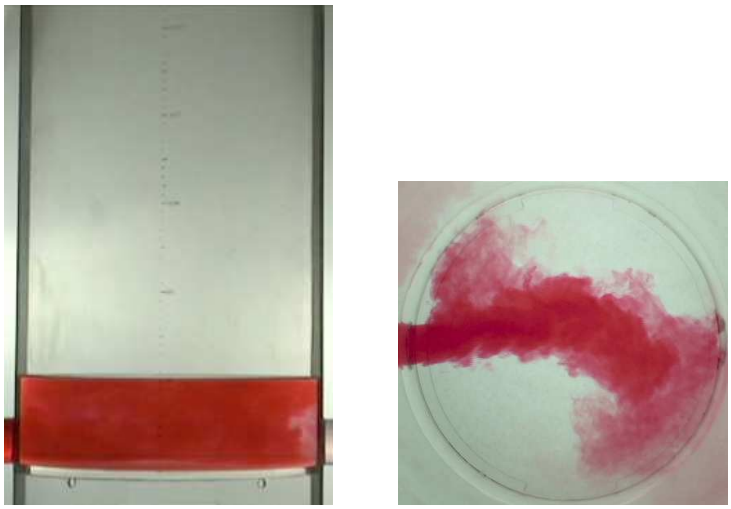

(a) CVP (b) CHP

Figure 6.29: A video screen shot of a laboratory dye trace experiment, s = 50 mm, Q = 0.3 l/s, D_M = 388 mm, D_p = 50 mm, D_M/D_p = 7.76

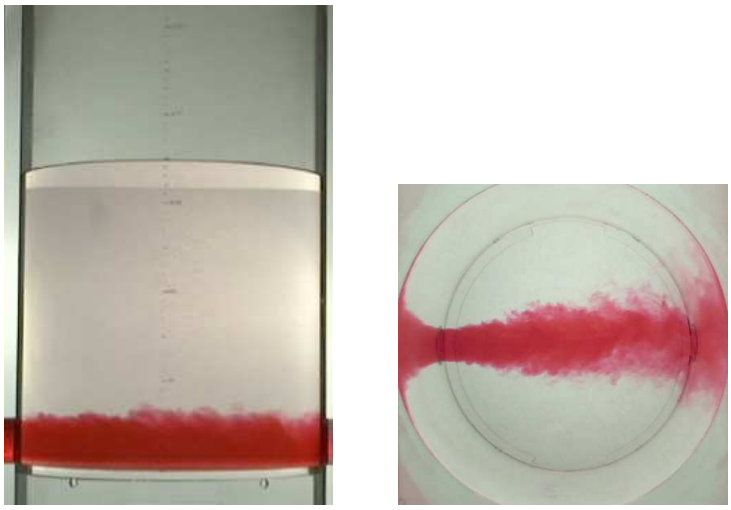

(a) CVP (b) CHP

Figure 6.30: A video screenshot of a laboratory dye trace experiment, s = 300 mm, Q = 0.3 l/s, D_M = 388 mm, D_p = 50 mm, D_M/D_p = 7.76

quirements may dictate the positions necessary. The results presented in chapter 6.3 have assumed mean pipe flow for the length of pipe within the model. The validity of this assumption was tested. Extra monitoring locations were added to a below-threshold, 800 mm manhole configuration (Q = 1 l/s, s = 29 mm). The location of these additional monitors is shown in table 6.4. From this the mean travel time for the length of pipe experienced (all experienced the initial 0.95 m of upstream pipe) and the manhole was recorded (from particle tracking data). This allowed for the calculation of an expected 'Manhole Travel Time'. Manhole travel times were compared as the length of pipe experienced increased until incorporating the whole pipe within the model. The resultant errors were then calculated. The results (shown in table 6.4) show that as the length of pipe downstream of the manhole increases, the resultant error decreases. This shows that the mean pipe flow assumption is not entirely accurate as well-developed flow conditions have not yet been established immediately downstream of the manhole (where the errors in pipe flow are greatest). However the maximum error encountered is 0.53% and is therefore negligible. This information may be useful for future studies looking to improve the location of fluorometers (and was subsequently used by Jones (2012) to improve mass recovery by adding additional fluorometers.

Pipe length (m)	Mean travel time (s)	Mean pipe travel time (s)	Manhole travel time (s)	Normalised manhole travel time	Error (%)
0.9500	5.81	5.84	-	-	0.50
1.1875	110.26	7.30	102.96	1.055	0.53
1.4250	111.70	8.76	102.94	1.055	0.51
1.6625	113.14	10.22	102.92	1.055	0.49
1.9000	114.10	11.68	102.41	1.050	-

Table 6.4: A comparison of normalised manhole travel times calculated using a mean pipe flow assumption against direct CFD monitoring

6.4 Conclusions

Below the hydraulic threshold (previously identified by Guymer *et al.* (2005a) the flow regime behaves as a transitional zone. At its highest surcharge level (just below the threshold), the incoming jet is highly asymmetric causing a large amount of mixing. As surcharge decreases, this jet becomes less asymmetric and the amount of short-circuiting increases. There is not one characteristic CRTD to represent this zone in its entirety.

A third hydraulic regime exists at very-low surcharge levels (s / D_M < 0.025). This regime is dominated by the highest degree of short circuiting and small recirculations causing a 'stepped' shape to the remaining portion of the CRTD.

Below $D_M/D_p = 4.4$, there is no hydraulic threshold. As the CRTDs pertaining to manholes below this limit indicate a rapid, high mass recovery (90%) due to short-circuiting of the jet, the solute transport characteristics of the manhole are currently best ignored by sewer modelling software (such as MOUSETRAP and Infoworks).

The threshold (s') previously identified by Guymer *et al.* (2005a) as 0.258 D_M appears lower in CFD simulations and is in strong agreement with the jet diffusion limit shown by Albertson *et al.* (1950). Within this study s' = 0.2 D_M (equation 6.3.5).

In manholes with a $D_M/D_p < 4.4$, the jet diffusion region (Albertson *et al.* (1950)) is restrained by the geometry of the manhole. This causes the high velocity core

of the jet to pass more easily to the manhole outlet and ultimately leads to the disappearance of the hydraulic threshold.

'Sewers for Adoption' (Water Research Centre PLC (2006)) suggests that manholes with D_M/D_p ratio > 4.4 are unlikely to be found in practice and can therefore be ignored.

Assuming mean pipe flow conditions within pipe sections surrounding the modelled manholes is acceptably accurate (99.5%). However, the modelled errors suggest that laboratory experiments may wish to place fluorometers further from the manhole centre if possible in future studies.

Chapter 7

Conclusions and Further Work

7.1 Conclusions

The initial aim of this study was to investigate the feasibility of extending previous work (Guymer and O'Brien (2000), Guymer *et al.* (2005a), Saiyudthong (2003) and Lau (2008)) into 'more realistic' unsteady conditions. However, section 3.5.2 ultimately showed it to be unnecessary due to the time scales involved (short travel times compared with modelling time steps).

Whilst investigating the feasibility of extending work into unsteady conditions, a highly validated CFD modelling protocol was developed (capable of replicating laboratory results in a number of manhole configurations). This was subsequently used to asses the solute transport characteristics of manholes with D_M/D_p ratios regularly found in UK sewer networks (Water Research Centre PLC, 2006) not previously studied.

The main conclusions from this work are listed below:

- The FLUENT CFD software has been shown to be a robust modelling tool for characterising solute transport within complex flow fields under unsteady inflow conditions allowing for multiple overlapping traces.
- The complexity of 3D unsteady free-surface models (without species modelling) resulted in problems with simulation instability and computational

time requirements that were judged ultimately to be impractical (section 4.2.1.5).

- A method for evaluating dispersion coefficient under time-varying conditions has been proposed and validated using steady flow data.

$$\frac{1}{2}(x_2 - x_1)^2 \frac{1}{(\overline{t_2} - \overline{t_1})} \left(\frac{{\sigma_v}^2(x_2) - {\sigma_v}^2(x_1)}{(\overline{V_2} - \overline{V_1})^2} \right) \tag{7.1}$$

  The generalised method steps are shown in Appendix 1.

- Section 3.2.6 demonstrated that the impact of unsteady conditions on dispersion within a pipe is minor.

- Section 3.5.2 also suggested that solute travel times in manhole are small relative to the time-scales associated with the underlying hydraulics / hydrodynamics of the sewer/manhole system.

- The k-ϵ Realizable turbulence model was shown to reproduce laboratory based PIV flow fields and solute-trace derived CRTDs well under both high and low surcharge conditions. It produced similar levels of agreement to the more computationally expensive RSM model (both models out-performed the k-ϵ RNG model used previously by Lau (2008)).

- A large sample was used to determine the number of particles required for the stochastic Discrete Random Walk (DRW) model to return injection independent results. The results are shown in table 4.7.

- The discrete-phase particle tracking model was chosen to model solute. Its sensitivity to the Time Scale Constant (TSC) allowed for an improved goodness of fit with laboratory trace data (when convolved). Uncoupled particle tracking was found to be roughly ten times more computationally efficient than the alternative species transport model.

- The TSC requires a trial and error approach to obtain a usable value. Its effect is minor, therefore the default value (TSC = 0.15) may be assumed for the majority of solutions.

- An unstructured mesh independency study showed a grid spacing of 3 mm to be appropriate for producing mesh independent results.

- Three VOF schemes were evaluated. The Geo-reconstruct explicit formulation offered the sharpest air-water interface.

- Structured fixed ('rigid') lid and free-surface VOF (pseudo-steady) models were compared. The fixed ('rigid') lid assumption was shown to be a valid way of representing the free-surface and ultimately offered better results for significantly less computational expense. However, it requires prior knowledge of the location of the free surface.

- Table 4.7 provides a summary of the final, validated modelling protocol developed in chapter 4.

- Chapter 5 showed the validated modelling protocol developed in chapter 4 to be capable of replicating t_{50} results for a wide range of flowrates and surcharge depths in a 388 mm manhole.

- A normalisation procedure using the nominal travel time (V/Q) was presented. It showed results to be independent of flowrate and identified clear groupings of curves (attributed to the different hydraulic regimes).

- t_{50} was shown to be a good indicator of the hydraulic threshold.

- The hydraulic threshold in the 388 mm manholes was identified as lying between 0.2 D_M and 0.258 D_M which was in agreement with Jones (2012).

- Below the hydraulic threshold (previously identified by Guymer *et al.* (2005a)) the flow regime behaves as a transitional zone. At its highest surcharge level (just below the threshold), the incoming jet is highly asymmetric causing a large amount of mixing. As surcharge decreases, this jet becomes less asymmetric and the amount of short-circuiting increases. There is not one characteristic CRTD to represent this zone in its entirety.

- A third hydraulic regime exists at very-low surcharge levels ($s / D_M < 0.025$). This regime is dominated by the highest degree of short circuiting and small recirculations causing a 'stepped' shape to the remaining portion of the CRTD.

- Assuming mean pipe flow conditions within pipe sections surrounding the modelled manholes is acceptably accurate (99.5%). However, the modelled

errors suggest that laboratory experiments may wish to place fluorometers further from the manhole centre if possible in future studies.

- The threshold (s') previously identified by Guymer *et al.* (2005a) as $0.258D_M$ appears lower in CFD simulations and is in strong agreement with the jet diffusion limit shown by Albertson *et al.* (1950). Within this study s' = $0.2D_M$.
- In manholes with a $D_M/D_p < 4.4$, the jet diffusion region (Albertson *et al.*, 1950) is restrained by the geometry of the manhole. This causes the high velocity core of the jet to pass more easily to the manhole outlet and ultimately leads to the disappearance of the hydraulic threshold.
- 'Sewers for Adoption' (Water Research Centre PLC, 2006) suggests that manholes with $D_M/D_p > 4.4$ (i.e. with a hydraulic threshold) are unlikely to be found in practice and can therefore be ignored.

It is evident that three conditions are required to induce the well-mixed condition previously termed pre-threshold (Guymer *et al.*, 2005a):

- the manhole diameter must be > 4.4 times the pipe diameter (D_p)
- the surcharge depth must be < 0.2 times the manhole diameter (D_M)
- there is no benching (shown previously by Saiyudthong (2003)).

7.2 Further Work

Throughout this study, avenues of potential future work outside of its scope have become apparent. These are as follows:

- Saiyudthong (2003) investigated benched and unbenched manholes containing a change in direction. This available data would allow for further validation of the modelling methodology presented in chapter 4 and could be extended further to investigate other configurations of manholes (e.g. multiple inlets).

- PIV data from Lau (2008) allowed for insight into the flow fields found within a manhole and formed a basis on which to refine the CFD methodology detailed (chapter 4). However, no such data exists for the very low-surcharge condition identified. Despite this condition being confirmed (visually) by Jones (2012), PIV data would allow for more rigorous confirmation.

- When combined sewer networks are over-capacity, manholes can be surcharged to the point at which they over top. At this point over-land flow occurs. A laboratory or CFD based study could investigate this with the aim of improving water quality flow predictions of these (potentially foul) flows. Djordjević *et al.* (2011) investigates interactions between above and below ground drainage systems and presents preliminary results showing that complex 3D flow features can be replicated using (VOF) CFD (OpenFOAM) models.

- Although this study found free-surface multiphase flows to be both unnecessary and computationally expensive, situations exist in other, more hydrodynamic structures where the fixed ('rigid') lid assumption may be impossible to implement. A rigorous parametric study of the modelling options available for multiphase flows combined with the ever increasing computational power offered by improvements in technology, may allow for these flows to be investigated. Similarly a well validated CFD methodology would provide scope for industry to use CFD instead of scale models.

- At the time of use, the deconvolution code (section 2.4.8) used to obtain the CRTDs from non-instantaneous upstream injections only considered one goodness of fit measure, R_t^2 (Young *et al.*, 1980). Whilst this measure appeared to be fit for purpose it seemed highly sensitive to the lack of secondary peak shown in the Lau (2008) laboratory data. Further development of the code, including an evaluation of other appropriate measures of goodness of fit would be advantageous for future work using CRTDs to classify the solute transport characteristics of any urban drainage structure. Work to this effect is currently being undertaken by *Sonnenwald* within the University of Sheffield. Developments thus far are presented in Sonnenwald *et al.* (2011).

7.2.1 Further considerations

Whilst this study used FLUENT CFD software due to the knowledge base and experience of other users at The University of Sheffield, an open source alternative is gaining in popularity. OpenFOAM is:

'a free, open source CFD software package produced by OpenCFD Ltd. It has a large user base across most areas of engineering and science, from both commercial and academic organisations. OpenFOAM has an extensive range of features to solve anything from complex fluid flows involving chemical reactions, turbulence and heat transfer, to solid dynamics and electromagnetics. It includes tools for meshing, notably snappyHexMesh, a parallelised mesher for complex CAD geometries, and for pre- and post-processing. Almost everything (including meshing, and pre- and post-processing) runs in parallel as standard, enabling users to take full advantage of computer hardware at their disposal.' OpenFOAM (2012).

As the fundamental equations governing CFD are the same, and OpenFOAM contains the turbulence models investigated in this study (k-ϵ RNG, k-ϵ Realizable and RSM) it now presents a very real alternative with a high level of online user support and guidance without associated licensing costs. The main point of difference however is its *'highly modular code design'*. For studies such as these where a validated modelling methodology is created this allows for multiple files to be batch processed efficiently without the need for individual model setup procedures (although this can be done to a certain degree using journal files). Furthermore, one distribution of the software contains a third party post-processor named Paraview. This is a highly powerful tool for flow visualisation offering functionality beyond that found as standard within FLUENT. It is possible to combine visualisations of more than one parameter allowing for a higher level of insight into flow fields. Examples of OpenFoam use are given in Tabor (2010).

7.2.2 Limitations of the Study

- A large proportion of this study concentrates on validation against existing laboratory data sets. None of these laboratory tests were carried out (or

supervised) by the author (despite being able to influence the programme of work carried out by Jones (2012) in order to gain complimentary data sets).

- The initial pipe rig used by Lau (2008) contained a large number of bends due to limited laboratory space. This laboratory rig was used to determine the roughness value (subsequently used throughout), calculated based on energy loss. A more accurate measure of roughness could likely be gained by using a laboratory rig without unnecessary bends.

- PIV data generated by Lau (2008) also contains a degree of uncertainty. It is unclear as to whether regions inside of the flow domain were influenced by conditions outside of the manhole itself (leading to poor data neighbouring boundaries). It is also unclear how far this influence might extend into the manhole domain. Despite this, the PIV data used for validation was capable of demonstrating the large flow structures apparent within the manholes.

- Secondary validation used data from Lau (2008) (in conjunction with an early version of the deconvolution code adapted by Stovin *et al.* (2010)) to produce a 'laboratory data CRTD' for comparison with those generated using CFD. Again, it is unclear as to the quality of this data both before and after deconvolution. Ideally, multiple data sets would have been used.

- In future work, it would be desirable (whenever turbulence models are utilised) to repeat simulations to take into account their random nature. Within this study this was not possible due to time constraints and the large number of simulations required to investigate modelling options.

- Initially this work relied heavily on FLUENT (2005a) which is not a peer reviewed document (despite being based upon peer reviewed material). It was necessary to add additional references (minor amendments), in order to confirm the suggestions of FLUENT (2005a) and check for any commercial bias (or errors).

- Ultimately any computational based study will be limited by the technology available at the time. As advances are made in this area, ever more complex flow simulations may be undertaken using more advanced and computationally expensive models.

References

Adamsson, A., Stovin, V. and Bergdahl, L. (2003). 'Bed shear stress boundary condition for storage tank sedimentation.' *Journal of Environmental Engineering-ASCE*, vol. 129(7), pp. 651–658.

Adeniji-Fashola, A. and Chen, C. (1990). 'Modeling of confined turbulent fluid-particle flows using eulerian and lagrangian schemes.' *International journal of heat and mass transfer*, vol. 33(4), pp. 691–701.

Albertson, M., Dai, Y., Jensen, R. and Rouse, H. (1950). 'Diffusion of submerged jets.' *trans. ASCE*, vol. 115, pp. 639–697.

Asztely, M. and Lyngfelt, S., 'Threedimensional modelling of energy losses in a manhole.' In *7 th International conference on urban drainage, Hanover, Germany* (1996), pp. 647–652.

Aubin, J., Fletcher, D. and Xuereb, C. (2004). 'Modeling turbulent flow in stirred tanks with cfd: the influence of the modeling approach, turbulence model and numerical scheme.' *Experimental thermal and fluid science*, vol. 28(5), pp. 431–445.

Bennett, P., Stovin, V. and Guymer, I. (2011). 'Improved CFD simulation approaches for manhole mixing investigations.' *Proceedings of the 12th International Conference on Urban Drainage*.

Bowden, K. (1965). 'Horizontal mixing in the sea due to a shearing current.' *J. Fluid Mech*, vol. 21(2), pp. 83–95.

Butler, D. and Davies, J., *Urban drainage* (Taylor & Francis, 2004).

Buxton, A. (2002). *The Development of a Computational Methodology for the Prediction of the Sediment Retention Performance of Invert Traps in Combined Sewer Systems*. Ph.D. thesis, University of Sheffield, Department of Civil and Structural Engineering.

Chadwick, A. and Morfett, J., *Hydraulics in civil and environmental engineering*, vol. 1 (Spon press, 1998).

Coroneo, M., Montante, G., Paglianti, A. and Magelli, F. (2011). 'Cfd prediction of fluid flow and mixing in stirred tanks: Numerical issues about the rans simulations.' *Computers & Chemical Engineering*, vol. 35(10), pp. 1959–1968.

Danckwerts, P. (1958). 'Local residence-times in continuous-flow systems.' *Chemical Engineering Science*, vol. 9(1), pp. 78–79.

Dennis, P. (2000). *Longitudinal dispersion due to surcharged manholes*. Ph.D. thesis, University of Sheffield.

Djordjević, S., Saul, A., Tabor, G., Blanksby, J., Galambos, I., Sabtu, I. and Sailor, G. (2011). 'Experimental and numerical investigation of interactions between above and below ground drainage systems.' *Proceedings of the 12th International Conference on Urban Drainage*.

Dufresne, M., Vazquez, J., Terfous, A., Ghenaim, A. and Poulet, J., 'Three-dimensional flow measurements and CFD modelling in a storm-water tank.' In *Novatech: 6th Int. Conf. Lyon, France* (2007).

Feng, X.-P., Zhao, S.-H., Li, J.-X. and Cao, Q. (2011). 'Numerical simulation of swirling flow with different turbulent models.' *Hangkong Dongli Xuebao/Journal of Aerospace Power*, vol. 26(6), pp. 1209–1214.

Fink, J. and Andoh, R., 'CFD as applied to the development of a hydrodynamic vortex mixer.' In *World Environmental and Water Resources Congress 2011@ sBearing Knowledge for Sustainability* (ASCE, 2011), pp. 1472–1483.

Fischer, H. (1973). 'Longitudinal dispersion and turbulent mixing in open-channel flow.' *Annual Review of Fluid Mechanics*, vol. 5(1), pp. 59–78.

FLUENT, *TGrid User's Guide: Release 2.2* (Fluent Inc., 1994).

FLUENT, *Fluent User Manual* (2005a).

FLUENT (2005b). 'Gambit modelling guide.' *Gambit Modelling Guide*.

Grimm, J. (2003). *An Evaluation of Alternative Methodologies for the Numerical Simulation of Solute Transport*. Ph.D. thesis, University of Sheffield, Department of Civil and Structural Engineering.

Guymer, I., Dennis, P., O'Brien, R. and Saiyudthong, C. (2005a). 'Diameter and surcharge effects on solute transport across surcharged manholes.' *Journal of Hydraulic Engineering*, vol. 131, pp. 312.

Guymer, I., Dennis, P., O'Brien, R. and Saiyudthong, C. (2005b). 'Diameter and surcharge effects on solute transport across surcharged manholes.' *Journal of Hydraulic Engineering*, vol. 131(4), pp. 312–321.

Guymer, I. and Dutton, R. (2007). 'Application of transient storage modelling to solute transport across a surcharged manhole.' *Water Science and Technology*, vol. 55(4), pp. 65–73.

Guymer, I. and O'Brien, R. (1995). 'The effects of surcharged manholes on the travel time and dispersion of solutes in sewer systems.' *Water Science and Technology*, vol. 31(7), pp. 51–59.

Guymer, I. and O'Brien, R. (2000). 'Longitudinal dispersion due to surcharged manhole.' *Journal of Hydraulic Engineering*, vol. 126, pp. 137.

Guymer, I., O'Brien, R., Mark, O. and Dennis, P. (1998). 'An investigation of fine sediment mixing within free-flowing and surcharged manholes.' *Water Science and Technology*, vol. 37(1), pp. 215–222.

Guymer, I. and Stovin, V. (2011). 'One-dimensional mixing model for surcharged manholes.' *Journal of Hydraulic Engineering*, vol. 137(10), pp. 1160–1172.

Harwood, R. and Saul, A. (2001). 'Modelling the performance of combined-sewer overflow chambers.' *Journal of the Chartered Institution of Water and Environmental Management*, vol. 15(4), pp. 300–304.

Hattersley, J., Evans, N., Hutchison, C., Cockwell, P., Mead, G., Bradwell, A. and Chappell, M., 'Nonparametric prediction of free-light chain generation in multiple myeloma patients.' In *World Congress*, vol. 17 (2008), pp. 8091–8096.

Hirt, C. and Nichols, B. (1981). 'Volume of fluid (VOF) method for the dynamics of free boundaries.' *Journal of computational physics*, vol. 39(1), pp. 201–225.

Holley, E. and Harleman, D. (1965). 'Dispersion of pollutants in estuary-type flows, hydrodynamic lab. report 74.' *School of Engineering, Massachusetts Institute of Technology*.

Jarman, D., Faram, M., Tabor, G. and Butler, D. (2007). 'A review of the opportunities presented through the application of computational fluid dynamics (CFD) to water management challenges.' *Proceedings of the Combined International Conference of Computing and Control for the Water Industry*, pp. 151–157.

Jones, A. (2012). *Solute Dispersion across Manholes under Time-Varying Flow Conditions*. Ph.D. thesis, University of Warwick School of Engineering.

Kallis, G. and Butler, D. (2001). 'The EU water framework directive: measures and implications.' *Water Policy*, vol. 3(2), pp. 125–142.

Kim, S. and Choudhury, D. (1995). 'A near-wall treatment using wall functions sensitized to pressure gradient.' *Separated and complex flows*, pp. 273–280.

Kim, S., Choudhury, D. and Patel, B. (1999). 'Computations of complex turbulent flows using the commercial code fluent.' *ICASE LaRC Interdisciplinary series in Science and Engineering*, vol. 7, pp. 259–276.

Kluck, J. (1997). *The design of optimally functioning storm water settling tanks*. Ph.D. thesis, Delft University of Technology.

Kouyi, G., Bret, P., Didier, J., Chocat, B. and Billat, C. (2011). 'The use of CFD modelling to optimise measurement of overflow rates in a downstream-controlled dual-overflow structure.' *Water Science and Technology*, vol. 64(2), pp. 521–527.

Lau, S.D., Stovin, V.R. and Guymer, I. (2007). 'The prediction of solute transport in surcharged manholes using CFD.' *Water Science and Technology*, vol. 55(4), pp. 57–64.

Lau, S. (2008). *Scaling Dispersion Processes in Surcharged Manholes*. Ph.D. thesis, University of Sheffield, Department of Civil and Structural Engineering.

Lau, S., Stovin, V. and Guymer, I. (2008). 'Scaling the solute transport characteristics of a surcharged manhole.' *Urban Water Journal*, vol. 5(1), pp. 33–42.

Lau, S., Stovin, V., Guymer, I. and Saul, A. (2004). 'Prediction of storm tank performance using Computational Fluid Dynamics.' *4th Int. Symp. on Environmental Hydraulics, IAHR, Hong Kong*, pp. 1509–1514.

Launder, B., Reece, G. and Rodi, W. (1975). 'Progress in the development of a reynolds-stress turbulence closure.' *Journal of fluid mechanics*, vol. 68(03), pp. 537–566.

Levenspiel, O. (1958). 'Longitudinal mixing of fluids flowing in circular pipes.' *Industrial & Engineering Chemistry*, vol. 50(3), pp. 343–346.

Liu, C., Huhe, A. and Ma, W. (2002). 'Numerical and experimental investigation of flow over a semicircular weir.' *Acta Mechanica Sinica/Lixue Xuebao*, vol. 18(6), pp. 594–602.

Madden, F., Godfrey, K., Chappell, M., Hovorka, R. and Bates, R. (1996). 'A comparison of six deconvolution techniques.' *Journal of Pharmacokinetics and Pharmacodynamics*, vol. 24(3), pp. 283–299.

Mignot, E., Bonakdari, H., Knothe, P., Kouyi, G., Bessette, A., Rivière, N. and Bertrand-Krajewski, J. (2011). 'Experiments and 3d simulations of flow structures in junctions and of their influence on location of flowmeters.' *Proceedings of the 12th International Conference on Urban Drainage*.

Niño, Y. and Tamburrino, A. (2004). 'Flow and transport equations in surface waters.' *HIDRODINAMICA AMBIENTAL*, vol. 71.

Özkan, F., Wörner, M., Wenka, A. and Soyhan, H. (2007). 'Critical evaluation of cfd codes for interfacial simulation of bubble-train flow in a narrow channel.' *International Journal for Numerical Methods in Fluids*, vol. 55(6), pp. 537–564.

Pathapati, S. and Sansalone, J. (2009). 'CFD modeling of a storm-water hydrodynamic separator.' *Journal of Environmental Engineering*, vol. 135, pp. 191.

Pattamatta, A. and Singh, G. (2012). 'Assessment of turbulence models in the prediction of flow field and thermal characteristics of wall jet.' *Frontiers in Heat and Mass Transfer*, vol. 3(2).

Rutherford, J., *River mixing* (John Wiley & Son Ltd, 1994).

Saiyudthong, C. (2003). *Effect of Changes in Pipe Direction Across Surcharged Manholes on Dispersion and Head Loss*. Ph.D. thesis, University of Sheffield.

Shih, T., Liou, W., Shabbir, A., Yang, Z. and Zhu, J. (1995). 'A new k-ϵ eddy viscosity model for high reynolds number turbulent flows.' *Computers & Fluids*, vol. 24(3), pp. 227–238.

Skilling, J. and Bryan, R. (1984). 'Maximum entropy image reconstruction-general algorithm.' *Monthly Notices of the Royal Astronomical Society*, vol. 211, pp. 111.

Sokolichin, A., Eigenberger, G., Lapin, A. and Lübert, A. (1997). 'Dynamic numerical simulation of gas-liquid two-phase flows euler/euler versus euler/lagrange.' *Chemical Engineering Science*, vol. 52(4), pp. 611–626.

Sonnenwald, F., Stovin, V. and Guymer, I. (2011). 'The influence of outlet angle on solute transport in surcharged manholes.' *Proceedings of the 12th International Conference on Urban Drainage*.

Stefan, H. and Demetracopoulos, A. (1981). 'Cells-in-series simulation of riverine transport.' *Journal of the Hydraulics Division, ASCE*, vol. 107(HY6, Proc. Paper, 16349), pp. 675–697.

Stovin, V. (1996). *The prediction of sediment deposition in storage chambers based on laboratory observations and numerical simulation*. Ph.D. thesis, The University of Sheffield, Department of Civil and Structural Engineering.

Stovin, V., Grimm, J., Buxton, A. and Tait, S. (2002a). 'Parametric studies on CFD models of sewerage structures.' *Global Solutions for Urban Drainage*, pp. 1–15.

Stovin, V., Grimm, J. and Lau, S. (2008a). 'Solute transport modeling for urban drainage structures.' *Journal of Environmental Engineering*, vol. 134(8), pp. 640–650.

Stovin, V., Grimm, J. and Saul, A. (2002b). 'Fine sediment retention in storage chambers: an assessment of time-dependent effects.' *Water Science and Technology: a journal of the International Association on Water Pollution Research*, vol. 45(7), pp. 123–132.

Stovin, V., Guymer, I., Chappell, M. and Hattersley, J. (2010). 'The use of deconvolution techniques to identify the fundamental mixing characteristics of urban drainage structures.' *Water Science and Technology: a journal of the International Association on Water Pollution Research*, vol. 61(8), pp. 2075.

Stovin, V., Guymer, I. and Lau, S., 'Approaches to validating a 3D CFD manhole model.' In *11th Int. Conf. on Urban Drainage* (2008b).

Stovin, V. and Saul, A. (1998). 'A computational fluid dynamics (CFD) particle tracking approach to efficiency prediction.' *Water Science and Technology*, vol. 37(1), pp. 285–293.

Stovin, V., Saul, A., Drinkwater, A. and Clifforde, I. (1999). 'Field testing CFD-based predictions of storage chamber gross solids separation efficiency.' *Water Science and Technology*, vol. 39(9), pp. 161–168.

Stovin, V., Schellart, A., Tait, S., Ashley, R. and Burkhard, R., 'Sewer invert trap design using laboratory and CFD models and continuous simulation.' In *Proceedings of the 10th International Conference on Urban Drainage (10ICUD), Copenhagen, Denmark* (2005), pp. 21–26.

Stovin, V. R., Grimm, J. P. and Lau, D. S. (2007). 'Modelling longitudinal dispersion an upstream temporal concentration profile-independent approach.' *Fifth International Symposium on Environmental Hydraulics.*

Stovin, V. R., Grimm, J. P. and Lau, S.-T. D. (2008). 'Solute transport modeling for urban drainage structures.' *Journal of Environmental Engineering*, vol. 134(8), pp. 640–650.

Ta, C., 'Computational fluid dynamic model of storm tank.' In *Proc. the Eighth International Conference on Urban Storm Drainage* (1999).

Tabor, G. (2010). 'Openfoamr: An Exeter perspective.' *European Conference on Computational Fluid Dynamics.*

Taylor, G. (1953). 'Dispersion of soluble matter in solvent flowing slowly through a tube.' *Proceedings of the Royal Society of London. Series A. Mathematical and Physical Sciences*, vol. 219(1137), pp. 186.

Taylor, G. (1954). 'The dispersion of matter in turbulent flow through a pipe.' *Proceedings of the Royal Society of London. Series A. Mathematical and Physical Sciences*, vol. 223(1155), pp. 446.

Turnbull, J. (2003). *A novel approach to reduce the computation time for CFD; hybrid LES–RANS modelling on parallel computers.* Ph.D. thesis, Cranfield University.

Tyack, J. and Fenner, R. (1999). 'Computational fluid dynamics modelling of velocity profiles within a hydrodynamic separator.' *Water Science and Technology*, vol. 39(9), pp. 169–176.

Ubbink, O., *Numerical prediction of two fluid systems with sharp interfaces* (University of London UK, 1997).

Versteeg, H. and Malalasekera, W., *An introduction to computational fluid dynamics: the finite volume method* (Prentice Hall, 2007).

Wacławczyk, T. and Koronowicz, T. (2008). 'Comparison of cicsam and hric high-resolution schemes for interface capturing.' *Journal of theoretical and applied mechanics*, vol. 46(2), pp. 325–345.

Water Research Centre PLC, *Sewers for Adoption - A Design and Construction Guide for Developers - Sixth Edition* (Water Research Centre PLC, 2006).

Young, P., Jakeman, A. and McMurtrie, R. (1980). 'An instrumental variable method for model order identification.' *Automatica*, vol. 16(3), pp. 281–294.

Youngs, D. (1982). 'Time-dependent multi-material flow with large fluid distortion.' *Numerical methods for fluid dynamics*, vol. 24, pp. 273–285.

Zhu, J. and Shih, T. (1994). 'Computation of confined coflow jets with three turbulence models.' *International journal for numerical methods in fluids*, vol. 19(10), pp. 939–956.

Appendix 1: Derivation of Equation 3.3

To estimate dispersion for unsteady and non-uniform flows, consider a number of cases (each flowing full).

Case 1	Case 2	Case 3
Area constant, $\frac{dA}{dx} = 0$	Area, A = f(x)	Area constant, $\frac{dA}{dx} = 0$
Discharge steady (t)	Discharge steady (t)	Discharge = f(t)
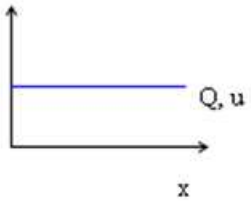	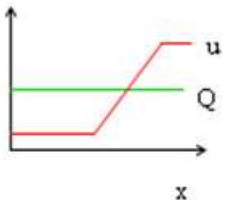	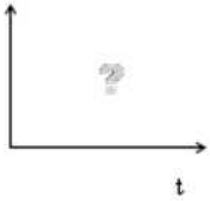
No temporal variation $A = area\ (m^2)$ $u = velocity\ (m/s)$	No temporal variation	If Q, A and u are constant with respect to x and steady with respect to time

Taylor (1953, 1954) showed that downstream from a source, equilibrium established between longitudinal dispersion (transverse velocity shear) and transverse mixing, after this point variance (spatial) increases linearly with time.

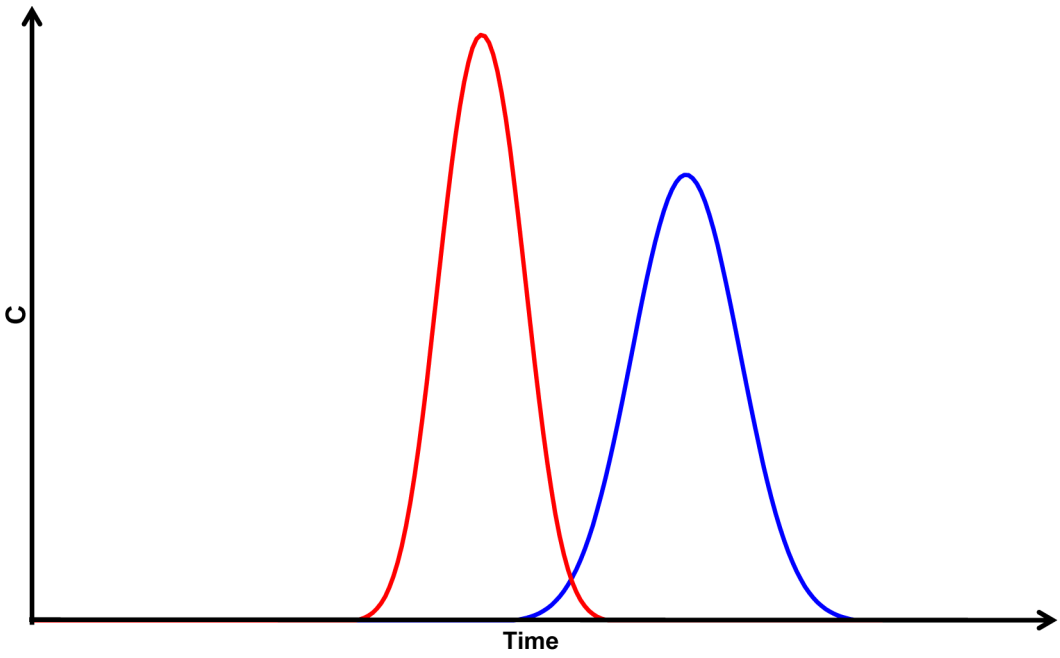

This is valid for Case 1 - constant area and steady flow gives:

$$D = \frac{1}{2}\frac{D{\sigma_x}^2 t}{dt} = \frac{1}{2}\frac{1}{(\overline{t_2} - \overline{t_1})}({\sigma_x}^2(t_2) - {\sigma_x}^2(t_1)) \tag{2}$$

where:

- ${\sigma_x}^2$ = spatial variance

If in the equilibrium zone, i.e. x or t constant, then:

$$D = \frac{1}{2}u^2\frac{d{\sigma_t}^2}{t} = \frac{1}{2}\left[\frac{(x_2 - x_1)}{(\overline{t_2} - \overline{t_1})}\right]^2\left(\frac{{\sigma_t}^2(x_2) - {\sigma_t}^2(x_1)}{\overline{t_2} - \overline{t_1}}\right) \tag{3}$$

where:

- ${\sigma_x}^2(x_i)$ = spatial variance at x_i

Application of this to either spatially varying conditions or temporally varying flows is invalid. However, Holley and Harleman (1965) and Fischer (1973) reported results from oscillatory flow in pipes showing that the *'dispersion coefficient was the same as if the flow had been steady with a velocity equal to the*

mean absolute velocity of the oscillatory flow'. Bowden (1965) showed the same analytically. These studies referred to work carried out where Q = f(t) and A = f(x).

The problem with using equation 3 to evaluate cases 2 and 3 is that if velocity increase at site 2, then the cloud of tracer may appear to reduce 'temporal spread'. Whilst assumptions are invalid it may be possible to obtain an illustrative value of D by considering spread as a function of volumetric flow.

For case 3, velocity u = f(t)

$$D = \frac{1}{2}u^2\frac{d{\sigma_t}^2}{t} = \frac{1}{2}\left[\frac{(x_2 - x_1)}{(\overline{t_2} - \overline{t_1})}\right]^2\left(\frac{{\sigma_t}^2(x_2) - {\sigma_t}^2(x_1)}{\overline{t_2} - \overline{t_1}}\right) \tag{4}$$

where:

- ${\sigma_t}^2(x_i)$ = temporal variance at x_i

The suggested alternative approach using (c,V) plot:

$$D = \frac{1}{2}u^2\frac{d{\sigma_t}^2}{t} = \frac{1}{2}\left[\frac{(x_2 - x_1)}{(\overline{t_2} - \overline{t_1})}\right]^2\left(\frac{{\sigma_v}^2(x_2) - {\sigma_v}^2(x_1)}{\overline{V_2} - \overline{V_1}}\right) \tag{5}$$

where:

- ${\sigma_v}^2(x_i)$ = volumetric variance at x_i
- $\overline{t_1}$,$\overline{t_2}$ obtained by calculating $\overline{V_2}$ and $\overline{V_1}$ and then (V,t) plot to determine $\overline{t_2}$ and $\overline{t_1}$/

Check:

If velocity u = constant; discharge, Q = constant, then $Volume = Q \cdot t$ and equation 5 gives the same as equation 4

It is not possible to obtain a general form of equation 5 as this depends on the Q(t) variation. However for laboratory and CFD data this is determinable:

$$\frac{1}{2}(x_2 - x_1)^2 \frac{1}{(\overline{t_2} - \overline{t_1})} \left(\frac{{\sigma_v}^2(x_2) - {\sigma_v}^2(x_1)}{(\overline{V_2} - \overline{V_1})^2} \right) \tag{6}$$

The generalised method steps are shown below:

- Using (C,t) data (laboratory or CFD) and a knowledge of Q(t); generate (C,V) plots
- For each site determine centroid, $\overline{V}$ and variance ${\sigma_v}^2$
- For $\overline{V}$ values determine equivalent $\bar{t}$
- Use equation 6 to determine an estimated D (m^2/s)

Appendix 2: A Summary of Material Data

This appendix contains a summary of material data which was used for validation work throughout this study, covering manhole diameter, pipe diameter, surcharge, flowrate and flow (as well as other) conditions (i.e. steady/unsteady and benched/unbenched).

Lau (2008) is used for validation work in chapter 4 and used a RANS based approach for CFD simulations with Enhanced Wall Treatment (EWT). Jones (2012) is used for validation work in chapter 5. Guymer *et al.* (2005b) is used for validation work in chapter 6.

Table 3.5 contains a 'Standard Modelling Protocol for Manhole Simulations' (after Lau 2008). Table 6.2 details D_M/D_p manhole sizes modelled for comparison with Guymer *et al.* (2005b).

For CFD based studies used for validation, uncertainty exists in the accuracy and quality of the mesh, selection of the correct turbulence model, the number of repeat runs carried out (to allow for the inherent random nature of modelled turbulence) as well as residual accuracy and overall convergence. Models such as the species, and discrete phase particle tracking, also add another element of uncertainty to any modelled results. However, Lau (2008) carried out a large amount of validation work and showed results that represented the main features of the mean flow field well.

The uncertainties regarding PIV measurements used for validation are discussed

Original Study	Type	D_m (mm)	D_p (mm)	Surcharge Ratio (S)	Flowrate, Q (l/s)	Conditions	Benching
Lau (2008)	PIV	218	24	1.17, 3.27	0.35	Steady	No
Lau (2008)	CFD, k-ϵ RNG	218	24	1.17, 3.27	0.35	Steady	No
Lau (2008)	CFD, k-ϵ RSM	218	24	1.17, 3.27	0.35	Steady	No
Lau (2008)	Laboraotry Traces	218	24	1.17, 3.27	0.35	Steady	No
Lau (2008)	Derived CRTDs	218	24	1.17, 3.27	0.35	Steady	No
Jones (2012)	Laboratory Traces	388	50	0 - 5.3	0.273, 0.308, 0.351, 0.472, 0.727, 1.322, 1.473	Steady	No
Jones (2012)	Laboratory Visualisations	388	50	0 - 5.3	0.273, 0.308, 0.351, 0.472, 0.727, 1.322, 1.473	Steady	No
Jones (2012)	Derived CRTDs	388	50	0 - 5.3	0.273, 0.308, 0.351, 0.472, 0.727, 1.322, 1.473	Steady	No
Guymer *et al.* (2005b)	Travel Times	385, 485, 600, 800	88	0.0625 - 0.625	1, 4	Steady	No
Guymer *et al.* (2005b)	Laboratory Traces	385, 485, 600, 800	88	0.0625 - 0.625	1, 4	Steady	No
Guymer *et al.* (2005b)	Derived CRTDs	385, 485, 600, 800	88	0.0625 - 0.625	1, 4	Steady	No

Table 1: Summary of Material Data used for Validation work

in section 7.2.2 as well as in chapter 4. These relate to uncertainties surrounding measurements near the manhole boundaries. Uncertainties regarding laboratory cut-off techniques and fluorometer noise are discussed in section 5.5 and appear to have incorrectly lead to the artificial cut-off of the small scale secondary circulations evident in solute traces conducted by this study.

The limitations of this study are summarised in section 7.2.2.

Appendix 3: The CHP and CVP

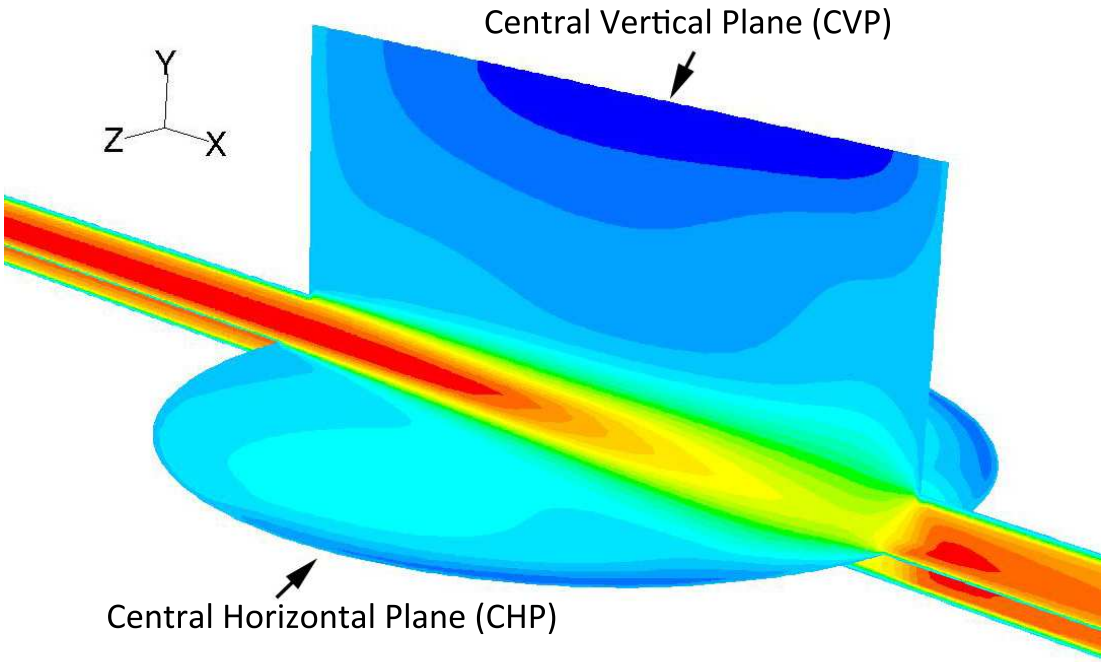

Figure 1: The Central Horizontal and Central Vertical Planes